UCL

Department of Electronic and Electrical Engineering

Doctor of Philosophy

Pulsed dynamics in silicon and diamond photonic nanostructures

Author:

Victor Manuel Fernandez Laguna

August 2023

Declaration

I, Victor Manuel Fernandez Laguna confirm that the work presented in my thesis is my own. Where information has been derived from other sources, I confirm that this has been indicated in the thesis.

Abstract

The work carried out in this thesis has been motivated by the promising applicability of photonic nanostructures in optical communications, internet data centers (ICD) and biosensing, to name a few. In particular, the dispersion and nonlinear engineering that silicon photonic crystal waveguides (Si-PhCWGs) and diamond-fin waveguides allow, can be exploited in the design of important photonic components, such as frequency comb generators, Raman amplifiers or filters. Within such objectives, we present rigorous and comprehensive theoretical models where all relevant linear and nonlinear optical effects, including modal dispersion, waveguide loss, free-carrier (FC), Kerr and Raman effects are considered. In the case of the newly developed subwavelength diamond-fin waveguides, we complete a detailed characterization of their dispersion and nonlinear optical properties, along with an analysis of pulsed dynamics in these structures. As a relevant application, we demonstrate how these waveguides can be employed to efficiently generate soliton frequency combs in the visible spectral domain. With regards to Si-PhCWGs, we firstly explore the effect of stimulated Raman scattering in the slow-light regime, and demonstrate that signal amplification without pulse distortion can be achieved. Secondly, we add photonic crystal cavities (PhCCs) alongside the Si-PhCWG, with the associated inter-cavity coupling and waveguide-cavity interactions. Therefore, we describe a novel mathematical model and its corresponding computational tool that solves the dynamics of the forwards and backwards propagating pulses, the energy in the cavities and the FCs at the waveguide and at the cavities. Finally, we show the potential practical use of the model by simulating a photonic drop-filter with back reflection nulling.

Impact statement

The theoretical work carried out in this thesis has led to interesting discoveries that could bring different benefits both to academia and industry.

On the one hand, the impact that this work could have in academia is centered mainly on the application of new numerical methods to solve complex mathematical problems, thus bringing broad benefits, since these methods could be employed into various disciplines or applied sciencies. Indeed, the methods and algorithms described, developed and demonstrated throughout this work can serve as example or source of ideas to students and researchers who may have the challenge to solve similar problems. In addition, this thesis can help Master or PhD students to understand the linear and nonlinear physics involved in the propagation of pulses through photonic waveguides, which is key to effectively manage the capabilities and limitations that are important at system level.

On the other hand, with regards to the impact outside academia, different topics deserve to be mentioned.

Firstly, the work described in Chapter 4 could motivate the development of diamond photonic platforms, which we have demonstrated that can enable key nonlinear functions in the visible spectral domain. This would be an appealing alternative to well-established, more mature photonic platforms, such as silicon-on-insulator, silicon nitride, or compound semiconductor on-insulator. Importantly, the subwavelength diamond waveguides we have studied could enable the development of photonic systems that incorporate cheaper light sources, such as vertical-cavity surface-emitting lasers (VCSELs) at 850 nm, exten-

sively used in data centers, therefore helping the photonics industry to become more cost-effective. Furthermore, the work in this thesis on the frequency comb generator based on diamond-fin ring resonator could bring attention towards the development of diamond photonics for nonlinear applications. All the above could also facilitate the establishment of this platform for quantum computing, which is believed to be one of the future core applications of diamond.

Secondly, the results shown in Chapter 5 could encourage photonic designers, foundries and chip manufacturers to exploit Raman amplification in silicon photonic chips, which could dramatically change the current industrial ecosystem in which the need of fabricating complex heterogeneous structures made of photonic integrated circuits from different technologies is required in order to fill the gap that silicon has in light generation due to having an indirect bandgap. Note that this would become an important development applicable to multiple practical fields where silicon photonics have been the most successful commercial platform.

Finally, the comprehensive mathematical model described in Chapter 6 could be beneficial to photonic design and simulation software companies, who could take some of the concepts and ideas employed here in order to enhance the fidelity on their platforms to the complex physics involved in these problems. More specifically, although several approaches have been applied to similar problems, these have been limited to continuous wave signals or do not include free-carrier (FC) dynamics. On the contrary, in this work we present a novel methodology which is applicable to pulse propagation and incorporates the key effects of FCs in both the waveguide and cavities situated alongside it, including FC dispersion and FC absorption, as well as, two-photon-absorption (TPA), the nonlinear Kerr effect and the waveguide dispersive effects. Furthermore, the employment of this model to analyse the scenario consisting on photonic crystal cavities alongside a photonic crystal waveguide could benefit different applications, from biosensing, given the light-matter interaction can be enhanced through the use of photonic crystals, to communications, since these structures could be employed to design filters or delay lines.

Research paper declaration form

Paper 1

1. **For a research manuscript that has already been published:**

   (a) **What is the title of the manuscript?** Pulsed dynamics in a system of coupled silicon photonic crystal cavity-waveguide nanostructures

   (b) **Please include a link to or doi for the work:** https://doi.org/10.1117/12.2526658

   (c) **Where was the work published?** SPIE

   (d) **Who published the work?** SPIE

   (e) **When was the work published?** 2019

   (f) **List the manuscript's authors in the order they appear on the publication:** Victor Manuel Fernandez Laguna, Qun Ren, and Nicolae C. Panoiu

   (g) **Was the work peer reviewed?** Yes

   (h) **Have you retained the copyright?** Yes

   (i) **Was an earlier form of the manuscript uploaded to a preprint server (e.g. medRxiv)? If Yes, please give a link or doi** No

   If No, please seek permission from the relevant publisher and check the box next to the below statement:

   ☒ *I acknowledge permission of the publisher named under 1d to include in this thesis portions of the publication named as included in 1c.*

2. **For multi-authored work, please give a statement of contribution covering all authors :** The first author, as the PhD student and author of this thesis, carried out the definition and implementation of the numerical method, the photonic crystal waveguide modes characterisation, full system simulations and results presentation via the manuscript. The second author, also PhD student at the time, provided the simulations for the photonic crystal cavity modes, and, finally, the third author, as the supervisor of the PhD students, provided the grounds of the mathematical model, guidance, technical and theoretical support throughout the project, as well as the revision of the manuscript.

3. **In which chapter(s) of your thesis can this material be found?** Chapter 6.

Paper 2

1. **For a research manuscript that has already been published :**

   (a) **What is the title of the manuscript?** Nonlinear optics in diamond-fin photonic nanowires: soliton formation and frequency comb generation

   (b) **Please include a link to or doi for the work:** https://doi.org/10.1364/OE.468922

   (c) **Where was the work published?** Optics Express

   (d) **Who published the work?** Optica Publishing Group

   (e) **When was the work published?** 2022

   (f) **List the manuscript's authors in the order they appear on the publication:** Victor M. Fernandez Laguna and Nicolae C. Panoiu

   (g) **Was the work peer reviewed?** Yes

   (h) **Have you retained the copyright?** Yes, under the terms of the Creative Commons Attribution 4.0 License.

   (i) **Was an earlier form of the manuscript uploaded to a preprint server (e.g. medRxiv)? If Yes, please give a link or doi** No

If No, please seek permission from the relevant publisher and check the box next to the below statement:

☒ *I acknowledge permission of the publisher named under 1d to include in this thesis portions of the publication named as included in 1c.*

2. **For multi-authored work, please give a statement of contribution covering all authors :** The first author, as the PhD student and author of this thesis, carried out the mathematical modelling, the simulations and results presentation via the manuscript. The second author, as the supervisor of the PhD student, provided guidance, technical and theoretical support throughout the project, as well as the revision of the manuscript.

3. **In which chapter(s) of your thesis can this material be found?** Chapter 4.

Paper 3

1. **For a research manuscript prepared for publication but that has not yet been published :**

   (a) **What is the current title of the manuscript?** Raman interaction in one-dimensional silicon photonic crystal slab waveguides

   (b) **Has the manuscript been uploaded to a preprint server 'e.g. medRxiv'? If 'Yes', please please give a link or doi:** No

   (c) **Where is the work intended to be published?** Phys. Rev. A

   (d) **List the manuscript's authors in the intended authorship order:** Victor M. Fernandez Laguna and Nicolae C. Panoiu

   (e) **Stage of publication:** In submission

2. **For multi-authored work, please give a statement of contribution covering all authors :** The first author, as the PhD student and author of this thesis,

carried out the mathematical modelling, the simulations and results presentation via the manuscript. The second author, as the supervisor of the PhD student, provided guidance, technical and theoretical support throughout the project, as well as the revision of the manuscript.

3. **In which chapter(s) of your thesis can this material be found?** Chapter 5.

Paper 4

1. **For a research manuscript prepared for publication but that has not yet been published :**

   (a) **What is the current title of the manuscript?** Pulsed dynamics in coupled cavity-waveguide silicon photonic crystal structures

   (b) **Has the manuscript been uploaded to a preprint server 'e.g. medRxiv'? If 'Yes', please please give a link or doi:** No

   (c) **Where is the work intended to be published?** Phys. Rev. B

   (d) **List the manuscript's authors in the intended authorship order:** Victor Manuel Fernandez Laguna, Qun Ren, and Nicolae C. Panoiu

   (e) **Stage of publication:** In submission

2. **For multi-authored work, please give a statement of contribution covering all authors :** The first author, as the PhD student and author of this thesis, carried out the definition and implementation of the numerical method, the photonic crystal waveguide modes characterisation, full system simulations and results presentation via the manuscript. The second author, also PhD student at the time, provided the simulations for the photonic crystal cavity modes, and, finally, the third author, as the supervisor of the PhD students, provided the grounds of the mathematical model, guidance, technical and theoretical support throughout the project, as well as the revision of the manuscript.

3. **In which chapter(s) of your thesis can this material be found?** Chapter 6.

e-Signatures confirming that the information above is accurate (this form should be co-signed by the supervisor/ senior author unless this is not appropriate, e.g. if the paper was a single-author work)**:**

Candidate: Victor Manuel Fernandez Laguna

Date: 09-06-2023

Supervisor/Senior Author signature : Prof. Nicolae C. Panoiu

Date: 09-06-2023

Nicolae-Coriolan Panoiu

Digitally signed by Nicolae-Coriolan Panoiu
Date: 2023.08.24 10:34:42 +01'00'

Acknowledgments

I am deeply grateful to Prof. Nicolae C. Panoiu for the invaluable time he has spent with me, for his huge scientific insight, bright ideas and patient way of teaching and guiding me, through which I have been able to complete challenging projects, design strategies to solve the different problems I have encountered and think smartly over the results of any research activity. The analytical and problem-solving mindset I have acquired from him will probably be the best takeaway from this journey.

I would also like to thank my fellow colleagues Dr. Abiola Oladipo, who originally introduced me to Prof. Nicolae C. Panoiu's group; Qun Ren, for her kindness and technical contribution to the cavity - waveguide project; and Dr. Jian Wei You for being a great office colleague. Additionally, I would like to mention Jie You and Spyros Lavdas who are not part of the group any more, but who were key to help me get up and running at the beginning of my PhD.

Special thanks to my life partner, whose infinite understanding, patience and empathy have definitely allowed me to carry on with a demanding part-time PhD alongside a full-time daily job. Thank you for helping me to disconnect from work and for making the most of every moment.

Obviously, I can not forget my family who have always supported me with everything I have decided to do in my life, and whose company has been an invaluable source of energy and positiveness.

Eventually, I would like to thank Anritsu and Airbus Defence and Space for their sponsorship and support to attend courses and conferences throughout my PhD.

List of peer-reviewed journal articles

1. V. M. Fernandez Laguna, Q. Ren and N. C. Panoiu, "Pulsed dynamics in a system of coupled silicon photonic crystal cavity-waveguide nanostructures," Proc. SPIE 11081, Active Photonic Platforms XI, 110812D (2019); https://doi.org/10.1117/12.2526658.

2. V. M. Fernandez Laguna and N. C. Panoiu, "Nonlinear optics in diamond-fin photonic nanowires: soliton formation and frequency comb generation", Opt. Express **30**, 36368-36378 (2022); https://doi.org/10.1364/OE.468922.

3. V. M. Fernandez Laguna and N. C. Panoiu, "Raman interaction in one-dimensional silicon photonic crystal slab waveguides", Phys. Rev. A (submitted).

4. V. M. Fernandez Laguna, Q. Ren and N. C. Panoiu, "Pulsed dynamics in coupled cavity-waveguide silicon photonic crystal structures", Phys. Rev. B (submitted).

List of conference presentations

1. V. M. Fernandez Laguna and N. C. Panoiu, "Raman amplification and pulse dynamics in silicon photonic crystal waveguides", OSA Advanced Photonics Congress, Zurich (2018).

2. V. M. Fernandez Laguna, Q. Ren and N. C. Panoiu, "Pulsed dynamics in a system of coupled silicon photonic crystal cavity-waveguide nanostructures", SPIE Nanoscience + Engineering, San Diego (2019).

3. V. M. Fernandez Laguna and N. C. Panoiu, "Soliton formation and frequency-comb generation in diamond-fin waveguides", OSA Nonlinear Optic, Virtual (2021).

List of acronyms

AGVD: anomalous group velocity dispersion

BGA: ball grid array

BOX: buried-oxyde-layer

CMOS: complementary metal-oxyde semiconductor

CMT: coupled-mode theory

CW: continuous wave

DFT: discrete Fourier transform

DSP: digital signal processor

EP-NLSE: externally-pumped nonlinear Schrödinger equation

FC: free-carriers

FCA: free-carrier absorption

FCD: free-carrier dispersion

FDFD: finite-difference frequency-domain

FDTD: finite-difference time-domain

FEM: finite element method

FFT: fast Fourier transform

FSR: free spectral range

FWM: four-wave mixing

GV: group velocity

GVD: group velocity dispersion

HPC: high-performance computing

IC: integrated circuit

ICD: internet data center

IDFT: inverse discrete Fourier transform

IR: infrared

LLE: Lugiato-Lefever equation

MMI: multi-mode interferometer

MPB: MIT photonic bands

MZI: Mach-Zehnder interferometer

nFETs: negative channel field-effect transistors

NoC: networks on chip

NLSE: non-linear Schrödinger equation

NRZ: non-return-to-zero

NV: nitrogen vacancy

PCB: printed circuit board

pFETs: positive channel field-effect transistors

PIC: photonic integrated circuit

PhC: photonic crystal

PhCC: photonic crystal cavity

PWE: plane-wave expansion

RF: radiofrequency

Si-PhCWG: silicon photonic crystal waveguide

SL: slow-light

SPM: self phase modulation

SPS: single-photon source

SPW: silicon photonic wire

SOI: silicon on insulator

SRS: stimulated Raman scattering

SS: self-steepening

SSF: split-step Fourier

TE: transversal electric

TM: transversal magnetic

TOD: third order dispersion

TPA: two photon absorption

UV: ultraviolet

VCSEL: vertical-cavity surface-emitting laser

VLSI: very large scale integration

WDM: wavelength-division multiplexing

XAM: cross absorption modulation

XPM: cross phase modulation

ZGVD: zero-group velocity dispersion

Contents

List of figures

Chapter 1

Introduction

Several reasons have inspired the intense research in photonics during the last two decades, mainly under the scope of networks-on-chip (NoC) applications. These applications include telecommunication systems, where avoiding the need to do optical-electrical conversions (and viceversa) to amplify the signal after travelling via optical fiber for some distance would make the overall system efficiency increase considerably; also biological sensors, where non-intrusive techniques to measure certain body molecules by controlling the light-skin interaction would facilitate and speed-up the diagnostic process; and, finally, Internet data centers (ICD) and high-performance computing (HPC), where the electrical interconnects have already shown important disadvantages such as poor bandwidth, large power dissipation and crosstalk between nearby electrical paths. Photonics, which spans the generation, manipulation and detection of light, provides the technological ground most suitable to solve all these problems [1, 2, 3, 4].

Since the early days of integrated photonics, on-chip optical devices such as switches or modulators had been built using semiconductors of the III-V bands due to their direct bandgap, e.g. allowing direct integration of light sources, high index of refraction and nonlinear properties [5, 6]. However, since III-V semiconductors are chemically incompatible with silicon complementary metal-oxyde semiconductor (CMOS) processing, a lot of attention was moved towards silicon photonics, which was rapidly considered a promising

platform to enable a cost-effective electronic-photonic integration. Furthermore, silicon provides a transparent window covering the entire telecommunication spectrum, and it also has a high refractive index, allowing the design of high-index contrast silicon photonic waveguides (Si-PhWGs), which produce a tight confinement of the electromagnetic field and therefore enhance the optical nonlinearities [7]. Based on this context, the design of CMOS-compatible, silicon photonic components for multiple applications can be found in the literature [8, 9]. Silicon-on-insulator (SOI) is the material of choice for passive photonic integrated circuits (PIC) which include multi-mode interferometers (MMI), directional couplers or mode converters, to name a few [10]. On the downside, silicon has an indirect bandgap, meaning that active building blocks such as lasers can not be easily realized in this technology. Despite of this, extensive research has been applied to demonstrate that Si-PhWGs can be used to enable key nonlinear processes, such as Raman amplification [11, 12], soliton propagation [13], supercontinuum generation [14], frequency conversion [15], modulation instability [16] and pulse compression [17, 18], among others. Furthermore, recent advances in the field include high speed silicon-based modulators, silicon/germanium detectors and integration of light sources by incorporating III-V active regions via special processes[19, 20].

Regardless of the positive results mentioned above, the need for smaller size, higher effiency and device versatility to respond to different applications, did encourage the research in photonic crystals (PhCs). Indeed, PhCs allow the design of dispersion engineered PhWGs while maximising the nonlinear effects through the exploitation of the slow-light regime [21]. Photonic crystals can enable these properties by introducing more adjustable dimensions. The way to do this consists on creating a periodic pattern in the photonic circuit, separating regions of different dielectric constants usually by a length a quarter the operating optical wavelength. This can be understood by considering the Fresnel reflections ocurring at subsequent interfaces between the different materials, which would interfere constructively after propagating an optical path length of half a wavelength, resulting in a strong reflection. Interestingly, depending on how the periodic

dielectric medium is defined, the device could be used for multiple purposes, from the design of ultra-small, narrow-band filters [22, 23] to omnidirectional mirrors, waveguides and bends [24, 25, 26]. In particular, this is possible thanks to the wide tuning of the group-velocity (GV) v_g of the propagating modes that PhCs allow. For instance, as we will show later on this work, the effectiveness of signal amplification based on stimulated Raman scattering can dramatically change with different values of the GV for the two optical modes taking place in the process. Particularly remarkable is the slow-light regime, where light-matter interaction is enhanced and both the linear and non-linear optical effects become substantially important [27, 28, 29, 30]. Indeed, relevant applications have emerged around the control over slow-light, such as optical buffering or time domain processing of optical signals [31, 32, 33]. Within this context, we present in this work the development of comprehensive numerical methods and computational tools that enable the analysis of linear and nonlinear pulsed dynamics in dispersion-engineered PhC structures. In particular, our analysis show that Raman amplification in silicon PhC waveguides (Si-PhCWGs) can outperform those appearing in the literature with amplification efficiencies one order of magnitude higher. In addition, with our novel methodology to analyse structures combining Si-PhCWGs and silicon PhC cavities (Si-PhCCs), we have shown how optical filters with minimised back-reflection can be implemented, therefore demonstrating the added-value our tools can have in the design of these components. It is noteworthy that the analysis we perform is focused on pulsed signals which is the typical scenario in the field of optical interconnects. For instance, considering the currently used common data rate of 25 Gb/s per wavelength with non-return-to-zero (NRZ) modulation, the signal shape is based on pulses as short as 40 ps width. In our simulations, we use pulse widths of this magnitude and also of few times shorter, which may be appreciated as relevant information for future faster interconnect standards.

Having understood the importance of silicon photonics in nowadays and future technologies, it is worth mentioning that commercial integrated optics are close to becoming a reality. In terms of fabrication, the most popular, efficient and precise technique to fab-

ricate CMOS nanophotonic structures is deep ultraviolet (UV) lithography [34], which can be used for both Si-PhWGs and Si-PhCWGs. As mentioned before, CMOS technology can integrate digital/analog electronic and nanophotonic elements, which can be achieved by simply adding extra masks into the CMOS processing flow. For instance, only an additional mask is required to integrate waveguides and electro-/thermo-optical modulators because the same silicon photonic layer is shared with the CMOS positive channel field-effect transistors (pFETs) and negative channel FETs (nFETs) [35]. Furthermore, similar to common surface-mounted electrical components, the package of the silicon CMOS nanophotonics chip can be terminated with a standard ball grid array (BGA) and then use flip-chip bonding techniques directly onto a laminate PCB board [36]. As an example, Figure 1.1 shows the packaging of an electronic chip flip-chip bonded on a silicon photonic device in this case [37].

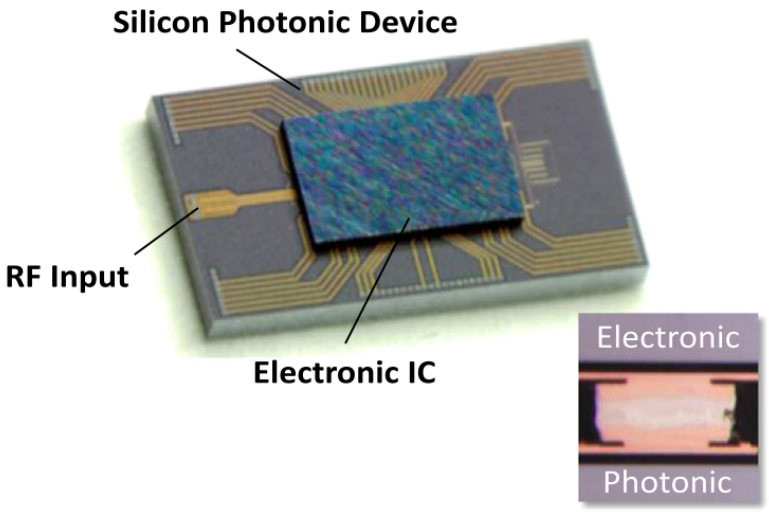

Figure 1.1: Silicon photonic wafer with an electronic IC (driver) packaging flip-flop bonded on top. The inset shows the interface between the electronic and the photonic worlds, in this case via a AgSnCu solder cap to form the bond between the devices [37].

An alternative solution other than PhCs to enable dispersion engineering in waveguides consists on creating sub-micron features in the waveguide structure. In Ref. [38], a review of optical properties of subwavelength waveguides is presented. While well-established, more mature photonic platforms, such as silicon-on-insulator [39], silicon

nitride [40], or compound semiconductor on-insulator [41] can be employed for this purpose, diamond is an appealing alternative to enable dispersion-engineered devices and applications in the visible spectrum. Indeed, diamond photonics offer important complementary advantages to silicon. Firstly, a large transparent window from UV to IR which extends the range offered by silicon while at the same time presenting strong third-order nonlinearity such as the Kerr effect. And secondly, great thermal properties combined with controllable colour centers which are important for quantum computing. In fact, quantum computing is believed to be the core application of future diamond photonic devices [42]. Based on these motivations, we present in this thesis our research about sub-wavelength nanostructures made of synthetic diamond, and the numerical methods we have developed to solve the nonlinear pulsed dynamics along them. Here, we concentrate on the first highlighted properties of diamond, e.g. being transparent at visible wavelengths and the strong nonlinearity, and we target the application of microring resonators based on diamond photonic waveguides to generate frequency combs at these wavelengths, which is a critical functionality in modern communication systems [43], biological sensors [44] and spectroscopy [45].

Having introduced the general topics we cover in this work, we describe in the next two sections of this introductory chapter the main objectives of this work and how the thesis is structured.

1.1 Main objectives of the work

The main objective of this work has been the development of rigorous, generic and comprehensive mathematical models to study the linear and nonlinear pulsed dynamic effects in dispersion engineered photonic nanostructures. Under this umbrella, we have targeted two different types of nanostructures: sub-micron diamond-fin waveguides and Si-PhCs, which, as justified in the previous section, are relevant candidates for the development of integrated photonic devices that could satisfy multiple applications.

With respect to diamond-fin waveguides, our objective has been to prove the applicability of these waveguides for dispersion engineered nonlinear processes such as frequency comb generation in a microring resonator. Therefore, a numerical method has been developed to solve the externally-driven NLSE governing the pulsed dynamics in this scenario.

Regarding Si-PhCs, we have tackled two scenarios with increasing complexity. Firstly, we have completed an in-depth study of Raman interaction in one-dimensional Si-PhC slab waveguides. Comprehensive numerical simulations have been performed to show the broad range of linear and nonlinear effects that determine the propagation of optical pulses through these waveguides, including self-phase modulation (SPM), two-photon absorption (TPA), free-carrier (FC) dynamics and group-velocity-dispersion (GVD), combined with the interaction between pulses via stimulated Raman scattering. In particular, we have concentrated on comparing how the fast-light and the slow-light regimes importantly influence the Raman dynamics alongside the waveguide, and we have demonstrated that clear amplification can be achieved.

In the second scenario, we have added Si-PhCCs alongside the Si-PhCWG which now incorporates the interaction between waveguide and cavity modes. This, indeed, increases considerably the problem complexity due to, for instance, the appearance of back-propagating pulses, FC dynamics both in the waveguide and in the cavities, and frequency dispersion effects caused by the waveguide-cavity coupling. In this case, not only the novel mathematical model to solve this type of problem has been described in detail, but also the computational algorithm developed, which is characterised by an original way of discretizing and solving the whole set of nonlinear differential equations. Last but not least, the model has been used to simulate a Si-PhC drop-filter with back reflection nulling.

Indeed, the mathematical models derived and utilised in this thesis are systems of complex, nonlinear, differential equations which are derived following the coupled mode theory (CMT) and then solved computationally by the use of certain numerical methods. Depending on the physical problem they represent and whether the relations between

unknowns are linear or nonlinear, different computational algorithms have been employed. Precisely, two main numerical methods can be highlighted: the split-step Fourier (SSF) method and the Newton-Raphson method for nonlinear systems of equations.

On the one hand, the SSF method can generically be used to solve nonlinear Schrödinger (NLS) equations [46], which, in our case, describe the pulse dynamics in diamond-fin waveguides and silicon photonic (crystal) waveguides, including more complex scenarios where Raman interaction is studied. The SSF method has been applied where there are no backward propagating optical waves, so that the computational solution is found step by step along a physical direction.

On the other hand, when adding cavities alongside a waveguide, which couple energy from and to propagating modes, backwards propagation has to be included. In this scenario, the system of NLS equations have been solved by the use of Newton-Raphson method, that is able to find the solution of all unknowns in all time and spatial simulation points at the same time.

Additionally, with respect to the frequency comb generation based on diamond-fin waveguides, the Newton-Raphson method has been employed to solve the set of equations arising from a discrete Fourier transform (DFT) method that is applied to the externally-driven NLSE that governs the physics of such problem.

In order to help the reader acquire a broader view on these topics, the structure of the thesis is outlined in the following subsection.

1.2 Outline

The thesis has been structured in the following manner:

The purpose of Chapter 2 is to present the context of this work, the background knowledge required to follow the rest of the chapters and, also, to describe the computational methods and simulations tools that have been employed. With this in mind, we start describing Maxwell equations for macroscopic media, followed by introducing the

concept of photonic crystals and how these can be modified to fabricate waveguides, e.g. by introducing line defects in the periodic lattice, and cavities, e.g. by introducing local defects. Once this is explained, we review the linear and nonlinear optical effects in photonic waveguides, in this case applied to silicon, which is of especial importance in order to understand how silicon photonics can be employed in a broad set of applications. Right after, we include a brief introduction to diamond photonics and its applications. Finally, we complete the chapter with a description of the numerical methods and simulation software tools developed and employed along this work.

In Chapter 3, we present the fundamental theoretical model we use to obtain the nonlinear Schrödinger (NLS) equations that mathematically describe the pulse dynamics in the scenarios under interest. For simplicity, we apply it to a generic silicon nanowire assumed to operate in single-mode propagation. This is of relevance since it helps the reader to better understand how the models in following chapters have been derived.

Within Chapter 4, we focus on sub-micron dispersion-engineered photonic waveguides based on diamond. More precisely, in this chapter we explore the designing tunability of novel diamond-fin waveguides, how they can operate in specific dispersive regimes, and we demonstrate how these waveguides can be used for supercontinuum generation, soliton propagation and generation of frequency combs.

Continuing with Chapter 5, we explore the effect of stimulated Raman scattering in one-dimensional Si-PhCWGs. We derive a mathematical model which describes the evolution of the interacting optical pulses, namely pump and signal, within a Raman-active medium and incorporate all relevant linear optical effects, including modal dispersion, waveguide loss, free-carrier (FC) dispersion and FC absorption, and nonlinear optical effects such as self- and cross-phase modulation (SPM, XPM). Following this approach, we present the results of numerical simulations for several combinations of pump and signal modes for which we vary their group velocities. In particular, we show how the device behaves differently when the pump and the signal are both in the slow-light regime, when they are in the fast-light regime and when the pump is in the slow-light and the signal

in the fast-light regime. Furthermore, our results reveal the importance of the walk-off length between pulses, which no doubt is one of the key parameters to take into account when designing and fabricating Si-PhCWGs for parametric Raman amplification.

In the last part of the thesis, which is contained in Chapter 6, we study the pulse dynamics in silicon photonic crystal waveguides with photonic crystal cavities placed alongside it. We present in detail the derivation of the theoretical model and the corresponding implementation as a computational tool to solve this problem. In this case, apart from the linear and nonlinear optical effects included in previous models, the dynamics take into account inter-cavity coupling and waveguide-cavity interactions, as well as counter-propagating waveguide modes. Based on this, we employ the simulation platform to study the pulse dynamics in a silicon photonic crystal system consisting of a couple of high-Q cavities placed alongside a waveguide where a slow-light mode propagates, for which our model predicts this system can potentially be used as a photonic drop-filter.

Finally, in Chapter 7, we conclude this work highlighting the main contributions to the fields of silicon and diamond photonics as well as discussing future perspectives of this work.

Chapter 2

Background concepts

In this chapter we present the main theoretical concepts required for the reader to understand the technical results contained in this thesis. Among the theoretical tools we present the Maxwell equations, introduce the concept of photonic crystals and outline their physical properties, and discuss the optical properties of photonic nanowires made of silicon or diamond.

2.1 Introduction

A thorough knowledge of how pulses propagate in photonic nanowires is of paramount importance in order to design photonic systems on the chip. The bulk of this work is built around this knowledge, which is applied both to silicon and diamond nanowires.

With respect to the former, silicon provides nearly perfect transparency in the spectral region extending from 1.2 μm to mid-infrared (mid-IR) regime [9, 47, 48]. To date, it has been demonstated the fabrication of small-loss, ultra compact, passive and active silicon photonic components. Indeed, silicon nanowires with ultra-small cross sections can be fabricated to enhance nonlinear optical effects thanks to the strong optical field confinement they create. Interesting phenomena such as third-order dispersion (TOD), two-photon absorption (TPA) and self-phase modulation (SPM) can lead to the devel-

opment of new applications not considered before [49]. Furthermore, understanding the theory around silicon photonic crystals (PhC) is undoubtly of high relevance due to their ability to control the light propagation. This is because, since any optical nanowire induces linear and nonlinear optical effects onto the propagating light, PhCs could be employed to reduce these effects to their minimum or take advantage of them to comply with the requirements of particular applications. Equally important, PhCs can facilitate the design of optical cavities with high Q factors, which could be used in the design of optical filters.

Regarding the latter, diamond possess very interesting optical properties such as large transparency window, ranging from ultraviolet (UV) to far-infrared (IR), very small optical absorption losses, and it can be synthesized with a high refractive index, $n_{di} \approx 2.4$, thus enabling enhanced optical waveguides mode confinement in a broad spectral range extending from 500 nm to 1000 nm. Equally important for its applications to active photonic devices, diamond possesses key nonlinear optical properties, including large Kerr nonlinearity that can be employed to frequency conversion and comb generation devices, and also strong Raman interaction at the operating wavelengths of $\sim$2 µm and with pump laser wavelengths in the telecom band at around $\sim$1.6 µm [50]. These important optical properties are accompanied by excellent thermal properties: firstly, synthetic diamond shows a high thermal conductivity, achieved via vibrations of its crystal lattice, in the order of 22 W/(cmK); secondly, it has a low thermo-optic coefficient; and, furthermore, it owns a thermal expansion coefficient which is half of silicon's, i.e. in the order of 1 ppm change in volume per Kelvin. These properties render it an ideal material for high-power applications and integration of electro-optic systems. In addition, this material has emerged as a promising low-temperature platform for quantum computing because of the possibility to create defects (color centers) in the crystal lattice. In particular, the nitrogen-vacancy (NV) centers are used for single photon emitters, perhaps one of the future core applications of diamond [51]. These NV centers are created by replacing a diamond atom by a nitrogen atom and its neighbour atom is left vacant. When a photon

interacts with the diamond lattice, the NV center sees a certain electron spin, i.e. the quantum bit can be stored in the electron spin of the NV center, with a long lifetime. Moreover, this electron spin can be controlled using radiofrequency (RF) or microwave fields, adding quantum logic. Finally, the information exchanged between the NV spin and an output photon can be collected. For this collection, integrated diamond photonic waveguides are important, since, compared with fiber optic counterparts, the loss through total internal reflection is reduced.

In this chapter we aim to provide the theoretical background for the entire work in the thesis, introducing and describing all the technical concepts that will be required to follow adequately the rest of the chapters. To this end, we begin by presenting the macroscopic Maxwell equations which govern the propagation of light in photonic devices, so that the reader becomes familiar with some of the properties of the electromagnetic field, dielectric media and electric polarization. We then continue with the introduction to PhCs, which bring a plethora of possibilities when designing optical devices thanks to the control of light they allow by the use of periodic dielectric lattices. After understanding how PhC can be used to create similar elements to those very well-known in high-frequency electronic circuits, such as waveguides or resonators, all most relevant linear and non-linear charactersitics of silicon nano wires will be described, given the potential of silicon as a key enabler for the integration of electronics and photonics on the same chip. We then continue with a technological survey of silicon and diamond photonics applications, ranging from wavelength-division multiplex (WDM) receivers to programmable photonic processors and pulse compression for ultra-fast optical interconnects. Finally, we complete the chapter by describing the main numerical methods and software tools that have been employed in this work.

2.2 Maxwell equations for macroscopic media

The Maxwell equations are at the center of solving any electromagnetic problem. By applying the Maxwell equations to a certain physical scenario and solving them, all electromagnetic modes supported by that specific medium are obtained. For macroscopic media, i.e. considering the matter far away from the atomic scale charges and quantum phenomena, the general form of the Maxwell equations in the frequency domain assuming a dielectric medium with no current densities ($\mathbf{J} = 0$) nor free charges ($\rho = 0$), is as follows:

$$\nabla \times \mathbf{E}(\mathbf{r}, \omega) = i\omega\mu\mathbf{H}(\mathbf{r}, \omega), \tag{2.1a}$$

$$\nabla \times \mathbf{H}(\mathbf{r}, \omega) = -i\omega[\epsilon_c(\mathbf{r}, \omega)\mathbf{E}(\mathbf{r}, \omega) + \mathbf{P}(\mathbf{r}, \omega)], \tag{2.1b}$$

$$\nabla \cdot \mathbf{H}(\mathbf{r}, \omega) = 0 \tag{2.1c}$$

$$\nabla \cdot [\epsilon_c(\mathbf{r}, \omega)\mathbf{E}(\mathbf{r}, \omega) + \mathbf{P}(\mathbf{r}, \omega)] = 0 \tag{2.1d}$$

where from top to bottom are the Faraday‘s law of induction, the Ampere‘s circuital law, the Gauss‘s law for magnetism and the Gauss‘s flux theorem. In these equations, $\mathbf{P}(\mathbf{r}, \omega)$ is the electric polarization of the medium or polarization density, $\epsilon_c(\mathbf{r}, \omega) = \epsilon_0\epsilon_r(\mathbf{r}, \omega)$ describes the dielectric media, μ is the magnetic permeability, which is assumed to be the vacuum permeability μ_0 for the materials used in this work, and $\mathbf{E}$ and $\mathbf{H}$ are the electric and magnetic fields. Note that the polarization term can contain every effect that produces changes on the refractive index of the media, for instance, caused by photogenerated free carriers (FCs), Raman scattering and Kerr effects, which will be described later in the chapter. In fact, Maxwell equations can also be presented with the displacement field $\mathbf{D}(\mathbf{r}, \omega) = \epsilon_c(\mathbf{r}, \omega)\mathbf{E}(\mathbf{r}, \omega) + \mathbf{P}(\mathbf{r}, \omega)$, which is the generalization of the electric field under the effect of the dielectric media.

The polarization term, as previoulsy said, will be a contribution of linear and nonlinear

effects:

$$\mathbf{P}(\mathbf{r},\omega) = \delta\mathbf{P}_{\text{lin}}(\mathbf{r},t) + \delta\mathbf{P}_{\text{nl}}(\mathbf{r},t), \tag{2.2}$$

where the first term can represent the linear change of the dielectric constant whereas the second term represents the non-linear change of it, i.e. the dielectric constant will vary non-linearly with the electric field. In more detail,

$$\mathbf{P}(\mathbf{r},\omega) = \epsilon_0\hat{\chi}^{(1)}(\mathbf{r},\omega)\mathbf{E} + \epsilon_0\hat{\chi}^{(2)}(\mathbf{r},\omega) : \mathbf{EE} + \epsilon_0\hat{\chi}^{(3)}(\mathbf{r},\omega)\vdots\mathbf{EEE} + O(\mathbf{E}^4), \tag{2.3}$$

where $\hat{\chi}^{(n)}(\mathbf{r},\omega)$ are the n-order nonlinear susceptibilities of the medium and depend on the structure of the crystal. For instance, in the case of silica fibres they are represented as scalar variables, but in the case of silicon crystal the $\hat{\chi}^{(n)}$ is a $(n+1)th$-rank tensor.

There is a conventional way to write how the nonlinear susceptibilities are physically related to the interacting optical frequencies [52]. Ignoring their spatial dependence, the second and third-order nonlinear susceptibilities can be specified as $\hat{\chi}^{(2)}(\omega_3;\omega_1,\omega_2)$ and $\hat{\chi}^{(3)}(\omega_4;\omega_1,\omega_2,\omega_3)$, respectively. For the second-order susceptibility tensor, the information within the brackets can be understood as follows: photons at frequency ω_1 and ω_2 interacting in a nonlinear medium produce photons at $\omega_3 = \omega_1 + \omega_2$. In other words, photons at frequencies ω_1 and ω_2 are destroyed and a photon of frequency ω_3 is simultaneously created in a single quantum-mechanical process. From the perspective of atomic energy levels, the absorption of radiation at ω_1 and ω_2 leverage the energy level of the atom from its ground state to a virtual level. Since these virtual levels are not energy eigen-levels of the free atom, but rather represent the combined energy of one of the energy eigenstates of the atom and of one or more photons of the radiation field, the simultaneously generated radiation at ω_3 makes that atom come back to a real level. Based on this, the first component before the semi-colon specifies the result of the photon interaction within the nonlinear medium or, in other words, the frequency of the photon generated by the nonlinear interaction, whereas the two or more following components after the semi-colon explain the interaction itself. Note also that the electric field vectors

multiplying the nonlinear susceptibilities are affected by this convention, that is, each of them will be evaluated at the corresponding interacting frequency in sequential order.

To illustrate how Maxwell equations are used, we can assume we have an infinite dielectric medium with constant values for the permittivity (ϵ_c) and permeability (μ) in all spatial points and for all frequencies, i.e. there is no dispersion. Then, applying the curl operator to Eq. 2.1a, we obtain:

$$\nabla \times \nabla \times \mathbf{E}(\mathbf{r}, \omega) = i\omega\mu \nabla \times \mathbf{H}(\mathbf{r}, \omega) \tag{2.4}$$

which can be simplified by introducing Eq. 2.1b as:

$$\nabla \times \nabla \times \mathbf{E}(\mathbf{r}, \omega) = \mu\epsilon_c\omega^2 \mathbf{E}(\mathbf{r}, \omega) \tag{2.5}$$

Finally, using the vector relation $\nabla \times (\nabla \times \mathbf{A}) = \nabla(\nabla \cdot \mathbf{A}) - \nabla^2\mathbf{A}$, where $\mathbf{A}$ is any vector function of $\mathbf{r}$, Eq. 2.5 can now be written as:

$$\nabla^2 \mathbf{E}(\mathbf{r}, \omega) + \mu\epsilon_c\omega^2 \mathbf{E}(\mathbf{r}, \omega) = 0 \tag{2.6}$$

where we have made use of Eq. 2.1d with no polarization term. Eq. 2.6 is the electromagnetic wave equation for the electric field in the frequency domain, which takes the form of the Helmholtz equation. For the solution of a plane wave, this is the field follows the form $\mathbf{E}(\mathbf{r}, \omega) = \mathbf{a}\exp(i\mathbf{k} \cdot \mathbf{r} + i\omega t)$ with wave vector $\mathbf{k}$, the factor $\mu\epsilon_c\omega^2$ must be equal to the absolute square value of the wave vector, i.e. $|\mathbf{k}|^2 = k^2 = \mu\epsilon_c\omega^2$, which implies a phase velocity of $\nu \equiv \omega/k = 1/\sqrt{\epsilon_c\mu}$. The phase velocity can also be expressed in terms of the refractive index, n, and the speed of light in vacuum, c, as $v = c/n$, which leads to the expression for the refractive index, $n = \sqrt{\epsilon_r\mu_r}$. For the magnetic field, a similar derivation can be followed.

2.3 Introduction to photonic crystals

A crystal is an arrangement of atoms or molecules in a periodic pattern, which is also called the crystal lattice. Depending on the material these structures are made of, they can present different conduction properties. Indeed, electrons propagating at a certain direction and with a certain energy may be able to travel through the crystal lattice without scattering. Similarly, other electrons with a different energy may have prohibited their propagation through the lattice. In this case, it is said there is a band-gap or a gap in the energy band structure of the crystal. In photonics, the concept of crystals can be emulated by synthetizing the periodic pattern of atoms or molecules by a periodic pattern of macroscopic media with differing dielectric constants, this is ϵ_c is a periodic function. Depending on how different these dielectric contants are and how they are arranged to form the desired periodicity, the photons travelling through the media will experience similar phenomena as the ones described for electrons, which would allow the design of devices for multiple different purposes, from ultra-small, narrow-band filters [22, 23] to omnidirectional mirrors, waveguides and bends [24, 25, 26].

As with any material, an electromagnetic field interacting with a photonic crystal will behave differently depending on the frequency and wave vector that characterizes the field. This leads us to introduce the following terms to describe these field configurations: localized modes, which are those electromagnetic fields that are confined within the crystal; extended or leaky modes, which are those that extend into both the crystal and the air or any other material surrounding it; and the evanescent modes, which correspond to cases where there exist a band-gap and the field frequency falls within it, which makes the modes wave amplitude decay exponentially into the crystal. The photonic band structure is the representation of all these possible modes for a specific photonic crystal. Since the lattice of a photonic crystal will be periodic in one or more directions, the band structure is obtained by solving Maxwell's equations for the unit cell, which is the repeated unit of the periodic dielectric system.

As an example, and taking into account we will focus on this structure in future chapters, Figure 2.1 shows a photonic crystal slab with a hexagonal lattice (sometimes referred to as triangular lattice). The slab is made of a dielectric material and is surrounded by homogeneous media. The hexagonal lattice is obtained by making holes in the dielectric slab, providing a 2D periodicity or discrete translational symmetry in z and y directions, while its finite thickness in x direction enables index guiding if the sourrounded medium has lower dielectric constant. The primitive lattice vectors can be defined as $\mathbf{a_1} = \frac{\sqrt{3}}{2}a\hat{z} + \frac{a}{2}\hat{y}$ and $\mathbf{a_2} = \frac{\sqrt{3}}{2}a\hat{z} - \frac{a}{2}\hat{y}$, for which the corresponding reciprocal lattice vectors are $\mathbf{b_1} = \frac{2\pi}{a\sqrt{3}}\hat{z} + \frac{2\pi}{a}\hat{y}$ and $\mathbf{b_2} = \frac{2\pi}{a\sqrt{3}}\hat{z} - \frac{2\pi}{a}\hat{y}$. The light yellow area highlights the unit cell area which should be used to obtain the band structure of the crystal.

Due to the discrete periodicity in z and y directions, it is known that the field for these components will be the result of the product of a plane wave with a periodic function.

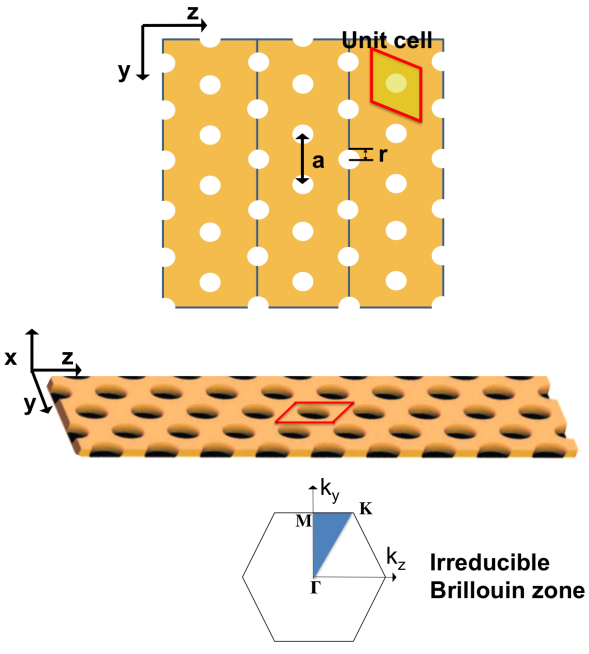

Figure 2.1: Top: 2D view of hexagonal lattice with a as lattice constant and r being the radius of the holes. The area in yellow represents the lattice unit cell. Middle: 3D view of hexagonal lattice slab and unit cell as above. Bottom: First or irreducible Brillouin zone (blue area) and lattice vectors corresponding to the hexagonal lattice.

This is the so called Bloch's theorem and, is expressed as:

$$\mathbf{E}(\mathbf{r}) \propto \mathbf{u_k}(\mathbf{r}) e^{i\mathbf{k}\cdot\mathbf{r}}. \tag{2.7}$$

Since the dielectric in z and y is invariant under translations through a multitude of lattice vectors $\mathbf{R} = l\mathbf{a_1} + m\mathbf{a_2}$ for some integers l and m, the primitive reciprocal lattice vectors $(\mathbf{b_1}, \mathbf{b_2})$ are defined so that $\mathbf{a_i} \cdot \mathbf{b_j} = 2\pi\delta_{ij}$. In the case of the PhC slab of Figure 2.1, the wave vectors k_z and k_y are periodic by $k_z = k_z + lb_1 \cdot \hat{z} = k_z + \frac{2\pi}{a\sqrt{3}}$ and $k_y = k_y + mb_2 \cdot \hat{y} = k_y + m\frac{2\pi}{a}$, being a the lattice constant and l, m arbitrary integers. This leads us to introduce the concept of irreducible Brillouin zone, obtained through these reciprocal lattice vectors as shown at the bottom of Figure 2.1. It can be realised that, by rotation or symmetry, the irreducible Brillouin zone can represent any lattice vector within the hexagon. The points represented are given the following values: $\Gamma = (0, 0)$, $M = (0, \frac{\pi}{a})$and $K = (-\frac{2\pi}{3a}, \frac{2\pi}{3a})$.

Any modes with $k_x = 0$, i.e. that propagate strictly in the yz plane, are invariant under reflections through the $x = 0$ plane. This allows us to classify the modes into TE-like (the dominant components of the electric field are those in the yz plane and the dominant one of the magnetic field is normal to that plane, this is H_x) and TM-like (the dominant components of the magnetic field are those in the yz plane and the dominant one of the electric field is E_x). Figure 2.2 shows the band structure of the hexagonal lattice after solving the problem for the unit cell in the plane-wave expansion (PWE) electromagnetic solver MPB [53]. The following parameters have been used: polarization, TE-like; height of the slab, $h = 0.6a$; radius of the holes, $r = 0.29a$; and slab index of refraction, $n = 3.4807$ of silicon. The dashed curve has been included to represent the light line, which separates the index-guided modes (under the line) from the extended modes (above the line). Indeed, the modes laying under the light cone are kept within the slab by index guiding, while the Poynting vector of the extended or leaky modes have the component in the transverse direction different from zero. However, we

can also notice there is a band-gap between frequencies 0.2426 and 0.2706 where light can not propagate trough the crystal. The slab thickness plays a very important role in the size of the band-gap. When the slab thickness is too small, the step in frequency between two consecutive bands increases, which makes all bands move above the light line and become weakly guided. However, when the slab thickness is too big, the higher order modes rather than the fundamental mode are pulled down in frequency and the gap decreases. Thus, if the purpose of the design is to obtain the widest band-gap, an optimal thickness must be used, which is approximately half an effective wavelength. This effective wavelength can be obtained by finding the electromagnetic solution of a material whose effective dielectric constant is calculated by the spatial average of the original dielectric profile weighted by the field profile.

2.3.1 Photonic crystal waveguides

Photonic crystal waveguides (PhCWG) can be designed by introducing a line defect in the periodic lattice as shown on Figure 2.3 a). That is, from the original structure in Figure 2.1, we have introduced a line defect by removing the holes of one of the rows in z direction. By doing this, we can confine light in x direction via index guiding and confine light in y direction by using the two remaining hexagonal periodic lattices at both sides to prohibit energy propagation in that direction. The consequence of the line defect in the band diagram is that two guided modes are formed into the band-gap.

In Figure 2.3 a), the yellow area highlights the new unit cell that has been used in MPB in order to obtain the band structure, which is shown in b). In this case, the band diagram is projected into the longitudinal z-axis, through which two guided modes can propagate and which lay within the band-gap. Finally, we show in the left (right) plot of subfigure c) at the bottom the amplitude of the normalized magnetic field H_x of the y-odd (y-even) mode, calculated in the plane $x = 0$ for group index $n_g = c/v_g = 6.91$, where v_g is the group velocity. Note that y-odd refers to the fact that the mode profile has opposite sign under symmetry inversion through the $y = 0$ plane, while y-even means

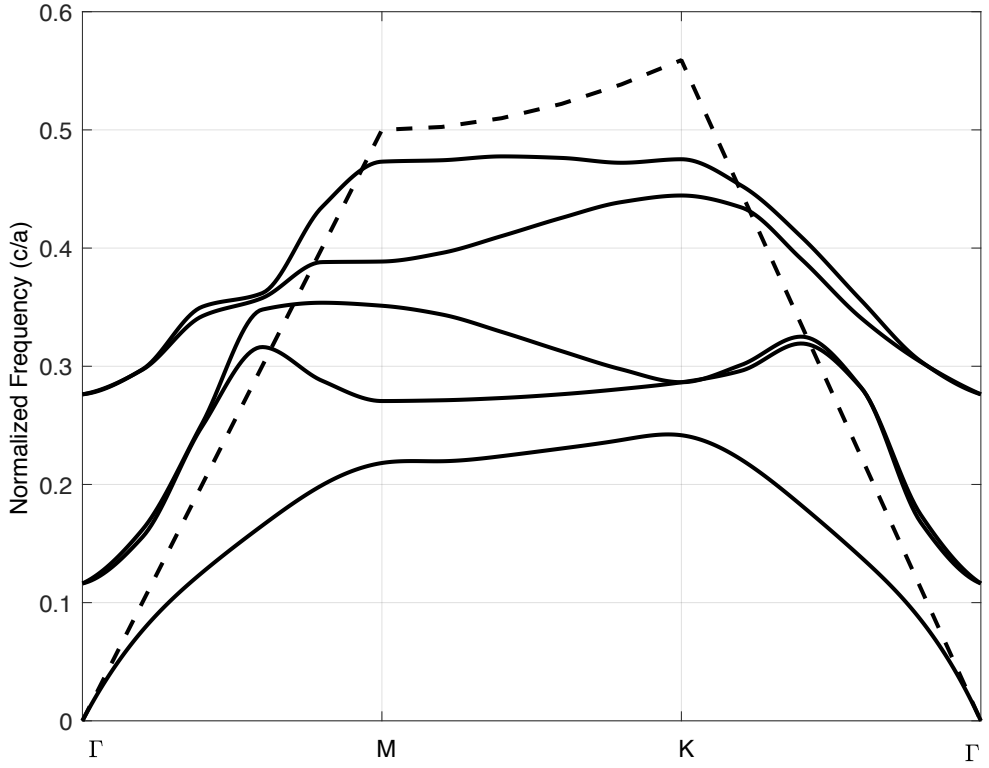

Figure 2.2: TE-like band diagram corresponding to the hexagonal lattice of Figure 2.1 with the radius of the holes being $r = 0.29a$, the height of the slab being $h = 0.6a$ and the slab made of silicon with index of refraction $n = 3.4807$. There are 5 bands below the light cone (dashed line) for which index guiding applies within the slab. All points above the light cone are extended modes. The maximum bandgap happens between the fundamental and second bands, where the gap-midgap ratio is of $\frac{\Delta\omega}{\omega_m} = 0.1091$, being ω_m the frequency at the middle of the bandgap.

the mode is invariant under symmetry inversion through the $y = 0$ plane. The higher frequency mode shows a more complex pattern, with more zero-crossings, than the lower frequency mode, which is a typical characteristic in any waveguide. This can be explained by the electromagnetic variational theorem which implies that the lowest-frequency mode corresponds to the field pattern that minimizes the electromagnetic energy functional [24]. Indeed, when the electric field is concentrated in the regions of higher dielectric constant and the amount of spatial oscillations is minimised, this energy functional is minimised as well.

2.3.2 Photonic crystal cavities

In a similar way to how waveguides are designed by applying line defects in the original periodic lattice, photonic crystal cavities can be created as shown in Figure 2.4. In this case, we introduce a local defect, which can be achieved simply by removing a single hole or, alternatively, a series of holes but within a limited area. Figure 2.4 shows that five of the holes have been removed from the original hexagonal lattice from Figure 2.1.

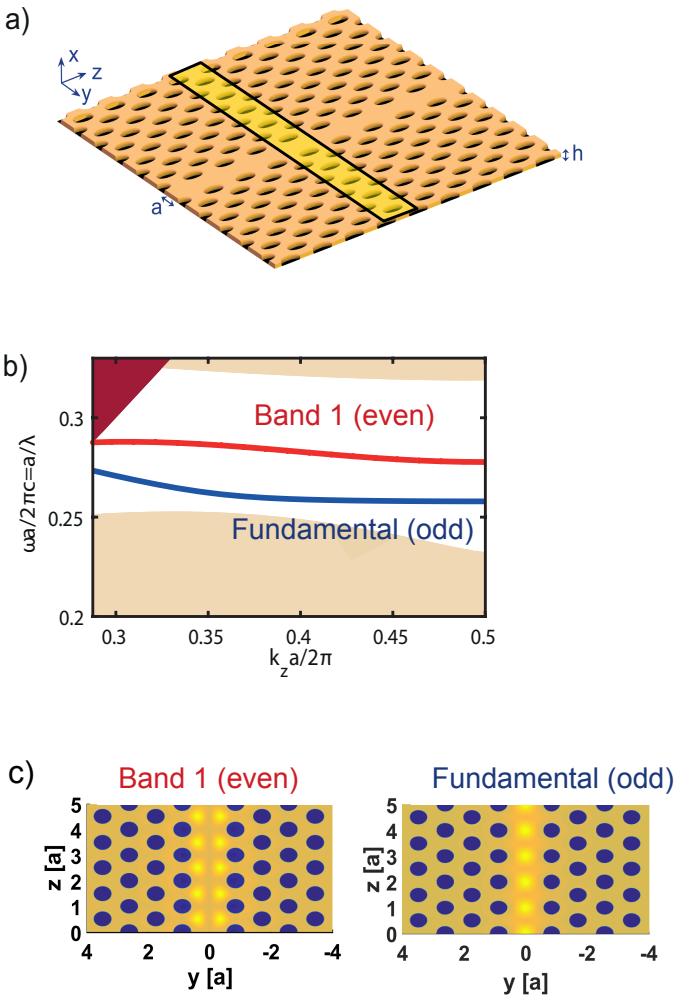

Figure 2.3: (a) Geometry of the silicon W1 PhCWG. The height of the slab is $h = 0.6a$ and the radius of the holes is $r = 0.29a$. (b) Projected band structure into the longitudinal z-axis. Dark magenta and light brown areas correspond to slab leaky and guiding modes, respectively. The red and blue curves represent the guiding modes of the 1D waveguides. (c)Representation of guided modes in the Si-PhC slab waveguide. Left (right) panel shows the amplitude of the normalized magnetic field H_x of the y-odd (y-even) mode, calculated in the plane $x = 0$ for group index $n_g = \frac{c}{v_g} = 6.91$.

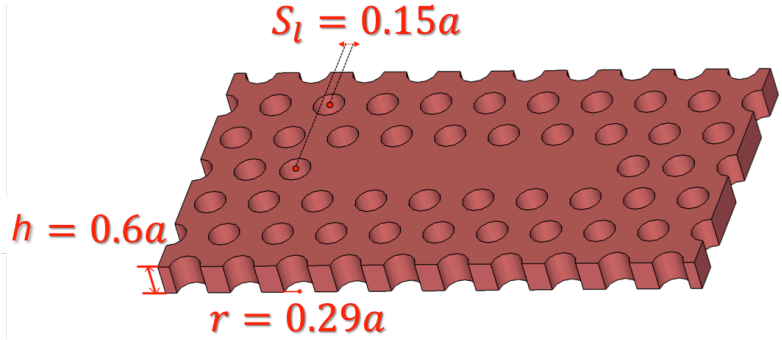

Figure 2.4: This figure shows the cavity structure based on the same hexagonal lattice slab of Figure 2.1. Five holes have been removed in order to create a localized mode. Additionally, the holes at the edge have been slightly displaced by S_l to enhance the Q factor of the cavity [54].

Now, the defect modes out of the modified structure are not perfectly localized, but they are leaky modes. Indeed, the resulting modes are resonances which couple energy into light cone modes with same frequency. The physical effect can be explained through the quality factor, $Q = \frac{\omega_0}{\gamma}$, where ω_0 is the frequency of the cavity mode and γ is the rate of energy loss. The Q factor is, in fact, the number of optical periods that elapse before the energy in the cavity decays by $e^{-2\pi}$. In order to improve the Q factor, the original holes at the edges have been slightly displaced as it can be noticed in Figure 2.4.

Figure 2.5 shows the resulting cavity modes in the band diagram by solving the structure using BandSOLVE [55]. The resonant frequency and Q factors are obtained by using the finite-difference time-domain (FDTD) simulation software MEEP [56]. For the mode at lower frequency, the Q factor obtained is $Q = 1.12 \times 10^5$, while for the mode at higher frequency, this is $Q = 1804$. Since these modes do not propagate through a specific direction, but remain localized at the same position, they become just straight lines in the diagram. As mentioned before, the part of these lines crossing the light line, which is shown in grey, represent the coupling of energy into the extended states of the light cone. Similarly to waveguide modes, the field patterns of higher frequency modes contain more zero-crossings than the lower frequency modes.

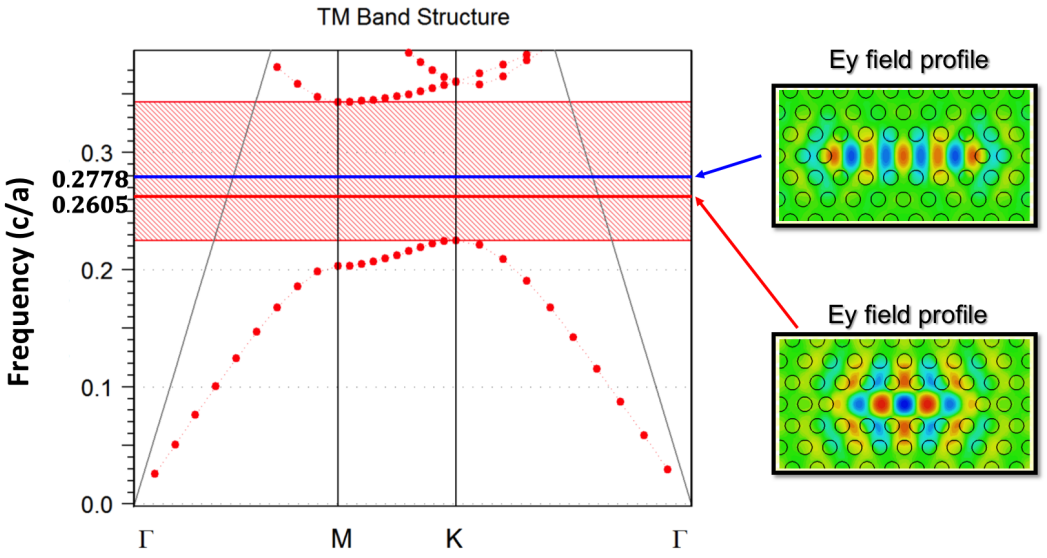

Figure 2.5: Band diagram corresponding to the structure from Figure 2.4 [54], where two localized modes or cavity modes have appeared at the middle of the bandgap. The height of the silicon slab is $h = 0.6a$ and the radius of the holes is $r = 0.29a$, whereas the displacement parameter $S_l = 0.15a$.

2.4 Linear optical properties of silicon photonic wires

Silicon photonic wires (SPWs), used as a general term to specify any kind of silicon waveguide with submicrometer cross-section, e.g. typically in the order of 450 nm width by 220 nm height, are characterized by strong optical dispersion due to the high-index contrast and the small dimensions they have, which cause a strong confinement of the electromagnetic field. Indeed, when the operating wavelength is bigger than the waveguide core size, waveguide dispersion dominates. This is contrary to what happens for optical fibers, where the intrinsic or material dispersion dominates since the wavelength is smaller than the fiber core size. Thus, controlling the dispersion of pulses propagating in SPWs is a key enabler for many applications, see section 2.6. In this part of the chapter we concentrate on explaining the most relevant dispersion effects in SPWs, which can be clasified in group velocity dispersion (GVD) effects and third-order dispersion (TOD) effects.

When the wave vector is projected along the propagation direction in a waveguide,

the variable β is normally used to represent the propagation constant and its frequency dispersion. In the case of the Si-PhCWG in Figure 2.3, since light propagates along the z-axis, the component k_z of the wave vector is renamed as $\beta(\omega) = k_z(\omega)$. By expanding $\beta(\omega)$ in Taylor series, we can determine the dispersion effects through the various expansion coefficients:

$$\beta(\omega) = \beta_0 + (\omega - \omega_0)\beta_1 + \frac{1}{2}(\omega - \omega_0)^2\beta_2 + \frac{1}{6}(\omega - \omega_0)^3\beta_3 + O(\omega^4), \tag{2.8}$$

where ω_0 is the frequency of the waveguide mode, β_0 is the propagation constant and the series coefficients are defined as $\beta_n = \frac{\partial^n \beta(\omega)}{\partial \omega^n}$. It can be understood that the dependence of $\beta(\omega)$ on the frequency is implicitly determined by the band diagram. Consequently, the Taylor coefficients can be obtained by numerically calculating the derivatives of these curves.

Apart from the propagation constant $\beta_0 = \beta(\omega = \omega_0)$ already introduced, the first order coefficient β_1 determines the group velocity of the mode. Specifically, $\beta_1 = \frac{1}{v_g}$, where v_g is the group velocity. Similarly, β_2 represents the GVD which generally results in pulse broadening, and β_3 determines the TOD effect. These coefficients are key parameters that define the optical pulses propagation in an optical medium.

2.4.1 Group velocity dispersion effects

The GVD effects are related to coefficient β_2 of Eq. (2.8). This coefficient represents the group velocity frequency dispersion, which affects the width of the pulse propagating through the medium. The GVD effect is quantified by the dispersion parameter D, defined as:

$$D = \frac{\partial \beta_1}{\partial \lambda} = -\frac{2\pi c}{\lambda^2}\beta_2. \tag{2.9}$$

The variation of the group velocity with the optical wavelength means that the frequency components of a pulse will travel at different speeds through the SPW, which for the normal GVD region ($\beta_2 > 0$) will make the pulse broaden the longer the distance it

travels. For this particular case, the higher wavelength components (red light) travel faster than lower wavelength components (blue light). However, when $\beta_2 < 0$, this is referred as anomalous GVD (AGVD) region, and in this case the lower wavelength components travel faster than the higher wavelength components, which has the effect of compressing the pulse. Based on this, one way of minimizing the effect of GVD is designing the SPW through the dimensions and/or aspect ratio of the core [57, 58, 59, 60] in order to achieve a zero GVD (ZGVD) at the central wavelength of the pulse.

2.4.2 Third-order dispersion effects

The most important effect of TOD in SPW is the asymmetric shape the optical pulse acquires after a certain propagation distance. Contrary to GVD, which makes the pulse shape change symmetrically, TOD produce asymmetries in the sidelobes of the pulse, which, obviously, has the same consequence on the spectra. To make it clear, when $\beta_3 > 0$, several ripples can appear at the trailing edge of the pulse whereas in the case when $\beta_3 < 0$ these appear at the leading edge of the pulse.

For SPW, the TOD effect is only noticeable in pulses whose widths are in the femtosecond range. This will be understood in further chapters when the concept of dispersion length is introduced.

2.5 Nonlinear optical properties of silicon photonic wires

Nonlinear optical properties are included in Maxwell equations by the polarization term, whose series expansion is expressed by the use of susceptibility tensors, as already introduced in Eq. (2.3). The first-order susceptibility tensor is of the order of unity for condensed matter, e.g. silicon and other dielectrics, whereas the higher order susceptibility tensors are much smaller and will depend on the crystalographic properties of

the material. In the case of crystalline silicon, which is a centrosymmetric crystal, i.e. its crystal lattice is invariant to an inversion symmetry transformation, the second-order nonlinear susceptibility, $\hat{\chi}^{(2)}$, cancels. Consequently, the first and most important nonlinear susceptibility for silicon is $\hat{\chi}^{(3)}$, whose origin comes from two different physical contributions explained in the following subsections.

2.5.1 Kerr and two-photon-absorption effects

There exist an electronic contribution in the third-order nonlinear susceptibility of silicon given by the Kerr and TPA (two photon absorption) effects, which contribute to the real and imaginary parts of $\hat{\chi}^{(3)}$, respectively. As explained in [61], considering the fact that silicon belongs to the m3m crystal point group, and that this crystal satisfies the Kleinman symmetry relations, the frequency dispersion of the electronic nonlinearity tensor can be neglected[62]. Moreover, the electronic nonlinearity has just one independent element, which is $\hat{\chi}^{e}_{iiii} = 2.30 \cdot 10^{-19} + i7.01 \cdot 10^{-20}$ m^{2}V^{-2}, and the relations $\hat{\chi}^{e}_{iiii} = 2.36\hat{\chi}^{e}_{iijj}$ and $\hat{\chi}^{e}_{iijj} = \hat{\chi}^{e}_{ijij} = \hat{\chi}^{e}_{ijji}$ apply [52].

On the one hand, the Kerr effect is given by the nonlinear electronic polarizability of silicon, i.e. bound charges that are polarized by the presence of an electromagnetic field and which is assumed to have an instantaneous response (approximately few femtoseconds). The Kerr effect is related to the intensity dependent refractive index or n_2, which in form of equation,

$$n = n_0 + 2n_2|E|^2, \tag{2.10}$$

where n_0 is the usual "weak field" refractive index. This means that the pulse will experience a phase shift when interacting with the optical medium, commonly referred as self-phase modulation (SPM), and which will increase as the pulse propagates.

Having introduced the GVD and the SPM effects, we now move on to explain the concept of soliton. This term refers to any optical field that does not change during propagation thanks to the balance between the GVD and the SPM effects in the medium.

In more detail, when the pulse experiences AGVD, i.e. $\beta_2 < 0$, and the strengths of both GVD and SPM effects are equal, one effect will exactly cancel the other and the pulse will preserve its temporal and spectral profile even over long propagation distances.

In our mathematical models, SPM will be expressed through the real part of the third-order electronic nonlinear susceptibility in the form $\hat{\chi}^e(\omega;\omega,-\omega,\omega)$. SPM is a parametric process since the initial and final quantum-mechanical states of the system are identical. In SPM, two photons at frequency ω are absorbed and remove the population from the ground state to a virtual level from where a new pair of photons is generated so the population comes back to the initial real level. In this conventional notation, the minus sign after the semicolon means generation, whereas the positive sign means absorption. Note that the negative frequency makes one of the electric field vectors multiplying the nonlinear susceptibility being complex conjugate. Figure 2.6 (a) shows schematically the nonlinear interaction between photons at the same frequency corresponding to SPM. The Kerr effect is also responsible for XPM or cross-phase modulation. In this case, one

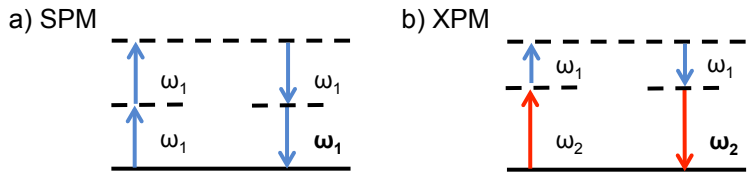

Figure 2.6: (a) SPM nonlinear process, showing how two photons of frequency ω_1 interacting with a Kerr nonlinear medium get absorbed and, simultaneously, the medium responds in a similar way generating two photons at the same frequency. (b) Equivalent process for XPM where signals at two different frequencies co-propagate in the medium.

pulse propagating at a certain frequency can induce a change of the refractive index at other frequency, leading to the phase shift of other pulses propagating at that different frequency. Describing it with the third-order nonlinear susceptibility tensor, the XPM interaction happens for photons at different frequencies, which means that the frequency combinations $\omega_1 = \omega_2 - \omega_2 + \omega_1$ or $\omega_2 = \omega_1 - \omega_1 + \omega_2$ would be applicable. The XPM process is shown in Figure 2.6 (b).

On the other hand, the second electronic contribution is related to the TPA coeffi-

cient or β_{TPA}, which, since it contributes to the imaginary part of $\hat{\chi}^{(3)}$, will lead to loss of energy. In fact, TPA is a process where two photons are absorbed simultaneously from the optical pulse and free electrons-hole pairs (so called free carriers, FC) are generated. Actually, these FC will not only absorb light, but will also induce an additional wavelength-dependent change in the refractive index. The density of FCs generated by the pulse along the SPW will not remain constant as free carriers can recombine. Indeed, silicon is characterized by a FC relaxation time τ_c of the order of nanoseconds. This means that, for pulse widths larger than the relaxation time, the free carrier density will contribute strongly to pulse reshaping, particularly on the trailing edge of the pulse because the leading part of it will generate the FC first and then the trailing part will experience the resulting induced change on the refractive index.

In the case of free carrier absorption (FCA) and the intrisic loss, their contribution in the polarization term can be expressed as linearly dependent with the electrical field as follows:

$$\delta\mathbf{P}_{\text{lin}}(\mathbf{r},t) = \left[\delta\epsilon_{\text{fc}}(\mathbf{r}) + \delta\epsilon_{\text{loss}}(\mathbf{r})\right]\mathbf{E}(\mathbf{r},t), \tag{2.11}$$

where as shown in Ref. [63]:

$$\delta\epsilon_{\text{fc}}(\mathbf{r}) = \left(2\epsilon_0 n\delta n_{\text{fc}} + i\frac{\epsilon_0 cn}{\omega}\alpha_{\text{fc}}\right)\Sigma(\mathbf{r}), \tag{2.12a}$$

$$\delta\epsilon_{\text{loss}}(\mathbf{r}) = i\frac{\epsilon_0 cn}{\omega}\alpha_{\text{in}}\Sigma(\mathbf{r}). \tag{2.12b}$$

where it has been assumed the medium response is nearly instantaneous. In detail, α_{in} is the intrinsic loss coefficient of the waveguide. It is known that the intrinsic loss coefficient accounts mainly for the amount of photons that are lost due to the waveguide wall roughness. $\Sigma(\mathbf{r})$ is a characteristic function used to take into account only the regions where FCs can be generated, this is $\Sigma = 1$ in the silicon regions and $\Sigma = 0$ otherwise. Following the Drude model, the FC-induced change of the index of refraction, δn_{fc}, and

the FC absorption coefficient, α_{fc}, are given by [64]:

$$\delta n_{\text{fc}} = -\frac{e^2}{2\epsilon_0 n\omega^2}\left(\frac{N_e}{m_{ce}} + \frac{N_h^{0.8}}{m_{ch}}\right), \tag{2.13a}$$

$$\alpha_{\text{fc}} = \frac{e^3}{\epsilon_0 cn\omega^2}\left(\frac{N_e}{\mu_e m_{ce}^2} + \frac{N_h}{\mu_h m_{ch}^2}\right), \tag{2.13b}$$

where e is the the electron charge, N_e (N_h) is the induced variation of the electrons (holes) density, $m_{ce} = 0.26m_0$ ($m_{ch} = 0.39m_0$) is the conductivity effective mass of the electrons (holes), with m_0 the mass of the electron, and μ_e (μ_h) is the electron (hole) mobility.

Similarly as in Ref. [61], we will assume that $N_e = N_h \equiv N$ and we will neglect the dispersion of δn_{fc} and α_{fc} since the pulse durations we consider (tens of ps) are much larger than the temporal response of the medium (few fs).

As we explained at the beginning of this section, TPA effect is related to the imaginary part of $\hat{\chi}^e$, and it is indeed in the calculation of the induced variation of electrons/holes density where the imaginary part of $\hat{\chi}^e$ is used. This will be understood in the following chapters where we derive the free carriers dynamics equations to obtain the value of N at every step in the propagated distance.

2.5.2 Raman effect

In silicon, there exists an additional third-order nonlinear optical process that couples photons and phonons, the latter being the quanta of vibrational mechanical energy associated to the lattice, and which is known as Raman effect. When a photon of frequency ω_p propagates in a Raman-active medium, it can get annihilated which, simultaneously, generate a Stokes photon of $\omega_s < \omega_p$, while leaving the crystal lattice vibrating in an excited state with energy $\hbar\omega_R$. The Raman vibrational frequency ω_R will vary for each different material [52]. A Raman anti-Stokes process can also occur, this is when the photon of ω_p is annihilated by the pre-excited lattice vibrating at ω_R, which generates an anti-Stokes photon of $\omega_s > \omega_p$. However, the anti-Stokes components are typically orders of magnitude less intense than the Stokes components, therefore such scenario will

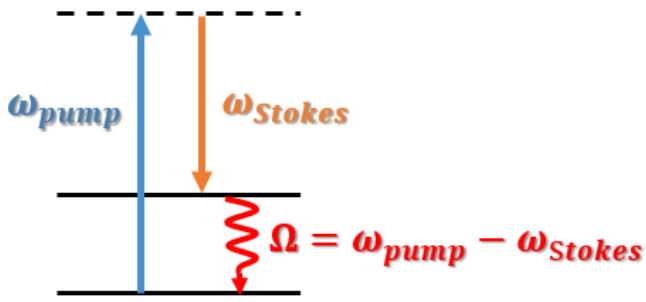

Figure 2.7: Stimulated Raman scattering process for the Stokes case. A photon of frequency ω_p propagating in a Raman-active medium gets annihilated and, simultaneously, produces a Stokes photon of $\omega_s < \omega_p$ while leaving the atom of the crystal vibrating in an excited state with energy $\hbar\omega_R = \hbar\Omega$.

not be considered in this thesis. Figure 2.7 shows the just described Raman scattering process. For crystalline silicon, this vibrational frequency is found to be $\frac{\omega_R}{2\pi} = 15.6$ THz [65]. However, this is not a pure frequency component, but it occupies a spectral width of $\Delta\omega/2\pi = 105$ GHz, which corresponds with a response time of $\tau \sim 10$ ps. This suggests, indeed, that intra-pulse Raman effects in crystalline silicon are not possible, since broad spectral pulses with spectral widths around Raman's would impose temporal widths below 100 fs, much lower than the Raman response time.

Similar to the electronic nonlinearity, the Raman response can be modelled as a third-order susceptibility tensor, $\hat{\chi}^R$, whose real part will drive a change in the refractive index the optical modes are probing, and whose imaginary part will lead to the depletion on one of the interacting modes and the amplification of the other. As per Ref. [66], the generic form of the third-order susceptibility tensor takes the following form:

$$\hat{\chi}^R_{ijkl}(\Omega) = \frac{\pi N_\nu}{3\hbar} \sum_\sigma \frac{\omega_\sigma(\alpha_{ij,\sigma}\alpha_{kl,\sigma} + \alpha_{ik,\sigma}\alpha_{lj,\sigma})}{\omega_\sigma^2 - \Omega^2 + 2i\Omega\Delta\omega}, \tag{2.14}$$

where $\Omega = \omega_p - \omega_s$, N_ν is the number of phonons per unit volume, ω_σ is the vibrational resonant frequency, and $\alpha_{ij,\sigma}$ are matrix elements given by the derivatives of the polarizability tensor $\hat{\alpha}$ with respect to the coordinate of each of the Raman-active optical phonons σ. Given the symmetry properties of crystalline silicon, which belongs to the

irreducible representation $\mathbf{\Gamma}_{25\prime}$, it can be found that the Raman tensor has just one independent component for $i = k$ and $j = l$, that is $\hat{\chi}^R_{1212}$, with the other non-zero elements given by $\hat{\chi}^R_{iijj} = 0.5\hat{\chi}^R_{ijij}$ [66].

It must be highlighted that, even though the spectral width of the Raman response can not be ignored, when the temporal widths of the interacting pulses are similar to the Raman response time, this can be just evaluated at the resonant frequency $\Omega = \omega_R$. If this is satisfied, the Raman susceptibility would become pure imaginary with $\hat{\chi}^R_{ijij} = -i\hat{\chi}^R = -i11.2 \cdot 10^{-18}\ m^2V^{-2}$, where $i, j = 1, 2, 3$ [67]. Furthermore, we also note that in future chapters we will consider that the silicon waveguides are fabricated along the $[1\hat{1}0]$ direction, which favors the cleaving of silicon during the fabrication stage. This means that a rotational matrix operation will be applied to the susceptibility tensor.

2.6 Applications of silicon photonics

Silicon photonics are appearing more and more often as the most suitable technology to develop integrated optical circuits, especially because its potential to be a low cost technology and its high compatibility with CMOS platforms. Silicon photonics are to be a fundamental part of the development of the next generation of computers and digital signal processors (DSPs). There have been impressive demonstrations already of the potential of programmable photonic processors made of single-mode silicon nanowires and controllable Mach-Zehnder interferometers (MZI) to study artificial neural networks or transport of quantum particles [68, 69]. Figure 2.8 [70] shows an artistic top view of a programmable photonic processor chip with more than two hundred phase shifters and beam splitters to control the amplitude and phase of beams at the waveguides intersections. This type of chip, which performs linear operations on signals could be potentially used to replace the electronic DSPs currently in the market when greater bandwidth capacity is required. In fact, not only an increase in bandwidth, but also a decrease in mass and weight could be key advantages to electronic DSPs that are used in spacecrafts, for

instance, to feed beamforming antenna elements by controlling the amplitude and phase of the optical signals within the chip.

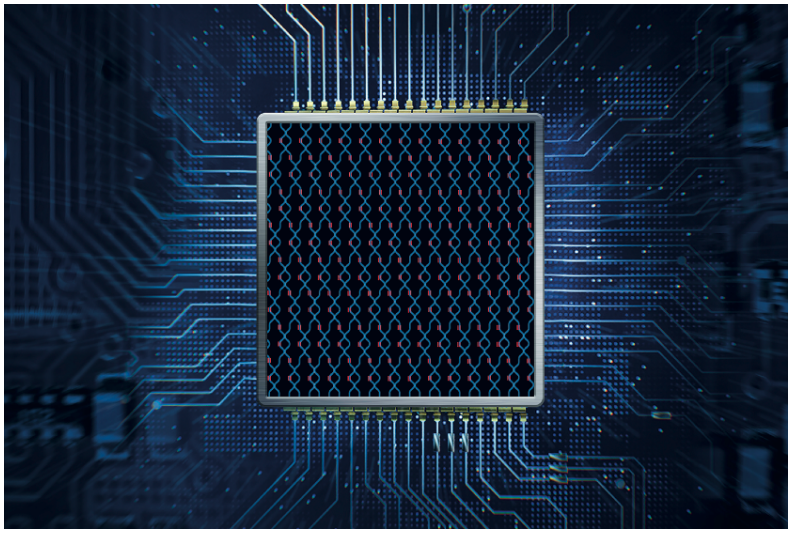

Figure 2.8: Artistic top view of a programmable photonic processor chip implementing a mesh of interconnected waveguides via MZIs, which are controlled by the phase shifters shown in red [70].

Silicon photonics are also great candidates to develop nonlinear devices that could be employed to generate and process optical signals, including amplification, modulation or frequency mixing. A good set of practical applications include [71]: supercontinuum generation, also called ultrabroadband spectra generation, makes use of the nonlinear SPM effect and is used in optical coherence tomography [72] and wavelength-division multiplexing (WDM) for single laser sources [73], among others; light amplification through the Raman effect, which we demonstrate it is possible in Chapter 5 of this work, even beyond the previously reported gains in the telecommunication regions [11, 74, 75] and the mid-infrared region [76]; wavelength-conversion via four-wave mixing (FWM) [77] or even modulation conversion by XPM [78]; and photonic sensing for health care, industrial applications or public safety, which is based on optical-matter interaction via the evanescent field out of a waveguide or a resonator, pertaining a detectable change on the optical field [79, 80].

An interesting application for WDM consists in combining the use of waveguides and cavities or resonators as follows [71]: firstly, by taking advantage of the SPM effect

through a long input waveguide, a narrow bandwidth optical pulse is broadened; and, secondly, by filtering different wavelengths through the resonators, these wavelengths are then extracted to the output waveguides which are coupled to the resonators. In fact, the mathematical model we present in Chapter 6 could be further developed to account for this type of application.

Applications that require more control over the optical modes lead to the inclusion into the optical circuit of silicon photonic crystals (Si-PhCs), which have clear advantages when the application under interest requires dispersion-engineered propagation [81], all-directions optical reflectors or strong light confinement. Especially remarkable is the design of Si-PhCs to exploit the numerous potential applications of slow-light propagation, which ranges from time-domain all-optical processing to data buffering and optical switches. Even if slow-light devices bring difficult challenges such as important high-order dispersion effects, several approaches have been demonstrated to eliminate this problem. For instance, by combining two or more photonic crystals with opposite GVD dispersion characteristics [82, 83]. In these cases, the chirped term of the silicon photonic crystal waveguide makes reference to the use of structural parameters that are gradually tuned along the length of the device so that the guided-mode band is smoothly coupled from one part to the other. Other approaches include zero-dispersion engineered devices made of several consecutive photonic crystal cavities [84].

Another important application of GVD-controlled devices is pulse compression. This technique can be used, for example, to increase the information capacity of connections in a computer. Recent studies [85] show that tapered silicon photonic waveguides can compress optical pulses by taking advantage of the strong dependence of the linear and nonlinear optical coefficients on the waveguide transverse cross-section. More interestingly, despite the challenges of high-order dispersion effects mentioned before, Si-PhCWGs have been dispersion-engineered to demonstrate pulse compression in slow-light regime [86].

In summary, we have shown how silicon photonics seem to be the strongest candidate for integrated optics, mainly due to the possibility to fabricate waveguides with

sub-micron transverse size, strong confinement of the optical modes and high nonlinear effects. Silicon photonic crystals help further to introduce dispersion-engineered devices and high-Q cavities, contributing in overall to a wide set of functional devices for the future technologies.

2.7 Introduction to diamond photonics and its applications

Despite the huge popularity that silicon photonics have reached and which we have covered in previous sections, in this work we also study diamond as a very promising material for photonic devices. Synthetic diamond presents numerous attractive properties for on-chip optical communications [42, 87, 88]. Among others, it offers a large transparency window, ranging from UV to far IR, with low absorption losses; it can be synthetized with a high refractive index of $n_{di} \approx 2.4$ enhancing the optical mode confinement in waveguides in the range of wavelengths from $\lambda = 500$ nm to $\lambda = 1000$ nm; its nonlinear properties are substantially important to enable Raman interaction, frequency conversion and comb generation; and furthermore it can be used for high power applications thanks to its excellent thermal properties, being a good thermal conductor with a low thermo-optic coefficient and low thermal expansion coefficient.

Diamond's crystal lattice presents inversion symmetry, which makes the lowest-order non-zero nonlinear susceptibility to be $\hat{\chi}^{(3)}$. The electronic nonlinearity, resulting from a deformation of the lattice electron cloud at high incident electric field intensities, has 3 independent coefficients for diamond, which is a typical characteristic of cubic crystals. The relationship between the 3 independent coefficients is $\hat{\chi}^3_{1111} = 3\hat{\chi}^3_{1221} = 3\hat{\chi}^3_{1122}$ [87]. Regarding the Raman nonlinearity of diamond, which is characterized by a vibrational frequency of the medium $\omega_r = 39.99$ THz, it can be 20 times stronger than its electronic nonlinearity, which makes it very attractive for the development of Raman lasers.

In the recent years, there has been one application which has brought the greatest

part of the attention to this novel photonic material: quantum optics. Colour centres are special defects in diamond that can act as quantum emitters of light. These defects function as bright single-photon sources (SPSs) at room temperature which can escape the crystal without absorption. Thanks to the numerous colour centres of diamond, which potentially can be precisely controlled, diamond has emerged as a promising low-temperature material for quantum computing, and this is, perhaps, the core application of future diamond photonic devices [42].

However, on the topic of this work, one of the most interesting benefits of diamond is its broad transparency window which includes visible light. This would permit the development of photonic devices that could operate with cheaper light sources such as VCSELs at 850 nm, which are extensively employed in data centers. Moreover, the nonlinear refractive index of diamond is relatively high for visible wavelenghts ($n_2 = 1.3 \cdot 10^{-19}\ m^2\ W^{-1}$) [88]. If this is combined with the low absorption losses and the non-existent two-photon absorption process, diamond-based waveguides are great candidates for the design of microring resonators for frequency comb generation, for which the round-trip loss must be minimised in order to offer high quality factors while the nonlinearity has to be strong enough so the soliton condition is satisfied. Based on all this, and due to the thermal properties introduced above, diamond-based waveguides would enable the design of high quality-factor, temperature-insensitive, microring resonators for the generation of combs at visible bands. Along these bases, in this thesis we present our study in the use of novel diamond fin waveguides for on-chip comb generation.

Kerr solitons are the main responsible behind frequency comb generation based on microring resonators. The optical field inside the microring resonator can be mathematically modelled as an externally pumped NLSE, whose stable solution corresponds to a train of Kerr solitons repeating at the cavity round-trip time, which is naturally translated to a comb in the frequency domain with a frequency-spectral-range (FSR) equal to the inverse of the round-trip time.

The main applications where microcombs are widely employed are microwave photonic

signal generation and WDM systems [89]. While the latter was discussed in Section 2.6, the idea behind the microwave signal generation is to mix in a photodetector two or more lines of a comb source which is characterised by a certain FSR, so every two lines mixed in the photodetector will produce a microwave signal at the frequency equal to the spacing betweent the two lines. Therefore, the microwave frequency output can range from the FSR to a multiple number of times the FSR. The concept of this microwave signal generation method is exploited in Ref. [89]. In this case, a continuous wave optical carrier is guided through the bus waveguide which then couples into the microring where the solitons are formed at a repetition rate of 20 GHz. The comb is then fed into a photodetector where the multiple lines are mixed and a microwave signal at 20 GHz is generated.

2.8 Numerical methods and simulation software

2.8.1 Split-step Fourier method

The computational method chosen to solve the coupled NLS system of equations that will be derived in the following chapters is the split-step Fourier method (SSF). The SSF method is categorized as a pseudospectral numerical method which uses the fast Fourier transform (FFT) [90] to achieve higher computational speeds than time-domain techniques. However, as mentioned before, the SSF method can only solve one-directional propagation.

In order to explain how it works, we consider a simpler NLS equation,

$$\frac{\partial A(z,T)}{\partial z} = (\hat{D} + \hat{N})A(z,T), \tag{2.15}$$

which describes the evolution with distance -z- of the amplitude -A- of an optical mode, and where the operator $\hat{D}$ accounts for linear effects such as dispersion and absorption and the operator $\hat{N}$ represents nonlinear effects including free-carrier absorption and free-

carrier change of index of refraction. Note also a change of variable has been applied so $T = t - \frac{z}{v_g}$. Typical forms of the linear and nonlinear operators for silicon photonic nanowires or silicon photonic crystal waveguides are as follows:

$$\hat{D} = \frac{\beta_2}{2}\frac{\partial^2}{\partial T^2} + i\frac{\beta_3}{6}\frac{\partial^3}{\partial T^3} - \frac{ic\kappa}{2nv_g}\alpha_{in}, \tag{2.16}$$

$$\hat{N} = -\gamma P_0|A|^2 - \frac{ic\kappa}{2nv_g}\alpha_{FC} - \frac{\omega\kappa}{nv_g}\delta n_{FC}, \tag{2.17}$$

where the terms α_{FC} and δn_{FC}, even if they seem to be linearly related to the pulse amplitude, they depend on the free-carrier generation which is proportional to the square power of the mode.

The solution of Eq. 2.15 has the following form:

$$A(z,T) = A(0,T)e^{(\hat{D}+\hat{N})z} \tag{2.18}$$

Now, writing Eq. 2.15 only over a small distance h, we could assume that $\hat{D}$ and $\hat{N}$ act independently, so that Eq. 2.18 is modified as follows:

$$A(z+h,T) \simeq e^{h\hat{D}}e^{h\hat{N}}A(z,T). \tag{2.19}$$

The nonlinear term $\hat{N}$ is z-dependent because it is proportional to the pulse amplitude $A(z,T)$ and to its square absolute value, including to the free carriers density at that z-point. Thus, the nonlinear term should be defined as:

$$e^{\int_z^{z+h}\hat{N}(z\prime)dz\prime} \simeq e^{\frac{h}{2}[\hat{N}(z)+\hat{N}(z+h)]}, \tag{2.20}$$

where the trapezoidal rule for the integral is applied. Alternatively, and especially if including the FC effects in the nonlinear term as we do, using a Runge-Kutta method to solve the differential equation $\frac{\partial A}{\partial z} = \hat{N}A$ is preferred for this step.

Finally, the equation is symmetrized to improve the accuracy of the SSF algorithm,

achieving an order of accuracy of $O(h^3)$,

$$A(z+h,T) \simeq e^{\frac{h}{2}\hat{D}} e^{\frac{h}{2}[\hat{N}(z)+\hat{N}(z+h)]} e^{\frac{h}{2}\hat{D}} A(z,T). \tag{2.21}$$

Based on this and moving from right to left in Eq. 2.21, the SSF algorithm starts calculating the dispersion contribution in the first $\frac{h}{2}$ step by transforming into the frequency domain the dispersion parameter $\hat{D}$ and the pulse shape $A(z,T)$, which simplifies the calculation. The result is taken back to the time domain and it is multiplied by the nonlinear factor at the midplane $z+\frac{h}{2}$ which represents the effect of nonlinearities over the whole segment h. The nonlinear part can be calculated in the time domain because it does not involve derivatives over time of the pulse amplitude. Note that the integral of the nonlinear term is computed before this step by using the pulse value just obtained at $z+\frac{h}{2}$. Finally, the result of it is transformed into the frequency domain and the remaining linear effects are applied for another $\frac{h}{2}$ step.

As with many other numerical methods to solve mathematical equations, SSF implicitly imposes periodic boundary conditions at the boundaries of the computational time window, although perfectly absorbing boundary conditions can be used as well. As a rule of thumb, in our simulations we chose the computational time window at least 30 times the value of the input pulse width. This way we ensure that any temporal or spectral broadening of the pulse due to linear and nonlinear dispersion can fit within the time window. Another issue is the choice of the number of temporal points, which, due to the use of the FFT in the SSF method, must be a power of 2 and large enough so that the time resolution is suitable for the specific problem. Similarly, the step size h must be small enough to achieve the required accuracy.

2.8.2 Newton-Raphson method for nonlinear systems of equations

The Newton-Raphson method is one of the most powerful and general methods for solving nonlinear systems of equations. It is a multidimensional root finding algorithm that generally converges fast to the solution, especially if a good initial guess is used.

Following the discretization procedure described in Chapter 6 (see also Ref. [91] for details about the numerical implementation), our set of equations to be solved consists of $M = (P-1)(N-2) + c_2(N-2) + 4(N-1) + NP$ nonlinear equations, with the same number of unknowns. These equations will have the general form:

$$\mathcal{F}_i(U_+^{n,p}, U_-^{n,p}, U_1^n, U_2^n, \mathcal{N}_w^{n,p}, \mathcal{N}_1^n, \mathcal{N}_2^n) = 0, \tag{2.22}$$

where $i = 1, 2..., M$, $n = 1, 2, ..., N$, $p = 1, 2, ..., P$ and the upper indexes n and p label the specific time and distance grid points, respectively, at which the unknowns are evaluated. In addition, a set of boundary conditions are used, as explained in Chapter 6.

We denote by $\boldsymbol{\mathcal{F}}$ and $\mathbf{x}$ the vectors constructed from the functions $\mathcal{F}_i$ and unknowns x_i, respectively. In the neighborhood of $\mathbf{x}$, the functions $\mathcal{F}_i$ can be expanded in Taylor series as follows:

$$\mathcal{F}_i(\mathbf{x} + \delta\mathbf{x}) = \mathcal{F}_i(\mathbf{x}) + \sum_{j=1}^{M} \frac{\partial \mathcal{F}_i}{\partial x_j} \delta x_j + \mathcal{O}(\|\delta\mathbf{x}\|^2). \tag{2.23}$$

If we introduce the Jacobian matrix as,

$$\mathcal{J}_{ij} = \frac{\partial \mathcal{F}_i}{\partial x_j}, \tag{2.24}$$

and keep only the linear terms in $\delta\mathbf{x}$, Eq. (2.23) can be recast in the following form:

$$\boldsymbol{\mathcal{F}}(\mathbf{x} + \delta\mathbf{x}) = \boldsymbol{\mathcal{F}}(\mathbf{x}) + \boldsymbol{\mathcal{J}}\, \delta\mathbf{x}. \tag{2.25}$$

If we now impose the condition $\boldsymbol{\mathcal{F}}(\mathbf{x}+\delta\mathbf{x}) = 0$, we obtain the following expression, which is used iteratively to obtain, at each step, the corrections of the unknowns $\delta\mathbf{x}$ that move all functions closer to zero,

$$\boldsymbol{\mathcal{J}}\,\delta\mathbf{x} = -\boldsymbol{\mathcal{F}}. \tag{2.26}$$

In a practical implementation, the algorithm starts with an initial guess $\mathbf{x}_0$, which is used to evaluate the vector function $\boldsymbol{\mathcal{F}}$ and the Jacobian matrix $\boldsymbol{\mathcal{J}}$ at $\mathbf{x} = \mathbf{x}_0$. Then, the matrix system of equations (2.26) is solved, and its solution $\delta\mathbf{x}_1$ is used to calculate the input vector of unknowns corrections at the second iteration, $\mathbf{x}_1 = \mathbf{x}_0 + \delta\mathbf{x}_1$. These steps are then repeated until the algorithm converges. If the algorithm converges, upon each iteration the norm $F = \|\boldsymbol{\mathcal{F}}\|^2$ must decrease. If, at some iteration, it does not decrease, a backtracking technique is used. This means that the new unknowns vector will be updated with a set of corrections in the Newton path, but after reducing the step size, namely $\mathbf{x}_{new} = \mathbf{x}_{old} + \lambda\delta\mathbf{x}_{new}$, with $0 < \lambda \leq 1$.

Even though the Newton-Raphson method requires large computing resources for the problem we want to solve, it shows a great efficiency in finding the roots even when the initial guess is not particularly close to the actual solution. Obviously, using boundary conditions guided by the proper physics of the problem greatly improves the convergence of this method.

2.8.3 Discrete Fourier transform method for externally-driven NLSE

In order to solve the equation which governs the physics inside a microring resonator, as shown in Chapter 4, here we describe the numerical method that can be implemented to obtain the steady-state solution of such problem.

The equation under interest is an externally-driven NLSE which for simplicity now

only contains up to second order dispersion terms:

$$\frac{\partial a(t,\tau)}{\partial t} = \frac{-\alpha' - i\delta_0}{t_R}a(t,\tau) - \frac{L}{v_g t_R}\frac{\partial a(t,\tau)}{\partial \tau} - \frac{iL\beta_2}{2t_R}\frac{\partial^2 a(t,\tau)}{\partial \tau^2} + \frac{i\gamma L}{t_R}|a(t,\tau)|^2 a(t,\tau) + \frac{\sqrt{\theta}}{t_R}a_{in}(\tau), \tag{2.27}$$

where $\alpha' = \frac{\alpha+\theta}{2}$, t_R is the roundtrip time, δ_0 is the detuning of the microring resonance closest to the driving field, θ is the coupling of the driving field in the microring, and

$$\alpha = L\frac{c\kappa\alpha_{in}}{nv_g}. \tag{2.28}$$

The steady-state solution of Eq. 2.27 corresponds to the case when $\frac{\partial a(t,\tau)}{\partial t} = 0$, i.e. we can just consider the τ dependency in the field amplitude.

The unknown $a(\tau)$ will have the form of a pulse which repeats periodically with t_R, therefore we will define it using the N-point discrete inverse Fourier transform (IDFT) as follows:

$$a(\tau) = \frac{1}{N}\sum_{k=0}^{N-1} A_k e^{\frac{-i2\pi k\tau}{N}}. \tag{2.29}$$

Similarly, the driving field, which is a continuous wave signal, takes the form:

$$a_{in}(\tau) = \frac{1}{N}\sum_{k=0}^{N-1} A_{in,k} e^{\frac{-i2\pi k\tau}{N}}, \tag{2.30}$$

where $A_{in,k} = A_{in}\delta_{k,N/2}$, being A_{in} an input parameter.

Based on the above expressions, we apply the IDFT to the steady-state solution of Eq. 2.27, obtaining:

$$\sum_{k=0}^{N-1} e^{\frac{-i2\pi k\tau}{N}}\left[\frac{-\alpha' - i\delta_0}{t_R}A_k + \frac{iL2\pi k}{v_g t_R N}A_k + \frac{iL\beta_2(2\pi k)^2}{2t_R N^2}A_k + \right. \tag{2.31}$$
$$\left. \frac{i\gamma L}{t_R}\frac{1}{N^2}\sum_{l=0}^{N-1}\sum_{m=0}^{N-1} A_k A^*{}_l A_m e^{\frac{-i2\pi(-l+m)\tau}{N}} + \frac{\sqrt{\theta}}{t_R}A_{in}\delta_{k,N/2}\right] = 0.$$

Now we multiply it by $e^{\frac{i2\pi j\tau}{N}}$ and integrate in τ:

$$\int_\tau \Bigg(\sum_{k=0}^{N-1} e^{\frac{-i2\pi(k-j)\tau}{N}} \Bigg[\frac{-\alpha' - i\delta_0}{t_R} A_k + \frac{iL2\pi k}{v_g t_R N} A_k + \frac{iL\beta_2(2\pi k)^2}{2t_R N^2} A_k + \frac{i\gamma L}{t_R} \frac{1}{N^2} \sum_{l=0}^{N-1} \sum_{m=0}^{N-1} A_k {A^*}_l A_m e^{\frac{-i2\pi(-l+m)\tau}{N}} + \frac{\sqrt{\theta}}{t_R} A_{in} \delta_{k,N/2} \Bigg] \Bigg) d\tau = 0. \tag{2.32}$$

We can arrange the above expression as follows:

$$\sum_{k=0}^{N-1} \left[\frac{-\alpha' - i\delta_0}{t_R} A_k + \frac{iL2\pi k}{v_g t_R N} A_k + \frac{iL\beta_2(2\pi k)^2}{2t_R N^2} A_k + \frac{\sqrt{\theta}}{t_R} A_{in} \delta_{k,N/2} \right] \int_\tau e^{\frac{-i2\pi(k-j)\tau}{N}} d\tau + \tag{2.33}$$

$$\sum_{k=0}^{N-1} \left[\frac{i\gamma L}{t_R} \frac{1}{N^2} \sum_{l=0}^{N-1} \sum_{m=0}^{N-1} A_k {A^*}_l A_m \int_\tau e^{\frac{-i2\pi(k-j-l+m)\tau}{N}} d\tau \right] = 0.$$

The integration of exponentials can be substituted by Kronecker delta functions,

$$\sum_{k=0}^{N-1} \left[\frac{-\alpha' - i\delta_0}{t_R} A_k + \frac{iL2\pi k}{v_g t_R N} A_k + \frac{iL\beta_2(2\pi k)^2}{2t_R N^2} A_k + \frac{\sqrt{\theta}}{t_R} A_{in} \delta_{k,N/2} \right] \delta_{k,j} + \tag{2.34}$$

$$\sum_{k=0}^{N-1} \left[\frac{i\gamma L}{t_R} \frac{1}{N^2} \sum_{l=0}^{N-1} \sum_{m=0}^{N-1} A_k {A^*}_l A_m \delta_{k+m,j+l} \right] = 0.$$

Therefore, we can define the following functions for each index j:

$$F_j = \left[\frac{-\alpha' - i\delta_0}{t_R} + \frac{iL2\pi j}{v_g t_R N} + \frac{iL\beta_2(2\pi j)^2}{2t_R N^2} \right] A_j + \frac{\sqrt{\theta}}{t_R} A_{in} \delta_{j,N/2} + \tag{2.35}$$

$$\frac{i\gamma L}{t_R} \frac{1}{N^2} \sum_{k=0}^{N-1} \sum_{l=0}^{N-1} \sum_{m=0}^{N-1} A_k {A^*}_l A_m \delta_{k+m,j+l}.$$

The Newton-Raphson method that was described in subsection 2.8.2 is then employed to solve the system of nonlinear equations F_j. Precisely, we can write:

$$F_j(\mathbf{A} + \delta\mathbf{A}) = F_j(\mathbf{A}) + \sum_{p=0}^{N-1} \frac{\partial F_j}{\partial A_p} A_p + O(\delta\mathbf{A}^2), \tag{2.36}$$

where the derivatives $\frac{\partial F_j}{\partial A_p}$ define the Jacobian matrix.

In fact, since the unknowns are complex variables, the unknown vector $\mathbf{A}$ will be of length $2N$ to accommodate the complex conjugate variables. Similarly, the number of functions F_j will be equal to $2N$ so half of them will correspond to the functions complex conjugates. Thus, the Jacobian matrix will be characterised by a size equal to $2N$ x $2N$, where the diagonal will contain both linear and nonlinear terms and the non-diagonal elements will contain only nonlinear terms. Based on this, the Jacobian matrix can be fully described by the following terms:

$$\frac{\partial F_j}{\partial A_p}|_{j=p} = \frac{-\alpha' - i\delta_0}{t_R} + \frac{iL2\pi j}{v_g t_R N} + \frac{iL\beta_2(2\pi j)^2}{2t_R N^2} + \frac{i\gamma L}{t_R}\frac{2}{N^2}\sum_m |A_m|^2, \tag{2.37}$$

$$\frac{\partial F_j}{\partial A_p}|_{j\neq p} = \frac{i\gamma L}{t_R}\frac{2}{N^2}\sum_{m\geq j-p} A^*_{m+p-j}A_m, \tag{2.38}$$

$$\frac{\partial F^*_j}{\partial A^*_p}|_{j=p} = \frac{-\alpha' - i\delta_0}{t_R} - \frac{iL2\pi j}{v_g t_R N} - \frac{iL\beta_2(2\pi j)^2}{2t_R N^2} - \frac{i\gamma L}{t_R}\frac{2}{N^2}\sum_m |A_m|^2, \tag{2.39}$$

$$\frac{\partial F^*_j}{\partial A^*_p}|_{j\neq p} = -\frac{i\gamma L}{t_R}\frac{2}{N^2}\sum_{m\geq j-p} A_{m+p-j}A^*_m, \tag{2.40}$$

$$\frac{\partial F_j}{\partial A^*_p}|_{j\neq p} = \frac{i\gamma L}{t_R}\frac{1}{N^2}\sum_{k\leq p+j} A_{p+j-k}A_k, \tag{2.41}$$

$$\frac{\partial F_j^*}{\partial A_p}|_{j\neq p} = -\frac{i\gamma L}{t_R}\frac{1}{N^2}\sum_{k\leq p+j} A^*_{p+j-k}A^*_k. \tag{2.42}$$

To validate the derived numerical method, we have simulated the same scenario appearing in Fig. 2 of Ref. [92], which corresponds to a 3.8 mm diameter MgF_2 whispering gallery mode resonator with a 40 μm mode-field diameter and parameters $Q = 1.90 \cdot 10^9$; $FSR = 18.2$ GHz; $\gamma = 0.032$ W^{1}km^1; $\beta_2 = 13$ ps^{2}km^1; $\alpha = \theta = 1.75 \cdot 10^5$; $P_{in} = 55.6$ mW; $L = 11.9$ mm; $\delta_0 = 0.0012$. In Fig.2.9 we plot the frequency and time domain results which tightly match the results published in Ref. [92].

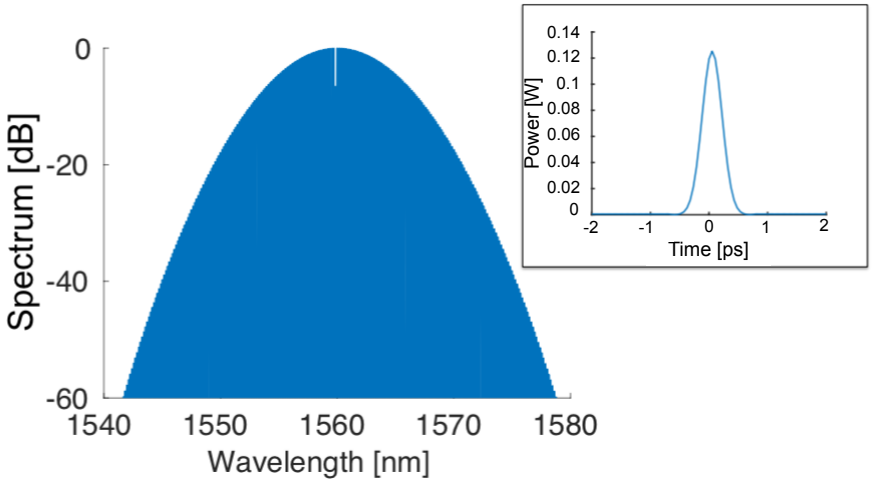

Figure 2.9: Simulation results of a 3.8 mm diameter MgF_2 whispering gallery mode resonator with a 40 μm mode-field diameter and parameters $Q = 1.90 \cdot 10^9$; $FSR = 18.2$ GHz; $\gamma = 0.032$ W^{1}km^1; $\beta_2 = 13$ ps^{2}km^1; $\alpha = \theta = 1.75 \cdot 10^5$; $P_{in} = 55.6$ mW; $L = 11.9$ mm; $\delta_0 = 0.0012$.

2.8.4 Modified split-step Fourier method for externally-driven NLSE

Equation (2.27) can also be solved using a modified version of the split-step Fourier method described in subsection 2.8.1.

In this case, the distance steps are replaced by time steps which can include multiple

roundtrips. For each roundtrip, all linear and nonlinear terms used are averaged by the microring length L. Note all terms appearing in Eq. (2.27) are dimensionless which means each step will correspond to an integer number of roundtrips rather than a physical length.

In order to introduce the pump term, one can exploit the step when the linear effects are applied by multiplying to the signal components in the frequency domain. As such, the constant power of the pump can be added at the corresponding frequency component.

While this method has a particular advantage compared with the stationary DFT method described previously, which is the possibility of watching the evolution of the comb until it reaches the stationary stage, it requires considerably more computational time. In addition, investigating the transient stage of the comb is not very relevant thinking in practical terms. Therefore, the simulations presented in Chapter 4 have been performed by using the stationary DFT method.

2.8.5 Simulation software

The simulation work as part of this thesis has been carried out by using different simulation software tools which we proceed to describe below.

Firstly, software tools based on the finite-difference frequency-domain (FDFD) method have been employed to solve Maxwell's equations in the frequency domain, using fully-vectorial and three-dimensional methods. FDFD works by expressing Maxwell's equations as $Ax = \omega^2 Bx$, which is an eigenproblem with eigenvectors x and eigenvalues ω^2. By fixing the wavevector $\mathbf{k}$, FDFD tools are capable to obtain the band structure $\omega(\mathbf{k})$ and the corresponding electromagnetic fields. Based on this, two FDFD software tools have been used: MIT Photonic Bands (MPB), a free and open-source simulation software package for calculating band diagrams and electromagnetic modes of periodic dielectric structures, and Rsoft BandSOLVE, a commercially available photonic band solver. Both tools use the plane wave expansion (PWE) algorithm to perform band computations on photonic crystal structures. The PWE method consists on expanding both the electro-

magnetic fields and the dielectric profile in terms of the Fourier series components along the reciprocal lattice vector, which are then used into the curl-curl relation in order to obtain the eigen equation. In other words, it computes definite-frequency eigenstates, also called harmonic modes, for arbitrary wavevectors. In this thesis, MPB has been employed to obtain the dispersion relations and electromagnetic modes of the photonic crystal waveguides presented in Chapters 5 and 6, while Rsoft BandSOLVE has been employed to validate the correct use of MPB by comparing the band diagrams obtained from both tools for the same photonic crystal structure.

In addition to these FDFD methods, the finite element method (FEM) has been employed to obtain the modes and dispersion curves of the diamond photonic waveguide presented in Chapter 4. The FEM method is widely known in many engineering disciplines and it is based on discretizing the space dimensions in a finite number of geometric elements, for instance triangles or rectangles, in such a way the unknown functions are approximated on those elements. In consequence, the problem results into a large system of equations which can then be solved by using different methods. FEM also solves Maxwell's equations in the frequency domain, on a frequency by frequency basis. In this case, Rsoft FemSIM has been used. This is a generalized full-vector electromagnetic mode solver based on the FEM that can calculate any number of transverse or cavity modes of an arbitrary structure on a non-uniform mesh.

Several Matlab programs have been written in order to calculate complex coefficients used in the various models, including the nonlinear Kerr and Raman terms and the higher order group velocity dispersion terms. In addition, the discrete Fourier transform method for externally-driven NLSE presented above has been fully implemmented in Matlab.

Two main simulation tools developed in C++ have been developed for this work, in particular for solving the NLSE appearing in Chapters 5 and 6. Both the split-step Fourier method and the Newton-Raphson method for nonlinear systems of equations presented above have been implemented in this platform.

Chapter 3

Fundamental theoretical model for pulse propagation in a silicon photonic nanowire

3.1 Introduction

In this chapter we derive the nonlinear Schrödinger (NLS) equation that describes the pulse propagation through a single mode silicon photonic waveguide, showing the origin of the linear and nonlinear optical effects introduced in Chapter 2. Starting from Maxwell equations and making use of the Lorentz reciprocity theorem, the differential NLS equation that describes the pulse dynamics through the waveguide, including the FC rate equation, will be obtained.

This chapter should be the reference to the methodology used to derive our mathematical models. In this case, since it is applied to a simple scenario considering just a single optical pulse, it will facilitate the understanding of the models derived in following chapters, which add more complexities, such as nonlinear interaction between several pulses, Raman nonlinear effect or interaction with cavities alongside the waveguide. Actually, a similar mathematical approach is applied either for silicon nanowires

or for silicon PhCWGs, just keeping in mind that the propagating modes for the latter follow a periodic relation along the waveguide as per Bloch's theorem.

It is important to stress here that the main differences with respect to the propagation equations for standard fibre optics [46]. Indeed, as already mentioned, silicon nonlinear optical susceptibilities are tensors, due to the anisotropic nature of this material, whereas for isotropic glass fibres these are scalar variables. Additionally, the nonlinear susceptibilities are highly dependent on the field confined within the waveguide, which is especially high for silicon, thus increasing the complexity to the problem to be solved.

3.2 Single pulse propagating through a silicon photonic waveguide

The Maxwell equations are the starting point of solving an electromagnetic problem. Their solution in the frequency domain over the photonic structure of interest will result in all the guiding modes with frequency ω that can be excited in that specific structure. In this chapter, the structure of interest is a silicon photonic wire (SPW), which is represented in Fig. 3.1. It is built of a rectangular silicon core, oriented along the $[1\hat{1}0]$ crystallographic direction, and burried into a SiO_2 substrate, around 1 μm thick. In practice, a 45° cleavage plane of Si is applied to achieve high-quality end facets. The dimensions, h -height- and w -width- of the silicon core, are in submicron region. Single-mode SPWs typically have dimensions of 200 to 300 nm in height and 400 to 500 nm in width. A_0 is the transverse area of the silicon core, which will appear as a relevant element in the NLS equations derived in this chapter.

Assuming an external perturbation represented by the polarization term $\mathbf{P}_{\text{pert}}(\mathbf{r},\omega)$, the form of the Maxwell equations becomes as follows:

$$\nabla \times \mathbf{E}(\mathbf{r},\omega) = i\omega\mu\mathbf{H}(\mathbf{r},\omega), \tag{3.1a}$$

$$\nabla \times \mathbf{H}(\mathbf{r},\omega) = -i\omega[\epsilon_c(\mathbf{r},\omega)\mathbf{E}(\mathbf{r},\omega) + \mathbf{P}_{\text{pert}}(\mathbf{r},\omega)], \tag{3.1b}$$

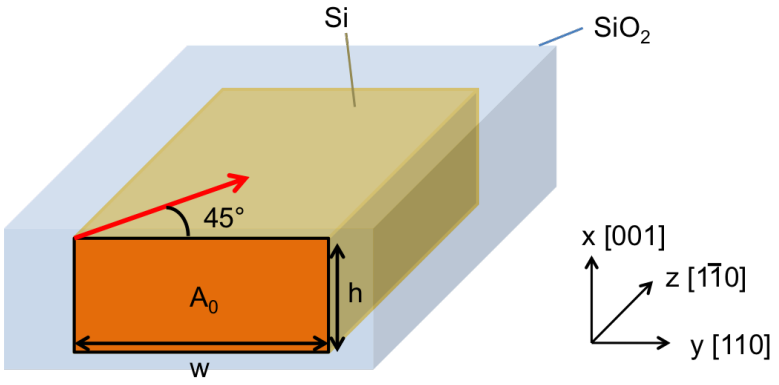

Figure 3.1: Sketch of silicon photonic nanowire burried in SiO_2.

where $\mathbf{E}(\mathbf{r},\omega)$ and $\mathbf{H}(\mathbf{r},\omega)$ are the electric and magnetic field of the propagating mode, $\epsilon_c(\mathbf{r},\omega)$ describes the dielectric constants composing the waveguide and μ is the magnetic permeability. The total polarization of the mode, $\mathbf{P}_{\text{pert}}$, is expressed as the sum of linear and nonlinear polarizations as in Chapter 2:

$$\mathbf{P}_{pert}(\mathbf{r},\omega) = \epsilon_0\hat{\chi}^{(1)}(\mathbf{r},\omega)\cdot\mathbf{E} + \epsilon_0\hat{\chi}^{(3)}(\mathbf{r},\omega)\vdots\mathbf{EEE} + O(\mathbf{E}^4), \tag{3.2}$$

where $\epsilon_0\hat{\chi}^{(1)}$ determines the linear part of the polarization, $\hat{\chi}^{(2)}$ vanishes for silicon and $\hat{\chi}^{(3)}$ determines the nonlinear component of the polarization. Thus, defining the linear polarization as $\mathbf{P}_{linear} = \epsilon_0\hat{\chi}^{(1)}\cdot\mathbf{E} = \delta\epsilon_c\cdot\mathbf{E}$, and considering only the electronic nonlinearity as a third-order nonlinear polarization, i.e. $\mathbf{P}_{nonlinear} = \epsilon_0\hat{\chi}^{e}(\mathbf{r},\omega)\vdots\mathbf{EEE}$, the total polarization is expressed as follows:

$$\mathbf{P}_{pert} = \mathbf{P}_{linear} + \mathbf{P}_{nonlinear} = \delta\epsilon_c\cdot\mathbf{E} + \epsilon_0\hat{\chi}^{e}(\omega;\omega,-\omega,\omega)\vdots\mathbf{E}(\mathbf{r},\omega)\mathbf{E}^*(\mathbf{r},\omega)\mathbf{E}(\mathbf{r},\omega), \tag{3.3}$$

where the linear part of it was detailed in Chapter 2 from Eq.(2.11) to (2.13), and $\hat{\chi}^{e}(\omega;\omega,-\omega,\omega)$ is the conventional notation for the third-order susceptibility tensor of silicon as explained in Chapter 2 as well, and which in this case is only related to SPM and TPA effects taking into account we assume we have just a narrow-band single pulse propagating through the waveguide and that the sum-frequencies processes are not phase

matched.

The theoretical method we use to derive the NLS equations starts by considering an unperturbed scenario where the nonlinear polarization vector is equal to zero and, then, a second scenario characterized by a polarization vector where the different linear and nonlinear effects are introduced. Once we have the fields for both scenarios described, we will apply the Lorentz reciprocity theorem to continue our derivation.

In the case of the unperturbed scenario, we can simply assume we have just a guiding mode whose frequency is ω_0 and which is an exact solution of the Maxwell equations (5.2) with $\mathbf{P}_{\text{pert}} = 0$. We will refer to $(\mathbf{E}_a, \mathbf{H}_a) \equiv (\mathbf{E}_0, \mathbf{H}_0)$ as the electromagnetic fields in the unperturbed waveguide, being in frequency domain:

$$\mathbf{E}_0(\mathbf{r}, \omega_0) = \frac{1}{\sqrt{P_0}} \mathbf{e}_0(\mathbf{r}, \omega_0) e^{i\beta_0 z}, \tag{3.4a}$$

$$\mathbf{H}_0(\mathbf{r}, \omega_0) = \frac{1}{\sqrt{P_0}} \mathbf{h}_0(\mathbf{r}, \omega_0) e^{i\beta_0 z}, \tag{3.4b}$$

where β_0 is the propagation constant and P_0 is the power carried by the mode, meaning the cross-sectional components of the electromagnetic field $\mathbf{e}_0$ and $\mathbf{h}_0$ can be normalized. The following relations applies for P_0:

$$\frac{1}{4} \int_{A_\infty} (\mathbf{e}_0 \times \mathbf{h}_0^* + \mathbf{e}_0^* \times \mathbf{h}_0) \cdot \hat{\mathbf{z}} dA = P_0, \tag{3.5a}$$

$$P_0 = W v_g, \tag{3.5b}$$

$$W = \frac{1}{2} \int_{A_\infty} \epsilon_c |\mathbf{e_0}(\mathbf{r}, \omega)|^2 dA, \tag{3.5c}$$

where A_∞ is a transverse cross-section extending to infinity, and W is the energy density of the mode in which we have assumed no frequency dispersion for the dielectric constant. Note also we have assumed the electric and magnetic energies of the mode are equal.

We refer now to the electromagnetic fields in the perturbed waveguide, $(\mathbf{E}_b, \mathbf{H}_b) \equiv$

$(\mathbf{E}, \mathbf{H})$, described as follows:

$$\mathbf{E}(\mathbf{r}, \omega) = \frac{1}{\sqrt{P_0}} a(z, \omega) \mathbf{e}_0(\mathbf{r}, \omega) e^{i\beta z}, \tag{3.6a}$$

$$\mathbf{H}(\mathbf{r}, \omega) = \frac{1}{\sqrt{P_0}} a(z, \omega) \mathbf{h}_0(\mathbf{r}, \omega) e^{i\beta z}, \tag{3.6b}$$

where ω is a generic frequency and where $a(z, \omega)$ represents the modified mode amplitudes due to the perturbations included. This means that the total energy carried by the electromagnetic field $(\mathbf{E}, \mathbf{H})$ of the perturbed waveguide is $|a(z, \omega)|^2$.

The Lorentz reciprocity theorem can be used to relate the electromagnetic fields of the unperturbed and perturbed scenarios of above. To this end, let us begin by considering the following integral identity, which can be easily derived from the divergence theorem:

$$\oint_{\partial S} \mathbf{F} \cdot \mathbf{n} dl + \frac{\partial}{\partial z} \int_S \mathbf{F} \cdot \hat{\mathbf{z}} dS = \int_S \nabla \cdot \mathbf{F} dS, \tag{3.7}$$

where $\mathbf{F}$ is an arbitrary vector field, S is the transverse section at position, z, and ∂S is the boundary of S. Note that this is the divergence theorem applied to a waveguide, which can be read as the flux of the field vector $\mathbf{F}$ escaping through the cross-section borders (line integral), in addition to the flux escaping transversally the cross-section along the propagation direction in the waveguide, must be equal to the outflow rate of the vector field $\mathbf{F}$, which is equivalent to the surface integral of the divergence of $\mathbf{F}$ over the area inside the boundary of S.

We now define the field $\mathbf{F}$ as $\mathbf{F} = \mathbf{E}_b \times \mathbf{H}_a^* + \mathbf{E}_a^* \times \mathbf{H}_b$, and assuming that the transverse section, S, is extended to infinity, the line integral in Eq. (3.7) vanishes, because the waveguide modes decay exponentially to zero at infinity. At this point, we make use of the Maxwell's equations and the vector identity $\nabla \cdot (\mathbf{A} \times \mathbf{B}) = \mathbf{B} \cdot (\nabla \times \mathbf{A}) - \mathbf{A} \cdot (\nabla \times \mathbf{B})$ to derive the r.h.s of Eq. (3.7), which beomes as follows:

$$\frac{\partial}{\partial z} \int_S \mathbf{F} \cdot \hat{\mathbf{z}} dS = i\mu_0(\omega_b - \omega_a) \int_S \mathbf{H}_a^* \cdot \mathbf{H}_b dS$$

$$+ i \int_S (\omega_b \epsilon_b - \omega_a \epsilon_a) \mathbf{E}_a^* \cdot \mathbf{E}_b dS. \tag{3.8}$$

Using Eq. 3.5a and taking into account the propagating constant and mode profile in the perturbed scenario will remain unchanged, the left term of Eq. 3.8 becomes as follows,

$$\frac{\partial}{\partial z} \int_S \mathbf{F} \cdot \hat{\mathbf{z}} dS = 4 \frac{\partial a(z,\omega)}{\partial z}. \tag{3.9}$$

Similarly, it can be demonstrated that the right term of Eq. 3.8 becomes

$$\begin{aligned} i\mu_0(\omega_b - \omega_a) \int_S \mathbf{H}_a^* \cdot \mathbf{H}_b dS + i \int_S (\omega_b \epsilon_b - \omega_a \epsilon_a) \mathbf{E}_a^* \cdot \mathbf{E}_b dS = \\ i \frac{a(z,\omega)}{P_0} \left[\int_S (\mu_0(\omega - \omega_0)) |\mathbf{h_0}|^2 dS + \int_S (\omega \epsilon(\omega) - \omega_0 \epsilon(\omega_0)) |\mathbf{e_0}|^2 dS \right]. \end{aligned} \tag{3.10}$$

Then, by making Eq. 3.9 equal to Eq. 3.10 and adding the polarization term, the following expression can be found:

$$\frac{\partial a(z,\omega)}{\partial z} = a(z,\omega) B(z,\omega) + \frac{i\omega}{4} \int_S \mathbf{E}_a^* \mathbf{P}_{pert}(\omega) dS, \tag{3.11}$$

where

$$B(z,\omega) = \frac{i}{4P_0} \left[\int_S (\mu_0(\omega - \omega_0)) |\mathbf{h_0}|^2 dS + \int_S (\omega \epsilon(\omega) - \omega_0 \epsilon(\omega_0)) |\mathbf{e_0}|^2 dS \right], \tag{3.12}$$

and the second term on the right can be obtained by deriving $\nabla \cdot (\mathbf{E}_b \times \mathbf{H}_a^* + \mathbf{E}_a^* \times \mathbf{H}_b)$ for $\mathbf{E}_a = \mathbf{E}_0$ and $\mathbf{E}_b$ following Maxwell equations with the polarization term.

The next step is to expand Eq. 3.12 in Taylor series around ω_0, which becomes:

$$B(z,\omega) \equiv \sum_{n \geq 1} \frac{i\beta_n}{n!} (\omega - \omega_0)^n, \tag{3.13}$$

where we define,

$$\beta_1(z) = \frac{\delta(z)}{v_g}, \tag{3.14}$$

$$\beta_n(z) = \delta(z)\frac{\partial^{n-1}}{\partial\omega^{n-1}}\left(\frac{1}{v_g}\right), n \geq 2. \tag{3.15}$$

Note that v_g is the group velocity of the propagating mode and that the function $\delta(z)$ can be averaged over the propagation distance, becoming equal to one. The higher order Taylor coefficients correspond to those shown on Eq. 2.8 in Chapter 2, i.e. β_2 is the GVD coefficient and β_3 is the TOD coefficient. Higher order may normally be discarded.

At this point, we derive the polarization term by sectioning $\mathbf{P}_{pert}$ in two parts: firstly, the linear polarization $\mathbf{P}_{lin} = \delta\epsilon_{FC}\cdot\mathbf{E}_b$ part as per Drude's model, and then the nonlinear polarization part $\mathbf{P}_{nlin}(\mathbf{r},\omega) = \epsilon_0\hat{\chi}^e(\omega)\vdots\mathbf{E}_b(\omega)\cdot\mathbf{E}_b^*(\omega)\cdot\mathbf{E}_b(\omega)$ using the electronic nonlinear susceptibilty. Although, in our calculations, we employ the full susceptility tensor, it is worth explaining the concept of the effective nonlinear susceptibility, defined by [39]:

$$\hat{\chi}^e_{eff} = \hat{\chi}^e_{1122}\Big[(\hat{a}^*\cdot\hat{b})(\hat{c}\cdot\hat{d})+(\hat{a}^*\cdot\hat{c})(\hat{b}\cdot\hat{d})+(\hat{a}^*\cdot\hat{d})(\hat{b}\cdot\hat{c})\Big]+(\hat{\chi}^e_{1111}-\hat{\chi}^e_{1122})\sum_{i=1}^{3}\hat{a}_i^*\hat{b}_i\hat{c}_i\hat{d}_i, \tag{3.16}$$

where $\hat{a}$ is a unit vector along the direction of the induced polarization, $\hat{b}$, $\hat{c}$, and $\hat{d}$ are unit vectors along the polarization direction of the interacting fields, and $\hat{a}_i$, $\hat{b}_i$, $\hat{a}_i$, and $\hat{d}_i$ are the direction cosines of these unit vectors. Since the effective nonlinear susceptibility is related to the intensity dependent refractive index n_2 and the TPA coefficient β_{TPA} as follows,

$$\frac{\omega}{c}n_2 + \frac{i}{2}\beta_{TPA} = \frac{3\omega}{4\epsilon_0 c^2 n^2}\hat{\chi}^e_{eff}, \tag{3.17}$$

this is, indeed, a way to measure the actual nonlinear susceptibility of the material.

Eventually, we must convert the equations to the time domain, so the nonlinear polarization term becomes:

$$\delta\mathbf{P}_{nlin}(\mathbf{r},t) = \frac{1}{2}[\delta\mathbf{P}^{(+)}_{nlin}(\mathbf{r},t) + c.c.] = \epsilon_0\hat{\chi}^e(\mathbf{r},t)\vdots\mathbf{E}_b(\mathbf{r},t)\mathbf{E}_b(\mathbf{r},t)\mathbf{E}_b(\mathbf{r},t), \tag{3.18}$$

where *c.c.* means complex conjugate and for which we define the electric field b in time domain as

$$\mathbf{E}_b(\mathbf{r},t) = \frac{1}{2}A(z,t)\frac{\mathbf{e}_0(\mathbf{r},\omega_m)}{\sqrt{P_0}}e^{i(\beta_0 z-\omega_0 t)} + c.c. \tag{3.19}$$

Now, the unknown $A(z,t)$ is obtained by applying the inverse Fourier transform to $a(z,\omega)$:

$$A(z,t) = \frac{1}{2\pi}\int_0^\infty a(z,\omega)e^{-i(\omega-\omega_0)t}d\omega, \tag{3.20}$$

and the following relations have to be considered also:

$$\int_0^\infty \omega a(z,\omega)e^{-i(\omega-\omega_0)t}d\omega \approx \omega_0 A(z,t), \tag{3.21}$$

$$\int_0^\infty (\omega-\omega_0)^n a(z,\omega)e^{-i(\omega-\omega_0)t}d\omega = \left(i\frac{\partial}{\partial t}\right)^n A(z,t). \tag{3.22}$$

At this point, we employ all expressions above and we arrive to the final NLS equation:

$$\begin{aligned} &i\left[\frac{\partial A}{\partial z}+\frac{1}{v_g}\frac{\partial A}{\partial t}\right]-\frac{\beta_2}{2}\frac{\partial^2 A}{\partial t^2}-i\frac{\beta_3}{6}\frac{\partial^3 A}{\partial t^3}= \\ &-\frac{\omega_0\delta n_{\mathrm{fc}}\kappa(z)}{nv_g}A-\frac{ic\kappa(z)}{2nv_g}(\alpha_{\mathrm{fc}}+\alpha_{\mathrm{in}})A-\gamma(z)|A|^2A, \end{aligned} \tag{3.23}$$

where κ is the overlap integral between the guiding section and the spatial field of the propagating mode and γ is the nonlinearity responsible for SPM on the pulse dynamics. More in detail,

$$\kappa(z) = \frac{\epsilon_0 n^2}{2W}\int_{S_{\mathrm{nl}}}|\mathbf{e}_0(\omega)|^2 dS, \tag{3.24a}$$

$$\gamma(z) = \frac{3\omega\epsilon_0}{16v_g^2}\frac{1}{W^2}\int_{S_{\mathrm{nl}}}\mathbf{e}_0^*(\omega)\cdot\hat{\chi}^e(\omega,-\omega,\omega)\vdots\mathbf{e}_0(\omega)\mathbf{e}_0^*(\omega)\mathbf{e}_0(\omega)dS, \tag{3.24b}$$

Finally, the last step of the derivation consists of formulating the FCs rate equation,

which describes the FCs dynamics in silicon waveguides and which will be coupled to the NLS equation Eq. 3.23. By discarding all terms in Eq. 3.23 that do not contribute to TPA, this is all linear terms, the NLS equation is simplified as follows:

$$\frac{\partial A}{\partial z} = i\gamma(z)|A|^2 A, \tag{3.25}$$

Then, on one hand, we multiply both sides of the equation by the complex conjugate of the mode amplitude A,

$$A^* \frac{\partial A}{\partial z} = i\gamma(z)|A|^4, \tag{3.26}$$

and, on the other hand, we apply the complex conjugate at both sides of Eq. 3.25 and then multiply it by A,

$$A \frac{\partial A^*}{\partial z} = -i\gamma^*(z)|A|^4, \tag{3.27}$$

the sum of Eq. 3.26 and Eq. 3.27 gives as result:

$$\frac{\partial |A|^2}{\partial z} = -\gamma(z)''|A|^4. \tag{3.28}$$

To finish with, considering the energy required to generate an electron-hole pair is $2\hbar\omega$, we convert the loss of energy per unit of distance into the number of electron-hole pairs generated via the absorption of two photons of same frequency, and we include it into the following rate equation:

$$\frac{\partial N}{\partial t} = -\frac{N}{\tau_c} + \frac{\gamma''}{2\omega\hbar A_0}|A|^4, \tag{3.29}$$

where τ_c is the characteristic lifetime of FCs, γ'' is the imaginary part of the nonlinear susceptibility term of equation Eq. 4.2b. and $\hbar$ is the reduced Planck's constant.

It shall be noted that only a fraction of the power of the electromagnetic mode contributes to the generation of free carriers as the mode profile only partially overlaps with the silicon waveguide. The characteristic lifetime, for silicon nanowires commonly used

for photonic applications, varies from sub-nanosecond to tens of nanoseconds, while for silicon photonic crystal slab waveguides is in the range of few hundred of picoseconds.

Chapter 4

Nonlinear optics in diamond-fin photonic nanowires: soliton formation and frequency comb generation

4.1 Introduction

Synthetic diamond is becoming an increasingly fashionable material platform for on-chip optical communications, particularly due to its attractive classical and quantum optical properties [42, 87, 88]. Central among these remarkable optical properties are its large transparency window, ranging from ultraviolet (UV) to far-infrared (IR), very small optical absorption losses, and it can be synthesized with a high refractive index, $n_{di} \approx 2.4$, thus enabling enhanced optical waveguides mode confinement in a broad spectral range extending from 500 nm to 1000 nm. Equally important for its applications to active photonic devices, diamond possesses key nonlinear optical properties, including large Kerr nonlinearity that can be employed to frequency conversion and comb generation devices, and also strong Raman interaction at the operating wavelengths of $\sim$2 µm and with pump

laser wavelengths in the telecom band at around $\sim$1.6 µm [50]. These important optical properties are accompanied by excellent thermal properties, synthetic diamond being good thermal conductor with low thermo-optic coefficient and low thermal expansion coefficient, properties that render it an ideal material for high-power applications and integration of electro-optic systems. In addition, due to the numerous color centers of diamond, which potentially can be precisely controlled, this material has emerged as a promising low-temperature platform for quantum computing, perhaps one of the future core applications of diamond [51].

The functionality of diamond is greatly broadened by the fact that photonic structures with subwavelength features, such as subwavelength waveguides, can be readily implemented in this platform (for a review of optical properties of subwavelength waveguides the reader is referred to Ref. [38]). This enables dispersion-engineered devices and applications in the visible spectrum and therefore makes diamond photonics an appealing alternative to well-established, more mature photonic platforms, such as silicon-on-insulator [39], silicon nitride [40], or compound semiconductor on-insulator [41]. For example, subwavelength diamond waveguides would enable the development of photonic systems that incorporate cheaper light sources, such as vertical-cavity surface-emitting lasers (VCSELs) at 850 nm, which are extensively used in data centers [93]. Moreover, the relatively large nonlinear refractive index coefficient of diamond in the visible spectrum, i.e. $n_2 = 1.3\times10^{-19}\,\mathrm{m^2\,W^{-1}}$ [88], in conjunction with the fact that it has an extremely small two-photon absorption coefficient, would enable the implementation of high quality-factor, temperature-insensitive, microring resonators [94] for the efficient generation of frequency combs in these frequency bands. This would further increase the interest in on-chip frequency comb generation [95], which is a key functionality widely employed in microwave photonic signal generation and wavelength-division multiplexing systems [89, 96, 97].

Motivated by these ideas, here we study pulsed dynamics in subwavelength diamond-fin waveguides, a recently developed type of diamond waveguide which, apart from the

advantages already highlighted, could improve the seamless integration with very large-scale integration (VLSI) electronics for on-chip optical communications [98]. This is because, in silicon photonics, the buried-oxide-layer (BOX) thickness required for optical confinement is much larger than the optimum for VLSI electronics. On the contrary, with this type of waveguide design, the confinement layer allows for the removal of the BOX.

Specifically, we demonstrate that diamond-fin waveguides can be designed to possess zero group-velocity dispersion (GVD) points, thus enabling soliton formation and efficient supercontinuum generation in ultracompact photonic devices, the latter being recently demonstrated [99]. To illustrate the versatility of this type of optical waveguide, we demonstrate that frequency comb generation can be readily implemented using such photonic structures.

The chapter is organized as follows. In the next section we present the structure of the investigated waveguide and the frequency dispersion properties of its optical modes. Then, in Section 3, we introduce a theoretical model that describes the optical pulse dynamics upon propagation in diamond fin waveguides. Furthermore, in Section 4 we discuss two applications of our diamond fin waveguides, namely soliton formation and frequency comb generation. Finally, in the last section we summarize the main conclusions of our study.

4.2 Waveguide structure and mode dispersion properties

The waveguide considered in this work, and which has been proposed in Ref. [98], is schematically shown in Fig. 4.1(a). It is a single-mode uniform waveguide consisting of a diamond substrate, from which a diamond light guiding fin of width w rises to a height $h_{fin} = h_b + t + h$ through lithography plus etching processes. A silicon dioxide buffer layer is grown from the substrate up to height h_b for which low-index growth and planarization processes are employed. On top of it, the edge of the fin wall rises by $t + h$, where t is

the thickness of a silicon nitride layer used to increase the refractive index contrast and thus enhance the field confinement. This is created by high-index growth and low-index etching processes.

With buffer layers thicker than about 1 µm, the propagation losses due to substrate leakage can be reduced below 0.15 dB cm^{-1} [98]. In Fig. 4.1(b), we show the waveguide cross-section with $h_b = 1\,\mu m$, $h = 350\,nm$, $t = 200\,nm$, and $w = 200\,nm$. For these waveguide parameters, we employed the finite-element method implemented in Synopsys's commercially available software FemSIM [55] to compute the optical guiding modes supported by the structure. The spatial profile of the dominant component (E_x) of the quasi-TE mode, calculated for $\lambda = 637\,nm$, is also depicted in Fig. 4.1(b). At this wavelength, the effective refractive index is $n_{eff} = 2.129$.

We investigate four waveguide designs, labeled A, B, C, and D, defined by the parameters: w was 200 nm, 300 nm, 400 nm, and 500 nm, h was 350 nm, 350 nm, 500 nm, and 600 nm, and h_b was 1 µm, 2.2 µm, 3.5 µm, and 7 µm, respectively. Overall, the variation of these three parameters satisfied the objective of demonstrating broadly different

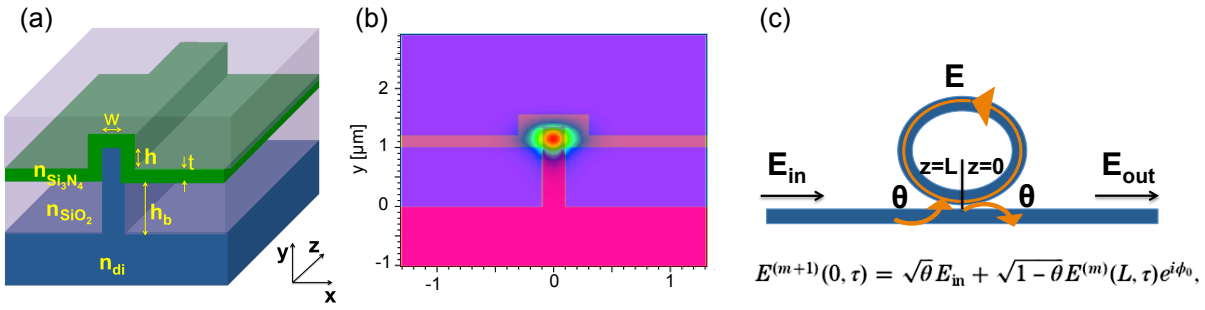

Figure 4.1: (a) Schematics of a diamond fin waveguide, consisting of a diamond substrate, a diamond light-guiding fin of width w, a silicon dioxide buffer layer of height h_b, and a silicon nitride layer of thickness t. (b) Spatial profile of the E_x-component of the quasi-TE mode (H_x and H_z components are very weak but not completely zero) supported by the optical waveguide. (c) Photonic circuit model for the frequency comb generation, in which a bus waveguide is coupled back and forth with a ring resonator of circumference L. The cavity boundary conditions are also included. The input electric field has a fraction θ of its power coupled to the ring. After propagating through a roundtrip, the field has been modified by the linear and nonlinear effects through the length L and phase shifted by ϕ_0. At that point, the fraction of power that does not couple back to the waveguide, interferes with the input field.

dispersion behaviours, including the crossing of the zero-GVD line, and mode confinement levels. While the width w and the height $h + t$ of the fin are varied up to a point to ensure single-mode operation, the key parameter we were interested to evaluate for different values was the buffer height h_b. This one can be increased in order to minimize the energy leakage down through the buffer, which maximises the nonlinear effects and minimises the propagation loss, but always within a limit due to fabrication considerations. In practice, waveguides with aspect ratios as large as 10:1 can be readily fabricated using anisotropic inductively coupled plasma reactive ion etching, so that our choice for the waveguide configuration is relevant from a practical point of view. For all these cases we computed the following waveguide dispersion coefficients: the first-order dispersion coefficient, $\beta_1 = d\beta/d\omega = 1/v_g$, where β and v_g are the propagation constant and group-velocity (GV), respectively, the GVD coefficient, $\beta_2 = d^2\beta/d\omega^2$, and the third-order dispersion (TOD) coefficient, $\beta_3 = d^3\beta/d\omega^3$; the frequency dependence of these coefficients are plotted in Fig. 4.2. We can notice that the most sensitive wavelength region is between 500 nm and 700 nm, this is because the effective wavelength of the propagating mode for those wavelengths is similar to the parameters w and h.

Figure 4.2(b) deserves particular attention as it illustrates that it is possible to design waveguides with $\beta_2 < 0$ (e.g. waveguides B, C, and D), which can support soliton propagation and efficient four-wave mixing, as well as waveguides that possess zero-GVD points defined by $\beta_2(\omega) = 0$ (e.g. waveguides B and C), which enable efficient supercontinuum generation. Especially of interest is the waveguide B, since it shows the smallest v_g for the widest wavelength range, which suggests it provides broadband enhanced Kerr nonlinearity.

A sensitivity analysis of the effective index on the key design parameters was performed in order to show the tolerance against potential fabrication errors. The dependence of the effective index on waveguide width and buffer height, determined for designs B and C, are plotted in Figs. 4.3(a), 4.3(b) and 4.3(c), 4.3(d), respectively. The results summarized in these plots suggest that the variation of the effective index and, conse-

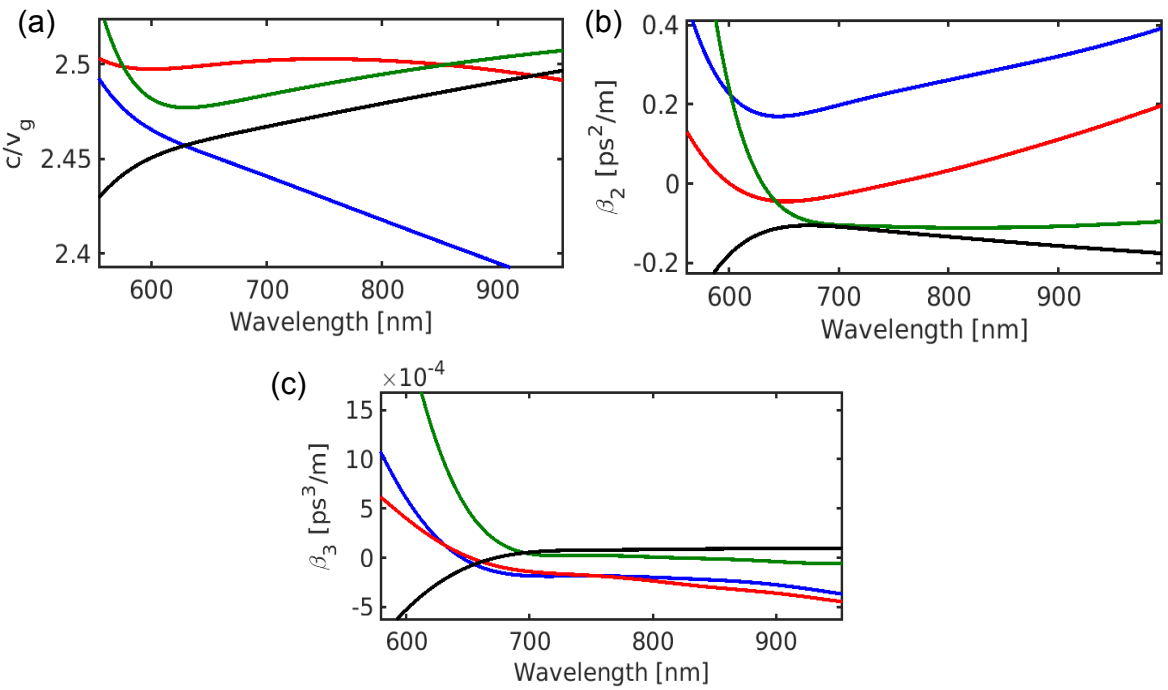

Figure 4.2: (a), (b), (c) Group index, second-order dispersion coefficient, and third-order dispersion coefficient, respectively, determined for four diamond-fin waveguides. The colors blue, red, green, and black correspond to the designs *A*, *B*, *C*, and *D*, respectively, described in the text of the chapter.

quently, of the waveguide mode, is very small for both waveguides *B* and *C*. Note that, in this study, the wavelength is fixed to 750 nm; in addition, the width used for the study of the impact of height variations is the nominal width for each waveguide as detailed earlier, and similar applies for the analysis of the variation of the width, *e.g.* the height employed is the nominal value for each waveguide.

4.3 Theoretical model and simulation of pulse dynamics

Within the standard slowly-varying envelope approximation, the pulse dynamics in the diamond-fin waveguide is described by the well-known nonlinear Schrödinger equation

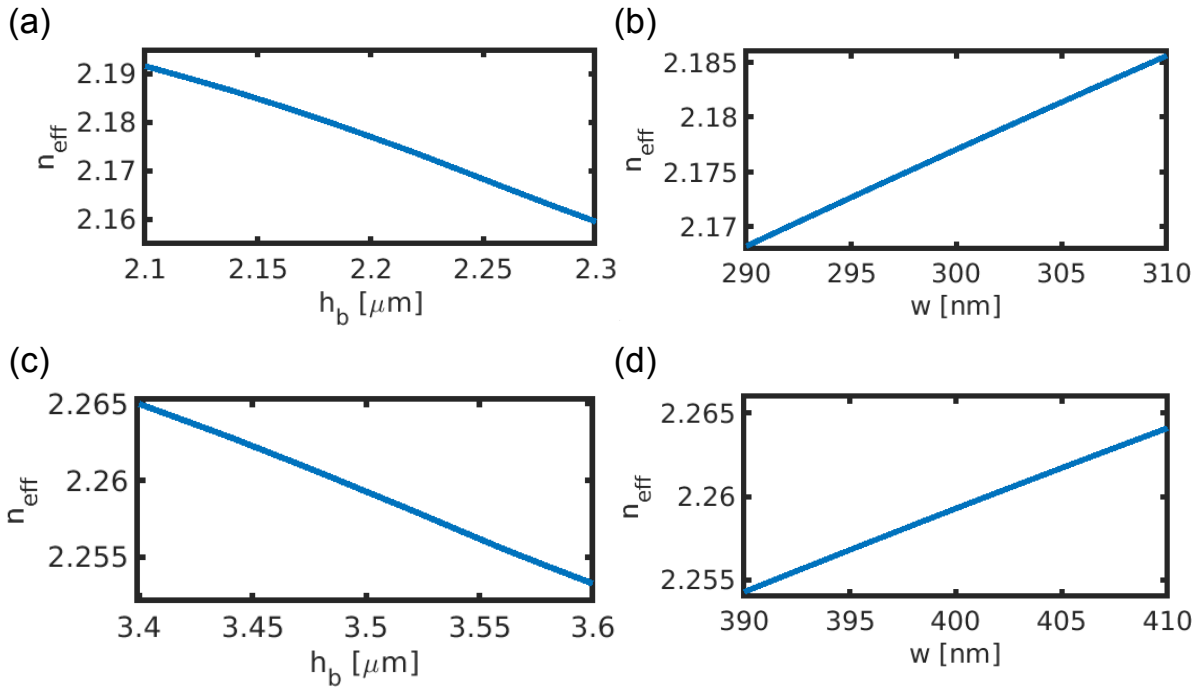

Figure 4.3: Dependence of the effective index on the waveguide width w and buffer height h_b, determined for the designs B (top panels) and C (bottom panels).

(NLSE):

$$i\left(\frac{\partial u}{\partial z}-\frac{1}{v_g T_0}\frac{\partial u}{\partial \tau}\right)-\frac{\beta_2}{2T_0^2}\frac{\partial^2 u}{\partial \tau^2}-i\frac{\beta_3}{6T_0^3}\frac{\partial^3 u}{\partial \tau^3}+i\frac{c\kappa\alpha_{in}}{2n_{di}v_g}u+\gamma P_0|u|^2u=0, \tag{4.1}$$

where $\tau = t/T_0$ and $u = a(z,\tau)/\sqrt{P_0}$, with t, z, and a being the time, propagation distance, and pulse envelope, respectively, and T_0 and P_0 are the input pulse width and peak power, respectively. In Eq. (4.1), $\alpha_{in} = 1\,\mathrm{cm}^{-1}$ is the intrinsic loss of diamond [87], while the waveguide loss is obtained through the overlap integral κ, and γ is the nonlinear waveguide coefficient. These quantities are defined as [63, 100]:

$$\kappa = \frac{\epsilon_0 n_{di}^2}{2W}\int_{S_{wg}}|\mathbf{e}(\omega)|^2 dS, \tag{4.2a}$$

$$\gamma = \frac{3\omega\epsilon_0}{16v_g^2}\frac{1}{W^2}\int_{S_{wg}}\mathbf{e}^*(\omega)\hat{\boldsymbol{\chi}}^{(3)}(\omega)\vdots\mathbf{e}(\omega)\mathbf{e}^*(\omega)\mathbf{e}(\omega)dS, \tag{4.2b}$$

where $\mathbf{e}(\mathbf{r};\omega)$ is the electric field component of the optical mode, W the energy density of the mode, and $\hat{\boldsymbol{\chi}}^{(3)}(\omega) \equiv \hat{\boldsymbol{\chi}}^{(3,e)}(\omega;\omega,-\omega,\omega)$ is the the third-order (electronic)

susceptibility tensor of diamond. As diamond has cubic crystal lattice, $\hat{\boldsymbol{\chi}}^{(3)}$ has three independent components. The relationships between these 3 independent components are $\hat{\boldsymbol{\chi}}^{(3)}_{1111} = 3\hat{\boldsymbol{\chi}}^{(3)}_{1221} = 3\hat{\boldsymbol{\chi}}^{(3)}_{1122}$ [87], so that in the case of diamond $\hat{\boldsymbol{\chi}}^{(3)}$ has only one independent component. The corresponding Kerr coefficient is similar or larger than that of commonly used nonlinear optical materials, e.g. silica ($n_2 \sim 2.5{\times}10^{-20}\,\mathrm{m^2\,W^{-1}}$), SiN ($n_2 \sim 2.5{\times}10^{-19}\,\mathrm{m^2\,W^{-1}}$) [101], and SiC ($n_2 \sim 5{\times}10^{-18}\,\mathrm{m^2\,W^{-1}}$).

There are several reasons why in our study we considered only the Kerr nonlinearity of diamond: *i*) The main characteristic of the waveguide investigated in our work is that it is made of diamond, so that we primarily investigate the influence of the optical nonlinearity of diamond on pulse propagation in such waveguides. *ii*) In principle, one could use a covering layer made of a different material or a waveguide configuration in which this layer is absent altogether, and therefore there could be many potential contributions to the effective nonlinear optical coefficient of the waveguide. The particular configuration of the diamond waveguide studied in this chapter was inspired by the results reported in Ref. [98], e.g. tight field confinement in the order of $\kappa \approx 0.7$ at the same time as small substrate leakage of 0.15 dB/cm or less, and where the fabrication of such waveguides is discussed. *iii*) The optical mode is mostly confined in the diamond region, so that the contribution from the SiN layer can be omitted. Thus, whereas the confinement factor, κ, is smaller than in the SOI configuration, where $\kappa > 0.95$ can be readily achieved, a confinement factor $\kappa > 0.7$ can still be obtained without even trying to optimize the waveguide configuration. Moreover, the fact that a relatively small amount of optical field spills into the SiN region does not negatively affect the nonlinear optical properties of the waveguide because SiN has a large Kerr coefficient, too, and therefore the optical field that propagates in the SiN region contributes to nonlinearly induced phase shifts. *iv*) Finally, the contribution of the silica region to the waveguide nonlinearity can be neglected, too, since the Kerr nonlinearity of silica is much weaker than that of diamond. As a consequence of all these ideas, the overlap integrals in Eqs. (4.2) were restricted to the diamond cross-section area.

The frequency dependence of the nonlinear coefficient, γ, and waveguide loss coefficient $\alpha = c\kappa\alpha_{in}/(2n_{di}v_g)$ defined in Eqs. (4.2) are shown in Fig. 4.4. Note that the mode confinement decreases (less of the optical field is contained inside the waveguide) as the wavelength increases, a property that affects both waveguide coefficients. This is true particularly in the case of the waveguide with the smallest transverse cross-section (A, blue curves), whose coefficients γ and α decrease significantly when the wavelength increases.

The data presented in Fig. 4.4 also guided our choice for the waveguide design we considered in more detail in our study. Thus, to be suitable for nonlinear optical applications, a waveguide must have large nonlinear optical coefficient and small loss coefficient. Among our four waveguides the design B best satisfies these requirements, so that in what follows we restrict our analysis to this waveguide.

Before discussing applications of these diamond fin waveguides, we would like to explain why we can neglect the influence on pulse dynamics of two nonlinear optical effects often included in the NLSE Eq. (4.1), namely the self-steepening (SS) effect and stimulated Raman scattering (SRS). To this end, let us consider first the contribution of SS effects to the pulse evolution. Following the approach introduced in [102], we calculated the shock time, $\tau_s = \dfrac{\partial ln(\gamma)}{\partial \omega}$, which quantifies the strength of SS effects. To

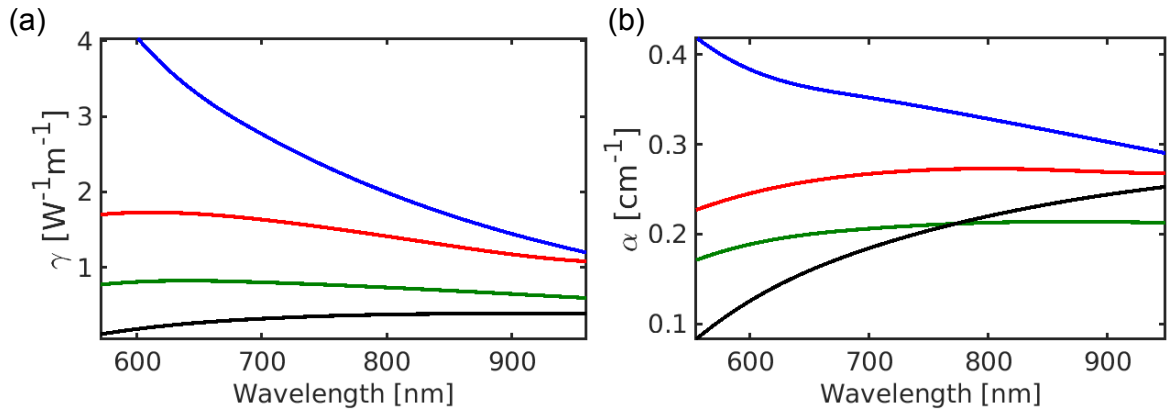

Figure 4.4: (a) Frequency dispersion of the nonlinear waveguide coefficient. (b) Waveguide loss coefficient vs. wavelength. The colors blue, red, green, and black correspond to designs A, B, C, and D, respectively.

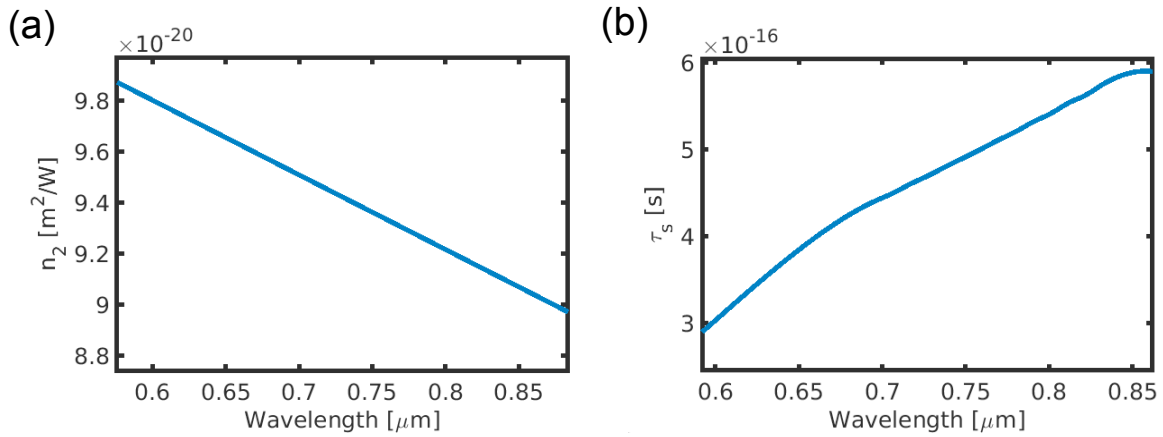

Figure 4.5: (a) Dependence on wavelength of the nonlinear refractive index n_2 of diamond. (b) Shock time parameter of the diamond waveguide (design B), with contributions from both material and waveguide dispersion being included.

do this, we have included in the calculation of the nonlinear waveguide coefficient γ the contribution of the material dispersion $n_2(\omega)$, taken from [103] and plotted in Fig. 4.5(a), as well as that of the waveguide dispersion shown in Fig. 4.4(a). The results of these calculations are depicted in Fig. 4.5(b). They demonstrate that $\tau_s \lesssim 0.6\,\text{fs}$, which means that for pulses with width of tens of fs, as those considered in this work, SS effects can be neglected.

Furthermore, we have similarly assessed the relevance of the SRS effects on pulse dynamics by calculating the characteristic time T_R, which quantifies the Raman effect contribution to pulse reshaping. Specifically, this contribution can be accounted for by adding to Eq. (4.1) the term $-\gamma P_0 \frac{T_R}{T_0} u \frac{\partial |u|^2}{\partial \tau}$, where T_0 and $T_R = \int_0^\infty tR(t)dt$ are the pulse width and the first moment of the nonlinear response function, $R(t)$, respectively. Using the expression given in Ref. [104] for the nonlinear response function of diamond, this is $R(t) = \frac{\tau_1^2+\tau_2^2}{\tau_1 \tau_2^2} e^{\frac{-t}{\tau_2}} \sin(\frac{t}{\tau_1})$, we obtain the following relation:

$$T_R = \int_0^\infty tR(t)dt = \frac{2\tau_2}{1+(\frac{\tau_2}{\tau_1})^2} \sim 2\frac{\tau_1^2}{\tau_2}, \tag{4.3}$$

where the parameters $\tau_1 \approx 4\,\text{fs}$ and $\tau_2 \approx 5.7\,\text{ps}$ are the vibrational period and the decay time of the Raman response in diamond, respectively. Using these specific values of τ_1 and

τ_2 in Eq. (4.3) and a pulse with $T_0 = 10\,\text{fs}$ one obtains $\frac{T_R}{T_0} = 5.6 \times 10^{-4} \ll 1$. This leads us to conclude that the SRS effects can be neglected, too. By comparison, in the case of optical fibers and for the same pulse parameters $\frac{T_R}{T_0} = 0.81$ (for optical fibers $\tau_1 \approx 12.2\,\text{fs}$ and $\tau_2 \approx 32\,\text{fs}$), which explains why in that case SRS effects must be incorporated in the theoretical model.

4.4 Applications to soliton formation and frequency comb generation

In what follows, we will illustrate how the diamond-fin waveguides analyzed in the preceding section can be used to implement important nonlinear optics applications, namely pulse reshaping, soliton generation, and frequency comb generation. To begin with, we consider the waveguide design B and select the wavelength $\lambda = 665\,\text{nm}$, which is in the anomalous dispersion regime ($\beta_2 < 0$) but close to the zero-GVD point. This ensures that key nonlinear optical phenomena, such as soliton formation and supercontinuum generation, can be achieved. At this wavelength, the waveguide parameters are $n_g = c/v_g = 2.5$, $\beta_2 = -0.043\,\text{ps}^2\,\text{m}^{-1}$, $\beta_3 = -5.6 \times 10^{-5}\,\text{ps}^3\,\text{m}^{-1}$, $\alpha = 0.262\,\text{cm}^{-1}$, and $\gamma = 1.687\,\text{W}^{-1}\,\text{m}^{-1}$. Using these parameters, we first determined the pulse dynamics in a waveguide with length $L_{wg} = 5\,\text{cm}$, by integrating Eq. (4.1) with the standard split-step Fourier method [46]. More specifically, we seek to determine the input pulse parameters, i.e P_0 and T_0, for which phenomena such as soliton formation and spectral broadening occur.

The temporal pulse profiles calculated for several z-distances are depicted in Fig. 4.6(a). These calculations correspond to a case when we launched in the waveguide a Gaussian pulse with input peak power larger than the soliton formation threshold power. Specifically, we chose an input pulse width of $T_0 = 25\,\text{fs}$, meaning that the dispersion length is $L_D = T_0^2/|\beta_2| = 1.5\,\text{cm} < L_{wg}$, and input power $P_0 = 60\,\text{W}$. Under these conditions, the power threshold for soliton formation, defined by the relation $L_D = L_{nl}$, where

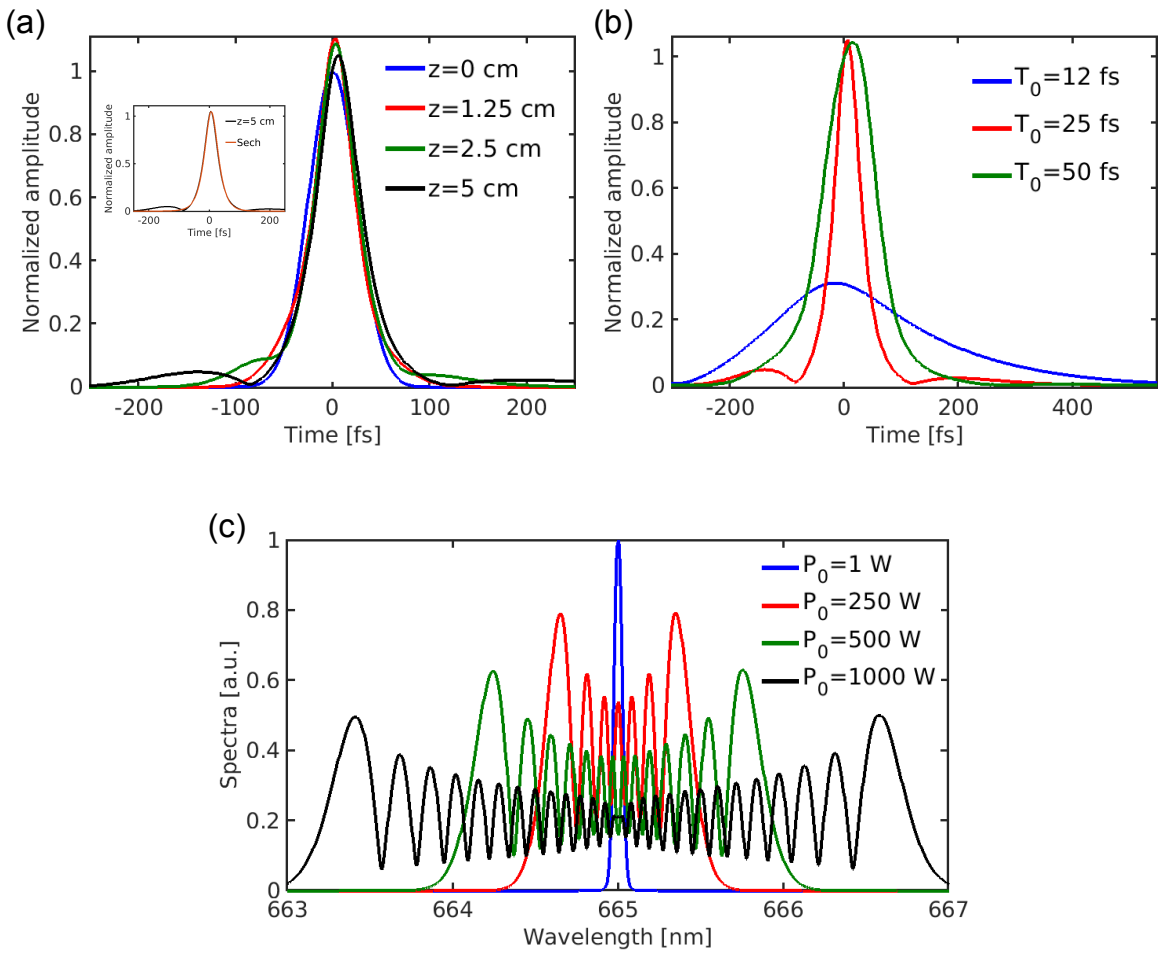

Figure 4.6: (a) Temporal pulse profiles at different propagation lengths for a Gaussian input pulse with $P_0 = 60\,\mathrm{W}$ and $T_0 = 25\,\mathrm{fs}$. Inset shows the output pulse and its sech-fit. (b) Output pulse profile determined for different pulse widths and $P_0 = 60\,\mathrm{W}$. (c) Output pulse spectra for different input peak powers when $T_0 = 10\,\mathrm{ps}$. In all cases, $L_{wg} = 5\,\mathrm{cm}$.

$L_{nl} = 1/(\gamma P_0)$ is the nonlinearity length, is $P_{th} = 40\,\mathrm{W} < P_0$. These numerical simulations show that the input pulse evolves into a soliton superimposed on a pedestal, that is the well-known scenario of soliton formation at peak powers larger than the soliton threshold power. Note that for our parameters $L_{wg} \ll L'_D$, where $L'_D = T_0^3/|\beta_3| = 28\,\mathrm{cm}$ is the TOD length, so that the pulse shape remains symmetric upon propagation.

In Fig. 4.6(b) we illustrate how the temporal pulse profile at the waveguide output changes when varying the input pulse width. Thus, when $T_0 = 12\,\mathrm{fs}$, the dispersion length ($L_D = 0.3\,\mathrm{cm}$) is considerably smaller than L_{nl} and L_{wg}, which means that large pulse broadening is achieved. In addition, $L'_D = 3\,\mathrm{cm} < L_{wg}$, so that TOD effects

lead to pulse asymmetry. By contrast, when $T_0 = 50\,\text{fs}$, $L_D = 5.8\,\text{cm}$ is comparable with L_{wg}, meaning that in this case both dispersive and nonlinear effects influence the pulse dynamics. Furthermore, we illustrate in Fig. 4.6(c) that significant pulse spectral broadening can be achieved in the same waveguide length by using broader input pulses with larger input peak power, so that SPM effects become dominant in determining the pulse evolution. For example, the emergence of spectral modulations upon pulse propagation, for a pulse with $T_0 = 10\,\text{ps}$ can be clearly observed when the pulse peak power increases from 1 W to 1 kW.

From a practical point of view, perhaps an even more important application of diamond-fin waveguides, which we demonstrate in what follows, is frequency comb generation. This nonlinear optical phenomenon can be traced to the generation of dissipative solitons in optically driven Kerr cavities [105, 106, 107, 108, 109]. In particular, the nonlinear partial differential equation describing the evolution of the slowly-varying envelope of the electric component of an optical field propagating in an optical material with Kerr nonlinearity and driven by a continuous-wave (CW) monochromatic optical field, the so-called Lugiato-Lefever equation (LLE), was first derived in the context of optically driven nonlinear optical cavities [110] and shown to govern the generation of dissipative solitons. The temporal version of the LLE has been formulated in [111] and later extended to optical cavities containing nonlinear left-handed materials [112]. Its generalisation to an externally pumped NLSE with boundary conditions, a model relevant to the device we will investigate in what follows, has been first derived in Ref. [113].

To demonstrate frequency comb generation in a diamond-waveguide device as the one shown in Fig. 4.1(c), we consider a microring resonator of length L coupled to a straight optical bus, both made of diamond-fin waveguides. The boundary conditions for our model are provided in Fig. 4.1(c), whereas the externally pumped NLSE describing the pulse propagation in the microring [92] (and which establishes a link between the

dissipative soliton formation and frequency comb generation) is given below:

$$\frac{t_r}{L}\frac{\partial a(t,\tau)}{\partial t} = \frac{\sqrt{\theta}}{L}a_{in}(\tau) - \frac{\alpha' + i\delta}{L}a(t,\tau) - \frac{1}{v_g}\frac{\partial a(t,\tau)}{\partial \tau} - \frac{i\beta_2}{2}\frac{\partial^2 a(t,\tau)}{\partial \tau^2} + \frac{\beta_3}{6}\frac{\partial^3 a(t,\tau)}{\partial \tau^3} + i\gamma|a(t,\tau)|^2 a(t,\tau). \tag{4.4}$$

In this equation, the variable z has been substituted by a temporal variable equivalent to a number m of roundtrips, i.e. $t = mt_r$, $\alpha' = (\alpha_r + \theta)/2$, with $\alpha_r = \alpha L$, θ is the coupling constant of the driving field into the microring, and δ is the detuning of the microring resonance closest to the frequency of the driving field. The associated boundary conditions describe the coherent superposition of the field incoming from the pump and the field propagating inside the microring. More precisely, they show that the field starting the round $m+1$ can be viewed as being equal to the in-coupled pump field plus the part of the field from the previous round m that has not escaped out of the microring. This latter field has accumulated with respect to the pump field during the round trip the linear phase ϕ_0.

The steady-state solution of Eq. (4.4) consists of a train of solitons with repetition time equal to the cavity round-trip time. This is equivalent to a comb in the frequency domain, with a frequency-spectral-range equal to the inverse of the round-trip time. To find the steady-state solution of Eq. (4.4), we impose the condition $\frac{\partial a(t,\tau)}{\partial t} = 0$. The resulting equation, whose solution only depends on τ, is solved by combining a discrete Fourier transform (DFT) method with the Newton-Raphson algorithm for solving nonlinear systems of equations. It is important to note that the DFT method requires the use of wavelength dependent waveguide coefficients, so that the coefficients c/v_g, β_2, β_3, γ, and α are incorporated in the numerical method as wavelength dependent functions.

Following this approach, we considered a microring resonator based on waveguide B, of length $L = 628\,\mu\text{m}$ and operating at $\lambda = 665\,\text{nm}$. For simplicity, we assumed that $\theta = \alpha_r$, i.e. the system operates in the under-coupling regime [114], and the detuning parameter was set to $\delta = 0.05$. Note this assumption can be justified as the microring radius of

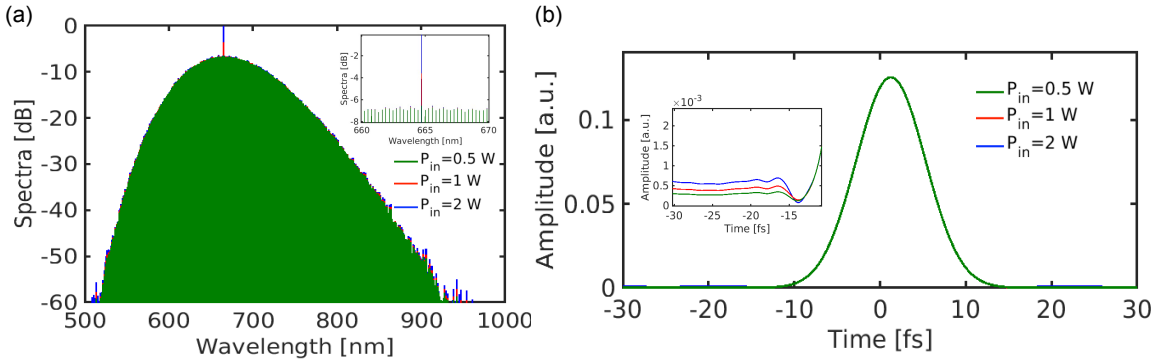

Figure 4.7: (a) Simulated frequency comb spectra for a microring of length $L = 628\,\mu\text{m}$ based on waveguide design B. The inset demonstrates the flatness of the comb around the driving wavelength. (b) Temporal pulse profile within the microring. The inset shows the variation of the CW background intensity with the input power.

100 μm is large enough to avoid a tight coupling gap spacing, and especially narrower than the fin width, by comparing it with smaller microrings found in the literature [115]. The spectra and pulse shapes are shown in Figs. 4.7(a) and 4.7(b), respectively. They demonstrate that diamond-fin waveguides can be used to generate frequency combs in visible range reaching close to one octave-span. The pulse train building up inside the microring sits onto a CW background and has width of $\sim$15 fs. Achieving such short pulses is made possible by the large nonlinearity (γ) of the system, which induces significant spectral broadening and thus the excitation of a large number of optical modes of the microring. Our simulations reveal that the lowest input power required to reach the steady state is $P_{in} \approx 0.5\,\text{W}$. When P_{in} increases, the comb is hardly affected, but the driving wavelength is slightly redshifted. In the time domain, increased P_{in} leads to larger CW background.

As a final observation, we mention that the NLSE Eq. (4.4) can be used directly to investigate the formation and evolution of the comb towards its stationary state [92], but this method would have required considerably more computational time without gaining much in return. Inasmuch as our study is geared towards applications to nonlinear optics of ultrasmall diamond waveguides, the specific nature of the soliton formation during the build-up process is not particularly relevant for the properties of the final frequency comb that is generated. In fact, this is why we chose to employ in our simulations a

numerical method tailored for computing directly the steady-state solution, and as such a method not suitable for the analysis of the transient regime. The advantage of our method, which is particularly relevant for practical application, is that it allows one to investigate extremely broad frequency combs as a very large number of spectral modes can be incorporated at minimum computational cost.

4.5 Conclusion

To conclude, we have presented the design of diamond-fin waveguides and analyzed in detail their linear and nonlinear optical properties. In particular, we have determined the frequency dependence of the main linear and nonlinear optical coefficients of the waveguides and analyzed the dependence of these parameters on the waveguide geometry. To do that, we have explored how three key waveguide parameters, namely the fin width w, the fin height $h + t$ and the buffer height h_b affect the optical mode supported by the structure, and its frequency dependence. Precisely, we have targeted designs that cross the zero-GVD line, so negative GVD can be exploited for soliton propagation, and we have observed that there is a sweet spot in the range of practical h_b values in which the energy leakage down through the buffer is minimised over the wavelength range under interest, while maximising the nonlinear effects. Therefore, by selecting one of the proposed waveguide designs with these optimum characteristics, we have simulated the pulsed dynamics through these structures by means of a comprehensive mathematical model based on NLSE. The results of our investigations suggest that these structures can enable efficient soliton formation and propagation and, potentially, supercontinuum generation. In addition, we have demonstrated how these waveguides can be employed to generate frequency combs operating in the visible spectral domain. Importantly, our simulations show that it is possible to generate almost one octave span stable combs in the visible range with input continuous-wave powers as low as 0.5 W.

Chapter 5

Raman amplification and pulse dynamics in silicon photonic crystal waveguides

5.1 Introduction

Several applications have inspired the huge research in photonics during the last two decades, but one that outstands clearly is the development of optical interconnects for chip-to-chip and intra-chip communications. The main reasons behind research in this area are the preceived limitations of electrical interconnects, such as poor bandwidth, large power dissipation, need for impedance matching or crosstalk between electrical paths [1, 2]. In contrast, optical interconnects are found capable of solving all of these challenges, including also that they can be developed in smaller form factors. On-chip optical devices such as switches or modulators have been already built using semiconductors of the III-V bands due to their high nonlinear optical properties [5, 6]. Nevertheless, silicon photonic waveguides (Si-PhWGs) have become a very good alternative to these devices since the high refractive index of silicon allows the design of high-index contrast waveguides, which also enhances the nonlinearities by a good confinement of the electromagnetic field [7].

Furthermore, given the transparent window of this material, which covers the entire telecommunication spectra, electronic and optical domains can be brought together into the same chip and CMOS-compatible designs can become realistic for several applications [8, 9]. Among many other breakthroughs, it has been proved that Si-PhWGs can be designed to synthesize key nonlinear processes such as Raman amplification [11, 12], soliton [13] and supercontinuum [14] generation, frequency conversion [15], modulation instability [16] and pulse compression [17, 18], between others. However, Si-PhWGs lack of engineering flexibility when a specific application requires the tuning of their optical properties.

A promising solution to this problem is the introduction of Photonic crystals (PhCs), which incorporate more designable dimensions. The way to do this consists on creating a periodic pattern in the photonic circuit, separating regions of different dielectric constants by a length similar to the operating optical wavelength. Certainly, depending how the periodic dielectric medium is defined, the device could be used for multiple different purposes, from the design of ultra-small, narrow-band filters [22, 23] to omnidirectional mirrors, waveguides and bends [24, 25, 26]. In particular, this is possible thanks to the wide tuning of the group-velocity (GV) v_g of the propagating modes that PhCs allow. Especially remarkable is the slow-light regime, where light-matter interaction is enhanced and both the linear and non-linear optical effects become substantially important [27, 28, 29, 30]. In fact, very interesting applications have emerged around the control over slow-light, such as optical buffering or time domain processing of optical signals [31, 32, 33].

By taking advantage of this notable property of PhCs, in this chapter we study how the result of pump-to-signal amplification based on stimulated Raman scattering can dramatically change with different values of the GV for the two optical modes taking place in the process. Raman scattering is the result of the interaction between two pulses at frequencies ω_1 and ω_2 whose spectral difference is close to the Raman vibrational frequency of the medium. In the practice, a source of light (pump) interacts with the medium and excites new frequency components (Stokes or signal) by a third order nonlinear effect.

Exactly at resonance, the nonlinear Raman susceptibility is pure imaginary, which can be translated into pump depletion and signal amplification. Whereas Raman scattering has been intensively investigated in PhC fibers [116, 117], in silicon waveguides with uniform cross-section [63], and also several studies have been carried out on silicon PhC waveguides (Si-PhCWGs) [118, 119], a complete study of Raman interaction in the latter combined with all relevant linear and nonlinear optical effects on the pulse dynamics, is not available yet.

In more detail, we present a comprehensive theoretical model that rigorously predicts the effect of stimulated Raman scattering on Si-PhCWGs. Our model integrates the Raman process with linear optical effects, which includes group-velocity dispersion (GVD), waveguide loss, FC dispersion (FCD) and FC absorption (FCA), and with nonlinear optical effects such as self-phase modulation (SPM), cross-phase modulation (XPM) and two-photon absorption (TPA). Importantly, we show with accuracy the mathematical derivation of the Raman nonlinear coefficients for the Si-PhCWG under interest. We also illustrate how our model can be employed to investigate various phenomena related to Raman interaction when the pump and the signal are in different GV regimes: slow pump - slow signal, fast pump - fast signal and slow pump - fast signal. Indeed, this is a noteworthy example of how completely different scenarios can be encountered in the same Si-PhCWG. Last but not least, we conlclude the discussion demostrating how relevant characteristic parameters such as the walk-off length between pulses can dramatically affect the pulse dynamics along the waveguide.

From this introduction onwards, the chapter is organized as follows. We begin with a brief theoretical overview of stimulated Raman scattering, including the description of the nonlinear tensor used to mathematically represent this process. Then, in Section 5.3, we incorporate the description and modal analysis of the Si-PhCWG considered for this work, with some emphasis into the linear dispersive effects that are present in the propagating optical modes. In Section 5.4, we derive the mathematical model based on coupled non-Linear Schrödinger equations that will allow us to study the interaction between

pulses, as well as we introduce the concept of linear and nonlinear characteristic lengths. Subsequently, in Section 5.5, we discuss the results of numerical simulations for different combinations of pump and signal modes. Eventually, we conclude this chapter with a summary of the main findings and the implications to future developments in this research area.

5.2 Theory of stimulated Raman scattering

The Raman response is considered a third-order nonlinear optical process that couples photons (quanta of light energy) and phonons (quanta of vibrational mechanical energy). In stimulated Raman scattering, a photon of frequency ω_p interacting with a Raman medium is annihilated and, as a consequence, leaves an atom of the crystal vibrating in an excited state with energy $\hbar\omega_R$, which will vary for each different material. Eventually, the vibrational state of the phonon will produce a Stokes photon at $\omega_s = \omega_p - \omega_R$ or an anti-Stokes photon at $\omega_s = \omega_p + \omega_R$, although the latter is less likely due to the higher energy levels involved [52]. For crystalline silicon, this vibrational frequency is found to be $\frac{\omega_R}{2\pi} = 15.6$ THz [65]. However, this is not a pure frequency component, but it occupies a spectral width of $\Delta\omega/2\pi = 105$ GHz, which corresponds with a response time of $\tau \sim 10$ ps. This suggests, indeed, that intra-pulse Raman effects in crystalline silicon are not possible, since broad spectral pulses with spectral widths around Raman's would impose temporal widths below 100 fs, much lower than the Raman response time.

As any other nonlinear process, the Raman response can be modeled as a susceptibility tensor. As per [120], the generic form of the third-order susceptibility tensor can be written as:

$$\hat{\chi}^R_{ijkl}(\Omega) = \frac{\pi N_\nu}{3\hbar} \sum_\sigma \frac{\omega_\sigma(\alpha_{ij,\sigma}\alpha_{kl,\sigma} + \alpha_{ik,\sigma}\alpha_{lj,\sigma})}{\omega_\sigma^2 - \Omega^2 + 2i\Omega\Delta\omega}, \tag{5.1}$$

where $\Omega = \omega_p - \omega_s$, N_ν is the number of phonons per unit volume, ω_σ is the vi-

brational resonant frequency, and $\alpha_{ij,\sigma}$ are matrix elements given by the derivatives of the polarizability tensor $\hat{\alpha}$ with respect to the coordinate of each of the Raman-active optical phonons σ. Given the symmetrical nature of crystalline silicon, which belongs to the irreducible representation $\mathbf{\Gamma}_{25'}$, it can be found that the Raman tensor has just one independent component for $i = k$ and $j = l$, this is $\hat{\chi}^R_{1212}$, with the other non-zero elements given by $\hat{\chi}^R_{iijj} = 0.5\hat{\chi}^R_{ijij}$ [66].

It must be highlighted that the real part of these nonlinear susceptibilities will drive a change in the refractive index the optical modes are perceiving, whereas the imaginary part leads to depletion on one of the interacting modes and amplification on the other. Even though the spectral width of the Raman response can not be ignored, when the temporal widths of the interacting pulses are similar to the Raman response time, this can be just evaluated at the resonant frequency $\Omega = \omega_R$. If this is satisfied, the Raman susceptibility would become pure imaginary with $\hat{\chi}^R_{ijij} = -i\hat{\chi}^R = -i11.2 \cdot 10^{-18}\ m^2V^{-2}$, where $i, j = 1, 2, 3$ [67]. Furthermore, we must also clarify that we will only consider Raman scattering along the $[1\hat{1}0]$ direction, which we assume is the direction the devices are fabricated along with and which, indeed, favors the cleaving of silicon during the fabrication stage.

5.3 Description of the photonic crystal waveguide

In this section we describe the geometrical and material properties of the Si-PhCWG structure considered for this work, which is commonly denoted as "W1 PhCWG". Based on the model presented in [118], the PhC structure is made by removing the central row in a honeycomb-type periodic lattice of air holes, built within a homogeneous silicon slab. Figure 5.1 shows, via subfigures (a) and (b), the geometry of the referred structure and the projected bands of the guided modes that it supports, respectively. The index of refraction considered for the silicon slab is $n_{Si} \equiv n = 3.48$, its height is $h = 0.6a$ and the radius of the holes is $r = 0.29a$, where a is the lattice constant of the crystal.

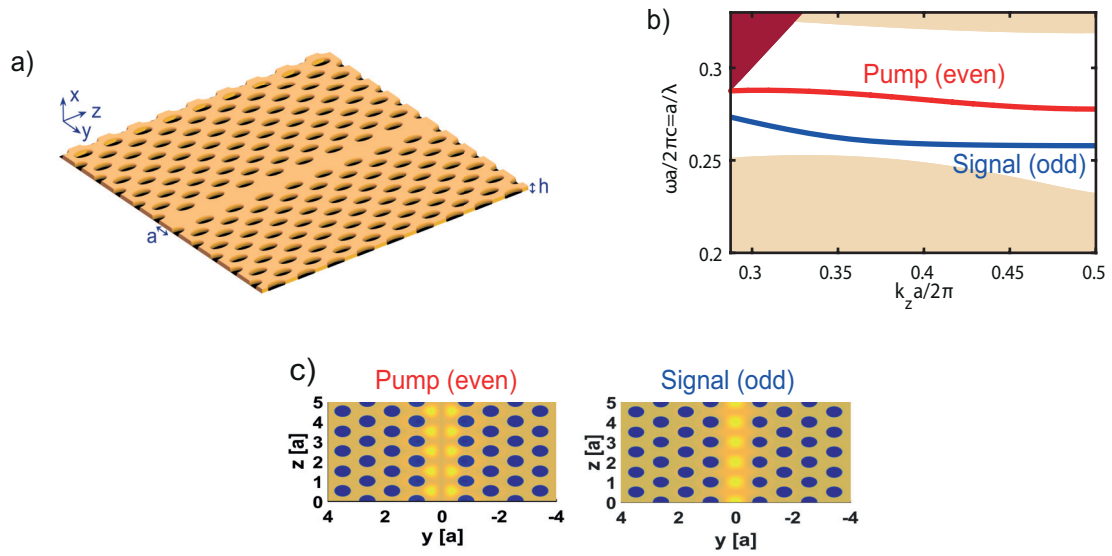

Figure 5.1: (a) Geometry of the silicon W1 PhCWG. The height of the slab is $h = 0.6a$ and the radius of the holes is $r = 0.29a$. (b) Projected band structure into the longitudinal z-axis. Dark magenta and light brown areas correspond to slab leaky and guiding modes, respectively. The red and blue curves represent the guiding modes of the 1D waveguides. (c)Representation of guided modes in the Si-PhC slab waveguide. Left (right) panel shows the amplitude of the normalized magnetic field H_x of the y-odd (y-even) mode, calculated in the plane $x = 0$ for group index $n_g = \frac{c}{v_g} = 6.91$.

The figure at the bottom shows an example of a guided mode at $k_z = 0.678\frac{\pi}{a}$ and with group velocity $v_g = 0.1448c$, being c the speed of light at vacuum. It clearly confirms the good confinement of the electromagnetic field within the missing row of the PhC, which enhances the non-linear effects.

The photonic band structure of the PhC and its waveguide modes have been obtained with the plane-wave expansion (PWE) electromagnetic solver MPB [53]. The calculations carried out by this tool are consistent with the Bloch's theorem, which, based on the structure presented in this chapter, states that the optical modes of the waveguide vary in all directions except with periodic translations along the z axis [24]. Consequently, the propagation constant k_z can be restricted just to the first Brillouin zone, which corresponds to $k_z \in [-\pi/a, \pi/a]$. Note also that, due to practical reasons, our analysis has been focused only to in-plane wave propagation, i.e. explicitly guided modes. The structure analysed is a supercell with dimensions $6a \times 19\sqrt{3}/2a \times a$ along the x-, y-, and z-axis, respectively. Additionally, the computational grid is chosen to be $a/60$, $a\sqrt{3}/120$,

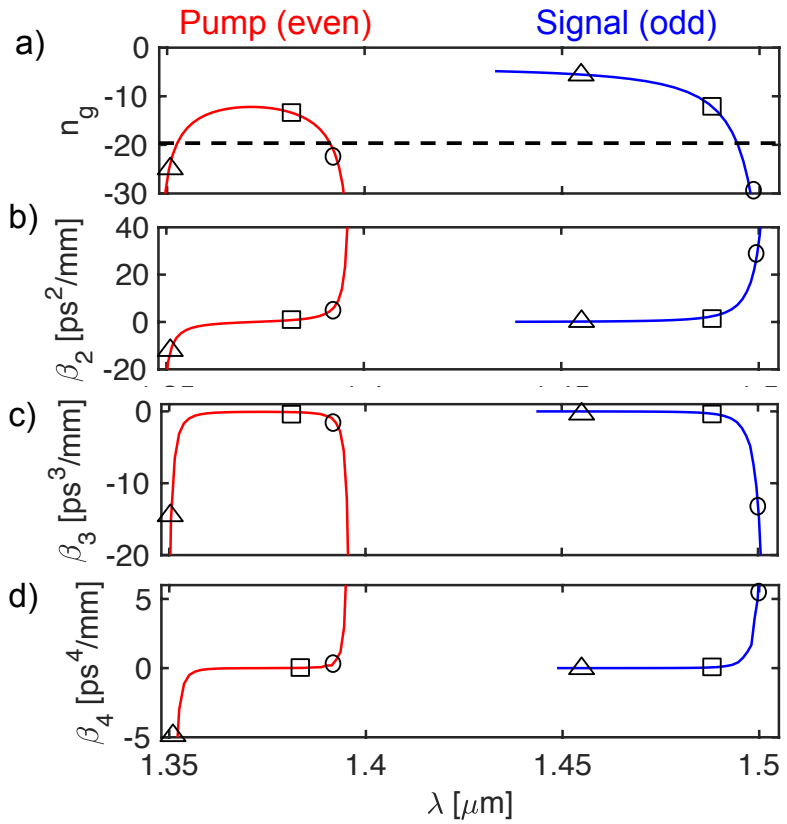

Figure 5.2: (a), (b), (c), and (d) Wavelength dependence of waveguide dispersion coefficients n_g, β_2, β_3, and β_4, respectively, determined for the even and odd modes with $a = 388$ nm. The dashed line in (a) represents the distinction between slow (below line) and fast (above line) regimes. The circles, squares and triangles illustrates the three different scenarios we analyze in this chapter: slow-slow, fast-fast and slow-fast, respectively.

and $a/60$, for x, y, and z, respectively. As Figure 5.1(b) presents, the waveguide has two fundamental TE-like optical guiding modes located in the band-gap of the unperturbed PhC, one y-even and the other one y-odd.

The mathematical derivation of the coupled-mode equations that governs the pulse dynamics, which is described in the following section, employs a mapping between the dispersion coefficients of the waveguide modes and the linear terms of the NLS equations. These coefficients are calculated in the form of $\beta_n = d^n k_z/d\omega^n$ and some of them are directly related to physical properties. The first-order dispersion coefficient is related to the group velocity (GV) of the pulse as it propagates. In particular, it is defined as $\beta_1 = 1/v_g$ and it is, obviously, the parameter that will allow us to experiment with slow-

or fast-light modes. In consequence, the second-order coefficient quantifies the group-velocity dispersion (GVD) or how much the temporal profile of the pulse will broaden. If a pulse is strongly affected by GVD, its temporal profile will be broadened symmetrically. However, if it is affected by the third-order dispersion (TOD) parameter, the pulse shape will acquire a antisymmetrical shape. Figure 5.2 illustrates the wavelength dependance of the four first dispersion coefficients of our Si-PhCWG with $a = 388$ nm. In the top figure, we have also included a reference line through which we differentiate between slow- and fast-light regimes. The threshold value we assume is $v_g/c = 0.05$ or $ng = 20$, that is all greater values than this group index threshold will be considered as slow-light. Based on this, we have defined three study cases we focus on in this chapter. From now on, circles in figures will correspond to the slow-slow study case; squares will represent the fast-fast study case; and triangles will be mapped with the slow-fast study case, that is the pump will propagate in slow-light regime and the signal will do it in fast-light regime. Regarding the second-, third- and fourth-order dispersion coefficients, we can see they tend to infinity when the GV gets closer to zero. In particular, the even mode contains two slow-light regions, whereas the odd mode has only one. Finally, we can also notice that the even mode can have both positive and negative GVD, whereas the odd mode has normal GVD ($\beta_2 > 0$) throughout.

5.4 Derivation of the mathematical model

This section is devoted to the derivation of a system of coupled-mode equations used to predict the evolution of two optical pulses that mutually interact in a Si-PhCWG as they propagate together. Not only the Raman interaction, but several other linear and non-linear effects, including the impact of photogenerated FCs, will be considered into the model. The couple-mode equations we derive are based on the generic model developed in Ref. [63] for transversally uniform Si-PhWGs and in Ref. [100] for Si-PhCWGs. It is also important to clarify now that the model presented relays on several assumptions

that match with common experimental setups. In fact, we follow the same assumptions as made in Ref. [61]. Since the generic model of coupled-mode equations for an arbitrary number of optical pulses was exhaustively detailed in Ref. [61], we will simplify the derivation for $M = 2$ guiding modes, which correspond to the pump and the signal in this case. Moreover, we will assume there is only one frequency excited for each mode, that is ω_p for the pump and ω_s for the signal, and whose spectral difference matches the Raman vibrational frequency of crystalline silicon, this is $\frac{\omega_p - \omega_s}{2\pi} = \frac{\omega_R}{2\pi} = 15.6$ THz.

5.4.1 Optical modes of photonic crystal waveguides

Applying the frequency domain form of Maxwell equations over the Si-PhCWG under interest will result in all the guiding modes with frequency ω that can be excited in this structure. Assuming an external perturbation represented by the polarization term $\mathbf{P}_{\text{pert}}(\mathbf{r}, \omega)$, the form of the Maxwell equations becomes as follows:

$$\nabla \times \mathbf{E}(\mathbf{r}, \omega) = i\omega\mu\mathbf{H}(\mathbf{r}, \omega), \tag{5.2a}$$

$$\nabla \times \mathbf{H}(\mathbf{r}, \omega) = -i\omega[\epsilon_c(\mathbf{r}, \omega)\mathbf{E}(\mathbf{r}, \omega) + \mathbf{P}_{\text{pert}}(\mathbf{r}, \omega)], \tag{5.2b}$$

where $\epsilon_c(\mathbf{r}, \omega)$ describes the dielectric constants composing the structure of our Si-PhC, μ is the magnetic permeability, which will be assumed to be $\mu = \mu_0$ for silicon, and $\mathbf{E}$ and $\mathbf{H}$ are the electric and magnetic fields, respectively. For our study in this chapter, $\mathbf{P}_{\text{pert}}$ will contain the sum of polarizations that include the refractive index change induced by photogenerated FCs, the Raman effect and the Kerr effects.

In order to derive the effect of external perturbations on the optical modes of the PhCWG, we begin by considering the unperturbed system, this is for $\mathbf{P}_{\text{pert}} = 0$. As we clarified previously, we will assume the unperturbed structure supports two guiding modes, which correspond to the pump and the signal, and whose frequencies are ω_p and ω_s, respectively. These guiding modes are exact solutions of the Maxwell equations (5.2)

with $\mathbf{P}_{\text{pert}} = 0$. Thus, we can write the fields as follows:

$$\mathbf{E}_p(\mathbf{r}, \omega_p) = \mathbf{e}_p(\mathbf{r}, \omega_p) e^{i\beta_p z}, \tag{5.3a}$$

$$\mathbf{H}_p(\mathbf{r}, \omega_p) = \mathbf{h}_p(\mathbf{r}, \omega_p) e^{i\beta_p z}, \tag{5.3b}$$

$$\mathbf{E}_s(\mathbf{r}, \omega_s) = \mathbf{e}_s(\mathbf{r}, \omega_s) e^{i\beta_s z}, \tag{5.3c}$$

$$\mathbf{H}_s(\mathbf{r}, \omega_s) = \mathbf{h}_s(\mathbf{r}, \omega_s) e^{i\beta_s z}, \tag{5.3d}$$

where β_p and β_s are the propagation constants of the pump and signal modes, respectively. Following the Bloch's theorem, the mode amplitudes $\mathbf{e}_p(\mathbf{r}, \omega_p)$ and $\mathbf{e}_s(\mathbf{r}, \omega_s)$ will be periodic along the longitudinal axis of the waveguide, this is the z axis in our coordinate system, with period a.

Following the convention in Ref. [121, 122], we define the power carried by each guiding mode as:

$$P_i = \frac{W_i}{a} v_g = \frac{W_i^{\text{el}} + W_i^{\text{mag}}}{a} v_g, \tag{5.4}$$

where $W_i = W_i^{\text{el}} + W_i^{\text{mag}}$ and

$$W_i^{\text{el}} = \frac{1}{4} \int_{V_{\text{cell}}} \frac{\partial}{\partial \omega} (\omega \epsilon_c) |\mathbf{e}_i(\mathbf{r}, \omega)|^2 dV, \tag{5.5a}$$

$$W_i^{\text{mag}} = \frac{1}{4} \int_{V_{\text{cell}}} \mu_0 |\mathbf{h}_i(\mathbf{r}, \omega)|^2 dV, \tag{5.5b}$$

are the electric and magnetic energy of the pump ($i \equiv p$) and signal ($i \equiv s$) modes, respectively, and V_{cell} is the volume of the unit cell of the PhC. We can assume that the frequency dispersion of ϵ_c in Eq. (5.5a) for PhC waveguides is neglectful since the waveguide dispersion is much larger than the material dispersion.

5.4.2 Perturbations of the photonic crystal waveguide

The polarization term $\mathbf{P}_{\text{pert}}(\mathbf{r}, \omega)$ in Eq. (5.2b), which describes the perturbation $\delta\epsilon(\mathbf{r}, \omega)$ on the dielectric constant the optical modes are truly perceiving as they propagate

through the waveguide, becomes different to zero if we consider the photogeneration of FCs, the Raman effect and the Kerr effects. Thus, we define the polarization term as we did in Chapter 2 Eq. 2.2, with the sum of the contributions of each of these effects and where the nonlinear polarization term is $\delta\mathbf{P}_{\mathrm{nl}}(\mathbf{r},t) = \delta\mathbf{P}_{\mathrm{R}}(\mathbf{r},t) + \delta\mathbf{P}_{\mathrm{K}}(\mathbf{r},t)$.

The linear term in Eq. 2.2 is considered as a linear effect because it does not depend on the square of the field intensity, like the other two do. In this case, $\delta\mathbf{P}_{\mathrm{lin}}(\mathbf{r},t)$ represents the linear change of the dielectric constant due to the generation of FCs, the absorption of energy by these FCs and also the loss of energy caused by defects in the waveguide walls. Assuming the medium response is nearly instantaneous, we can write the linear contribution as we did in Chapter 2 Eqs. 2.11 to 2.13. Note that the intrinsic loss appearing in these equations will be translated into the corresponding linear propagation loss for each mode once we introduce the overlap integral parameter κ_i later on. In our simulations, we will consider the intrinsic loss to be $\alpha_{in}^{dB} = 40$ dB/cm, which corresponds to $\alpha_{in} = 9.21$ cm^{-1}.

The Raman and Kerr nonlinear terms are both described by third-order susceptibilities that, in general, are related to the electromagnetic field as follows:

$$\delta\mathbf{P}_{\mathrm{R}}(\mathbf{r},t) = \epsilon_0\hat{\chi}^{R}(\mathbf{r})\vdots\mathbf{E}(\mathbf{r},t)\mathbf{E}(\mathbf{r},t)\mathbf{E}(\mathbf{r},t), \tag{5.6a}$$

$$\delta\mathbf{P}_{\mathrm{K}}(\mathbf{r},t) = \epsilon_0\hat{\chi}^{K}(\mathbf{r})\vdots\mathbf{E}(\mathbf{r},t)\mathbf{E}(\mathbf{r},t)\mathbf{E}(\mathbf{r},t). \tag{5.6b}$$

In relation to the Raman term, as already indicated in Section 5.2, we will consider the scenario when pump and signal are exactly at Raman resonance. In the case of the Kerr nonlinearity, this term will normally contain both real and imaginary parts different from zero. The first one represents nonlinear processes such as SPM, XPM and FWM. On the contrary, the imaginary part will describe TPA and XAM mechanisms that will impact the electron and holes densities N. As explained in Ref. [61], considering again the fact that silicon belongs to the m3m crystal point group, that this crystal satisfies the Kleinman symmetry relations, that the frequency dispersion of the Kerr tensor can

be neglected due to the pulse widths we use and, final but not least, bringing the result of experimental studies [62], it is totally acceptable to assume the Kerr nonlinearity has just one independent element, which is $\hat{\chi}^K_{iiii} = 2.30 \cdot 10^{-19} + i7.01 \cdot 10^{-20}\ m^2/V^2$, and that the relations $\hat{\chi}^K_{iiii} = 2.36\hat{\chi}^K_{iijj}$ and $\hat{\chi}^K_{iijj} = \hat{\chi}^K_{ijij} = \hat{\chi}^K_{ijji}$ apply [52].

5.4.3 Coupled-mode equations for the optical field

By applying the Lorentz reciprocity theorem, we can derive the two coupled-mode equations that will describe the propagation of pump and signal pulses along the Si-PhCWG [63, 100, 121, 123]. This method consists on defining two solutions to the Maxwell equations (5.2), one for the unperturbed system, $[\mathbf{E}_a(\mathbf{r}, \omega_a), \mathbf{H}_a(\mathbf{r}, \omega_a)]$, and another one for the perturbed system, $[\mathbf{E}_b(\mathbf{r}, \omega_b), \mathbf{H}_b(\mathbf{r}, \omega_b)]$. These actually suggest that the spatial distribution of the dielectric constant is different from system a to system b. In more detail, assuming the material dispersion can be neglected, the dielectric constant for system a can be written as $\epsilon_a = \epsilon_c(\mathbf{r})$ and the corresponding one for the perturbed system b can be formulated as $\epsilon_a = \epsilon_c(\mathbf{r}) + \delta\epsilon(\mathbf{r}, \omega)$. Applying now the Lorentz integral identity as it was explained in Chapter 3,

$$\int_S \nabla \cdot \mathbf{F} dS = \frac{\partial}{\partial z} \int_S \mathbf{F} \cdot \hat{\mathbf{z}} dS + \oint_{\partial S} \mathbf{F} \cdot \mathbf{n} dl, \tag{5.7}$$

where $\mathbf{F} = \mathbf{E}_b \times \mathbf{H}^*_a + \mathbf{E}^*_a \times \mathbf{H}_b$, S is the transverse section at a longitudinal point, z, and ∂S is the boundary of S, we can make use of the Maxwell equations and the following expression can be found:

$$\begin{aligned} \frac{\partial}{\partial z} \int_S \mathbf{F} \cdot \hat{\mathbf{z}} dS &= i\mu_0(\omega_b - \omega_a) \int_S \mathbf{H}^*_a \cdot \mathbf{H}_b dS \\ &+ i \int_S (\omega_b \epsilon_b - \omega_a \epsilon_a) \mathbf{E}^*_a \cdot \mathbf{E}_b dS - \oint_{\partial S} \mathbf{F} \cdot \mathbf{n} dl. \end{aligned} \tag{5.8}$$

At this point, we focus the derivation to the specific scenario we want to study. In our case, a quasi-monochromatic pump wave at frequency ω_p is propagated in our crystalline

Si medium, which is a Raman-active solid medium. Consequently, it will produce a scattered Stokes signal at a lower frequency ω_s. Assuming we have a single mode at each of the frequencies and that they propagate forwards, the fields for the unperturbed scenario take the following form:

$$\mathbf{E}_a(\mathbf{r},\omega_i) = \frac{\mathbf{e}_i(\mathbf{r},\omega_i)}{\sqrt{P_i}} e^{i\beta_i z}, \tag{5.9a}$$

$$\mathbf{H}_a(\mathbf{r},\omega_i) = \frac{\mathbf{h}_i(\mathbf{r},\omega_i)}{\sqrt{P_i}} e^{i\beta_i z}, \tag{5.9b}$$

where $i = p, s$ for the pump and the signal, respectively.

Introducing now the perturbation into the system, the set of equations become:

$$\mathbf{E}_b(\mathbf{r},\omega) = a_p(z,\omega)\frac{\mathbf{e}_p(\mathbf{r},\omega_p)}{\sqrt{P_p}} e^{i\beta_p z} + a_s(z,\omega)\frac{\mathbf{e}_s(\mathbf{r},\omega_s)}{\sqrt{P_s}} e^{i\beta_s z}, \tag{5.10a}$$

$$\mathbf{H}_b(\mathbf{r},\omega) = a_p(z,\omega)\frac{\mathbf{h}_p(\mathbf{r},\omega_p)}{\sqrt{P_p}} e^{i\beta_p z} + a_s(z,\omega)\frac{\mathbf{h}_s(\mathbf{r},\omega_s)}{\sqrt{P_s}} e^{i\beta_s z}, \tag{5.10b}$$

where the mode amplitudes $a_i(z,\omega)$, with $i = p, s$, represent the change in the original fields due to the perturbations included, and are measured in units of $\sqrt{W}$.

As indicated earlier, the basis of the model used in this chapter can be referred to the generic mathematical formulation previously published in Ref. [61], so here we simply focus on the derivation of the Raman contribution. However, we shall summarize the process we follow to obtain the coupled-mode equations. Initially, the fields given by Eqs. (5.9) and Eqs. (5.10) are inserted in the Lorentz equation (5.8), in which we can neglect the line integral since it cancels for exponentially decaying guiding modes. Once we have the system of coupled equations in the frequency domain, we apply the Fourier transform to convert it to the time domain. It is important to clarify here that, in order to obtain the model in the time domain, we assume that both the time-dependent fields and

polarization can be decomposed into two components, one containing positive frequencies and the other containing negative frequencies. This means that the electromagnetic fields are given by:

$$\begin{aligned}\mathbf{E}(\mathbf{r},t) &= \frac{1}{2}\int_0^\infty \sum_{i=p,s} a_i(z,\omega)\frac{\mathbf{e}_i(\mathbf{r},\omega_i)}{\sqrt{P_i}} \\ &\times e^{i(\beta_i z-\omega t)}d\omega + c.c. \equiv \frac{1}{2}\left[\mathbf{E}^{(+)}(\mathbf{r},t)+\mathbf{E}^{(-)}(\mathbf{r},t)\right], \qquad (5.11a)\\ \mathbf{H}(\mathbf{r},t) &= \frac{1}{2}\int_0^\infty \sum_{i=p,s} a_i(z,\omega)\frac{\mathbf{h}_i(\mathbf{r},\omega_i)}{\sqrt{P_i}} \\ &\times e^{i(\beta_i z-\omega t)}d\omega + c.c. \equiv \frac{1}{2}\left[\mathbf{H}^{(+)}(\mathbf{r},t)+\mathbf{H}^{(-)}(\mathbf{r},t)\right], \qquad (5.11b)\end{aligned}$$

where $\mathbf{E}^{(+)}(\mathbf{r},t)$, $\mathbf{H}^{(+)}(\mathbf{r},t)$ and $\mathbf{E}^{(-)}(\mathbf{r},t)$, $\mathbf{H}^{(-)}(\mathbf{r},t)$ are the positive and negative frequency parts of the spectrum, respectively. Similarly, the polarization term can be written as:

$$\begin{aligned}\mathbf{P}_{\text{pert}}(\mathbf{r},t) &= \frac{1}{2}\int_0^\infty \mathbf{P}_{\text{pert}}(\mathbf{r},\omega)e^{-i\omega t}d\omega + c.c. \\ &\equiv \frac{1}{2}\left[\mathbf{P}^{(+)}_{\text{pert}}(\mathbf{r},t)+\mathbf{P}^{(-)}_{\text{pert}}(\mathbf{r},t)\right]. \qquad (5.12)\end{aligned}$$

Eventually, after some mathematical manipulations and discarding the fast time-varying terms, this approach take us to the following time-domain coupled-mode equations for the envelopes of the pump and signal pulses:

$$\begin{aligned}\frac{\partial A_i(z,t)}{\partial z} &= i\sum_{q\geq 1}\frac{\beta_{q,i}}{q!}\left(i\frac{\partial}{\partial t}\right)^q A_i(z,t) \\ &+ \frac{i\omega_i e^{-i(\beta_i z-\omega_i t)}}{4\sqrt{P_i}}\int_S \mathbf{e}_i^*\cdot\mathbf{P}^{(+)}_{\text{pert}}(\mathbf{r},t)dS, \qquad (5.13)\end{aligned}$$

where:

$$A_i(z,t) = \int_0^\infty a_i(z,\omega)e^{-i(\omega-\omega_i)t}d\omega, \qquad (5.14)$$

are the envelopes of the interacting pulses in the time domain, and

$$\tag{5.15}$$

$$\beta_{1,i} = \frac{1}{v_{g,i}}, \tag{5.16}$$

$$\beta_{n,i} = \frac{\partial^{n-1}\beta_{1,i}}{\partial\omega^{n-1}},\ n \geq 2, \tag{5.17}$$

are the n^{th} order dispersion coefficients. Please note that from now on, the subindexes i and j represent the pump mode (p) or the signal mode (s), with $i \neq j$ when appearing both in the same formula.

To continue with the derivation, we introduce the time domain linear and nonlinear polarizations into the last term of Eq. 5.13. As mentioned before, we will just focus on the derivation for the nonlinear Raman polarization. To do this, we write the Raman term following the common convention in the bibliography [124]:

$$\begin{aligned}\delta\mathbf{P}_{\mathrm{R,i}}(\mathbf{r},t) = \frac{3}{2}\epsilon_0[\hat{\chi}^R(-\omega_R)\vdots\mathbf{E}(\mathbf{r},\omega_s)\mathbf{E}^*(\mathbf{r},\omega_s)\mathbf{E}(\mathbf{r},\omega_p)\delta(\omega-\omega_p)+\\ \hat{\chi}^R(\omega_R)\vdots\mathbf{E}(\mathbf{r},\omega_p)\mathbf{E}^*(\mathbf{r},\omega_p)\mathbf{E}(\mathbf{r},\omega_s)\delta(\omega-\omega_s)] =\\ \frac{3}{2}\epsilon_0\hat{\chi}^R(\omega_j-\omega_i)\vdots\mathbf{e}_j(\mathbf{r},\omega_j)\mathbf{e}_j^*(\mathbf{r},\omega_j)\mathbf{e}_i(\mathbf{r},\omega_i)|A_j|^2A_i\frac{e^{i(\beta_i z-\omega_i t)}}{P_j\sqrt{P_i}}.\end{aligned} \tag{5.18}$$

We now derive the Raman contribution by introducing Eq. 5.18 into the last term of Eq. 5.13 and again discarding the fast time-varying terms,

$$\frac{i\omega_i e^{-i(\beta_i z-\omega_i t)}}{4\sqrt{P_i}}\int_S \mathbf{e}_i^*\cdot\delta\mathbf{P}_{R,i}(\mathbf{r},t)dS = i2\gamma_R^i|A_j|^2A_i, \tag{5.19}$$

where:

$$\gamma_R^i(z) = \frac{3\omega_i\epsilon_0a^2}{16v_{g,i}v_{g,j}}\frac{1}{W_iW_j}\int_{S_{nl}}\mathbf{e}_i^*\cdot\hat{\chi}^R(\omega_j-\omega_i)\vdots\mathbf{e}_j(\mathbf{r},\omega_j)\mathbf{e}_j^*(\mathbf{r},\omega_j)\mathbf{e}_i(\mathbf{r},\omega_i)dS. \tag{5.20}$$

After including the effect of photogenerated FCs on the pulse dynamics as in Ref. [61], we obtain the final coupled-mode equations for the pump and the signal combined with the carrier dynamics rate equation:

$$i\left[\frac{\partial A_p}{\partial z}+\frac{1}{v_{g,p}}\frac{\partial A_p}{\partial t}\right]-\frac{\beta_{2,p}}{2}\frac{\partial^2 A_p}{\partial t^2}-\frac{\beta_{3,p}}{6}\frac{\partial^3 A_p}{\partial t^3}+\frac{\omega_p\delta n_{\mathrm{fc}}\kappa_p(z)}{nv_{g,p}}A_p+\frac{ic\kappa_p(z)}{2nv_{g,p}}(\alpha_{\mathrm{fc}}+\alpha_{\mathrm{in}})A_p+$$
$$\left[\gamma_p(z)|A_p|^2+2\gamma_{ps}(z)|A_s|^2\right]A_p+2\gamma_R^p|A_s|^2A_p=0, \tag{5.21a}$$

$$i\left[\frac{\partial A_s}{\partial z}+\frac{1}{v_{g,s}}\frac{\partial A_s}{\partial t}\right]-\frac{\beta_{2,s}}{2}\frac{\partial^2 A_s}{\partial t^2}\frac{\beta_{3,s}}{6}\frac{\partial^3 A_s}{\partial t^3}+\frac{\omega_s\delta n_{\mathrm{fc}}\kappa_s(z)}{nv_{g,s}}A_s+\frac{ic\kappa_s(z)}{2nv_{g,s}}(\alpha_{\mathrm{fc}}+\alpha_{\mathrm{in}})A_s+$$
$$\left[\gamma_s(z)|A_s|^2+2\gamma_{sp}(z)|A_p|^2\right]A_s+2\gamma_R^s|A_p|^2A_s=0, \tag{5.21b}$$

$$\frac{\partial N}{\partial t}=-\frac{N}{\tau_c}+\frac{1}{\hbar A_{wg}}\sum_{i=p,s}\left[\frac{\gamma_i''(z)}{\omega_i}|A_i|^4+\sum_{\substack{j=p,s\\ j\neq i}}\frac{4\gamma_{ij}''(z)}{\omega_i+\omega_j}|A_i|^2|A_j|^2\right], \tag{5.21c}$$

where $\tau_c\approx 500$ ps is the FC recombination time in Si-PhCWGs [125], the effective transverse area of the region in which FCs are generated has been assumed to be the waveguide transverse area $A_{wg}=ah$ and the $''$ refers to the imaginary part of the nonlinear coefficients. Note that degenerate and non-degenerate TPA effects are implicit in Eq. 5.21c via the imaginary parts of the nonlinear susceptibilities [126]. In more detail, the whole set of linear and nonlinear coefficients in Eqs. (5.21) are defined as follows:

$$\kappa_i(z)=\frac{\epsilon_0 an^2}{2W_i}\int_{S_{\mathrm{nl}}}|\mathbf{e}_i(\omega_i)|^2dS, \tag{5.22a}$$
$$\gamma_i(z)=\frac{3\omega_i\epsilon_0a^2}{16v_{g,i}^2}\frac{1}{\bar{W}_i^2}\int_{S_{\mathrm{nl}}}\mathbf{e}_i^*(\omega_i)\cdot\hat{\chi}^K(\omega_i,-\omega_i,\omega_i)\vdots\mathbf{e}_i(\omega_i)\mathbf{e}_i^*(\omega_i)\mathbf{e}_i(\omega_i)dS, \tag{5.22b}$$
$$\gamma_{ij}(z)=\frac{3\omega_i\epsilon_0a^2}{16v_{g,i}v_{g,j}}\frac{1}{\bar{W}_i\bar{W}_j}\int_{S_{\mathrm{nl}}}\mathbf{e}_i^*(\omega_i)\cdot\hat{\chi}^K(\omega_j,-\omega_j,\omega_i)\vdots\mathbf{e}_j(\omega_j)\mathbf{e}_j^*(\omega_j)\mathbf{e}_i(\omega_i)dS, \tag{5.22c}$$
$$\gamma_R^i(z)=\frac{3\omega_i\epsilon_0a^2}{16v_{g,i}v_{g,j}}\frac{1}{W_iW_j}\int_{S_{nl}}\mathbf{e}_i^*\cdot\hat{\chi}^R(\omega_j-\omega_i)\vdots\mathbf{e}_j(\mathbf{r},\omega_j)\mathbf{e}_j^*(\mathbf{r},\omega_j)\mathbf{e}_i(\mathbf{r},\omega_i)dS, \tag{5.22d}$$

where $S_{nl}(z)$ is the transverse area of the region filled with nonlinear material, κ_i measures

the grade of confinement of the field in the nonlinear region, γ_i corresponds to the SPM effect and contributes to the TPA process with its imaginary part, γ_{ij} is related to the XPM effect and to the XAM process with its imaginary part and γ_R^i corresponds to the Raman effect.

5.4.4 Characteristic lengths

Despite of the considerable complexity of the coupled-mode equations we obtained to investigate the properties of Raman interaction in Si-PhCWGs, one can easily identify the key effects that will disturb the propagating pulses by defining characteristic lengths [39]. These indicators can be used to measure the strength of the different linear and nonlinear effects based on a certain waveguide length and, also, the input power. In order to derive them, let us normalize the system of coupled-mode equations Eqs. 5.21 by applying the change of variable $t = T_0\tau$, where T_0 is the pulses' temporal widths, and the n^{th} derivative term over time becomes:

$$\frac{\partial}{\partial t^n} = \frac{1}{T_0^n}\frac{\partial}{\partial \tau^n}. \tag{5.23}$$

Since the variation with the distance of the optical modes A_i is still included in the normalized coupled-mode equations by the $\frac{\partial A_i}{\partial z}$ term, it is trivial to understand that the inverse of each factor multiplying the optical modes' envelope or its derivatives will own units of distance. Consequently, we define the following characteristic lengths:

$$L_D = \frac{T_0^2}{|\beta_2|}, \tag{5.24a}$$

$$L'_D = \frac{T_0^3}{|\beta_3|}, \tag{5.24b}$$

$$L_{SPM,i} = \frac{1}{|\gamma_i| P_{0,i}}, \tag{5.24c}$$

$$L_{XPM,i} = \frac{1}{2|\gamma_{ij}| P_{0,j}}, \tag{5.24d}$$

$$L_{R,i} = \frac{1}{2|\gamma_R^i| P_{0,j}}, \tag{5.24e}$$

where, respectively, these are named second order dispersion length, third order dispersion length, SPM length, XPM length and Raman length. Note that, from now on, we will just make reference to the Raman length from the signal point of view, this is $L_R = L_{R,s}$.

Last but not least, we shall introduce as well the concept of walk-off length between pulses, which is related to the fact that each pulse will propagate through the waveguide more slowly or more rapidly depending on their respective wavelengths. Although we could assume the pump and signal pulses could be simultaneously launched into the waveguide input, they will eventually get separated after some distance. Precisely, the Raman and Kerr cross-interaction between the pulses will have an effect only when they are overlapping. Therefore, the walk-off length is an important indicator as it measures the distance from which we can assume the pulses have separated from each other, and consequently, the distance from which we can expect almost no further interaction between them. Similarly as shown in [46], the walk-off length is defined as follows:

$$L_{w-off} = \frac{T_0}{|\frac{1}{v_{g,p}} - \frac{1}{v_{g,s}}|}. \tag{5.25}$$

For the remaining of the chapter, these characteristic lengths we have just defined will be frequently employed in order to help with the understanding and explanation of the different results.

5.5 Simulation results and discussion

In this section we illustrate how our theoretical model can be used to investigate various phenomena related to Raman interaction in Si-PhCWGs. In particular, we define three study cases which are characterised by different combinations of group velocities for the pump and the signal. As mentioned in section 5.3 and shown in Fig. 5.2, in the first study case we simulate the Si-PhCWG when both pulses belong to the slow-light regime; in the second study case we will set up both pulses in the fast-light regime, while, in the third study case, we will employ a pump in the slow-light regime and a signal in the fast-light

regime.

In terms of the selected algorithm to solve the system of equations Eqs. 5.21, we have used a combination between the split-step Fourier method [46] and a fifth-order Runge-Kuta method for the integration of the FCs terms in the nonlinear term. Even though our mathematical model accounts for the z-dependence on the linear and nonlinear coefficients, we will average them over the lattice constant length, since as shown in the appendix of Ref. [61], the results obtained with this simplified model are comparable to the ones obtained by the original models.

This section is divided into two parts. On the one hand, the first part will show the simulation results for each of the three study cases based on the same Si-PhCWG, e.g. the lattice constant will be fixed to $a = 388$ nm for all cases, so we will concentrate our investigation in understanding the effects of changing the pulse width T_0. Indeed, this investigation indirectly demonstrates one of the main advantages of these photonic crystal structures: this is, the same device can support different group velocity combinations between the pump and the signal without varying its geometry and dimensions. On the other hand, in the second part of this section, we will discuss about the effects of varying the walk-off length between pulses. In this case, the lattice constant of the device will be allowed to vary for each scenario.

5.5.1 Results of study cases in the same Si-PhCWG

Let us consider our Si-PhCWG with $a = 388$ nm. Following section 5.4.4, we start analyzing in figure Fig. 5.3 the second- and third-order dispersion lengths for the pump and the signal against various pulse widths, T_0. The black dashed line represents the reference waveguide length we take into account on our simulations, being $L_{wg} = 500$ μm, which is a standard fabrication length. The circles, squares and triangles illustrate the three study cases we analyze in this chapter: slow pump - slow signal, fast pump - fast signal and slow pump - fast signal, respectively.

Based on the above values, the slow-slow study case corresponds to a strong dispersion

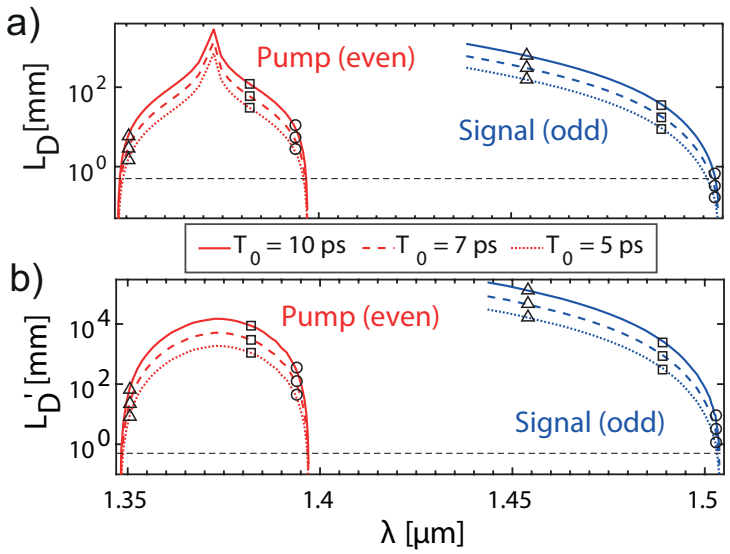

Figure 5.3: Second-order (up) and third-order (bottom) dispersion lengths for the pump and the signal for different pulse widths and $a = 388$ nm. The circles, squares and triangles illustrate the three different scenarios we analyze in this chapter: slow-slow, fast-fast and slow-fast, respectively. The dashed black line represents the waveguide length, $L_{wg} = 500$ μm.

regime for the signal, both for second and third order effects, while the pump experiments also considerable second order effects. For the slow-fast case, the pump propagation is mainly affected by second order dispersion effects, especially for the shortest pulse width, while the signal is in a weak dispersive regime. Finally, in the fast-fast case, both pump and signal are in a weak dispersive regime.

Regarding to the nonlinear lengths, in Fig. 5.4 we plot their dependance with the pulse peak powers for the three study cases. Similarly as we found for the dispersion lengths, the nonlinear effects are much stronger for the slow-slow case. This is due to the effective nonlinear susceptibilities depending inversely with the group velocities. We can also notice that the Raman effect is clearly present in all scenarios for waveguide lengths below half a millimeter. However, the SPM effect will be mainly present in the pump and the XPM effect in the signal, due to the fact we are assuming initial pump peak powers more than two orders of magnitude bigger than signal peak powers.

The evolution of pump and signal pulses in the time domain for the slow-slow study case is shown in Fig. 5.5, up and bottom, respectively. The NLS equations have been

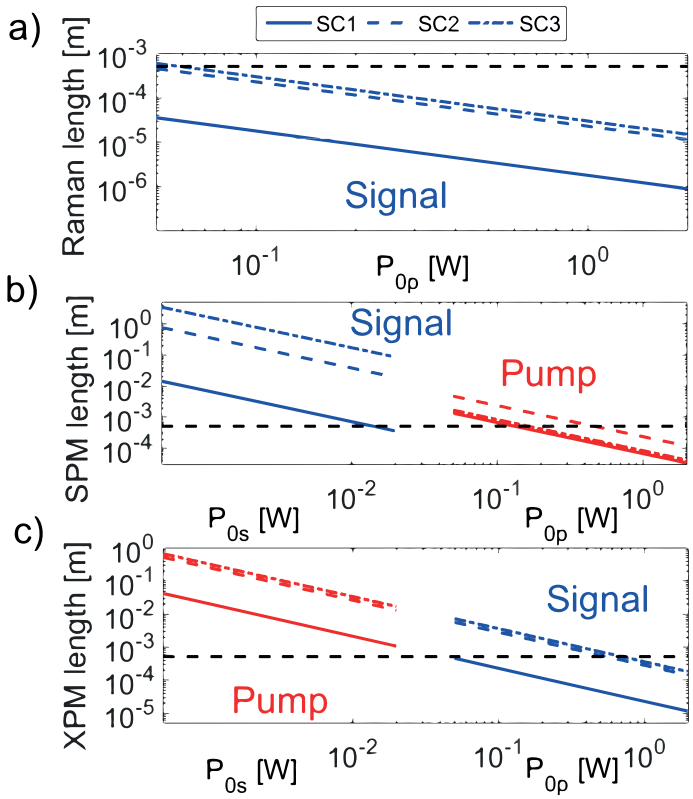

Figure 5.4: Pulses peak powers dependance of the Raman, SPM and XPM nonlinear lengths for the different study cases with $a = 388$ nm. The dashed black line represents the waveguide length, $L_{wg} = 500$ μm.

solved against the following initial conditions: pulse width, $T_0 = 7$ ps, signal peak power, $P_{0s}(z = 0) = 5 \times 10^{-4}$ W and pump peak power, $P_{0p}(z = 0) = 0.22$ W. Under these conditions, Raman is the leading effect in the pulse dynamics, considering that the weaker SPM and XPM terms are even more diminished by the strong attenuation of the waveguide as the pulses propagate. However, another important effect is the walk-off length between pulses, which for this scenario is $L_{w-off} = 27.8\mu m$. This explains the early splitting between pump and signal on Fig. 5.5b). In fact, it should be indicated at this point that the simulations have been carried out by applying a change of variable with temporal reference to the pump, i.e. $t - \frac{z}{v_{g,p}} = T_0\tau$. This is why the pump pulse evolves during the entire simulation domain over the $\tau = 0$ point, whereas the signal pulse moves away from it. The most noteworthy outcomes from this scenario are as follows. Primarily, we observe that the signal amplification grows very fast, thanks to the high value

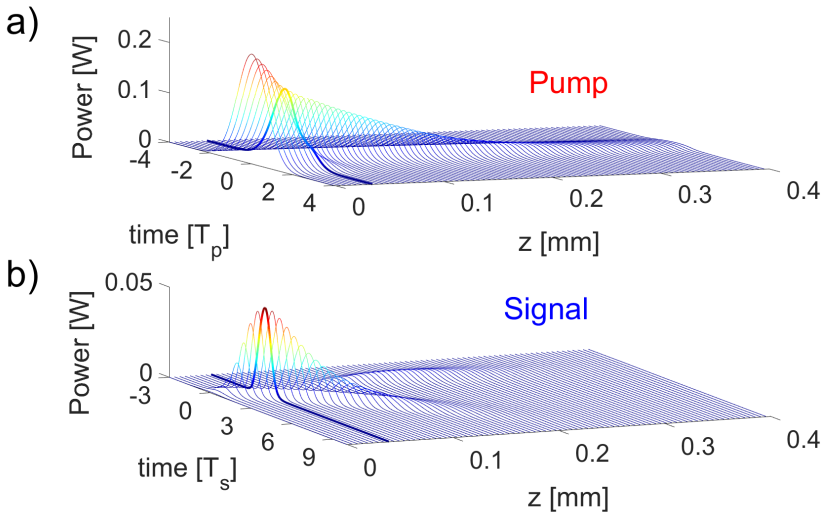

Figure 5.5: Pulse evolution in the time domain for $T_0 = 7$ ps, $P_{0s}(z = 0) = 5 \times 10^{-4}$ W and $P_{0p}(z = 0) = 0.22$ W. Results obtained for the slow-slow study case.

of the effective Raman susceptibility, and achieves its maximum before the pulses get separated. The eighth capture of the pump pulse along z illustrates how the pump gets depleted mostly by its trailling edge because it travels faster than the signal. Secondly, if we consider the wavelength domain, this actually means that the smaller wavelengths of the signal are interacting with the bigger wavelengths of the pump, whose consequence is a shift of the signal's frequency towards bigger wavelengths [46]. This is clearly seen in the signal's spectra of Fig. 5.6 at around $z = 100$ μm. Certainly, even though the pulses are getting more and more separated, the pump is still able to effectively transfer energy to a certain region of the signal's leading edge while this moves away.

By calculating the Raman amplification efficiency at the output of the waveguide, e.g. at $z = L_{wg}$, based on the following equation:

$$\eta[dB] = 10 \log \left[\frac{\int_{-\infty}^{\infty} |A_s(z = L_{wg}, t)|^2 dt}{\int_{-\infty}^{\infty} |A_s(z = 0, t)|^2 dt} \right], \tag{5.26}$$

we evaluate the Raman amplification dependence on the pump peak power for different pulse widths in Fig. 5.7. Here we show the efficiency of the energy transferred from the pump to the signal, leading to various interesting phenomena we proceed to explain. Firstly, for very low pump peak powers, the efficiency strongly relies on the pulse width.

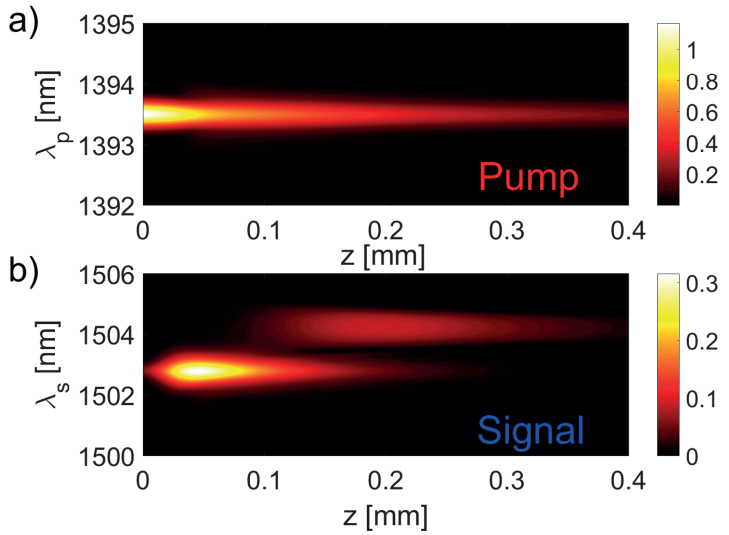

Figure 5.6: (a),(b) Evolution of pump and signal spectra along the waveguide, respectively. Results obtained under the same conditions as in Fig. 5.5.

The broader the pulse width is, the more interaction will occur between both pulses and the more Raman amplification will be achieved. However, due to the poor initial pump peak power, the waveguide losses will clearly outstand the Raman amplification and the signal level at the waveguide output will be very poor. The curves evolve linearly but, interestingly, with higher slopes for the narrower pulses. Indeed, we can notice the amplification for narrower pulses overcome those for broader pulses. The explanation is based on a perfect balance between the increased Raman factor due to the increase in peak power and the pulse broadening due to dispersive effects. Precisely, the narrower the pulse width is, the earlier the temporal dispersion will occur, which as shown in Fig. 5.3 is stronger for the signal. The next characteristic we observe is the appearance of a second contribution to the amplification efficiency η, mostly noticeable in the curve for $T_0 = 10$ ps when there is a change of slope. This is due to the effective transfer of energy from the trailling edge of the pump pulse to the leading edge of the signal pulse, as was shown in Fig. 5.5 and which leads to a maximum of energy transfer to the signal. After this inflexion point, all curves evolve towards a stable tendency. Certainly, just after this maximum, the Raman factor becomes so strong that the pump gets depleted very fast, up to the point that the trailling edge of the pump can no longer transfer energy to the

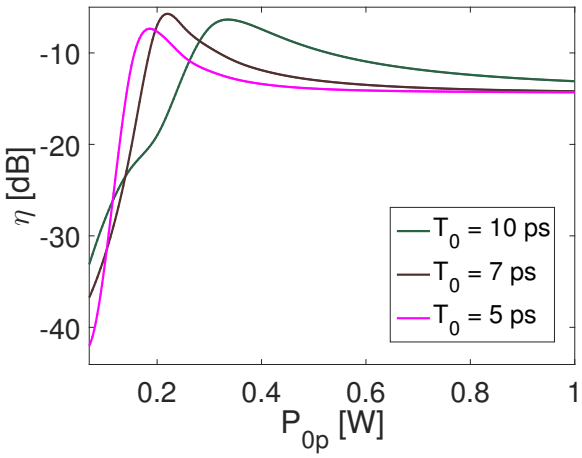

Figure 5.7: Pump peak power dependence of Raman amplification for different pulse widths. Results obtained for study case 1 (slow-slow), under same conditions as in Fig. 5.5.

leading edge of the signal.

Having shown the complex slow-slow scenario given by the strong nonlinear effects and certainly influencing dispersive effects, we move on the opposite case, this is when both the pump and the signal are in fast-light regimes. In this case, the dispersive effects will not play an important role. Additionally, both pulses own a very similar group velocity, such as the walk-off length is several times bigger than the waveguide length, this is $L_{w-off} = 4.6$ mm for a pulse width of $T_0 = 5$ ps. Under these conditions, we show in Fig. 5.8 the pulses evolution in the time domain when $P_{0s}(z = 0) = 5 \times 10^{-4}$ W and $P_{0p}(z = 0) = 1$ W. Even though the Raman coefficient is much smaller than in the slow-slow case, consequently establishing a slower transfer of energy, the interaction between pulses occur along the entire waveguide, which clearly contributes to a noticeable signal amplification. We can also highlight that the pump depletion is just given in the middle of the pulse since the pulses do not walk-off from each other.

With regards to the evolution of the spectra, this scenario can be used to illustrate clearly the effects of SPM and XPM. On the one hand, as indicated in Fig. 5.4, the pump was expected to show the consequences of SPM after propagating through the waveguide when using peak powers above 0.5 W, approximately. By using an initial pump peak

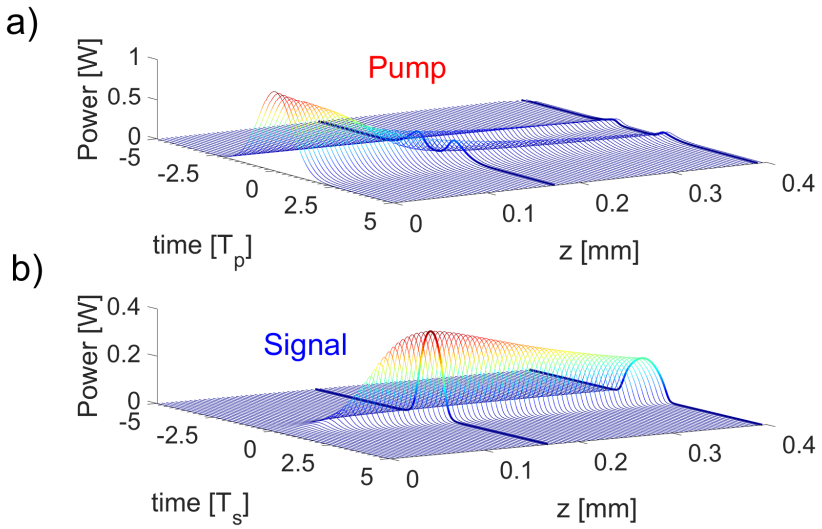

Figure 5.8: Pulse evolution in the time domain for $T_0 = 5$ ps, $P_{0s}(z = 0) = 5 \times 10^{-4}$ W and $P_{0p}(z = 0) = 1$ W. Results obtained for the fast-fast study case.

power of $P_{0p}(z = 0) = 1$ W, even considering the depletion of power due to the Raman effect, we can clearly map the SPM effect with the two sidelobes appearing on Fig. 5.9a). On the other hand, the signal was expected to show XPM for pump peak powers above 0.7 W, approximately. Indeed, there are two sidelobes that can be seen on Fig. 5.9b) which are the consequences of this effect.

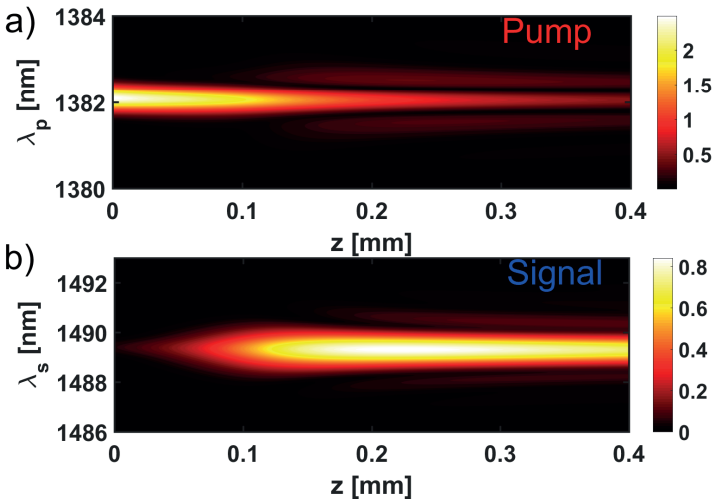

Figure 5.9: (a),(b) Evolution of pump and signal spectra along the waveguide, respectively. Results obtained under the same conditions as in Fig. 5.8.

To finish with the second study case, in Fig. 5.10 we plot the efficiency of the energy transfer from the pump to the signal for various pump peak powers. This figure clearly

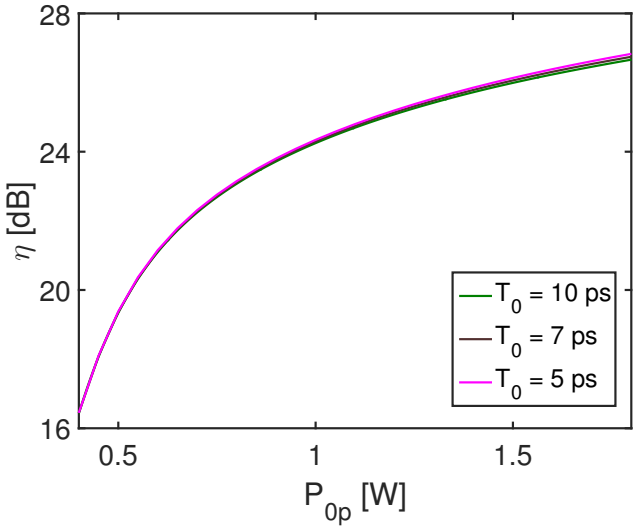

Figure 5.10: Pump peak power dependence of Raman amplification for different pulse widths. Results obtained for study case 2 (fast-fast), under same conditions as in Fig. 5.8.

states that this scenario is almost independent on the pulse widths used. Indeed, these efficiency curves correspond to classic amplification traces with a linearly growing region and a saturated tendency due to the rapid depletion of the pump. We should highlight that this scenario appears to be a potential candidate for designs of integrated optical Raman amplifiers, with efficiencies of 48 dB/(mmW), one order of magnitude above those experimentally or theoretically reported in the literature (see Refs. [12, 57]). Note that, although we are classifying this scenario as a fast-light one for both pump and signal, the group indexes of the modes in this Si-PhCWG are about three times bigger than those in conventional SOI rib and strip waveguides.

Once we have presented the results of the two opposite scenarios, we proceed with the last study case, in which we set the pump in the slow-light regime and the signal in the fast-light regime as a compromise situation. The signal and pump initial peak powers have been chosen $P_{0s}(z=0) = 5 \times 10^{-4}$ W and $P_{0p}(z=0) = 3.25$ W, respectively, and a pulse width of $T_0 = 5$ ps makes the walk-off length between pulses $L_{w-off} = 76.25$ μm. Since the signal is faster than the pump, we observe in Fig. 5.11 that the signal moves away from the pump in the opposite direction compared to Fig. 5.5. Indeed, the pump now gets depleted by its leading edge and the signal gets more energy on its trailing edge. Regarding the

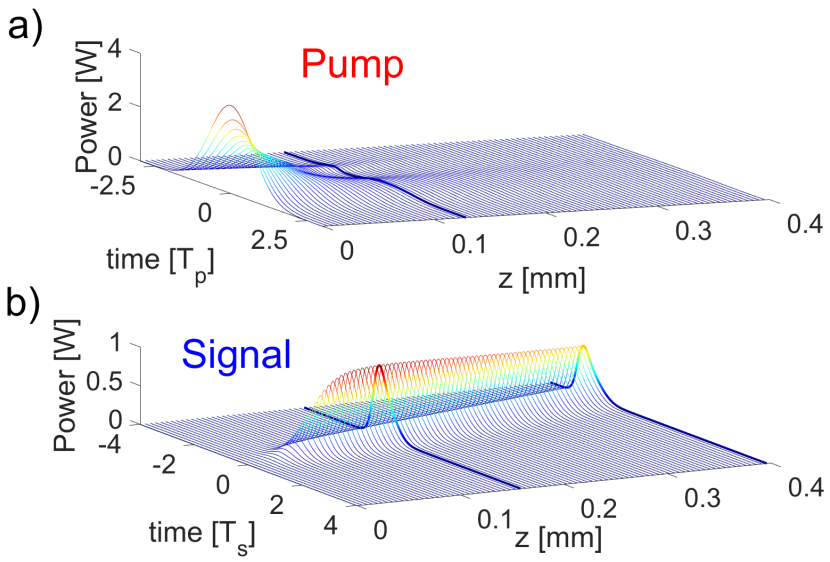

Figure 5.11: Pulse evolution in the time domain for $T_0 = 5$ ps, $P_{0s}(z = 0) = 5 \times 10^{-4}$ W and $P_{0p}(z = 0) = 3.25$ W. Results obtained for the slow-fast study case.

evolution of pump and signal spectra, we should firstly note that the bigger wavelengths of the pump are interacting also with the bigger wavelengths of the signal. In Fig. 5.12 we observe that both the pump and the signal have an asymmetric spectra. Actually, the ripples appearing on one side of the pump's spectra are given by a strong SPM, but this is only affecting to one side of the spectrum since the other side is being depleted. In the signal, we can also observe that the pulse is shifted towards smaller wavelengths, on the contrary to the slow-slow case. Additionally, a single ripple due to XPM is found on bigger wavelengths, which is also in line with our previous explanations. The pump peak power used in the scenario represented by Fig.5.11 corresponds to the crossing point between curves in Fig. 5.13. After this crossing point, the curve for the smallest pulse width goes over the other two. This behavior is noteworthy and is associated to two facts: firstly, the higher the pump peak power is, the stronger the Raman effect becomes and the earlier the total pump depletion occurs before the signal moves away; and secondly, the second-order dispersion effect on the pump is stronger for narrower pulses. Both reasons contribute to the smaller pulse widths overcoming the amplification achieved with the broader ones. Clearly, the pulse width is a key parameter that can change the dynamics

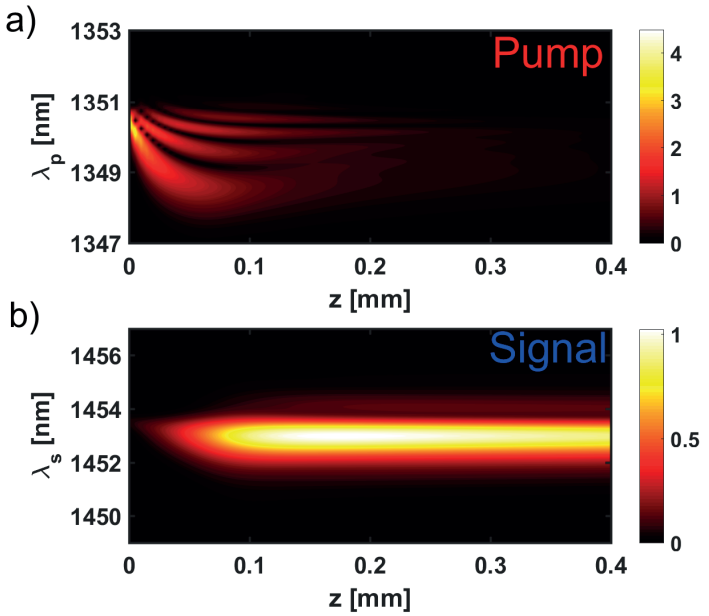

Figure 5.12: (a),(b) Evolution of pump and signal spectra along the waveguide, respectively. Results obtained under the same conditions as in Fig. 5.11.

more strongly than in the fast-fast case. This is due, again, to the short walk-off length between pulses.

5.5.2 Tuning the walk-off length between pulses

In the second part of this section we aim to study the effect of the walk-off length between pulses by modifying the lattice constant of the PhC structure we have been using so far. This is, indeed, of high interest given the relevancy of this parameter over the behavior of pulses along the waveguide. The procedure we have developed begins by selecting one of the scenarios shown for each study case and then tuning the group velocity of one of the modes. Obviously, when changing the group velocity and, consequently, the frequency of the chosen mode, the lattice constant of the PhC must be recalculated in order to satisfy Raman resonance frequency, this is:

$$\Omega_p - \Omega_s = \frac{f_R \cdot a}{c}, \tag{5.27}$$

where c is the speed of light at the vacuum and $f_R = 15.6$ THz.

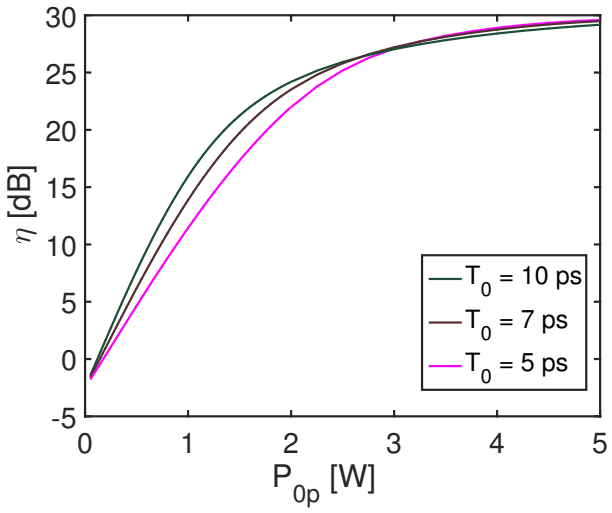

Figure 5.13: Pump peak power dependence of Raman amplification for different pulse widths. Results obtained for study case 3 (slow-fast), under same conditions as in Fig. 5.11.

Starting with the slow-slow study case, we fix the signal mode to $\Omega_s = 0.2582$ and $\frac{v_{g,s}}{c} = 0.01$. Thus, the pump mode is modified to the new modes shown in Table 5.1. As we can observe, we are bringing the pump group velocity closer to the signal's in order to increase the walk-off length. This can be done by reducing the lattice constant of the PhC. Fig. 5.14 shows the pump peak power dependence of Raman amplification for the different walk-off lengths when choosing a pulse width $T_0 = 10$ ps and an initial signal peak power $P_{0s} = 5 \times 10^{-4}$ W. It is noteworthy to explain what is happening at around $P_{0p} = 0.35$ W. Comparing the curves from the bottom to the top, we can notice that for smaller lattice constants, there is no peak. This can be explained since the smaller the lattice constant is, the slower the pump becomes, which makes the Raman coefficient grow and the pump gets depleted earlier. If the pump peak power is too high, the Raman coefficient grows so much that the pump gets depleted very soon and there

Table 5.1

pump mode	Ω_p	$\frac{v_{g,p}}{c}$	$\frac{L_{w-off}}{T_0}$ [m/s]	a [nm]
Original mode	0.2784	0.0407	3.97×10^6	388
Tuned mode 1	0.2781	0.0297	4.52×10^6	383
Tuned mode 2	0.2779	0.0181	6.72×10^6	379

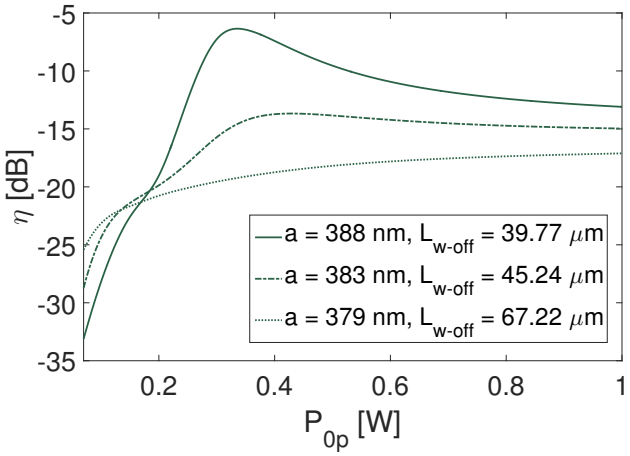

Figure 5.14: Pump peak power dependence of Raman amplification efficiency for different walk-off lengths. Smaller lattice constants are equivalent to slower pumps. Results obtained for study case slow-slow, with $P_{0s} = 5 \times 10^{-4}$ W, $T_0 = 10$ ps and $L_{wg} = 400$ μm.

is not remaining power to build the second signal that appeared in Fig. 5.5b). If the pump peak power is too small, the second signal is not built because there is just lack of power. However, for the right peak power, as soon as there is a balanced rate between the pump depletion speed and the walk-off between pulses, a second signal is created and the amplification curve shows a peak. In terms of spectra, the smaller the lattice constant is, i.e. the slower the pump is, the more important are the non-linear terms, so the more sidelobes will appear in the spectra.

The fast-fast scenario has been modified as shown in Table 5.2 to show the effects of the walk-off length between pulses. In this case, the pump mode has been fixed to $\Omega_p = 0.2807$ and $\frac{v_{g,p}}{c} = 0.0739$ and the signal mode has been moved towards higher group velocities. This means that now we are making the two modes more different in terms of group velocity by reducing the lattice constant, so the walk-off length will be reduced as well. We must note that, due to the closeness between group velocities in

Table 5.2

signal mode	Ω_s	$\frac{v_{g,s}}{c}$	$\frac{L_{w-off}}{T_0}$ [m/s]	a [nm]
Original mode	0.2605	0.076	9.27×10^8	388
Tuned mode 1	0.2609	0.0864	1.5×10^8	381
Tuned mode 2	0.263	0.1334	4.96×10^7	340

the initial situation, very little changes in the lattice constant will notably modify the walk-off length. For instance, by just reducing the lattice constant in 7 nm, there is a reduction of more than six times in the walk-off length between the original scenario and the first modified scenario. However, after this particular region, the walk-off length is not so variable with the lattice constant value, so the reduction in the walk-off length between the second and third scenarios are of three times, approximately, for a difference in the lattice constant of 41 nm.

Given the long walk-off lengths of this scenario, we have set up our simulations for a waveguide length of $L_{wg} = 1$ mm. In Fig. 5.15 we plot the efficiency of Raman amplification for $P_{0,s} = 5 \times 10^{-4}$ W and $T_0 = 10$ ps, with the three different cases we have included in Table 5.2. We can observe that the smaller the lattice constant is, the faster the signal travels, and the flatter the amplification growth is. The effect of the walk-off length is the most interesting fact. Since the pump does not only get depleted by the middle of the pulse, but also by one side, the amplification efficiency is improved because there is more energy transferred.

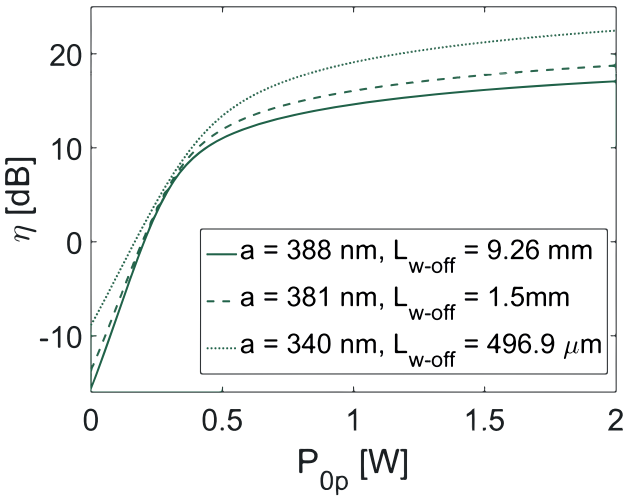

Figure 5.15: Pump peak power dependence of Raman amplification efficiency for different walk-off lengths. Smaller lattice constants are equivalent to faster signals. Results obtained for study case fast-fast, with $P_{0s} = 5 \times 10^{-4}$ W, $T_0 = 10$ ps and $L_{wg} = 1$ mm.

For the slow-fast case, we have kept the pump mode unvaried, being $\Omega_p = 0.2873$ and $\frac{v_{g,p}}{c} = 0.0398$. The different signals follow the characteristics shown in Table 5.3, where

it can be noticed that we are using bigger lattice constants to reduce the signal's group velocity and bring it closer to the pump's.

We have ran the simulations using a signal peak power of $P_{0s} = 5 \times 10^{-4}$ W and a waveguide length of $L_{wg} = 400$ μm. In Fig. 5.16 we illustrate the efficiency of Raman amplification for the selected signals. We must clarify that, in order to show the behaviors for different enough walk-off lengths, we have not fixed the pulse width for the three scenarios, but we have used $T_0 = 5$ ps for $a = 388$ nm, $T_0 = 10$ ps for $a = 479$ nm and $T_0 = 20$ ps for $a = 515$ nm. Based on this, we can observe that the slower we make the signal, i.e. the longer the walk-off length becomes, the earlier the Raman saturation point is reached. Furthermore, it is noticeable that, for pump peak powers below 0.2 W, the amplification at the end of the waveguide is higher for faster signals. This can be explained since, even though the pump is transferring energy more slowly, the energy of one of the pulse sides is being transferred also due to the walk-off between pump and signal. However, for pump peak powers between 0.2 W and 2 W, the strength of the Raman factor is clearly determined by the group velocities and by the Raman susceptibilities. Thus, the Raman factors for the three scenarios are so different now that the walk-off length is not a key differentiator any more, and the amplification efficiency becomes clearly better for slower signals. Eventually, when the pump peak power is increased enough, this parameter becomes again the key contributor in the value of the Raman factor. In other words, the differences in the signal's group velocity and in the Raman susceptibilities for the different scenarios are not as important as before, but it is the pump peak power. Consequently, the walk-off between pulses is again the main responsible of the growth of the energy transfer. In terms of spectra, the slower the signal

Table 5.3

signal mode	Ω_s	$\frac{v_{g,s}}{c}$	$\frac{L_{w-off}}{T_0}$ [m/s]	a [nm]
Original mode	0.2669	0.1827	15.25×10^6	388
Tuned mode 1	0.2624	0.1216	17.74×10^6	479
Tuned mode 2	0.2605	0.0757	25.14×10^6	515

becomes, the more XPM occurs towards the pump and the more SPM affects the signal.

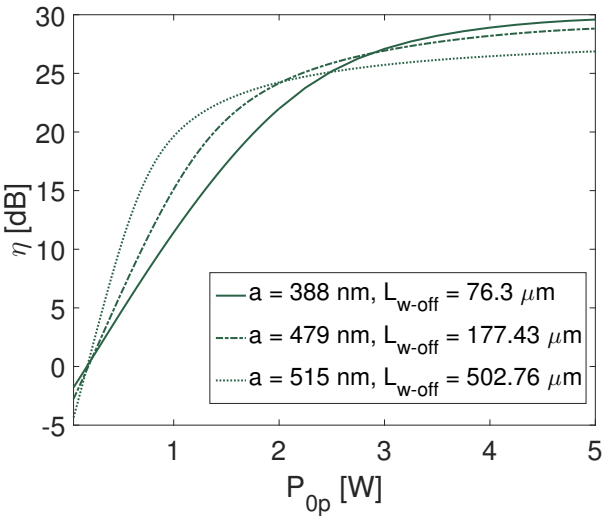

Figure 5.16: Pump peak power dependence of Raman amplification efficiency for different walk-off lengths. Bigger lattice constants are equivalent to slower signals. Results obtained for study case slow-fast, with $P_{0s} = 5 \times 10^{-4}$ W and $L_{wg} = 400$ μm. The pulse widths used are $T_0 = 5$ ps for $a = 388$ nm, $T_0 = 10$ ps for $a = 479$ nm and $T_0 = 20$ ps for $a = 515$ nm.

5.6 Conclusion

To conclude with this chapter, we have derived a comprehensive theoretical model which describes Raman amplification in one-dimensional photonic crystal slab waveguides made of silicon. Based on non-linear Schrödinger equations (NLSE), our model rigorously incorporate all key linear and nonlinear optical effects affecting the optical pulse dynamics, including modal dispersion, free-carrier absorption, self- and cross-phase modulation, two-photon absorption and Raman scattering. The characteristic lengths associated with each of these effects have been exhaustively explained and taken into account for the simulations given the valuable information they provide.

In order to make practical use of the mathematical model developed in this chapter, we have investigated the behavior of these devices for different combinations of pump and signal modes and demonstrated that clear signal amplification can be achieved. To

do so, we have firstly studied the effect of the group velocities (slow- or fast-light) by quantifying the energy transfer from pump to signal, also varying the input pulse width and peak power. The different scenarios have been simulated over the same device (same value for the lattice constant), which highlights how versatile PhCWGs can be by simply tuning the operating frequency. The most relevant result out of these is clearly the fast-fast scenario, in which energy transfer efficiencies of 48 dB/(mmW), independent on the input pulse width, have been shown. These figures are one order of magnitude above those found in the literature, which can be explained since, even for the fast-fast scenario, the group indexes of the modes in this Si-PhCWG are about three times bigger than those in conventional SOI rib and strip waveguides.

Secondly, we have focused on the impact the walk-off length between pulses has on the energy transfer efficiency curves for the same study cases, but now modifying the lattice constant of the photonic crystal. Indeed, our simulations show the importance of the walk-off length, which, for instance, must be clearly bigger than the waveguide length if it is required to amplify the signal and conserve its pulse shape simultaneously. For each study case, we have demonstrated how differently the device can perform depending on the value of the key parameters involved. Interestingly, the key observation can be done on the fast-fast scenario again, in which we have demonstrated that the energy transfer efficiency is quite insensitive to changes in the lattice constant value which, in practice, means the device would be very stable over fabrication accuracies. Precisely, we have shown that high gain values can be achieved even by varying the lattice constant several tens of nm.

As a final remark, in this work we have illustrated how important trade-offs between all design variables are required in order to succeed with the desired device behaviour. Within this framework, we aimed to set some reference scenarios for the development of active Si-PhCWGs, taking the proposed theoretical model as a reference to understand and compare measurements made on real devices.

Chapter 6

Cavity-waveguide interaction in silicon photonic crystals

6.1 Introduction

Achieving a seamless integration of photonics and electronics, a prerequisite for implementing many of the modern networks-on-chip (NoC) architectures, has recently been a powerful driver of research in photonics. In particular, it is envisioned that optical interconnects [2, 3, 4], the backbones of optical NoCs, would not be hampered by the limitations associated to copper-based electrical interconnects, e.g., poor bandwidth, large power dissipation at high frequencies due to track losses, need for impedance matching, and crosstalk between electrical paths [1, 127]. One of the proposed material platform to successfully implement optical interconnects was III-V semiconductors [6, 128]. Despite their high-index of refraction property, which facilitates a strong confinement of the optical field, and large optical nonlinearity required for efficient all-optical signal processing, various restrictions imposed by the corresponding fabrication processes makes it difficult to integrate these semiconductor materials with current electronic circuitry.

In this context, silicon photonics has emerged as a key material platform, which enables a seamless integration of photonics and electronics. Indeed, given that the trans-

parency window of silicon covers the entire optical telecommunication spectrum, electronic and optical domains can be brought together into the same chip. In particular, CMOS-compatible designs have been demonstrated in several application areas related to NoCs [7, 9, 8]. In this context, a key photonic device is the silicon photonic waveguide (Si-PhWG), which represents the backbone of on-chip optical networks. Unlike its counterparts made of III-V semiconductors, fabrication of silicon photonic nanowires is CMOS-compatible. Equally important, the high-index contrast provided by the silicon-on-insulator (SOI) material platform ensures a high degree of confinement of the optical field and, consequently a significantly reduced device footprint. An additional advantage offered by the optical field enhancement in SOI devices is that nonlinear optical effects, which are particularly important for all-optical signal processing, are dramatically enhanced [7]. In particular, key nonlinear processes in Si-PhWGs have been demonstrated, including Raman amplification [11, 12, 63], soliton [13] and supercontinuum [14] generation, frequency conversion [15], modulation instability [16], and pulse compression [17, 18]. For a review of nonlinear optics in silicon photonic nanowires see Refs. [39, 129, 130, 131].

Although Si-PhWGs with uniform cross-section are much more dispersive than silica-based optical waveguides, such as optical fibers, their frequency dispersion cannot be varied too much, e.g. by varying their geometrical parameters. This, in turn, limits the potential for miniaturization of photonic devices containing Si-PhWGs. Photonic crystals (PhCs) can mitigate this drawback as the optical dispersion coefficients of silicon PhC waveguides (Si-PhCWGs) with size comparable to that of Si-PhWGs with uniform cross-section can be orders of magnitude larger than those of the latter ones. These ideas have been implemented in a broad array of photonic devices based on PhCs, from narrow-band optical filters [22, 23] to omnidirectional mirrors, waveguides, and bends [24, 25, 26].

Tuning the geometrical parameters of a Si-PhCWG allows one not only to achieve orders-of-magnitude variation of the waveguide dispersion coefficients but also to reach the so-called slow-light (SL) regime in which the group-velocity (GV), v_g, of the optical modes is significantly smaller that the speed of light, c, i.e., $c/v_g \gg 1$. In this SL regime

the light-matter interaction is strongly enhanced and both the linear and nonlinear optical effects increase substantially [27, 28, 29, 30]. In particular, important applications based on the control of light propagation in the SL regime, including optical buffering or time domain processing of optical signals [31, 32, 33].

In this chapter, we explore the complex interaction between high-Q photonic crystal cavities and slow-light Si-PhCWG modes. The effect of placing a number of cavities alongside the waveguide not only affects the forwards propagating mode by coupling energy back and forth, but also produces the appearance of backwards propagating pulses. In our case, we are interested in studying the cavity-waveguide interaction on a Si-PhC slab with hexagonal lattice as shown in Fig. 6.1, where the ideal hexagonal lattice has been modified by adding a line defect to allow guided modes (appearance of defect bands) and local defects to create resonant cavities which couple energy between themselves and between them and the waveguide. For this purpose, a more complex theoretical model to the ones described in Chapters 3 and 5 has to be derived and, similarly, a different approach in the computational method is necessary. In the literature, several approaches have been applied to similar problems [132, 133, 134, 135], but have been limited to continuous wave signals or do not include free-carrier (FC) dynamics. In this work we

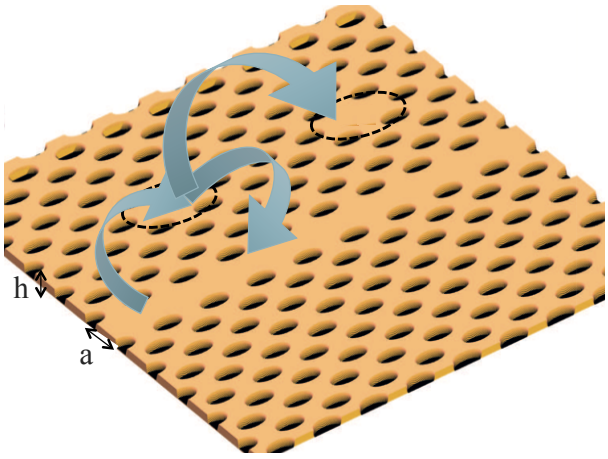

Figure 6.1: Illustration of the photonic crystal structure under interest, in which a line defect in the crystal lattice is created to allow guided modes, and local defects are created to form a cavity. The slab dimensions are $h = 0.6a$, $r = 0.29a$, with a the lattice constant of the phtonic crystal.

present a novel methodology which is applicable to pulse propagation and incorporates the key effects of FCs in the cavities and waveguide modes, such as FC dispersion and FC absorption, as well as, two-photon-absorption (TPA), the nonlinear Kerr effect and the waveguide dispersive effects. Furthermore, we demonstrate how it is possible to obtain the value of all unknowns together by computationally solving the matrix system of coupled nonlinear Schrödinger equations (NLSE) using the Newton-Raphson technique for nonlinear systems of partial differential equations.

This chapter is divided in the following way. Beginning with the next section, 6.2, we describe the Si-PhC slab considered for this work and how this is modified to create a waveguide and a cavity, for which we present the electromagnetic modes these support. After that, the description of the theoretical model has been structured in two parts: firstly, we define the main properties of the PhC waveguides and PhC cavities modes; while, secondly, we derive in detail the mathematical model, including the FC dynamics equations, plus the simplification and normalization of the whole system. In the subsequent section, 6.6, we explain how the mathematical model has been discretized so it can be entered into the computational domain, as well as the algorithm used to solve the equations. The chapter follows with the simulation results section 6.7, in which, in particular, we solve the pulse dynamics of forward- and backward-propagating pulses, both in time and frequency domains; the time dependence of the energy at each cavity; and the FC dynamics in the cavities and waveguide. Moreover, the influence of different system parameters, such as the separation between cavities, the distance between cavities and waveguide, and the width of the input pulse, is investigated, too. In particular, we illustrate how the computational tool can be employed to find the optimum separation between cavities that minimizes the amplitude of the backward-propagating pulse at the input.

6.2 Description of the photonic system

The Si-PhC structure considered in this work consists of a honeycomb-type periodic lattice of air holes with radius, r, perforated in a homogeneous silicon slab of thickness, h. The lattice constant of the PhC is a. A one-dimensional (1D) PhC waveguide commonly called W1-PhCWG is created in this structure by filling in a row of lattice holes, thus creating a so-called line defect. Photonic crystal cavities (PhCCs), on the other hand, are created by filling in a certain number of holes, and can be viewed as 0D defects in the ideal lattice. A schematic representation of a structure consisting of two interacting PhC cavities coupled to a PhCWG is presented in Fig. 6.2(a). In this figure, the blue arrows indicate the optical coupling between the PhCWG and PhCCs, whereas the red arrow indicate the optical coupling between cavities. Furthermore, we assume that the center-to-center distance between the cavities is l_p.

The photonic band structure of the periodic crystal, the frequency dispersion of the waveguide modes and their field profiles, as well as the frequency of the cavity modes and their field profiles have been computed using the plane-wave expansion (PWE) method implemented in MPB [53], a freely available electromagnetic solver. All these calculations were validated with BandSOLVE [55], a commercially available software. In addition, the Q-factor of the PhCCs has been determined using the finite-difference time-domain method (FDTD) implemented in MEEP [56], a freely available software. In the PWE-based calculations we use supercells with size along the x-, y-, and z-axis of $6a \times 19\sqrt{3}/2a \times a$, respectively, for the PhCWG, and $6a \times 6\sqrt{3}a \times 17a$, respectively, for the PhCC. Additionally, the computational grid in the FDTD calculations was chosen to be $a/60$, $a\sqrt{3}/120$, and $a/60$, for the x-, y-, and z-axis, respectively. Note that in order to control and enhance the Q-factor of the PhCCs the centers of the holes at their edges have been outwardly shifted by $s = 0.15a$. Unless otherwise specified, in all of the following calculations the index of refraction of silicon was $n_{Si} \equiv n = 3.48$, $a = 333\,\text{nm}$, $h = 0.6a$, and $r = 0.29a$.

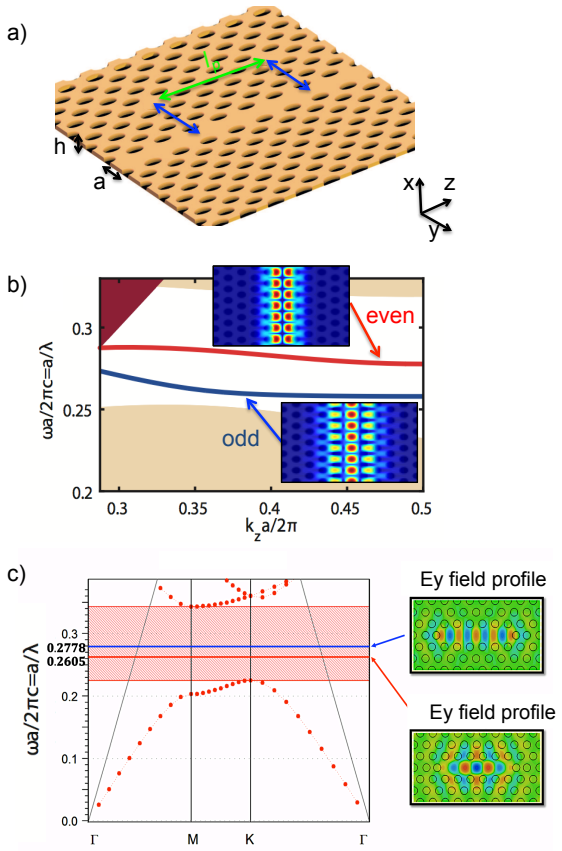

Figure 6.2: (a) Schematic representation of a photonic structure consisting of two interacting photonic crystal cavities coupled to a photonic crystal waveguide. (b) Projected band structure of the photonic crystal slab and dispersion curves of the two photonic crystal waveguide modes. The insets represent the field profiles for the two photonic crystal waveguide modes, specifically the normalized amplitude of the magnetic field component, H_x, calculated for $k_z = 0.435$, in the plane $x = 0$. (c) Transverse-magnetic band structure of the photonic crystal slab and the two photonic crystal cavity modes. The E_y field profile of the cavity modes are shown in the right panels.

The PhCWG has two TE-like optical guiding modes located in the band-gap of the unperturbed PhC, one y-even and the other y-odd. The frequency dispersion curves of the two modes are presented in Fig. 6.2(b), the corresponding spatial profile of the normalized amplitude of the magnetic field component, H_x, calculated for $k_z = 0.435$, in the plane $x = 0$, is presented in the insets. In the following analysis, we consider a cavity mode with normalized frequency $\bar{\omega}_c = 0.2605$, the corresponding Q-factor of the cavity being $Q_c = 1.17 \times 10^5$. Here, $\bar{\omega} = a/\lambda$ is the normalized frequency. In the SL regime, for the same normalized frequency $\bar{\omega}_c = 0.2605$ and normalized wave vector $k_z = 0.435$

the waveguide mode has group-velocity of $v_g = 0.0121c$ and corresponding group-index $n_g = c/v_g = 82.64$.

The transverse-magnetic (TM) band diagram of the PhC slab is presented in Fig. 6.2(c), as well as the optical modes of the PhCC. The band diagram shows a frequency bandgap, and two cavity modes with frequencies $\omega_1 = 1572.5\,\mathrm{THz}$ ($\bar{\omega}_1 = 0.2605$) and $\omega_2 = 1474.6\,\mathrm{THz}$ ($\bar{\omega}_2 = 0.2778$) located in this bandgap. Note that the two cavity modes are separated by the Raman frequency of silicon, $\omega_1 - \omega_2 = \Omega_{Si} = 2\pi \times 15.6\,\mathrm{THz}$, so that the PhCCs can be employed for Raman amplification [137]. In this chapter, however, this matter is not considered any further, given the problem complexity is already very high without including the Raman effect and that this is the first time this theoretical model is developed and demonstrated.

The permittivity of the system, $\epsilon_s(\mathbf{r})$, can be decomposed in several alternative ways. Thus, if one considers the cavities to be a perturbation of the waveguide, one can write:

$$\epsilon_s(\mathbf{r}) = \epsilon_w(\mathbf{r}) + \sum_{p=1}^{N_c} \epsilon_p^d(\mathbf{r}), \tag{6.1}$$

where N_c is the number of cavities, $\epsilon_w(\mathbf{r})$ is the permittivity distribution defining the waveguide, and $\epsilon_p^d(\mathbf{r})$ describes the dielectric cylinders filling the holes of the pth cavity. In Fig. 6.3 we present the graphical illustration of this dielectric system. It can be seen that the distribution of $\epsilon_p^d(\mathbf{r})$ also includes the displacement of the holes at the edges of the cavity so as to increase the mode Q-factor. An alternative way to decompose $\epsilon_s(\mathbf{r})$ is:

$$\epsilon_s(\mathbf{r}) = \epsilon_p(\mathbf{r}) + \sum_{q \neq p} \epsilon_q^d(\mathbf{r}) + \epsilon_w^d(\mathbf{r}), \tag{6.2}$$

where $\epsilon_p(\mathbf{r})$ is the permittivity distribution defining the pth cavity and $\epsilon_w^d(\mathbf{r})$ describes the dielectric cylinders filling the holes of the waveguide.

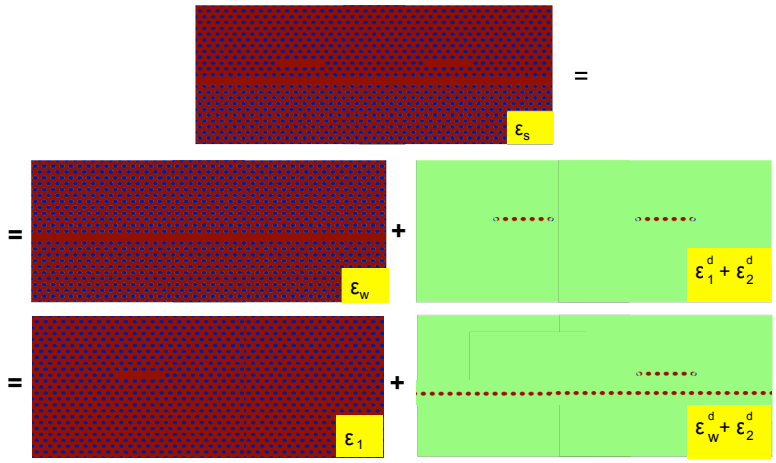

Figure 6.3: Schematic illustration of the decomposition of the permittivity of the waveguide/cavity system ($\epsilon_s(\mathbf{r})$, top panel) either as a PhC waveguide, $\epsilon_w(\mathbf{r})$, and the dielectric cylinders filling the holes of the PhC cavities (middle panels) or a certain pth PhC cavity, $\epsilon_p(\mathbf{r})$, $p = 1, \ldots, N_c$, and the dielectric cylinders filling the holes of the remaining PhC cavities and the PhC waveguide (bottom panels).

6.3 Optical properties of silicon PhC waveguides and PhC cavities

In this section we briefly review the properties of optical modes of PhC waveguides and PhC cavities, as well as the linear and nonlinear perturbations that occur upon light propagation in silicon PhC waveguides and light interaction with silicon PhC cavities.

6.3.1 Main properties of optical modes of PhC waveguides and PhC cavities

The electric and magnetic fields of the mode of an isolated 1D PhCWG can be expressed in the following form, respectively:

$$\mathbf{E}_\beta(\mathbf{r},\omega) = \frac{\mathbf{e}_\alpha(\mathbf{r},\omega)}{\sqrt{P}} e^{i\alpha\beta(\omega)z}, \tag{6.3a}$$

$$\mathbf{H}_\beta(\mathbf{r},\omega) = \frac{\mathbf{h}_\alpha(\mathbf{r},\omega)}{\sqrt{P}} e^{i\alpha\beta(\omega)z}, \tag{6.3b}$$

where α indicates the direction of mode propagation, namely $\alpha = +1$ ($\alpha = -1$) for forward (backward) propagating modes for $e^{-i\omega t}$ harmonic time dependence of the fields, and P is a normalization constant. If we choose this normalization constant such that

$$\frac{1}{4}\int_{A_\infty} (\mathbf{e}_\alpha^* \times \mathbf{h}_\alpha + \mathbf{e}_\alpha \times \mathbf{h}_\alpha^*) \cdot \hat{\mathbf{z}} dA = \alpha P, \tag{6.4}$$

where A_∞ is a transverse cross-section extending to infinity, the mode $\{\mathbf{E}_\beta, \mathbf{H}_\beta\}$ in Eq. (6.3) carries 1 W along the longitudinal z-axis. In the absence of optical losses (the crystal permittivity is real-valued function) the forwards and backwards propagating modes are related by the following relations:

$$\mathbf{e}_+ = \mathbf{e}_-^*; \quad \mathbf{h}_+ = -\mathbf{h}_-^*, \tag{6.5}$$

The mode power is related to the mode energy contained in one unit cell, $\mathcal{W}$, and the group velocity, v_g, via the relation [121, 122]:

$$P = \frac{\mathcal{W}}{a} v_g = \frac{\mathcal{W}^{\text{el}} + \mathcal{W}^{\text{mag}}}{a} v_g, \tag{6.6}$$

where $\mathcal{W} = \mathcal{W}^{\text{el}} + \mathcal{W}^{\text{mag}}$ is the sum between the electric ($\mathcal{W}^{\text{el}}$) and magnetic ($\mathcal{W}^{\text{mag}}$) energy in the mode. These quantities are defined as:

$$\mathcal{W}^{\text{el}} = \frac{1}{4}\int_{V_{\text{cell}}} \frac{\partial}{\partial\omega}(\omega\epsilon_w)|\mathbf{e}_\alpha(\mathbf{r},\omega)|^2 dV, \tag{6.7a}$$

$$\mathcal{W}^{\text{mag}} = \frac{1}{4}\int_{V_{\text{cell}}} \mu_0 |\mathbf{h}_\alpha(\mathbf{r},\omega)|^2 dV, \tag{6.7b}$$

where $\epsilon_w(\mathbf{r},\omega))$ is the permittivity of the PhC waveguide and V_{cell} is the volume of the unit cell.

The optical modes of the PhCCs can be expressed as

$$\mathbf{E}_m(\mathbf{r},\omega) = \frac{\mathbf{e}_m(\mathbf{r},\omega)}{\sqrt{W_m}}, \tag{6.8a}$$

$$\mathbf{H}_m(\mathbf{r},\omega) = \frac{\mathbf{h}_m(\mathbf{r},\omega)}{\sqrt{W_m}}, \tag{6.8b}$$

where m is the mod index and W_m is a normalization constant. If one chooses this normalization constant as

$$W_m = \frac{1}{4}\int_{V_{\text{cell}}} \left[\frac{\partial}{\partial\omega}(\omega\epsilon_c)|\mathbf{e}_m(\mathbf{r},\omega)|^2 + \mu_0|\mathbf{h}_m(\mathbf{r},\omega)|^2\right] dV, \tag{6.9}$$

where $\epsilon_c(\mathbf{r},\omega)$ is the permittivity of the PhC cavity, a cavity mode defined by Eqs. (6.8) contains an amount of energy equal to 1 J.

6.3.2 Linear and nonlinear perturbations in silicon PhC waveguides and PhC cavities

Due to the photogeneration of FCs and nonlinear optical effects, the dielectric constant of Si-PhCWGs undergoes a certain local variation, $\delta\epsilon(\mathbf{r})$, upon the propagation of optical pulses in the waveguide. This variation is related to a perturbation polarization, $\mathbf{P}_{\text{pert}}(\mathbf{r},t)$, which, considering the nature of the perturbation, can be divided in two components: a linear part, $\delta\mathbf{P}_{\text{lin}}(\mathbf{r},t)$, originating from the linear change of the dielectric constant *via* generation of FCs and a nonlinear component, $\delta\mathbf{P}_{\text{nl}}(\mathbf{r},t)$, that accounts for the nonlinearly induced variation of the index of refraction.

Assuming an instantaneous response of the medium, the linear contribution to $\mathbf{P}_{\text{pert}}$, $\delta\mathbf{P}_{\text{lin}}(\mathbf{r},t)$, is written as we did in Chapter 2 Eqs. 2.11 to 2.13.

The nonlinear contribution to $\mathbf{P}_{\text{pert}}$, $\delta\mathbf{P}_{\text{nl}}(\mathbf{r},t)$, is described by a third-order nonlinear susceptibility, $\hat{\boldsymbol{\chi}}^{(3)}(\mathbf{r})$, and can be written as:

$$\delta\mathbf{P}_{\text{nl}}(\mathbf{r},t) = \epsilon_0\hat{\chi}^{(3)}(\mathbf{r})\vdots\mathbf{E}(\mathbf{r},t)\mathbf{E}(\mathbf{r},t)\mathbf{E}(\mathbf{r},t). \tag{6.10}$$

The real part of the susceptibility $\hat{\boldsymbol{\chi}}^{(3)}$ describes parametric optical processes in which the energy of the photons involved in the process is conserved, such as SPM, XPM, and

FWM, while the imaginary part of $\hat{\boldsymbol{\chi}}^{(3)}$ corresponds to non-conservative processes like TPA and XAM. Note that in this study we neglect the stimulated Raman scattering effect as it is assumed that the frequencies of the interacting pulses do not satisfy the condition required for an efficient, resonant Raman interaction.

Since silicon belongs to the crystallographic point group $m3m$, the susceptibility tensor $\hat{\boldsymbol{\chi}}^{(3)}$ has 21 nonzero elements, of which only 4 are independent: $\chi^{(3)}_{1111}$, $\chi^{(3)}_{1122}$, $\chi^{(3)}_{1212}$, and $\chi^{(3)}_{1221}$ [52]. In addition, the frequency dispersion of the nonlinear susceptibility can be neglected as we consider optical pulses with duration of a few picoseconds or larger. Therefore, the Kleinman symmetry relations imply that $\chi^{(3)}_{1122} = \chi^{(3)}_{1212} = \chi^{(3)}_{1221}$. Moreover, experimental studies have shown that $\chi^{(3)}_{1111} = 2.36\chi^{(3)}_{1122}$ [62] within a broad frequency range. Therefore, the nonlinear optical effects considered here can be described by only one element of the tensor $\hat{\boldsymbol{\chi}}^{(3)}$.

Because of fabrication considerations, in many instances the waveguide is not aligned with any of the crystal principal axes and as such these axes are different from the coordinate axes in which the optical modes are calculated. Therefore, one has to transform the tensor $\hat{\boldsymbol{\chi}}^{(3)}$ from the crystal principal axes into the coordinate system in which the optical modes are calculated [63],

$$\chi^{(3)}_{ijkl} = R_{i\alpha}R_{j\beta}R_{k\gamma}R_{l\delta}\chi'^{(3)}_{\alpha\beta\gamma\delta}, \tag{6.11}$$

where $\hat{\boldsymbol{\chi}}'^{(3)}$ is the nonlinear susceptibility in the crystal principal axes and $\hat{\mathbf{R}}$ is the rotation matrix that transforms one coordinate system into the other. In our case, $\hat{\mathbf{R}}$ is the rotation matrix that transforms the crystal principal axes to the laboratory system of coordinates.

6.4 Derivation of the equations describing the optical field and free-carriers dynamics

In this section, we derive the set of equations that governs the dynamics of the optical field in the system of a Si-PhCWG coupled to optical cavities, as well as the corresponding FC dynamics in the system. To simplify the derivation, we consider only two cavities, referred to as c_1 and c_2, whose resonant frequencies are ω_1 and ω_2, respectively. However, the mathematical model derived here can be easily extended to the general case of an arbitrary number of cavities. Furthermore, we assume that the Si-PhCWG operates in a single-mode regime, the carrier frequency of the pulse propagating in the waveguide being ω_w.

Our theoretical model rigorously describes the main linear and nonlinear optical phenomena pertaining to this photonic system. Thus, the linear phenomena can be divided in two classes, those related to the passive interaction between the optical field and silicon and those related to the linear interaction between the optical field and FCs. To be more specific, the optical pulse dynamics in the waveguide is affected by dispersive effects as well as the linear coupling with the cavities, whereas, reversely, the optical field in the cavities is affected by the linear coupling with the waveguide. Furthermore, the optical field in the waveguide and cavities generate FCs in the waveguide and cavities, respectively, which leads to a variation of the index of refraction and, consequently, a FCs-mediated self-interaction of the corresponding optical fields. Finally, the evanescent part of the optical field in the waveguide induces a variation of the FCs in the cavities, and *vice-versa*, an effect that leads to FC-induced linear coupling between the optical fields in the waveguide and cavities.

Regarding the nonlinear optical effects that governs the optical field dynamics in our system, they can be classified as nonlinear self- and cross-interactions. Thus, the forward- and back-ward propagation pulses in the waveguide and the optical field in the cavities are affected by the self-induced variations of the index of refraction in the

waveguide and cavities, respectively, via the Kerr effect. Furthermore, the forward- and backward-propagating pulses in the waveguide are coupled via cross-phase modulation effects. Finally, another type of cross-phase modulation interaction is between the optical field propagating in the waveguide and those in the cavities. Thus, the evanescent part of the optical field in the waveguide induces a variation of the index of refraction in the cavities, and *vice-versa*, which induces nonlinear coupling via Kerr effect between the optical fields in the waveguide and cavities. It should be noted that not all these linear and nonlinear effects have comparative strengths, so that part of our analysis is to estimate which are the dominant ones and in which conditions.

In the remaining of this chapter, we will derive the dynamical equations for the amplitude of the waveguide modes by assuming that the FC and nonlinear optical effects as well as the perturbations represented by the optical cavities act on the unperturbed waveguide modes. Similarly, we will derive the time dependence of the cavity mode amplitudes by considering that the waveguide modes, FC and nonlinear effects perturbatively affect the unperturbed cavity modes. Finally, we employ energy conservation arguments to determine the dynamics of the FC density in the waveguide and cavities.

6.4.1 Dynamical equations for the evolution of waveguide mode amplitudes

In order to derive the system of equations governing the dynamics of the amplitudes of the optical waveguide modes, we employ the conjugated form of the Lorentz reciprocity theorem [63, 100, 121, 123, 136]. To this end, let us begin by considering the following integral identity, which can be easily derived from the divergence theorem:

$$\int_S \nabla \cdot \mathbf{F} dS = \frac{\partial}{\partial z} \int_S \mathbf{F} \cdot \hat{\mathbf{z}} dS + \oint_{\partial S} \mathbf{F} \cdot \mathbf{n} dl, \tag{6.12}$$

where $\mathbf{F}$ is an arbitrary vector field, S is the transverse section at position, z, and ∂S is the boundary of S. If we define the field $\mathbf{F}$ as $\mathbf{F} = \mathbf{E}_b \times \mathbf{H}_a^* + \mathbf{E}_a^* \times \mathbf{H}_b$, where

$[\mathbf{E}_a(\mathbf{r},\omega_a),\mathbf{H}_a(\mathbf{r},\omega_a)]$ and $[\mathbf{E}_b(\mathbf{r},\omega_b),\mathbf{H}_b(\mathbf{r},\omega_b)]$ are two solutions of the Maxwell equations corresponding to two electromagnetic systems described by the permittivities, $\epsilon_a(\mathbf{r},\omega_a)$ and $\epsilon_b(\mathbf{r},\omega_b)$, respectively, one can readily demonstrate that Eq. (6.12) can be cast in the following form:

$$\frac{\partial}{\partial z}\int_S \mathbf{F}\cdot\hat{\mathbf{z}}dS + \oint_{\partial S}\mathbf{F}\cdot\mathbf{n}dl = i\mu_0(\omega_b-\omega_a)\int_S \mathbf{H}_a^*\cdot\mathbf{H}_b dS + i\int_S(\omega_b\epsilon_b-\omega_a\epsilon_a)\mathbf{E}_a^*\cdot\mathbf{E}_b dS. \tag{6.13}$$

Note that in deriving this relation we used Maxwell equations for harmonic fields with time dependence of $e^{-i\omega t}$.

Now we choose the two electromagnetic systems and the corresponding solutions of the Maxwell equations. As the first system we choose an unperturbed PhC waveguide described by the permittivity, $\epsilon_a(\mathbf{r}) = \epsilon_w(\mathbf{r})$, and an unperturbed optical mode given by Eq. (6.3):

$$\mathbf{E}_a(\mathbf{r},\omega_a) = \frac{\mathbf{e}_\alpha(\mathbf{r},\bar{\omega})}{\sqrt{P}}e^{i\alpha\bar{\beta}z}, \tag{6.14a}$$

$$\mathbf{H}_a(\mathbf{r},\omega_a) = \frac{\mathbf{h}_\alpha(\mathbf{r},\bar{\omega})}{\sqrt{P}}e^{i\alpha\bar{\beta}z}, \tag{6.14b}$$

where $\alpha = 1$ and $\alpha = -1$ corespond to forward- and backward-propagating modes, respectively, $\bar{\omega} = \omega_a$ is the carrier frequency, and $\bar{\beta} = \beta(\bar{\omega})$. The second electromagnetic system is the full system consisting of the waveguide and optical cavities, described by $\epsilon_b(\mathbf{r}) = \epsilon_s(\mathbf{r}) + \delta\epsilon_s(\mathbf{r})$, with $\epsilon_s(\mathbf{r})$ decomposed as per Eq. (6.1), and perturbed by linear and nonlinear optical effects described by the perturbation, $\delta\epsilon_s(\mathbf{r})$. In this second case, we choose the frequency $\omega_b = \omega$, such that $\omega \approx \bar{\omega}$. The corresponding perturbed solution is expressed as a superposition of waveguide and cavity modes:

$$\mathbf{E}_b(\mathbf{r},\omega_b) = \sum_{\sigma=\pm1} a_\sigma(z,\omega)\frac{\mathbf{e}_\sigma(\mathbf{r},\bar{\omega})}{\sqrt{P}}e^{i\sigma\bar{\beta}z}$$

$$+\sum_{p=1}^{N_c} a_p(\omega)\frac{\mathbf{e}_p(\mathbf{r},\bar{\omega}_p)}{\sqrt{W_p}}, \tag{6.15a}$$

$$\mathbf{H}_b(\mathbf{r},\omega_b) = \sum_{\sigma=\pm 1} a_\sigma(z,\omega)\frac{\mathbf{h}_\sigma(\mathbf{r},\bar{\omega})}{\sqrt{P}}e^{i\sigma\bar{\beta}z} + \sum_{p=1}^{N_c} a_p(\omega)\frac{\mathbf{h}_p(\mathbf{r},\bar{\omega}_p)}{\sqrt{W_p}}, \tag{6.15b}$$

where $a_\sigma(z,\omega)$ represent the slowly-varying amplitudes of the forward- ($\sigma = +$) and backward-propagating ($\sigma = -$) waveguide modes and $a_p(\omega)$ and $\bar{\omega}_p$ are the amplitude and resonance frequency of the optical mode of the pth cavity, respectively. Note that in order to achieve an efficient coupling between the waveguide and cavities, the condition $\bar{\omega}_p \simeq \bar{\omega}$ must be fulfilled.

If the transverse section, S, is extended to infinity, the line integral in the l.h.s. of Eq. (6.13) vanishes because both the waveguide and cavity modes decay exponentially to zero at infinity. Therefore, with the definitions introduced in Eqs. (6.14) and Eqs. (6.15), the l.h.s. of Eq. (6.13) ca be written as:

$$\frac{\partial}{\partial z}\int_{S_\infty} \mathbf{F}\cdot\hat{\mathbf{z}}dS = 4\alpha\frac{\partial a_\alpha(z)}{\partial z} + \sum_{p=1}^{N_c}\frac{a_p}{\sqrt{PW_p}}\frac{\partial}{\partial z}\int_{S_\infty}\left[\mathbf{e}_p\times\mathbf{h}_\alpha^* + \mathbf{e}_\alpha^*\times\mathbf{h}_p\right]e^{-i\alpha\bar{\beta}z}dS, \tag{6.16}$$

where the orthogonality relations for the waveguide modes have been used. This equation can be further simplified if one uses the Lorentz theorem expressed in Eq. (6.13), written for a waveguide mode described by Eqs. (6.14) (the "a" fields) and permittivity $\epsilon_a(\mathbf{r}) = \epsilon_w(\mathbf{r})$ and a cavity mode given by Eqs. (6.8) (the "b" fields) and permittivity $\epsilon_b(\mathbf{r}) = \epsilon_p(\mathbf{r})$. With this choice, Eq. (6.13) becomes:

$$\frac{\partial}{\partial z}\int_{S_\infty}\left[\mathbf{e}_p\times\mathbf{h}_\alpha^* + \mathbf{e}_\alpha^*\times\mathbf{h}_p\right]e^{-i\alpha\bar{\beta}z}dS = ie^{-i\alpha\bar{\beta}z} \times\int_{S_\infty}\left[\mu_0(\bar{\omega}_p-\bar{\omega})\mathbf{h}_\alpha^*\cdot\mathbf{h}_p + (\bar{\omega}_p\bar{\epsilon}_p - \bar{\omega}\bar{\epsilon}_w)\mathbf{e}_\alpha^*\cdot\mathbf{e}_p\right]dS, \tag{6.17}$$

where $\bar{\epsilon}_p = \epsilon_p(\mathbf{r}, \bar{\omega}_p)$ and $\bar{\epsilon}_w = \epsilon_w(\mathbf{r}, \bar{\omega})$. By combining Eqs. (6.16) and (6.17) one arrives to the relation:

$$\frac{\partial}{\partial z}\int_{S_\infty} \mathbf{F}\cdot\hat{\mathbf{z}}dS = 4\alpha\frac{\partial a_\alpha(z)}{\partial z} + i\sum_{p=1}^{N_c} a_p \frac{e^{-i\alpha\bar{\beta}z}}{\sqrt{PW_p}} \times \int_{S_\infty} \left[\mu_0(\bar{\omega}_p - \bar{\omega})\mathbf{h}_\alpha^*\cdot\mathbf{h}_p + (\bar{\omega}_p\bar{\epsilon}_p - \bar{\omega}\bar{\epsilon}_w)\mathbf{e}_\alpha^*\cdot\mathbf{e}_p\right] dS. \tag{6.18}$$

On the other hand, by inserting Eqs. (6.14) and (6.15) in the r.h.s. of Eq. (6.13), one arrives to the following relation:

$$\begin{aligned} & i\int_{S_\infty} \left[\mu_0(\omega_b - \omega_a)\mathbf{H}_a^*\cdot\mathbf{H}_b + (\omega_b\epsilon_b - \omega_a\epsilon_a)\mathbf{E}_a^*\cdot\mathbf{E}_b\right] dS \\ & = i\sum_{\sigma=\pm1} a_\sigma \frac{e^{i(\sigma-\alpha)\bar{\beta}z}}{P}\int_{S_\infty}\left[\mu_0(\omega-\bar{\omega})\mathbf{h}_\alpha^*\cdot\mathbf{h}_\sigma \right. \\ & \left. +(\omega\epsilon_s + \omega\delta\epsilon_s - \bar{\omega}\bar{\epsilon}_w)\mathbf{e}_\alpha^*\cdot\mathbf{e}_\sigma\right] dS + i\sum_{p=1}^{N_c} a_p\frac{e^{-i\alpha\bar{\beta}z}}{\sqrt{PW_p}} \\ & \times\int_{S_\infty}\left[\mu_0(\omega-\bar{\omega})\mathbf{h}_\alpha^*\cdot\mathbf{h}_p + (\omega\epsilon_s+\omega\delta\epsilon_s-\bar{\omega}\bar{\epsilon}_w)\mathbf{e}_\alpha^*\cdot\mathbf{e}_p\right] dS. \end{aligned} \tag{6.19}$$

Combining Eqs. (6.13), Eqs. (6.18), and (6.19), we obtain the equation describing the dynamics of the waveguide field amplitudes in the frequency domain:

$$\begin{aligned} \alpha\frac{\partial a_\alpha}{\partial z} &= i\sum_{\sigma=\pm1} a_\sigma\frac{e^{i(\sigma-\alpha)\bar{\beta}z}}{4P}\int_{S_\infty}\left[\mu_0(\omega-\bar{\omega})\mathbf{h}_\alpha^*\cdot\mathbf{h}_\sigma \right. \\ &\left. +(\omega\epsilon_s - \bar{\omega}\bar{\epsilon}_w)\mathbf{e}_\alpha^*\cdot\mathbf{e}_\sigma\right] dS + i\sum_{p=1}^{N_c} a_p\frac{e^{-i\alpha\bar{\beta}z}}{4\sqrt{PW_p}} \\ &\times\int_{S_\infty}\left[\mu_0(\omega-\bar{\omega}_p)\mathbf{h}_\alpha^*\cdot\mathbf{h}_p + (\omega\epsilon_s-\bar{\omega}_p\bar{\epsilon}_p)\mathbf{e}_\alpha^*\cdot\mathbf{e}_p\right] dS \\ &+ i\frac{\omega}{4}\int_{S_\infty}\frac{\mathbf{e}_\alpha^*}{\sqrt{P}}e^{-i\alpha\bar{\beta}z}\cdot\delta\epsilon_s\left(\sum_{\sigma=\pm1} a_\sigma\frac{\mathbf{e}_\sigma}{\sqrt{P}}e^{i\sigma\bar{\beta}z}\right. \\ &\left. + \sum_{p=1}^{N_c} a_p\frac{\mathbf{e}_p}{\sqrt{W_p}}\right) dS. \end{aligned} \tag{6.20}$$

Note that the integrand in the last term of the r.h.s. of this equation represents the scalar

product between the unperturbed waveguide mode and the perturbation polarization, namely $\mathbf{E}_\alpha^* \cdot \mathbf{P}_{\text{pert}}$.

Using Eq. (6.1), we can derive the following relation:

$$\begin{aligned}\omega\epsilon_s - \bar{\omega}\bar{\epsilon}_w &= \omega\epsilon_w - \bar{\omega}\bar{\epsilon}_w + \omega\sum_{p=1}^{N_c}\epsilon_p^d \\ &= \sum_{n\geq 1}\frac{(\omega-\bar{\omega})^n}{n!}\left.\frac{\partial^n(\omega\epsilon_w)}{\partial\omega^n}\right|_{\bar{\omega}} + \omega\sum_{p=1}^{N_c}\epsilon_p^d. \end{aligned} \tag{6.21}$$

Similarly, Eq. (6.2) can be used to establish the following equation:

$$\begin{aligned}\omega\epsilon_s - \bar{\omega}_p\bar{\epsilon}_p &= \omega\epsilon_p - \bar{\omega}_p\bar{\epsilon}_p + \omega\sum_{q\neq p}\epsilon_q^d + \omega\epsilon_w^d \\ &= \sum_{n\geq 1}\frac{(\omega-\bar{\omega}_p)^n}{n!}\left.\frac{\partial^n(\omega\epsilon_p)}{\partial\omega^n}\right|_{\bar{\omega}_p} + \omega\tilde{\epsilon}_p^d + \omega\epsilon_w^d. \end{aligned} \tag{6.22}$$

Here, we have introduced the notation $\tilde{\epsilon}_p^d = \sum_{q\neq p}\epsilon_q^d$, which describes all the cylinders filling the holes of the cavities, except for those defining the pth cavity.

Inserting Eqs. (6.21) and (6.22) in Eq. (6.20), one can write the equation governing the dependence of the waveguide mode amplitudes on the propagation distance as:

$$\begin{aligned}\alpha\frac{\partial a_\alpha}{\partial z} &= i\sum_{n\geq 1}(\omega-\bar{\omega})^n\frac{\beta_\alpha^{(n)}}{n!}a_\alpha + i\sum_{\sigma\neq\alpha}\sum_{n\geq 1}(\omega-\bar{\omega})^n\frac{\beta_{\alpha\sigma}^{(n)}}{n!}a_\sigma \\ &+ i\omega\sum_\sigma c_{\alpha\sigma}a_\sigma + i\sum_{p=1}^{N_c}(\omega-\bar{\omega}_p)c_{\alpha,p}^c a_p + i\omega\sum_{p=1}^{N_c}c_{\alpha,p}^w a_p \\ &+ i\omega\sum_{p=1}^{N_c}c_{\alpha,p}a_p + i\frac{\omega}{4}\int_{S_\infty}\mathbf{E}_\alpha^*\cdot\mathbf{P}_{\text{pert}}dS. \end{aligned} \tag{6.23}$$

The dispersion coefficients $\beta_\alpha^{(n)}$ and $\beta_{\alpha\sigma}^{(n)}$ in this equation are the nth order, z-dependent, mode dispersion and cross-mode dispersion coefficients, respectively, and are defined by

the following formulae:

$$\beta_{\alpha}^{(1)}(z) = \frac{\delta_{\alpha}(z)}{v_{g,\alpha}}, \tag{6.24a}$$

$$\beta_{\alpha}^{(n)}(z) = \delta_{\alpha}(z)\frac{\partial^{n-1}}{\partial\omega^{n-1}}\left(\frac{1}{v_{g,\alpha}}\right),\ n \geq 2, \tag{6.24b}$$

where

$$\delta_{\alpha}(z) = \frac{a}{4\mathcal{W}}\int_{S_{\infty}}\left[\mu_0|\mathbf{h}_{\alpha}|^2 + \left.\frac{\partial(\omega\epsilon_w)}{\partial\omega}\right|_{\bar{\omega}}|\mathbf{e}_{\alpha}|^2\right]dS, \tag{6.25}$$

and

$$\begin{aligned}\beta_{\alpha\sigma}^{(1)}(z) =& \frac{ae^{i(\sigma-\alpha)\bar{\beta}z}}{4v_g\mathcal{W}}\int_{S_{\infty}}[\mu_0\mathbf{h}_{\alpha}^{*}\cdot\mathbf{h}_{\sigma} \\ &+ \left.\frac{\partial(\omega\epsilon_w)}{\partial\omega}\right|_{\bar{\omega}}\mathbf{e}_{\alpha}^{*}\cdot\mathbf{e}_{\sigma}\Big]dS, \quad \alpha \neq \sigma,\end{aligned} \tag{6.26a}$$

$$\beta_{\alpha\sigma}^{(n)}(z) = \frac{\partial^{n-1}\beta_{\alpha\sigma}^{(1)}}{\partial\omega^{n-1}},\ n \geq 2, \quad \alpha \neq \sigma. \tag{6.26b}$$

Since $\frac{1}{a}\int_{z_0}^{z_0+z}\delta_{\alpha}(z)dz = 1$, one can easily see that the averaged dispersion coefficient, defined as $\tilde{\beta}_{\alpha}^{(1)} \equiv \frac{1}{a}\int_{z_0}^{z_0+z}\beta_{\alpha}^{(1)}(z)dz = \frac{1}{v_{g,\alpha}}$, is the first-order waveguide dispersion coefficient characterizing waveguides with uniform cross-section.

Moreover, the coupling coefficients in Eq. (6.23) are defined as:

$$c_{\alpha\sigma}(z) = \frac{ae^{i(\sigma-\alpha)\bar{\beta}z}}{4v_g\mathcal{W}}\int_{S_{\infty}}\left(\sum_{p=1}^{N_c}\epsilon_p^d\right)\mathbf{e}_{\alpha}^{*}\cdot\mathbf{e}_{\sigma}dS, \tag{6.27a}$$

$$\begin{aligned}c_{\alpha,p}^{c}(z) =& \frac{e^{-i\alpha\bar{\beta}z}}{4\sqrt{PW_p}}\int_{S_{\infty}}[\mu_0\mathbf{h}_{\alpha}^{*}\cdot\mathbf{h}_{p} \\ &+ \left.\frac{\partial(\omega\epsilon_p)}{\partial\omega}\right|_{\bar{\omega}_p}\mathbf{e}_{\alpha}^{*}\cdot\mathbf{e}_{p}\Big]dS,\end{aligned} \tag{6.27b}$$

$$c_{\alpha,p}^{w}(z) = \frac{e^{-i\alpha\bar{\beta}z}}{4\sqrt{PW_p}}\int_{S_{\infty}}\epsilon_w^d\mathbf{e}_{\alpha}^{*}\cdot\mathbf{e}_{p}dS, \tag{6.27c}$$

$$c_{\alpha,p}(z) = \frac{e^{-i\alpha\bar{\beta}z}}{4\sqrt{PW_p}}\int_{S_{\infty}}\tilde{\epsilon}_p^d\mathbf{e}_{\alpha}^{*}\cdot\mathbf{e}_{p}dS. \tag{6.27d}$$

They describe the linear optical coupling between the optical waveguide modes and between the waveguide modes and cavities, which is solely due to perturbations in the configuration of the PhC. In particular, $c_{\alpha\sigma}$ quantifies the strength of the coupling between the α- and σ-mode, mediated by the presence of the cavities, $c^{c}_{\alpha,p}$ describes the frequency dispersion of the coupling between the waveguide mode and the mode of the pth cavity, $c^{w}_{\alpha,p}$ describes the strength of the coupling between the waveguide mode and the mode of the pth cavity, and $c_{\alpha,p}$ quantifies the influence of all the cavities other than the pth cavity onto the coupling between the waveguide mode and the mode of the pth cavity. The contribution from the qth cavity to the latter coefficient is negligibly small if the distance between the pth and qth cavities is relatively large, as in this case the overlap between the functions $\epsilon^{d}_{q}(\mathbf{r})$ and $\mathbf{e}_{p}(\mathbf{r})$ is vanishingly small.

In the last two steps of our derivation we first evaluate the contribution of the last term in Eq. (6.23) on the mode amplitude dynamics then transform this equation in the time domain. The perturbation polarization can be decomposed as the sum between the contribution of the linear polarization, induced by FC generation and intrinsic loss, and the nonlinear polarization. The variation of the permittivity related to the former contribution to the perturbation polarization can be written as:

$$\delta\epsilon_{\mathrm{lin}} = \delta\epsilon_{\mathrm{fc}} + \delta\epsilon_{\mathrm{loss}} = \delta\epsilon_{\mathrm{fc},w} + \sum_{p=1}^{N_c} \delta\epsilon^{d}_{\mathrm{fc},p} + \delta\epsilon_{\mathrm{loss}}, \tag{6.28}$$

where the permittivity perturbation due to the generation of FCs, $\delta\epsilon_{\mathrm{fc}}$, has been decomposed in a way similar to that indicated by Eq. (6.1). The first two terms in the r.h.s. of Eq. (6.28) are defined as:

$$\delta\epsilon_{\mathrm{fc},w}(\mathbf{r}) = \left(2\epsilon_0 n\delta n^{w}_{\mathrm{fc}} + i\frac{\epsilon_0 cn}{\omega}\alpha^{w}_{\mathrm{fc}}\right)\Sigma_{w}(\mathbf{r}), \tag{6.29a}$$

$$\sum_{p=1}^{N_c} \delta\epsilon^{d}_{\mathrm{fc},p} = \sum_{p=1}^{N_c} \left(2\epsilon_0 n\delta n^{p}_{\mathrm{fc}} + i\frac{\epsilon_0 cn}{\omega}\alpha^{p}_{\mathrm{fc}}\right)\Sigma^{d}_{p}(\mathbf{r}) \equiv \delta\tilde{\epsilon}^{d}_{\mathrm{fc}}(\mathbf{r}), \tag{6.29b}$$

where $\delta n^{w}_{\mathrm{fc}}$ and α^{w}_{fc} are the variation of the index of refraction and FC loss coefficient

induced by the FCs generated in the waveguide region, $\delta n_{\rm fc}^p$ and $\alpha_{\rm fc}^p$ are, respectively, have similar meaning but they correspond to the perturbation domain that defines the pth cavity, and $\Sigma_w(\mathbf{r})$ and $\Sigma_p^d(\mathbf{r})$ are the characteristic functions associated to the waveguide domain and the perturbation domain that defines the pth cavity, respectively (see also Fig. 6.3). The quantities $\delta n_{\rm fc}^w$ and $\alpha_{\rm fc}^w$ depend on the FC density in the waveguide, $N_w(z,t)$, whereas $\delta n_{\rm fc}^p$ and $\alpha_{\rm fc}^p$ are related to the FC density in the pth cavity, $N_p(t)$, as described by Eqs. (2.13). The FC density in the waveguide region can be written as $N_w(z,t) = N_+(z,t) + N_-(z,t)$, where $N_\pm(z,t)$ are the FC densities generated by the forward- and backward-propagating modes.

Based on these considerations, the contribution of the linear part of the perturbation polarization, $\delta\mathbf{P}_{\rm lin}$, to the r.h.s. of Eqs. (6.23) can be expressed as:

$$\begin{aligned} i\frac{\omega}{4}\int_{S_\infty}\mathbf{E}_\alpha^*\cdot\delta\mathbf{P}_{\rm lin}dS &= i\frac{\omega e^{-i\alpha\bar{\beta}z}}{4\sqrt{P}}\int_{S_\infty}\delta\epsilon_{\rm lin}\mathbf{e}_\alpha^* \\ &\cdot\left[\sum_{\sigma=\pm1}a_\sigma\frac{\mathbf{e}_\sigma}{\sqrt{P}}e^{i\sigma\bar{\beta}z}+\sum_{p=1}^{N_c}a_p\frac{\mathbf{e}_p}{\sqrt{W_p}}\right]dS \\ &= i\omega\left[\sum_{\sigma=\pm1}\left(\theta_{\alpha\sigma}^w+\theta_{\alpha\sigma}^c\right)a_\sigma+\sum_{p=1}^{N_c}\left(\theta_{\alpha,p}^w+\theta_{\alpha,p}^c\right)a_p\right], \end{aligned} \tag{6.30}$$

where the coefficients in this equation are defined as:

$$\theta_{\alpha\sigma}^w(z) = \frac{ae^{i(\sigma-\alpha)\bar{\beta}z}}{4v_g\mathcal{W}}\int_{S_\infty}\left(\delta\epsilon_{{\rm fc},w}+\delta\epsilon_{\rm loss}\right)\mathbf{e}_\alpha^*\cdot\mathbf{e}_\sigma dS, \tag{6.31a}$$

$$\theta_{\alpha\sigma}^c(z) = \frac{ae^{i(\sigma-\alpha)\bar{\beta}z}}{4v_g\mathcal{W}}\int_{S_\infty}\delta\tilde{\epsilon}_{\rm fc}^d\mathbf{e}_\alpha^*\cdot\mathbf{e}_\sigma dS, \tag{6.31b}$$

$$\theta_{\alpha,p}^w(z) = \frac{e^{-i\alpha\bar{\beta}z}}{4\sqrt{PW_p}}\int_{S_\infty}\left(\delta\epsilon_{{\rm fc},w}+\delta\epsilon_{\rm loss}\right)\mathbf{e}_\alpha^*\cdot\mathbf{e}_p dS, \tag{6.31c}$$

$$\theta_{\alpha,p}^c(z) = \frac{e^{-i\alpha\bar{\beta}z}}{4\sqrt{PW_p}}\int_{S_\infty}\delta\tilde{\epsilon}_{\rm fc}^d\mathbf{e}_\alpha^*\cdot\mathbf{e}_p dS. \tag{6.31d}$$

In these equations, $\theta_{\alpha\sigma}^w$ describes the coupling between the waveguide modes via the intrinsic loss and FCs generated in the waveguide region, $\theta_{\alpha\sigma}^c$ measures the mutual interaction between the waveguide modes mediated by the FCs generated in the cavities, $\theta_{\alpha,p}^w$

quantifies the strength of the coupling between the waveguide modes and the mode of the pth cavity via the intrinsic loss and FCs generated in the waveguide region, and $\theta^c_{\alpha,p}$ determines the coupling between the waveguide modes and the mode of the pth cavity via the FCs generated in all of the cavities. Because of the evanescent nature of the cavity modes, this last effect is chiefly determined by the FCs generated in the pth cavity.

The contribution of the nonlinear polarization, $\delta\mathbf{P}_{\rm nl}$, to the r.h.s. of Eqs. (6.23) can more conveniently be calculated directly in the time domain. For this, we introduce first the time-domain envelopes of the waveguide and cavity modes, $A_\alpha(z,t)$, $\alpha = \pm 1$, and $A_p(t)$, $p = 1, \ldots, N_c$, defined by the relations:

$$A_\alpha(z,t) = \int_0^\infty a_\alpha(z,\omega) e^{-i(\omega-\bar{\omega})t} d\omega, \quad \alpha = \pm 1, \tag{6.32a}$$

$$A_p(t) = \int_0^\infty a_p(\omega) e^{-i(\omega-\bar{\omega}_p)t} d\omega, \quad p = 1, \ldots, N_c. \tag{6.32b}$$

Note that in these relations the carrier frequencies, $\bar{\omega}$ and $\bar{\omega}_p$, have been incorporated in the Fourier transform, so that the amplitudes $A_\alpha(z,t)$ and $A_p(t)$ vary slowly in time. Since the fast-varying term $e^{i\alpha\bar{\beta}z}$ has also been factored out, $A_\alpha(z,t)$ is a slowly-varying function with the propagation distance, z, too.

With these definitions, the optical field in the coupled waveguide-cavities system can be expressed as:

$$\begin{aligned}\mathbf{E}(\mathbf{r},t) = \frac{1}{2}\Bigg[&\sum_{\sigma=\pm1} \frac{\mathbf{e}_\sigma(\mathbf{r},\bar{\omega})}{\sqrt{P}} e^{i(\sigma\bar{\beta}z-\bar{\omega}t)} A_\sigma(z,t) \\ &+ \sum_{p=1}^{N_c} \frac{\mathbf{e}_p(\mathbf{r},\bar{\omega}_p)}{\sqrt{W_p}} e^{-i\bar{\omega}_p t} A_p(t)\Bigg] + c.c. \equiv \frac{1}{2}\Bigg[\sum_{\sigma=\pm1} \mathbf{E}^{(+)}_\sigma(\mathbf{r},t) \\ &+ \sum_{p=1}^{N_c} \mathbf{E}^{(+)}_p(\mathbf{r},t)\Bigg] + c.c.,\end{aligned} \tag{6.33}$$

where "*c.c.*" stands for complex conjugate and the positive- and negative-frequency parts of the spectrum have been explicitly separated.

Inserting this formula in Eq. (6.10), one can easily derive the expression for the non-

linear polarization that affects the waveguide modes:

$$\delta\mathbf{P}_{\mathrm{nl},w}(\mathbf{r},t) = \frac{3}{4}\epsilon_0\hat{\chi}^{(3)}(\mathbf{r})\vdots\left\{\mathbf{E}_w^{(+)}(\mathbf{r},t)\left[\mathbf{E}_w^{(+)}(\mathbf{r},t)\mathbf{E}_w^{(-)}(\mathbf{r},t)\right.\right.$$
$$\left.+2\sum_{p=1}^{N_c}\mathbf{E}_p^{(+)}(\mathbf{r},t)\mathbf{E}_p^{(-)}(\mathbf{r},t)\right] + \sum_{p=1}^{N_c}\mathbf{E}_p^{(+)}(\mathbf{r},t)$$
$$\left.\left[\mathbf{E}_p^{(+)}(\mathbf{r},t)\mathbf{E}_p^{(-)}(\mathbf{r},t) + 2\mathbf{E}_w^{(+)}(\mathbf{r},t)\mathbf{E}_w^{(-)}(\mathbf{r},t)\right]\right\}, \tag{6.34}$$

where $\mathbf{E}_w^{(\pm)}(\mathbf{r},t) = \sum_{\sigma=\pm1}\mathbf{E}_\sigma^{(\pm)}(\mathbf{r},t)$ is the total field in the waveguide oscillating at the carrier frequency, $\pm\bar{\omega}$. In this formula, the first and third terms describe self-modulation effects, whereas the second and last terms govern the cross-phase interactions between the fields in the waveguide and cavities.

Regarding Eq. (6.34), two observations are needed to better clarify the assumptions on which it is based. First, we retained terms oscillating at the carrier frequency of the waveguide pulses, $\bar{\omega}$, and the frequencies of the cavities, $\bar{\omega}_p$, $p = 1,\ldots,N_c$, because we assumed that the difference between these frequencies is very small. Second, we neglected the cross-phase modulation effects associated to the fields of different cavities because of the evanescent nature of the cavity modes.

We now have all the ingredients needed to establish the formula that describes the dynamics of the waveguide mode amplitudes. Thus, by Fourier transforming Eq. (6.23) to the time domain and using Eq. (6.30) and Eq. (6.34), we arrive to the following partial differential equation for the waveguide mode amplitudes, $A_\alpha(z,t)$, $\alpha = \pm1$:

$$i\alpha\frac{\partial A_\alpha}{\partial z} + \sum_{n\geq1}\frac{\beta_\alpha^{(n)}}{n!}\left(i\frac{\partial}{\partial t}\right)^n A_\alpha + \sum_{\sigma\neq\alpha}\sum_{n\geq1}\frac{\beta_{\alpha\sigma}^{(n)}}{n!}\left(i\frac{\partial}{\partial t}\right)^n A_\sigma$$
$$+\sum_{\sigma=\pm1}\bar{\omega}\left(c_{\alpha\sigma}+\theta_{\alpha\sigma}^w+\theta_{\alpha\sigma}^c\right)A_\sigma + \sum_{p=1}^{N_c}e^{-i(\bar{\omega}_p-\bar{\omega})t}$$
$$\times\left[c_{\alpha,p}^c i\frac{dA_p}{dt} + \bar{\omega}_p\left(c_{\alpha,p}^w + c_{\alpha,p} + \theta_{\alpha,p}^w + \theta_{\alpha,p}^c\right)A_p\right]$$
$$+\sum_{\vec{\sigma}}\gamma_{\alpha,\vec{\sigma}}A_{\sigma_1}A_{\sigma_2}A_{\sigma_3}^* + 2\sum_{\sigma=\pm1}\left(\sum_{p=1}^{N_c}\gamma_{\alpha,\sigma p}|A_p|^2\right)A_\sigma$$

$$+\sum_{p=1}^{N_c} e^{-i(\bar{\omega}_p-\bar{\omega})t}\left[2\sum_{\sigma_1,\sigma_2=\pm1}\gamma_{\alpha,\sigma_1\sigma_2 p}A_{\sigma_1}A^*_{\sigma_2}\right.$$
$$\left.+\,\gamma_{\alpha,p}|A_p|^2\right]A_p=0, \tag{6.35}$$

where the notation $\sum_{\vec{\sigma}} \equiv \sum_{\sigma_1=\pm1}\sum_{\sigma_2=\pm1}\sum_{\sigma_3=\pm1}$ has been introduced. In this equation, the nonlinear coefficients that describe the nonlinear interactions between the waveguide modes and between waveguide and cavity modes are defined as:

$$\gamma_{\alpha,\vec{\sigma}}(z)=\frac{3\epsilon_0\bar{\omega}a^2e^{i(\sigma_1+\sigma_2-\sigma_3-\alpha)\bar{\beta}z}}{16v_g^2\mathcal{W}^2}\int_{S_\infty}\mathbf{e}^*_\alpha\cdot\hat{\chi}^{(3)}\vdots\mathbf{e}_{\sigma_1}\mathbf{e}_{\sigma_2}\mathbf{e}^*_{\sigma_3}dS, \tag{6.36a}$$

$$\gamma_{\alpha,\sigma p}(z)=\frac{3\epsilon_0\bar{\omega}ae^{i(\sigma-\alpha)\bar{\beta}z}}{16v_g\mathcal{W}W_p}\int_{S_\infty}\mathbf{e}^*_\alpha\cdot\hat{\chi}^{(3)}\vdots\mathbf{e}_{\sigma}\mathbf{e}_{p}\mathbf{e}^*_{p}dS, \tag{6.36b}$$

$$\gamma_{\alpha,\sigma_1\sigma_2 p}(z)=\frac{3\epsilon_0\bar{\omega}a^{3/2}e^{i(\sigma_1-\sigma_2-\alpha)\bar{\beta}z}}{16v_g^{3/2}\mathcal{W}\sqrt{\mathcal{W}W_p}}\int_{S_\infty}\mathbf{e}^*_\alpha\cdot\hat{\chi}^{(3)}\vdots\mathbf{e}_{\sigma_1}\mathbf{e}^*_{\sigma_2}\mathbf{e}^*_{p}dS, \tag{6.36c}$$

$$\gamma_{\alpha,p}(z)=\frac{3\epsilon_0\bar{\omega}a^{1/2}e^{-i\alpha\bar{\beta}z}}{16v_g^{1/2}W_p\sqrt{\mathcal{W}W_p}}\int_{S_\infty}\mathbf{e}^*_\alpha\cdot\hat{\chi}^{(3)}\vdots\mathbf{e}^*_{p}\mathbf{e}_{p}\mathbf{e}^*_{p}dS. \tag{6.36d}$$

More specifically, $\gamma_{\alpha,\vec{\sigma}}$ describes the four-wave mixing of waveguide modes, $\gamma_{\alpha,\sigma p}$ and $\gamma_{\alpha,\sigma_1\sigma_2 p}$ quantify the strength of the cross-phase modulation between waveguide and cavity modes, whereas $\gamma_{\alpha,p}$ describes the influence on the waveguide modes of the Kerr effects induced in the pth cavity.

The nonlinear optical coefficients defined by Eqs. (6.36) depend on the propagation distance, z, through the phase factors multiplying the integrals and the integrals themselves. The latter dependence is due to the fact that the waveguide and cavity modes are z-dependent. The phase factors are rapidly oscillating functions and therefore the nonlinear coefficients are negligibly small except when the interacting modes are phase-matched. For example, the first nonlinear coefficient in Eqs. (6.36) can be neglected except when the phase-matching condition $\sigma_1+\sigma_2-\sigma_3-\alpha=0$ is satisfied. Incidentally, the phase factors of the last two nonlinear optical coefficients cannot be phase matched, and therefore the corresponding terms in Eq. (6.35) can be neglected. Moreover, the values of the integrals in Eqs. (6.36) are maximized when there is an optimum overlap

between the optical fields. As a result, the dominant nonlinear coefficient is $\gamma_{\alpha,\vec{\sigma}}$ and its maximum value is attained when the interacting modes are phase-matched.

It should be noted that when Fourier transforming Eq. (6.23) to the time domain we used the following relations, which can be easily established:

$$\int_0^\infty \omega a_\sigma e^{-i(\omega-\bar{\omega})t}\, d\omega = i\frac{\partial A_\sigma}{\partial t} + \bar{\omega} A_\sigma \simeq \bar{\omega} A_\sigma, \tag{6.37a}$$

$$\begin{aligned}\int_0^\infty \omega a_p e^{-i(\omega-\bar{\omega})t}\, d\omega &= \left(i\frac{dA_p}{dt} + \bar{\omega}_p A_p\right) e^{-i(\bar{\omega}_p-\bar{\omega})t} \\ &\simeq \bar{\omega} A_p e^{-i(\bar{\omega}_p-\bar{\omega})t}.\end{aligned} \tag{6.37b}$$

6.4.2 Dynamical equations for the evolution of cavity mode amplitudes

We now switch our attention to the derivation of the equations describing the time evolution of the cavity mode amplitudes. As in the previous case, we use the conjugated form of the Lorentz theorem applied for two electromagnetic configurations: the first configuration ("a") corresponds to the isolated qth cavity described by the fields in Eqs. (6.8) and permittivity $\epsilon_a(\mathbf{r}) = \epsilon_q(\mathbf{r})$, whereas the second configuration ("b") corresponds to the coupled waveguide-cavity system and is characterized by the fields given in Eqs. (6.15) and permittivity $\epsilon_b(\mathbf{r}) = \epsilon_s(\mathbf{r}) + \delta\epsilon_s(\mathbf{r})$. The frequency in the two configurations is $\bar{\omega}_q$ and ω, respectively.

More specifically, the permittivity distribution of the coupled waveguide-cavities system, expressed in terms of the qth cavity, takes the following form:

$$\begin{aligned}\epsilon_s(\mathbf{r}) &= \epsilon_q(\mathbf{r}) + \sum_{r\neq q} \epsilon_r^d(\mathbf{r}) + \epsilon_w^d(\mathbf{r}) \\ &= \epsilon_q(\mathbf{r}) + \tilde{\epsilon}_q^d(\mathbf{r}) + \epsilon_w^d,\end{aligned} \tag{6.38}$$

which describes all the cavities other than the qth cavity and the waveguide as perturbations to the unperturbed system. Then, the dielectric function for the perturbed system

configuration is $\epsilon_b = \epsilon_s(\mathbf{r},\omega)+\delta\epsilon_s(\mathbf{r},\omega)$, whereby $\delta\epsilon_s(\mathbf{r},\omega)$ describes the influence of linear and nonlinear polarization effects.

We now choose a domain, V_q, centered on the qth cavity, which is large enough that the fields of the cavity mode become vanishingly small on its boundary, ∂V_q. Then, the divergence theorem applied to the vector field $\mathbf{F} = \mathbf{E}_b \times \mathbf{H}_a^* + \mathbf{E}_a^* \times \mathbf{H}_b$ leads to the following relation:

$$\int_{V_q} \nabla \cdot \mathbf{F} dV = \oint_{\partial V_q} \mathbf{F} \cdot d\mathbf{S} = 0. \tag{6.39}$$

Using the Maxwell equations for harmonic fields, we can cast this equation to the form:

$$\int_{V_q} \left[\mu_0(\omega_b - \omega_a)\mathbf{H}_a^* \cdot \mathbf{H}_b + (\omega_b\epsilon_b - \omega_a\epsilon_a)\mathbf{E}_a^* \cdot \mathbf{E}_b\right] d\mathbf{r} = 0. \tag{6.40}$$

With the specific expressions for the "a" and "b" fields, given by Eqs. (6.8) and Eqs. (6.15), respectively, this equation can be written as:

$$\begin{aligned}
&\mu_0(\omega - \bar{\omega}_q)\left(\sum_{\sigma=\pm1}\int_{V_q}\frac{a_\sigma e^{i\sigma\bar{\beta}z}}{\sqrt{PW_q}}\mathbf{h}_q^*\cdot\mathbf{h}_\sigma d\mathbf{r}\right.\\
&\left.+\sum_{p=1}^{N_c} a_p\int_{V_q}\frac{1}{\sqrt{W_qW_p}}\mathbf{h}_q^*\cdot\mathbf{h}_p d\mathbf{r}\right)+\sum_{\sigma=\pm1}\int_{V_q}\frac{a_\sigma e^{i\sigma\bar{\beta}z}}{\sqrt{PW_q}}\\
&\times(\omega\epsilon_s+\omega\delta\epsilon_s-\bar{\omega}_q\bar{\epsilon}_q)\mathbf{e}_q^*\cdot\mathbf{e}_\sigma d\mathbf{r}+\sum_{p=1}^{N_c}a_p\int_{V_\infty}\frac{1}{\sqrt{W_qW_p}}\\
&\times(\omega\epsilon_s+\omega\delta\epsilon_s-\bar{\omega}_q\bar{\epsilon}_q)\mathbf{e}_q^*\cdot\mathbf{e}_p d\mathbf{r}=0.
\end{aligned} \tag{6.41}$$

The integral of an arbitrary vector function, $\mathbf{A}(\mathbf{r})$, over the volume V_q can be expressed as $\int_{V_q}\mathbf{A}(\mathbf{r})d\mathbf{r} = \int_{-l_q}^{l_q}\int_{S_\infty}\mathbf{A}(\mathbf{r})dzdS$, where S_∞ is the transverse cross-section of the qth cavity and $2l_q$ is the length of the qth cavity along the z-axis.

Let us now rewrite Eq. (6.22) in terms of the qth cavity, namely:

$$\omega\epsilon_s - \bar{\omega}_q\bar{\epsilon}_q = \sum_{n\geq1}\frac{(\omega-\bar{\omega}_q)^n}{n!}\left.\frac{\partial^n(\omega\epsilon_q)}{\partial\omega^n}\right|_{\bar{\omega}_q} + \omega\tilde{\epsilon}_q^d + \omega\epsilon_w^d. \tag{6.42}$$

Then, by inserting Eq. (6.42) into Eq. (6.41), we arrive at the following equation:

$$
\begin{aligned}
&i(\omega-\bar{\omega}_q)\sum_{\sigma=\pm1}\int_{-l_q}^{l_q}C^c_{\sigma,q}(z)a_\sigma dz + i\omega\sum_{\sigma=\pm1}\int_{-l_q}^{l_q}C^w_{\sigma,q}(z)a_\sigma dz \\
&+ i\omega\sum_{\sigma=\pm1}\int_{-l_q}^{l_q}C_{\sigma,q}(z)a_\sigma dz + i(\omega-\bar{\omega}_q)\sum_{p=1}^{N_c}C_{qp}a_p \\
&+ i\omega\sum_{p=1}^{N_c}(C^c_{q,p}+C^w_{qp})a_p + \frac{i\omega}{4\sqrt{W_q}}\int_{V_q}\mathbf{e}_q^*\cdot\mathbf{P}_{\text{pert}}dV = 0,
\end{aligned}
\tag{6.43}
$$

where we have used the fact that

$$
\mathbf{P}_{\text{pert}} = \delta\epsilon_s\left(\sum_{\sigma=\pm1}a_\sigma\frac{\mathbf{e}_\sigma}{\sqrt{P}}e^{i\sigma\bar{\beta}z} + \sum_{p=1}^{N_c}a_p\frac{\mathbf{e}_p}{\sqrt{W_p}}\right).
$$

The coefficients appearing in Eq. (6.43) are defined as follows:

$$
C^c_{\sigma,q}(z) = \frac{e^{i\sigma\bar{\beta}z}}{4\sqrt{PW_q}}\int_{S_\infty}\left[\mu_0\mathbf{h}_q^*\cdot\mathbf{h}_\sigma + \left.\frac{\partial(\omega\epsilon_q)}{\partial\omega}\right|_{\bar{\omega}_q}\mathbf{e}_q^*\cdot\mathbf{e}_\sigma\right]dS, \tag{6.44a}
$$

$$
C^w_{\sigma,q}(z) = \frac{e^{i\sigma\bar{\beta}z}}{4\sqrt{PW_q}}\int_{S_\infty}\epsilon_w^d\mathbf{e}_q^*\cdot\mathbf{e}_\sigma dS, \tag{6.44b}
$$

$$
C_{\sigma,q}(z) = \frac{e^{i\sigma\tilde{\beta}z}}{4\sqrt{PW_p}}\int_{S_\infty}\tilde{\epsilon}_q^d\mathbf{e}_q^*\cdot\mathbf{e}_\sigma dS, \tag{6.44c}
$$

$$
C_{qp} = \frac{1}{4\sqrt{W_qW_p}}\int_{V_q}\left[\mu_0\mathbf{h}_q^*\cdot\mathbf{h}_p + \left.\frac{\partial(\omega\epsilon_q)}{\partial\omega}\right|_{\bar{\omega}_q}\mathbf{e}_q^*\cdot\mathbf{e}_p\right]dV, \tag{6.44d}
$$

$$
C^c_{q,p} = \frac{1}{4\sqrt{W_qW_p}}\int_{V_q}\tilde{\epsilon}_q^d\mathbf{e}_q^*\cdot\mathbf{e}_p dV, \tag{6.44e}
$$

$$
C^w_{qp} = \frac{1}{4\sqrt{W_qW_p}}\int_{V_q}\epsilon_w^d\mathbf{e}_q^*\cdot\mathbf{e}_p dV. \tag{6.44f}
$$

By comparing Eqs. (6.27) and Eqs. (6.44) one can see that the coefficients c's and C's satisfy the following relations: $c^c_{\sigma,q} = C^{c*}_{\sigma,q}$, $c^w_{\sigma,q} = C^{w*}_{\sigma,q}$, and $c_{\sigma,q} = C^*_{\sigma,q}$.

The coefficients defined by Eqs. (6.44) describe the coupling between the optical mode of the qth cavity and the waveguide mode, as well as the coupling between the optical mode of the qth cavity and the optical modes of the remaining cavities. Thus, $C^c_{\sigma,q}$ determines the frequency dispersion of the optical coupling between the waveguide mode

and the optical mode of the qth cavity, $C^w_{\sigma,q}$ quantifies the strength of the coupling between the waveguide mode and the optical mode of the qth cavity, mediated by the waveguide, $C_{\sigma,q}$ determines the coupling between the waveguide mode and the optical mode of the qth cavity, mediated by the perturbation of all of the cavities, except the qth cavity, C_{qp} determines the frequency dispersion of the optical coupling between the qth and pth cavity modes, $C^c_{q,p}$ quantifies the strength of the coupling between the qth and pth cavity modes, mediated by all of the cavities except the qth one, and C^w_{qp} measures the strength of the coupling between the qth and pth cavity modes, mediated by the waveguide.

Similarly to the approach used to treat the dynamics of the waveguide mode amplitudes, we express the variation of the linear part of the electric permittivity, $\delta\epsilon_{\text{lin}}$, as follows:

$$\delta\epsilon_{\text{lin}} = \delta\epsilon_{\text{fc}} + \delta\epsilon_{\text{loss}} = \delta\epsilon_{\text{fc},q} + \delta\tilde{\epsilon}^d_{\text{fc},q} + \delta\epsilon^d_{\text{fc},w} + \delta\epsilon_{\text{loss}}, \tag{6.45}$$

in which $\delta\epsilon_{\text{fc},q}$, $\delta\tilde{\epsilon}^d_{\text{fc},q}$, and $\delta\epsilon^d_{\text{fc},w}$ are the variations of the permittivity due to the FCs generated inside the qth cavity, in the cylinders defining all the cavities except the qth one, and in the cylinders that form the waveguide, respectively. By using Eq. (6.45), the linear part of the polarization term in Eq. (6.43) can be written as:

$$\begin{aligned}\frac{i\omega}{4\sqrt{W_q}}\int_{V_q}\mathbf{e}^*_q\cdot\delta\mathbf{P}_{\text{lin}}dV = i\omega\Bigg\{\sum_{\sigma=\pm1}\int_{-l_q}^{l_q}\big[\theta^c_{q,\sigma}(z)+\theta_{q,\sigma}(z)\\ +\ \theta^w_{q,\sigma}(z)\big]\,a_\sigma dz+\sum_{p=1}^{N_c}(\theta^c_{qp}+\theta_{qp}+\theta^w_{qp})a_p\Bigg\},\end{aligned} \tag{6.46}$$

where the corresponding coefficients are defined as below:

$$\theta^c_{q,\sigma}(z) = \frac{e^{i\sigma\bar{\beta}z}}{4\sqrt{PW_q}}\int_{S_\infty}(\delta\epsilon_{\text{fc},q}+\delta\epsilon_{\text{loss}})\mathbf{e}^*_q\cdot\mathbf{e}_\sigma dS, \tag{6.47a}$$

$$\theta_{q,\sigma}(z) = \frac{e^{i\sigma\bar{\beta}z}}{4\sqrt{PW_q}}\int_{S_\infty}\delta\tilde{\epsilon}^d_{\text{fc},q}\mathbf{e}^*_q\cdot\mathbf{e}_\sigma dS, \tag{6.47b}$$

$$\theta^w_{q,\sigma}(z) = \frac{e^{i\sigma\bar{\beta}z}}{4\sqrt{PW_q}}\int_{S_\infty}\delta\epsilon^d_{\text{fc},w}\mathbf{e}^*_q\cdot\mathbf{e}_\sigma dS, \tag{6.47c}$$

$$\theta_{qp}^{c} = \frac{1}{4\sqrt{W_q W_p}} \int_{V_q} (\delta\epsilon_{\mathrm{fc},q} + \delta\epsilon_{\mathrm{loss}}) \mathbf{e}_q^* \cdot \mathbf{e}_p dV, \tag{6.47d}$$

$$\theta_{qp} = \frac{1}{4\sqrt{W_q W_p}} \int_{V_q} \delta\tilde{\epsilon}_{\mathrm{fc},q}^{d} \mathbf{e}_q^* \cdot \mathbf{e}_p dV, \tag{6.47e}$$

$$\theta_{qp}^{w} = \frac{1}{4\sqrt{W_q W_p}} \int_{V_q} \delta\epsilon_{\mathrm{fc},w}^{d} \mathbf{e}_q^* \cdot \mathbf{e}_p dV, \tag{6.47f}$$

The coefficients defined by the equations above have the following physical meaning: $\theta_{q,\sigma}^{c}$ describes the coupling between the optical mode of the qth cavity and the waveguide mode *via* the FCs generated in the cavity and the intrinsic loss in Si, $\theta_{q,\sigma}$ represents the coupling between the optical mode of the qth cavity and the waveguide mode, mediated by the FCs generated in the cylinders defining all the cavities in the system, except the qth one, $\theta_{q,\sigma}^{w}$ quantifies the strength of the coupling between the optical mode of the qth cavity and the waveguide mode, mediated by the FCs generated in the cylinders defining the waveguide, θ_{qp}^{c} describes the coupling between the optical modes of the qth and pth cavities *via* the FCs generated in the qth cavity and the intrinsic loss in Si, θ_{qp} represents the coupling between the optical modes of the qth and pth cavities, mediated by the FCs generated in the cylinders defining all the cavities in the system, except the qth one, and θ_{qp}^{w} quantifies the strength of the coupling between the optical mode of the qth cavity and the waveguide mode, mediated by the FCs generated in the cylinders defining the waveguide.

It should be noted that, due to the evanescent nature of the cavity modes, the coefficients θ_{qp}^{c}, θ_{qp}, and θ_{qp}^{w} are vanishingly small when the qth and pth cavities are separated by a relatively large distance. Moreover, the coupling coefficients defined by Eqs. (6.47) depend explicitly on the cavity modes $\mathbf{e}_q$ and $\mathbf{e}_p$, as well as the waveguide mode $\mathbf{e}_\sigma$; however, they depend implicitly on all of the optical modes present in the system as all these optical modes generate FCs.

Similarly to the case of the nonlinear polarization affecting the waveguide modes, described by Eq. (6.34), the nonlinear polarization affecting the qth cavity, $\delta\mathbf{P}_{\mathrm{nl},c}^{q}(\mathbf{r},t)$,

can be expresses as:

$$\delta\mathbf{P}^{q}_{\mathrm{nl},c}(\mathbf{r},t) = \frac{3}{4}\epsilon_0\hat{\chi}^{(3)}(\mathbf{r}) \vdots \left\{\mathbf{E}^{(+)}_{q}(\mathbf{r},t)\left[\mathbf{E}^{(+)}_{q}(\mathbf{r},t)\mathbf{E}^{(-)}_{q}(\mathbf{r},t)\right.\right.$$
$$\left. +2\mathbf{E}^{(+)}_{w}(\mathbf{r},t)\mathbf{E}^{(-)}_{w}(\mathbf{r},t)\right] + \mathbf{E}^{(+)}_{w}(\mathbf{r},t)\left[\mathbf{E}^{(+)}_{w}(\mathbf{r},t)\mathbf{E}^{(-)}_{w}(\mathbf{r},t)\right.$$
$$\left.\left. +2\mathbf{E}^{(+)}_{q}(\mathbf{r},t)\mathbf{E}^{(-)}_{q}(\mathbf{r},t)\right]\right\}. \tag{6.48}$$

In this equation, the first and the third terms describe self-phase modulation effects in the qth cavity and waveguide, respectively, whereas the second and last terms describe cross-phase modulation effects between the optical mode of the qth cavity and the waveguide mode. Note that the cross-phase modulation effects between the cavity modes can be neglected due to their evanescent nature.

We now have all the ingredients needed to establish the equation governing the dynamics of the amplitudes of the cavity modes. To this end, we insert Eq. (6.46) and Eq. (6.48) in Eq. (6.43) and Fourier transform the resulting equation into the time domain. Upon performing these mathematical manipulations, we arrive at the following equation, which holds for $q = 1, \ldots, N_c$:

$$\sum_{p=1}^{N_c} e^{-i(\bar{\omega}_p-\bar{\omega}_q)t}\left\{C_{qp}\left[i\frac{dA_p}{dt} + (\bar{\omega}_p-\bar{\omega}_q)A_p\right]\right.$$
$$\left. +\bar{\omega}_p(C^{c}_{q,p} + C^{w}_{qp} + \theta^{c}_{qp} + \theta_{qp} + \theta^{w}_{qp})A_p\right\} + \sum_{\sigma=\pm1} e^{-i(\bar{\omega}-\bar{\omega}_q)t}$$
$$\times \int_{-l_q}^{l_q} dz\left\{C^{c}_{\sigma,q}(z)\left[i\frac{dA_\sigma}{dt} + (\bar{\omega}-\bar{\omega}_q)A_\sigma\right]\right.$$
$$\left. + \bar{\omega}\left[C^{w}_{\sigma,q}(z) + C_{\sigma,q}(z) + \theta^{c}_{q,\sigma}(z) + \theta_{q,\sigma}(z) + \theta^{w}_{q,\sigma}(z)\right]A_\sigma\right\}$$
$$+ \Gamma_{q,q}|A_q|^2A_q + 2\left[\int_{-l_q}^{l_q} dz \sum_{\sigma_1,\sigma_2=\pm1} \Gamma_{q,\sigma_1\sigma_2 q}(z)A_{\sigma_1}A^{*}_{\sigma_2}\right]A_q$$
$$+ e^{-i(\bar{\omega}-\bar{\omega}_q)t}\left\{\int_{-l_q}^{l_q} dz \sum_{\vec{\sigma}} \Gamma_{q,\vec{\sigma}}(z)A_{\sigma_1}A^{*}_{\sigma_2}A_{\sigma_3}\right.$$
$$\left. +2\left[\int_{-l_q}^{l_q} dz \sum_{\sigma=\pm1} \Gamma_{q,\sigma}(z)A_\sigma\right]|A_q|^2\right\} = 0, \tag{6.49}$$

where the nonlinear optical coefficients Γ's entering in this equation are defined as:

$$\Gamma_{q,q} = \frac{3\epsilon_0\bar{\omega}_q}{16W_q^2}\int_{V_q}\mathbf{e}_q^*\cdot\hat{\chi}^{(3)}\vdots\mathbf{e}_q^*\mathbf{e}_q\mathbf{e}_q^* dV, \tag{6.50a}$$

$$\Gamma_{q,\sigma_1\sigma_2 q}(z) = \frac{3\epsilon_0\bar{\omega}_q a e^{i(\sigma_1-\sigma_2)\bar{\beta}z}}{16v_g\mathcal{W}W_q}\int_{S_\infty}\mathbf{e}_q^*\cdot\hat{\chi}^{(3)}\vdots\mathbf{e}_{\sigma_1}\mathbf{e}_{\sigma_2}^*\mathbf{e}_q^* dS, \tag{6.50b}$$

$$\Gamma_{q,\vec{\sigma}}(z) = \frac{3\epsilon_0\bar{\omega}_q a^{3/2} e^{i(\sigma_1-\sigma_2+\sigma_3)\bar{\beta}z}}{16(v_g\mathcal{W})^{3/2}W_q^{1/2}}\int_{S_\infty}\mathbf{e}_q^*\cdot\hat{\chi}^{(3)}\vdots\mathbf{e}_{\sigma_1}\mathbf{e}_{\sigma_2}^*\mathbf{e}_{\sigma_3} dS, \tag{6.50c}$$

$$\Gamma_{q,\sigma}(z) = \frac{3\epsilon_0\bar{\omega}_q a e^{i\sigma\bar{\beta}z}}{16v_g\mathcal{W}W_q}\int_{S_\infty}\mathbf{e}_q^*\cdot\hat{\chi}^{(3)}\vdots\mathbf{e}_\sigma\mathbf{e}_q\mathbf{e}_q^* dS, \tag{6.50d}$$

From a physical point of view, $\Gamma_{q,q}$ describes the Kerr effect on the optical mode of the qth cavity, $\Gamma_{q,\sigma_1\sigma_2 q}$ and $\Gamma_{q,\sigma}$ quantify the strength of the cross-phase modulation between waveguide mode and the cavity mode of the qth cavity, whereas $\Gamma_{q,\vec{\sigma}}$ describes the influence on the cavity mode of the qth cavity induced by four-wave mixing interactions of the waveguide modes.

Upon performing the integrals over the variable z, the system of equations defined by Eqs. (6.49) reduces to a system of coupled ordinary-differential equations describing the dynamics of the cavity mode amplitudes. It should be noted, however, that the amplitudes of the waveguide modes enter explicitly in this system, as the waveguide and cavity modes are linearly and nonlinearly coupled. As a further comment, note that when Fourier transforming Eq. (6.43) to the time domain we used the following relations, which can be easily demonstrated:

$$\begin{aligned}\int_0^\infty \omega a_p e^{-i(\omega-\bar{\omega}_q)t}\,d\omega &= \left(i\frac{dA_p}{dt}+\bar{\omega}_p A_p\right)e^{-i(\bar{\omega}_p-\bar{\omega}_q)t}\\ &\simeq \bar{\omega}_p A_p e^{-i(\bar{\omega}_p-\bar{\omega}_q)t},\end{aligned} \tag{6.51a}$$

$$\begin{aligned}\int_0^\infty \omega a_\sigma e^{-i(\omega-\bar{\omega}_q)t}\,d\omega &= \left(i\frac{\partial A_\sigma}{\partial t}+\bar{\omega} A_\sigma\right)e^{-i(\bar{\omega}-\bar{\omega}_q)t}\\ &\simeq \bar{\omega} A_\sigma e^{-i(\bar{\omega}-\bar{\omega}_q)t}.\end{aligned} \tag{6.51b}$$

6.4.3 Dynamical equations for the evolution of free carriers

The final step in the development of our theoretical model consists in establishing a set of equations that describe the dynamics of FCs generated in the waveguide and cavities; we denote these quantities by $N_w(z,t)$ and $N_p(t)$, $p = 1, \ldots, N_c$, respectively. To this end, we use the fact that FCs are generated through two-photon absorption, namely we impose the condition that the energy absorbed due to TPA is equal to the energy needed to generate the FCs in the waveguide and cavities [63, 39].

Let us consider first the evolution of FCs in the waveguide. Thus, let us omit for now all linear terms in Eq. (6.35), as they do not contribute to TPA, and perform the following calculations: first, multiply Eq. (6.35) by αA_α^*, then multiply the complex conjugate of Eq. (6.35) by αA_α, subtract the two resulting equations, and finally sum over the subscript α. The result of these mathematical manipulations can be cast in the following form:

$$\sum_{\alpha=\pm 1} \frac{\partial |A_\alpha|^2}{\partial z} = -2\mathfrak{Im}\left[\sum_{\alpha=\pm 1}\sum_{\vec{\sigma}} \alpha \gamma_{\alpha,\vec{\sigma}}(z) A_{\sigma_1} A_{\sigma_2} A_{\sigma_3}^* A_\alpha^*\right]. \tag{6.52}$$

The sum on the l.h.s. of Eq. (6.52) is equal to the total optical power transferred to the FCs in the weveguide, within the distance dz. To calculate the corresponding infinitesimal volume dV in which these carriers are generated as a result of the energy transfer, we introduce the nonlinear effective area of the waveguide mode, $A_{\rm nl}$ (see also Ref. [100]):

$$A_{\rm nl}(z) = \frac{\left[\int_{S_{\rm nl}} |\mathfrak{Re}\left(\mathbf{e}_\alpha \times \mathbf{h}_\alpha^*\right)| \, dS\right]^2}{\int_{S_{\rm nl}} |\mathfrak{Re}\left(\mathbf{e}_\alpha \times \mathbf{h}_\alpha^*\right)|^2 \, dS}. \tag{6.53}$$

In this equation, the integrals are performed only over the Si regions as only in such domains FCs are generated. Moreover, although we kept in this definition the subscript α, the nonlinear effective area of the waveguide mode does not depend on the propagation direction of the mode.

Since the electron-hole pairs are generated via TPA, for the creation of each such pair,

it is required an amount of energy that is equal to $2\hbar\bar{\omega}$. As a result, the carriers dynamics in the waveguide is governed by the following rate equation:

$$\frac{\partial N_w(z,t)}{\partial t} = -\frac{N_w(z,t)}{\tau_c} + \frac{1}{\hbar\bar{\omega}A_{\rm nl}} \times \mathfrak{Im}\left[\sum_{\alpha=\pm 1}\sum_{\vec{\sigma}} \alpha\gamma_{\alpha,\vec{\sigma}}(z)A_{\sigma_1}A_{\sigma_2}A^*_{\sigma_3}A^*_{\alpha}\right], \tag{6.54}$$

where τ_c is the recombination time.

We now move on to develop the system of equations describing the carrier dynamics inside the optical cavities. As in the case of the FCs in the optical waveguide, we assume that the FCs in the qth cavity are generated *via* TPA occuring in the same qth cavity, where $q = 1, \ldots, N_c$. In other words, nonlinear cross-absorption modulation effects between cavities and between cavities and waveguide are neglected. Then, following a similar procedure as the one used to establish Eq. (6.52), we can easily derive the following equation, which describes the energy transfer from the optical field in the qth cavity to the FCs generated inside the cavity:

$$\frac{d|A_q|^2}{dt} = -2\Gamma''_{q,q}|A_q|^4, \quad q = 1, \ldots, N_c, \tag{6.55}$$

where we denoted by z'' the imaginary part of the complex number, z. Again, since the generation of each electron-hole pair in the qth cavity requires an amount of energy equal to $2\hbar\bar{\omega}_q$, the time evolution of the FC denity in the qth cavity, $N_q(t)$, is described by the following rate equation:

$$\frac{dN_q(t)}{dt} = -\frac{N_q(t)}{\tau_c} + \frac{\Gamma''_{q,q}}{\hbar\bar{\omega}_q V_{{\rm nl},q}}|A_q|^4, \quad q = 1, \ldots, N_c, \tag{6.56}$$

where $V_{{\rm nl},q}$ is the nonlinear effective volume of the qth cavity. It can be defined in a

similar manner to the nonlinear effective area of the waveguide, namely

$$V_{\mathrm{nl},q} = \frac{\left[\int_{V_{\mathrm{nl}}} |\mathbf{e}_q(\mathbf{r})|^2 \, dV\right]^2}{\int_{V_{\mathrm{nl}}} |\mathbf{e}_q(\mathbf{r})|^4 \, dV}, \tag{6.57}$$

where the integrals are performed only over the Si regions.

This concludes the derivation of the theoretical model describing the dynamics of the coupled optical fields of the cavities and waveguide, dynamics that in turn is coupled to the dynamics of the FCs generated inside the cavities and in the waveguide. More specifically, in practice one solves the coupled system of nonlinear differential equations consisting of Eq. (6.35), Eq. (6.49), Eq. (6.54), and Eq. (6.56).

6.5 Application to the case of a PhC waveguide coupled to two PhC cavities

In this section we illustrate how our formalism developed in the preceding section can be applied to a particular case of interest, namely that of a PhC waveguide coupled to two PhC cavities. To describe this photonic configuration in a convenient manner the system of coupled equations describing the dynamics of the optical fields and FCs are simplified in the following way: Firstly, since $N_c = 2$, all sums over the cavity index are replaced by the corresponding terms. Secondly, we normalize all functions and variables defining the system of coupled equations that we aim to solve, so that its numerical integration becomes more facile. To this end, we introduce a normalized distance, $\zeta = z/a$, a normalized time, $\tau = t/T_0$, where T_0 is the characteristic width of the pulses in the waveguide, the normalized frequency defined as $\Omega = \omega T_0$, the normalized envelopes of the pulses propagating in the waveguide, $U_{\pm} = A_{\pm}/\sqrt{P_0}$, where P_0 is the peak power of the input pulse, and $U_{1,2} = A_{1,2}/\sqrt{E_0}$, where E_0 is a characteristic energy stored in the PhC cavities. The specific value of this physical quantity, which can be viewed as the unit for the energy contained in the optical cavities, can be chosen as the threshold beyond

which nonlinear optical effects in the cavities can no longer be neglected. With these simplifications, the equations governing the dynamics of the waveguide mode amplitudes and amplitudes of the cavity modes are:

$$
\begin{aligned}
&i\left(\frac{\partial U_+}{\partial \zeta}+\frac{a}{T_0 v_g}\frac{\partial U_+}{\partial \tau}\right)-\frac{a\beta_2}{2T_0^2}\frac{\partial^2 U_+}{\partial \tau^2}+\frac{\bar{\Omega}a}{T_0}(c_{++}+\theta^w_{++})U_+\\
&+aP_0\left[\gamma_{+,+++}|U_+|^2+(\gamma_{+,+--}+\gamma_{+,-+-})|U_-|^2\right]U_+\\
&+\frac{\sqrt{E_0}a}{\sqrt{P_0}T_0}\left\{\left[\bar{\Omega}_1\left(c^w_{+,1}+\theta^w_{+,1}\right)U_1+ic^c_{+,1}\frac{dU_1}{d\tau}\right]e^{-i(\bar{\Omega}_1-\bar{\Omega})\tau}\right.\\
&\left.+\left[\bar{\Omega}_2\left(c^w_{+,2}+\theta^w_{+,2}\right)U_2+ic^c_{+,2}\frac{dU_2}{d\tau}\right]e^{-i(\bar{\Omega}_2-\bar{\Omega})\tau}\right\}=0, \qquad (6.58a)\\
&i\left(-\frac{\partial U_-}{\partial \zeta}+\frac{a}{T_0 v_g}\frac{\partial U_-}{\partial \tau}\right)-\frac{a\beta_2}{2T_0^2}\frac{\partial^2 U_-}{\partial \tau^2}+\frac{\bar{\Omega}a}{T_0}(c_{--}+\theta^w_{--})U_-\\
&+aP_0\left[\gamma_{-,---}|U_-|^2+(\gamma_{-,-++}+\gamma_{-,+-+})|U_+|^2\right]U_-\\
&+\frac{\sqrt{E_0}a}{\sqrt{P_0}T_0}\left\{\left[\bar{\Omega}_1\left(c^w_{-,1}+\theta^w_{-,1}\right)U_1+ic^c_{-,1}\frac{dU_1}{d\tau}\right]e^{-i(\bar{\Omega}_1-\bar{\Omega})\tau}\right.\\
&\left.+\left[\bar{\Omega}_2\left(c^w_{-,2}+\theta^w_{-,2}\right)U_2+ic^c_{-,2}\frac{dU_2}{d\tau}\right]e^{-i(\bar{\Omega}_2-\bar{\Omega})\tau}\right\}=0, \qquad (6.58b)
\end{aligned}
$$

and

$$
\begin{aligned}
&i\left(\frac{\partial U_1}{\partial \tau}+\frac{\bar{\Omega}_1}{Q_1}U_1\right)+\bar{\Omega}_1(C^w_{11}+\theta^c_{11})U_1+\bar{\Omega}_1E_0\Gamma_{1,1}|U_1|^2U_1\\
&+e^{-i(\bar{\Omega}-\bar{\Omega}_1)\tau}\sqrt{\frac{P_0}{E_0}}\left\{\bar{C}^c_{+,1}\left[i\frac{\partial U_+}{\partial \tau}+(\bar{\Omega}-\bar{\Omega}_1)U_+\right]\right.\\
&\left.+\bar{\Omega}(\bar{C}^w_{+,1}+\bar{\theta}^c_{1,+})U_++\bar{C}^c_{-,1}\left[i\frac{\partial U_-}{\partial \tau}+(\bar{\Omega}-\bar{\Omega}_1)U_-\right]+\bar{\Omega}(\bar{C}^w_{-,1}+\bar{\theta}^c_{1,-})U_-\right\}=0, \qquad (6.59a)\\
&i\left(\frac{\partial U_2}{\partial \tau}+\frac{\bar{\Omega}_2}{Q_2}U_2\right)+\bar{\Omega}_2(C^w_{22}+\theta^c_{22})U_2+\bar{\Omega}_2E_0\Gamma_{2,2}|U_2|^2U_2\\
&+e^{-i(\bar{\Omega}-\bar{\Omega}_2)\tau}\sqrt{\frac{P_0}{E_0}}\left\{\bar{C}^c_{+,2}\left[i\frac{\partial U_+}{\partial \tau}+(\bar{\Omega}-\bar{\Omega}_2)U_+\right]\right.\\
&\left.+\bar{\Omega}(\bar{C}^w_{+,2}+\bar{\theta}^c_{2,+})U_++\bar{C}^c_{-,2}\left[i\frac{\partial U_-}{\partial \tau}+(\bar{\Omega}-\bar{\Omega}_2)U_-\right]+\bar{\Omega}(\bar{C}^w_{-,2}+\bar{\theta}^c_{2,-})U_-\right\}=0, \qquad (6.59b)
\end{aligned}
$$

respectively. In the equations above the following coupling coefficients have been defined:

$$\bar{C}^{c,w}_{\sigma,q} = \int_{-l_q}^{l_q} C^{c,w}_{\sigma,q}(z)\, dz; \quad \bar{\theta}^{w}_{q,\sigma} = \int_{-l_q}^{l_q} \theta^{w}_{q,\sigma}(z)\, dz, \tag{6.60}$$

where $\sigma = \pm 1$ and $q = 1, 2$. To introduce these definitions we used the fact that the pulse envelopes $U_{\pm}(z,t)$ vary slowly with the propagation distance, z, so that they can be treated as constants in the integrals in Eq. (6.49).

Note that our coupled-mode theory does not account for the optical field radiated by the cavity, so that we introduced this effect in Eqs. (6.59) *via* the quality(Q)-factors $Q_{1,2}$ of the cavities. Moreover, in the equations above we have kept only the dominant coupling coefficients, both in the case of coupling coefficients C's defined by the perturbation of the system permittivity as well as θ's coupling coefficients determined by the generation of FCs. In fact, the coupling coefficients C's are much larger than the coupling coefficients θ's as the latter ones are determined by relatively small variations of the permittivity of the Si, with typical values being $\delta\epsilon_{\rm fc} \lesssim 10^{-2}$.

A further assumption made in order to simplify the equations governing the dynamics of the waveguide mode amplitudes and amplitudes of the cavity modes was that the cavities are relatively far from each other so that their linear coupling due to the overlap of the evanescent cavity modes can be neglected. We note, however, that our model does describe a linear coupling mechanism between the optical cavities, namely *via* the optical pulses propagating in the waveguide in the region located between the two optical cavities.

The weak overlap between the optical fields of the cavities also ensures that the corresponding cross-phase modulation effects can be neglected. In addition, the cavity and waveguide modes are evanescently coupled, so that the cross-phase modulations effects induced by the overlapping modes can be neglected, too. As a result of these considerations, we set $\Gamma_{q,\sigma_1\sigma_2 q} = \Gamma_{q,\vec{\sigma}} = \Gamma_{q,\sigma} = 0$, where $q = 1, 2$ and σ, $\sigma_{1,2} = \pm 1$. As a final remark regarding the equations governing the dynamics of the waveguide mode

amplitudes and amplitudes of the cavity modes we note that the symmetry properties of the nonlinear coefficients γ's imply that $\gamma_{+,+--} = \gamma_{+,-+-}$ and $\gamma_{-,-++} = \gamma_{-,+-+}$.

To conclude this section, we consider now the system of equations governing the dynamics of FCs generated in the optical cavities and waveguide. To this end, we normalize the FCs in the optical waveguide, $\mathcal{N}_w = N_w/N_0$, and optical cavities, $\mathcal{N}_{1,2} = N_{1,2}/N_0$, where N_0 is a certain characteristic carrier density. For example, one can define the value of N_0 such that the corresponding induced variation of the index of refraction, δn_{fc}, as given by Eq. (2.13a), has a certain value commonly encountered in experiments, say $\delta n_{\text{fc}} = 10^{-3}$. With these definitions, the rate equations Eq. (6.54) and Eq. (6.56) become, respectively:

$$\begin{aligned}\frac{\partial \mathcal{N}_w}{\partial \tau} =& -\frac{\mathcal{N}_w}{\tau_c} + \frac{P_0^2}{\hbar\bar{\Omega}A_{\text{nl}}N_0}\left[\gamma''_{+,+++}|U_+|^4 + \gamma''_{-,---}|U_-|^4\right.\\ &\left.+2\left(\gamma''_{+,+--} + \gamma''_{-,-++}\right)|U_+|^2|U_-|^2\right], \qquad (6.61a)\\ \frac{d\mathcal{N}_q}{d\tau} =& -\frac{\mathcal{N}_q}{\tau_c} + \frac{E_0^2\Gamma''_{q,q}}{\hbar\bar{\Omega}_q V_{\text{nl},q}N_0}|U_q|^4, \quad q = 1,2, \qquad (6.61b)\end{aligned}$$

where $\tau_c = t_c/T_0$ is the normalized recombination time. Note that the last rate equations for the optical cavities provide a convenient way to choose the characteristic energy E_0 (which can have a different value for each cavity). Thus, with N_0 fixed as discussed before, we choose E_0 such that each cavity is at steady-state. In other words, we impose the conditions that $\frac{\partial \mathcal{N}_q}{\partial \tau} = 0$ when $\mathcal{N}_q = N_0$ and $|U_q| = 1$, with $q = 1, 2$.

The system of equations (6.58), (6.59), and (6.61) describes the coupled dynamics of the optical fields and FCs in an PhC waveguide coupled to two optical PhC cavities. It takes into account a series of linear and nonlinear optical effects, including linear coupling and FC-induced coupling between the waveguide and cavities, group-velocity dispersion and FC-induced dispersion of forward- and backward-propagation pulses in the waveguide, FC recombination effects, the self-phase and cross-phase modulation of optical pulses in the waveguide, as well as two-photon absorption and cross-absorption modulation effects. In the next section, we present the numerical method we used to

solve this system of equations.

6.6 Computational method

In order to solve numerically the system of equations describing the coupled dynamics of the optical fields and FCs in an PhC waveguide coupled to optical PhC cavities, one chooses a computational grid in variables ζ and τ and discretize Eqs. (6.58), (6.59), and (6.61) on this computational grid. In addition, appropriate boundary conditions for the optical fields and FC densities must be imposed.

The normalized distance, ζ, is divided in N points, so that the normalized distance resolution will be

$$\Delta\zeta = \frac{L_{\text{sim}}}{N-1}, \tag{6.62}$$

with L_{sim} being the total normalized distance within which the waveguide and cavities are located. Moreover, the τ variable is similarly divided in M points, which implies a normalized time resolution of

$$\Delta\tau = \frac{\tau_{\text{sim}}}{M-1}, \tag{6.63}$$

where τ_{sim} the total normalized simulation time. The result of this discretization procedure is to create an $N \times M$ computational grid on which the functions $U_{\pm}(\zeta,\tau)$, $U_{1,2}(\tau)$, $\mathcal{N}_w(\zeta,\tau)$, and $\mathcal{N}_{1,2}(\tau)$ are discretized. Guided by the physics of the problem, suitable boundary conditions are imposed on these functions. An example of this procedure, applied for the forward-propagating mode, $U_+(\zeta,\tau)$, is schematically illustrated in Fig. 6.4, where the labels "c_1"and "c_2"indicate the location of the two optical cavities.

Considering the nature of the boundary conditions in the spatial dimension for the forward-propagating mode, it should be apparent that the backwards derivative discretization method should be used for the derivative of $U_+(\zeta,\tau)$, that is:

$$\left.\frac{\partial U_+(\zeta,\tau)}{\partial\zeta}\right|_{\zeta_n} = \frac{U_+(\zeta_n,\tau) - U_+(\zeta_{n-1},\tau)}{\Delta\zeta} + \mathcal{O}(\Delta\zeta), \tag{6.64}$$

where $1 \leq n \leq N-1$. Moreover, a similar formula is used to represent the τ-derivative of $U_+(\zeta,\tau)$, but with $1 \leq m \leq M-2$. Additionally, for the temporal dimension, the second-order partial derivative is discretized as follows:

$$\left.\frac{\partial^2 U_+(\zeta,\tau)}{\partial \tau^2}\right|_{\tau_m} = \frac{1}{(\Delta\tau)^2}\left[U_+(\zeta,\tau_{m+1}) - 2U_+(\zeta,\tau_m) + U_+(\zeta,\tau_{m-1})\right] + \mathcal{O}\left((\Delta\tau)^2\right). \tag{6.65}$$

Figure 6.4 illustrates some physical conditions we assume are satisfied in our problem. Firstly, the simulation time τ_{sim} must be long enough that the optical power carried by the forward-propagating pulse at the end of the simulation is negligible. In other words, at the end of the simulation, no optical power still flows in the forward direction. It should be noted that the forward-propagating optical pulse can undergo multiple scattering processes as it interacts with the optical cavities, so that at the output of the waveguide one can observe multiple pulses. Therefore, the simulation time should take into account not only the input pulse width and the time the forward-propagating pulse takes to

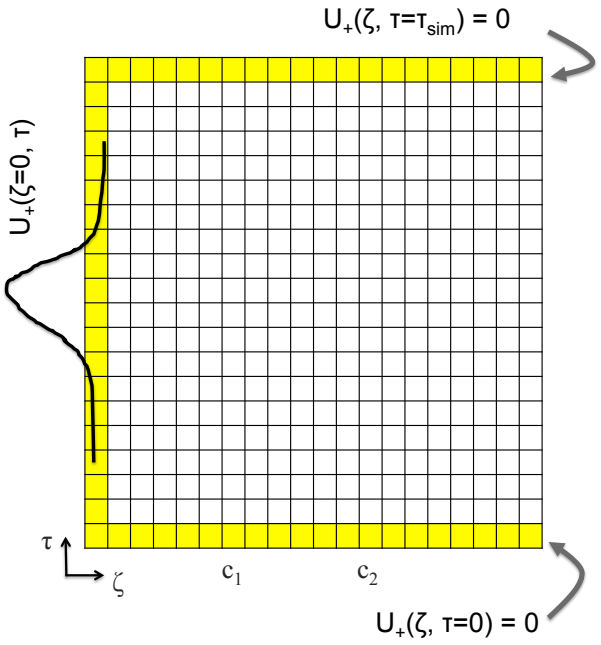

Figure 6.4: Schematic illustration of the discretization procedure used in our numerical method, as applied for the forward-propagating mode, $U_+(\zeta,\tau)$. The afferent boundary conditions are applied in the regions marked with yellow.

propagate through waveguide, but also the time needed for the energy coupled into the cavities to leaked out of the system via radiation or outcoupling into the waveguide modes. Moreover, we assume that the shape of the input pulse at $\zeta = 0$ is known.

Regarding the dynamics of the backward-propagating pulse, as described by Eq. (6.58b), we assume that at $\tau = 0$ the power carried by this pulse is zero throughout the system, that is, we assume that initially only the forward-propagating pulse exist. Another important point to stress here is that we assume that there is no backward-propagating pulse beyond the last cavity, c_2, i.e. no optical power is reflected at the end faced of the waveguide.

Given the specific form of Eq. (6.58b), it is apparent that one must use the forward discretization approach for the representation of the ζ-derivative of the backward-propagating pulse envelope, $U_-(\zeta, \tau)$:

$$\left.\frac{\partial U_-(\zeta,\tau)}{\partial \zeta}\right|_{\zeta_p} = \frac{U_-(\zeta_{p+1},\tau) - U_-(\zeta_p,\tau)}{\Delta\zeta} + \mathcal{O}(\Delta\zeta), \tag{6.66}$$

with p spanning the grid points between the input facet of the waveguide and the location of the cavity c_2. In addition, we used the same forward discretization approach when representing the time derivatives.

With respect to the dynamics of the cavity modes described by Eqs. (6.59), the discretization scheme is much simpler since the mode amplitudes only depend on time. In particular, we used the backward derivative method to discretize the amplitudes of the cavity modes. The boundary conditions in this case refer to the initial values of the mode amplitudes, which, for the sake of simplicity, are set to be equal to zero in all our simulations.

Finally, Eqs. (6.61) describing the FCs dynamics in the waveguide and cavities are discretized using the backward derivative method. As boundary conditions, we assume that initially the FC density in the waveguide and cavities is equal to zero, that is, $\mathcal{N}_w(\zeta, \tau = 0) = \mathcal{N}_1(\tau = 0) = \mathcal{N}_2(\tau = 0) = 0$.

The nonlinear system of equations obtained after the discretization of Eqs. (6.58), (6.59), and (6.61) was solved using the Newton-Raphson method, the corresponding computer code being developed in C++ using LAPACK libraries [138]; the algorithm is described in the Chapter 2, subsection 2.8.2. The algorithm requires as input all coupling coefficients, which have been calculated in Matlab with data from three computational tools: BandSOLVE and MEEP, to calculate the mode profile and Q-factors of the optical cavities, respectively, and MPB to calculate the spatial profile of the waveguide modes.

In order to illustrate some physical properties of cerain quantities defining our theoretical model, we present in Fig. 6.5 the dependence on distance of some of the key coupling coefficients. Firstly, we can observe that the c_{++} coefficient is different from zero only in the regions where the optical cavities are located. Interestingly enough, the c_{++} coefficient becomes negative in the regions corresponding to the holes at the cavity edges, which have been slightly displaced so as to improve the Q-factor, and it is positive where the silicon cylinders have been inserted to create the cavities. This coefficient, which is a real-valued function, models the optical coupling between the waveguide modes, me-

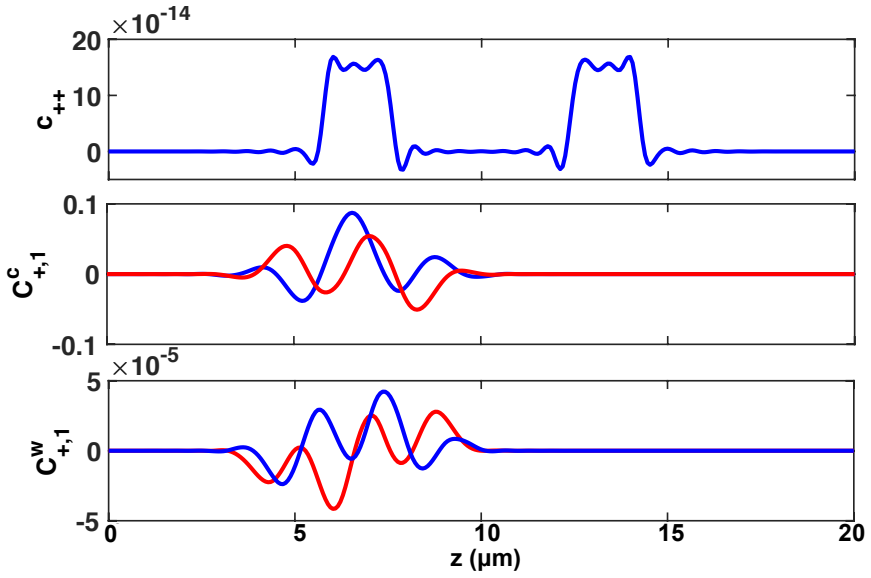

Figure 6.5: Top to bottom panels show the dependance on distance z of coupling coefficients c_{++}, $C^c_{+,1}$ (blue is real part, red is imaginary part), and $C^w_{+,1}$ (blue is real part, red is imaginary part), respectively. The cavity-cavity separation is $d_{cc} = 20a$ and the cavity-waveguide separation is $d_{cw} = 2.5a\sqrt{3}$.

diated by the presence of the cavities. The other two coupling coefficients presented in Fig. 6.5, $C^c_{+,1}$ and $C^w_{+,1}$, are complex-valued functions and are different from zero only at the location of the first cavity. These two coefficients model the frequency dispersion and the strength of the energy transfer from the cavity back to the waveguide mode.

6.7 Simulation results and discussion

In this section, we employ the theoretical model and numerical method developed in the preceding two sections and investigate the optical response of the system consisting of an optical PhC waveguide coupled to two PhC optical cavities. In particular, we assume that an input pulse with width T_0 is launched into the PhC waveguide and calculate the spatial and temporal dependence of the forward- and backward-propagating pulses in the waveguide and the corresponding FC density, as well as the temporal evolution of the optical fields and FC density in the two optical cavities. We also investigate the dependence of the optical response of the waveguide-cavities system on the key system parameters, including the pulse width T_0, the frequency detuning between the two optical cavities, $\Delta\omega_c = |\omega_1 - \omega_2|$, the separation between the cavities and the waveguide, d_{cw}, and the inter-cavity separation distance, d_{cc}.

In all numerical simulations presented in what follows, we assume that the distance between the input facet of the waveguide and the center of the first cavity is equal to $20a$. In addition, we assume that the same distance separates the second cavity and the output facet of the waveguide. The presence of these waveguide segments ensures the pulse dynamics are not perturbed by the input and output ends of the waveguide.

Figure 6.6 shows the spectra and temporal profiles of the forward- and backward-propagating pulses for a first scenario we analyse, namely a case in which the input pulse width is $T_0 = 10\,\mathrm{ps}$ and peak power $P_0 = 1\,\mathrm{mW}$, the two optical cavities are identical and are separated by a distance $d_{\mathrm{cc}} = 20a$, and the cavity-waveguide separation distance is $d_{\mathrm{cw}} = 2.5a\sqrt{3}$, corresponding to four rows of holes between the waveguide and the

cavities. Moreover, the wavelength of the input pulse and the resonance wavelength of the two cavities were $\lambda_0 = 1278.34\,\text{nm}$ and $\lambda_1 = \lambda_2 = 1278.31\,\text{nm}$, respectively. This scenario is of particular interest because, as we will demonstrate later on, it corresponds to the optimum optical coupling between the waveguide and the cavities.

Before we discuss the results summarized in Fig. 6.6, we would like to clarify a few ideas regarding the radiative characteristics of the two optical cavities, as quantified by their Q-factor. Thus, there are three loss channels that quantitatively determine the value of the cavity Q-factor: the radiative channel representing the energy lost through

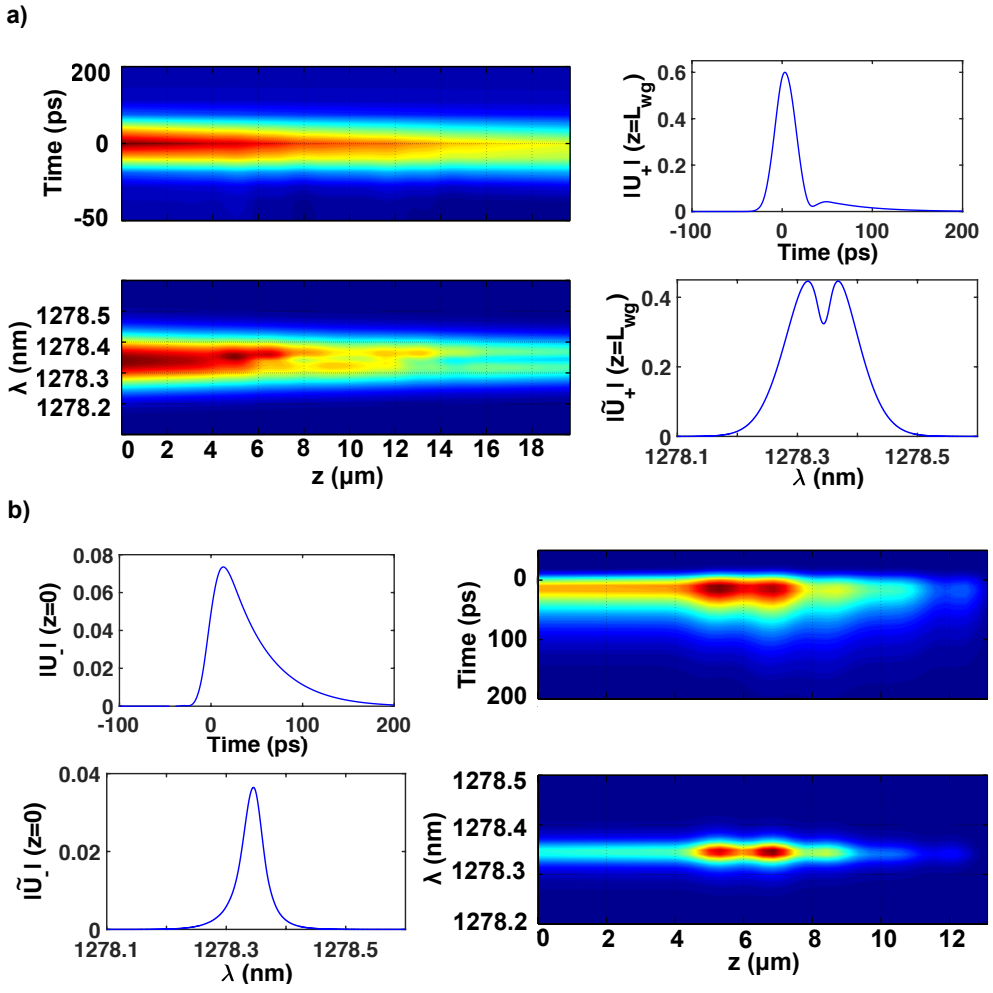

Figure 6.6: Dispersion maps of the temporal profile and spectra as well as the output temporal profile and spectra of (a) forward and (b) backward-propagating pulses. Note that the output forward- (backward-propagating) pulse is calculated at the output (input) port of the waveguide.

radiation into continuum, characterized by a Q-factor $Q_{0,p}$, the energy leaked into the optical waveguide defines the Q-factor $Q_{w,p}$, which is quantified by the coupling coefficient C_{pp}^{w}, whereas the energy absorbed in carrier recombination processes determines the Q-factor $Q_{\mathrm{fc},p}$, quantified by the coupling coefficient θ_{pp}^{c}, where $p = 1, 2$. Therefore, the cavity Q-factor can be expressed as:

$$\frac{1}{Q_p} = \frac{1}{Q_{0,p}} + \frac{1}{Q_{w,p}} + \frac{1}{Q_{\mathrm{fc},p}}, \quad p = 1, 2. \tag{6.67}$$

The cavity Q-factor, Q_p, can be extracted from the width of the spectrum of the optical field in the cavity, via the relation $Q_p = \omega_p/\Delta\omega$, where $\Delta\omega$ is the FWHM of the power spectrum. With this definition, our calculations showed that $Q_p = 27147$. This means that the characteristic time over which the optical cavity loses its energy is $\Delta t = 2Q_p/\omega_p = 36.8\,\mathrm{ps}$. Moreover, $Q_{0,p}$ can be determined numerically from the time evolution of the optical power stored in an isolated cavity, whereas $Q_{w,p}$ can be calculated using the coupling coefficient, C_{pp}^{w}, the combined contribution of these two loss channels being quantified by an equivalent Q-factor of 27514. From these results we can therefore conclude that the Q-factor associated to the FCs loss is $Q_{\mathrm{fc},p} = 229630$. In other words, the optical losses and, implicitly, the coupling coefficient θ_{pp}^{c}, can be neglected.

Let us now return to the results presented in Fig. 6.6 and discuss the physics they reveal. Thus, regarding the forward-propagating pulse, it can be seen in Fig. 6.6(a) that due to the various loss mechanisms, including propagation loss, FCA, and coupling to the cavities, by the time the pulse reached the waveguide output its optical peak power had decreased by more than 40 %. Moreover, the second, weaker pulse formed at its tail end is due to the energy radiated back into the waveguide by the two cavities. The pulse interaction with the cavity can be also observed in its spectrum, where the wavelength of the dip at the top of the pulse occurs at the resonance wavelength of the cavity.

The dispersion map of the forward-propagating pulse, shown in Fig. 6.6(a), provides a more detailed picture of the interaction between the optical pulse and cavities. Thus,

it can be seen that the first cavity, centered at $L_1 = 6.66\,\mu\text{m}$, begins to distort the pulse once it propagates beyond a distance of $4\,\mu\text{m}$, whereas the second cavity, located at $L_2 = 13.32\,\mu\text{m}$, further deepens the dip formed at the center of the pulse starting from about $14\,\mu\text{m}$ onwards. This pulse dynamics also shows that the pulse starts to interact with a cavity when is within a few lattice constants from the cavity center, which is explained by the fact the cavities have a size of a few lattice constants.

Regarding the backward-propagating pulse, whose temporal and spectral properties are presented in Fig. 6.6(b), it can be clearly seen that it is chiefly generated from the energy leaking from the two optical cavities into the waveguide. Indeed, the pulse builds up steeply as the forward-propagating pulse reaches the first cavity, which is followed by a slow, exponential decay at the tail end of the pulse, similar to the time dependence of the energy decrease in the cavity. The corresponding spectrum shows the wavelength of the peak power is equal to the resonance wavelength of the cavities and implicitly coincides with the wavelength of the dip in the spectrum of the forward-propagating pulse. These conclusions are validated by the dispersion maps presented in Fig. 6.6(b), which show that the backward-propagating pulse begins to build up primarily at the location of the first cavity although a weaker contribution from the second cavity can be observed, too. One can also see that the pulse decays as it propagates towards the input of the waveguide, which is due to the loss mechanisms we just discussed.

Deeper insights into the temporal and spectral characteristics of an optical pulse are provided by the pulse spectrogram $S(\zeta;\lambda,t)$, defined as the Fourier transform of the product between the optical pulse at a certain propagation distance and a delayed reference pulse, usually taken to be the input pulse. Mathematically, this physical quantity is expressed by the following formula:

$$S(\zeta;\lambda,t) = \left| \int U_+(\zeta,\tau) U_+(\zeta_{in},\tau - t) e^{i\frac{2\pi c}{\lambda}\tau}\, d\tau \right|. \tag{6.68}$$

The spectrogram of the forward-propagating pulse, calculated at the propagation dis-

tance corresponding to the output port of the waveguide, is shown in Fig. 6.7. This figure shows that there exist a tail of optical power extending towards longer times, which is due to the exponential decay of the energy contained into the two cavities into the forward-propagating optical mode. This tail contains slightly blue-shifted spectral components, as compared to the wavelength of the input pulse and resonance wavelength of the cavities. This effect can be explained by the fact that the presence of the waveguide induces a small spectral blue-shift of the cavity resonance wavelength, from $\lambda_p = 1278.31\,\text{nm}$ to $\lambda_p' = 1278.28\,\text{nm}$.

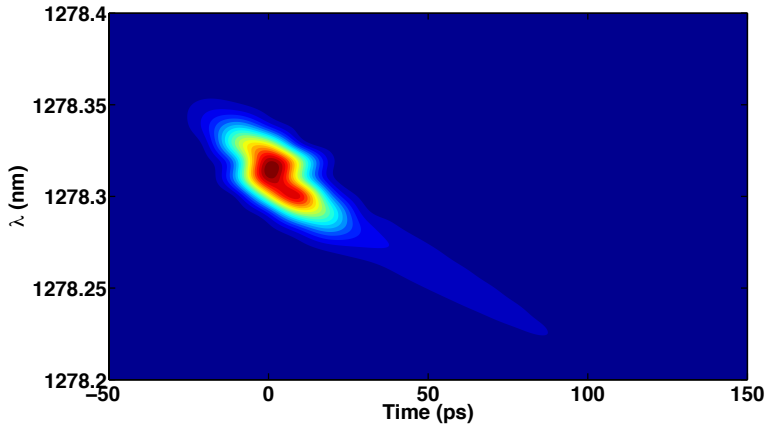

Figure 6.7: Spectrogram of the forward-propagating pulse, calculated at the propagation distance corresponding to the output port of the waveguide.

We now shift our attention to the optical field in the two cavities, whose dynamics are illustrate in Fig. 6.8. In our calculations, we assumed that the characteristic energy was $E_0 = 28.04\,\text{fJ}$. The data plotted in Fig. 6.8 show that, as expected, the maximum of the field amplitude is larger for the first cavity, as the excitation pulse has a larger peak power at the location of the first cavity. Moreover, the inset in Fig. 6.8, where we plot the real part of the field amplitude in the two cavities, shows that there is a phase difference between the field oscillations, which is due to the time needed for the excitation pulse to travel the distance separating the two cavities. Figure 6.8 also reveals a good agreement between the decay rate of the energy contained in the cavities and their Q-factor.

The plots in Figs. 6.9(a) and 6.9(b) represent the time evolution of the FC densities

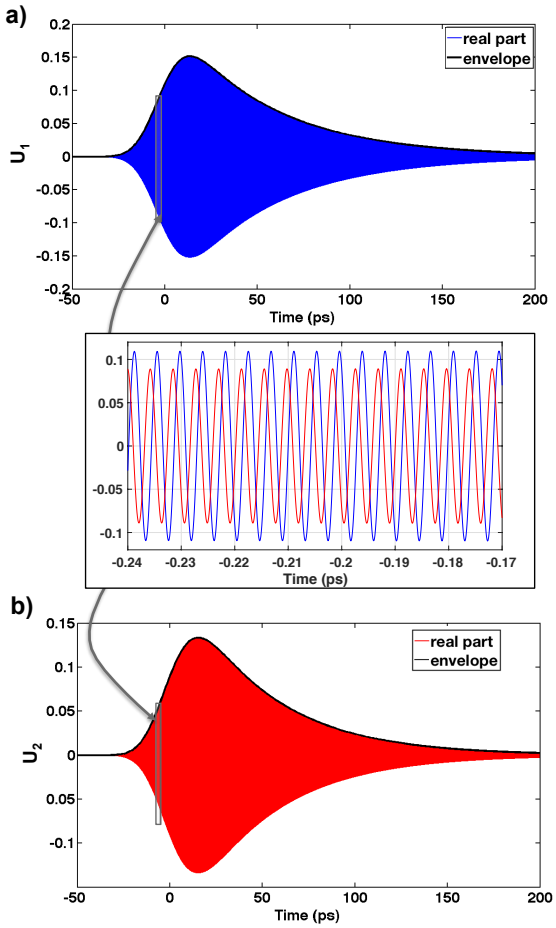

Figure 6.8: (a), (b) Time dependence of the real part of the normalized amplitudes U_1 and U_2, respectively. The black curves represent the field envelopes. The inset represents a zoomed-in temporal region and shows the real part of U_1 (blue) and U_2 (red).

in the waveguide and the two cavities, respectively. It can be seen from these figures that the largest FC density in the waveguide is at the input port, as at that location the peak power of the input optical pulse has the largest value. From there on, the FC density decreases along the waveguide due to the absorption of the excitation pulse. One can also observe that once the excitation pulse passes a certain point the FC density starts to decay exponentially due to FC recombination processes, as suggested by the rate equations describing the FC densities. This decay trend is somewhat distorted at around 5 µm, where the optical power of the backward-propagating pulse reaches its largest value. Regarding the FC density in the cavities, one can observe that, as expected, the FC density in the first cavity starts to build up before FCs begin to be generated

inside the second cavity.

The ratio between the maximum number of FCs created inside each cavity can be easily computed from the following relation,

$$\frac{|U_{1,max}|^4}{|U_{2,max}|^4} = 1.6691, \tag{6.69}$$

which exactly matches the difference between the maximum number of FCs at each cavity, this is:

$$\frac{|U_{1,max}|^4}{|U_{2,max}|^4} = \frac{\mathcal{N}_{1,max}}{\mathcal{N}_{2,max}}. \tag{6.70}$$

We consider now the case in which there is a certain detuning between the resonance frequency of the two cavities. Thus, we assume that the wavelength of the input optical

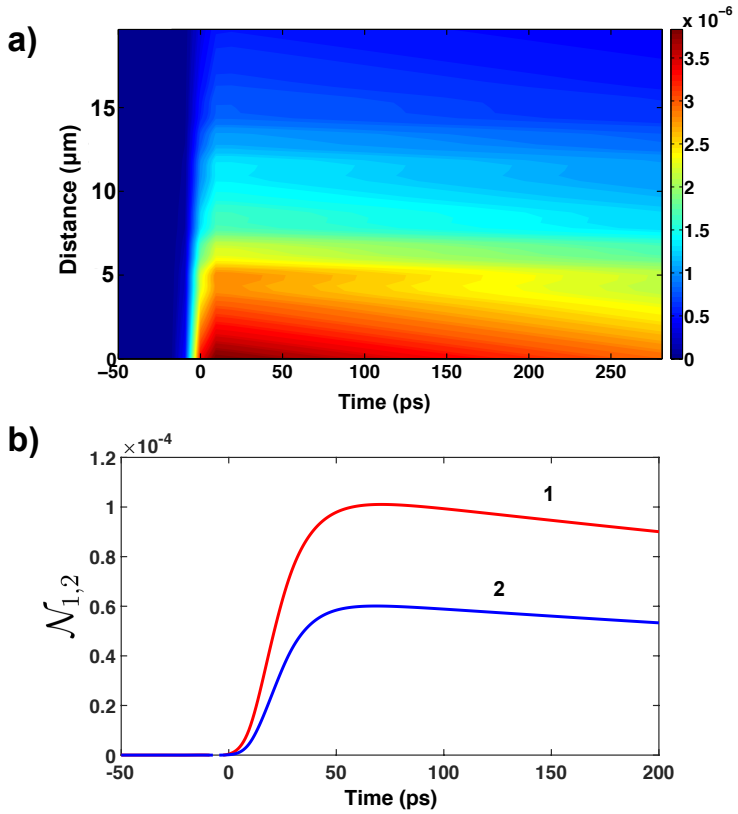

Figure 6.9: (a), (b) Temporal evolution of the FC density in the waveguide and the two cavities, respectively. The densities are normalized to the characteristic density value $N_0 = 7.343 \times 10^{24}\,\mathrm{m}^{-3}$.

pulse is $\lambda_0 = 1278.34\,\text{nm}$, its pulse width is $T_0 = 5\,\text{ps}$, and the resonance wavelengths of the two cavities are $\lambda_1 = 1278.25\,\text{nm}$ and $\lambda_2 = 1278.37\,\text{nm}$.

In Fig. 6.10, we summarize the results of our analysis of the pulse dynamics in this scenario. It can be seen in this figure that the spectrum of the forward-propagating pulse (top panes) displays two dips, almost symmetrically located with respect to the center of the spectrum, the corresponding wavelengths being equal to the resonance wavelengths of the two cavities. Moreover, the spectrum of the backward-propagating pulse, determined at the input port of the waveguide (bottom panel), contains two peaks, which are located at the resonance wavelength of the cavities. This illustrates the fact that the backward-propagation pulse is chiefly generated by the two cavities whose energy out-couples into the waveguide. In addition, the amplitude of the two spectral peaks differ from each other, with more energy being contained in the peak originating from the first cavity.

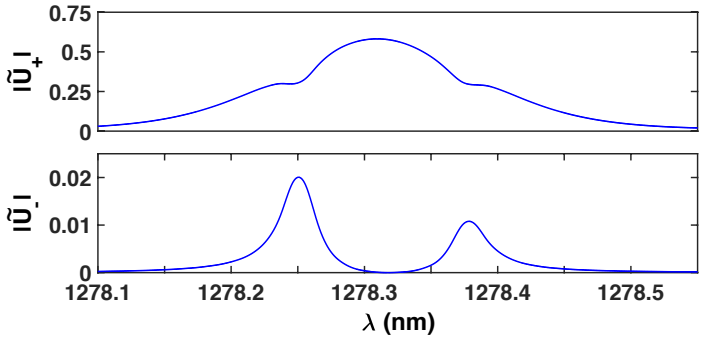

Figure 6.10: Transmission (top panel) and reflection (bottom panel) spectra for $\lambda_0 = 1278.34\,\text{nm}$, $\lambda_1 = 1278.25\,\text{nm}$, $\lambda_2 = 1278.37\,\text{nm}$, and $T_0 = 5\,\text{ps}$.

The influence of the width of the input pulse on the system dynamics becomes particularly important when it is comparable to the characteristic decay time of the energy stored in the cavities. This decay time can be controlled by varying the separation distance between cavities and waveguide, as in this case one varies the cavity-waveguide coupling coefficient, C_{pp}^{w}, with $p = 1, 2$. In particular, by reducing the distance between the cavity and waveguide to $d_{cw} = 2\sqrt{3}a$, the coupling coefficient becomes $C_{pp}^{w} = 1.5693 \times 10^{-4}$. As a result, the Q-factor of the cavities becomes $Q_p = 6028.3$, which implies a charac-

teristic time of 8.17 ps. Based on these considerations, we varied the pulse width in our simulations from 2 ps to 30 ps.

The results regarding the system dynamics corresponding to different values of the width of the input pulse are presented in Fig. 6.11, where we show, from the top to the bottom panels, the evolution over time of the forward-propagating pulse at the output port of the waveguide, the backward-propagating pulse at the input port, and the energy contained in the two cavities, respectively. For each panel, black, red, purple, and blue lines correspond to $T_0 = 30$ ps, $T_0 = 20$ ps, $T_0 = 10$ ps, and $T_0 = 2$ ps, respectively.

It can be observed from the plots presented in Fig. 6.11 that, when the pulse width T_0 is much smaller than the characteristic decay time of the cavity energy, the optical field at the input port consists of a series of short pulses, which are created as a result of several roundtrips performed by the optical field in the waveguide region between the cavities, roundtrips induced by wave scattering from the two cavities. In particular, the two most pronounced peaks correspond to the first reflected pulse from the first cavity and the first reflected pulse from the second cavity. This conclusion is validated by the dynamics of the optical field in the cavities. Thus, the energy in the cavities does not decrease monotonously and exponentially, an additional pulse being observed after the initial energy build up. The optical field evolution in the waveguide and cavities is different when the pulse width increases, as in this case the energy transfer from the input pulse to the cavity modes is done adiabatically. Moreover, it can be seen that, as the width of the input pulse decreases the pulse shape at the output port becomes increasingly more asymmetric.

Another important parameter that affects the optical response of the waveguide-cavities system is the distance between the waveguide and cavities. To illustrate this influence, we show in Fig. 6.12 the spectra of the transmitted and reflected optical pulses, determined when the waveguide and cavities are separated by two, four, and six holes, namely $d_{cw} = 1.5a\sqrt{3}$, $d_{cw} = 2.5a\sqrt{3}$ and $d_{cw} = 3.5a\sqrt{3}$, respectively. In this case, the pulse wavelength was equal to the resonance wavelength of the cavities,

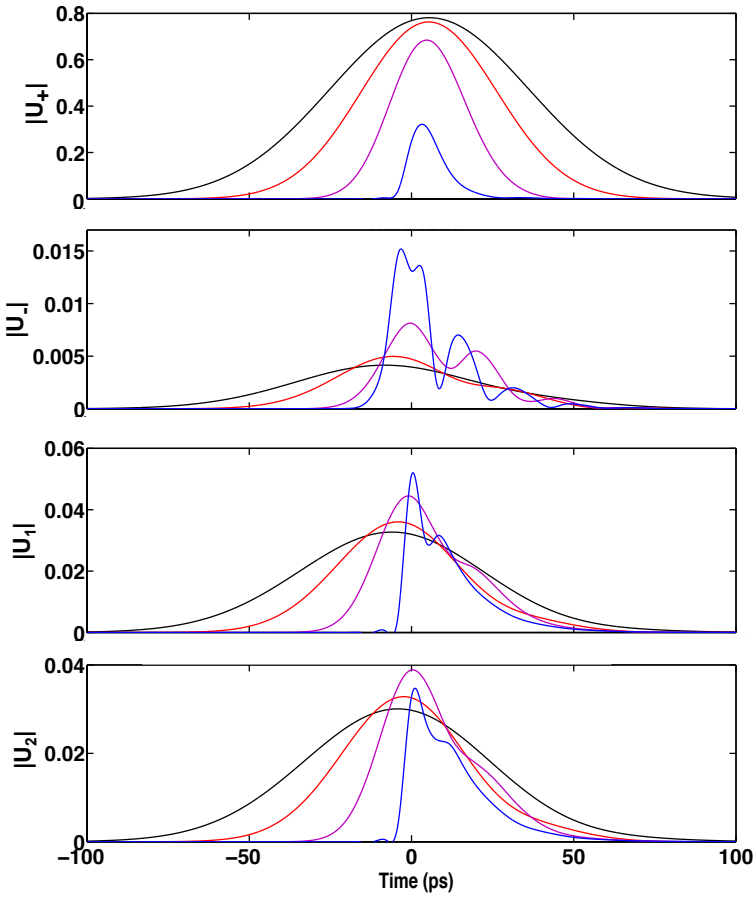

Figure 6.11: From top to bottom: effect of varying the pulse width on the forward pulse amplitude at the output port, the backwards pulse amplitude at the input port, the amplitude of the energy function in the first cavity and the amplitude of the energy function in the second cavity, respectively. Black lines correspond to $T_0 = 30$ ps, red to $T_0 = 20$ ps , purple to $T_0 = 10$ ps and blue to $T_0 = 2$ ps.

$\lambda_0 = \lambda_1 = \lambda_2 = 1278.31\,\text{nm}$.

To understand the results presented in Fig. 6.12 one has to take into account the perturbation of the cavity mode by the presence of the waveguide. As a result of this interaction, the resonance wavelength of the cavities is blue-shifted according to the formula:

$$\omega_p' = \omega_p(1 + C_{pp}^w), \quad p = 1, 2, \tag{6.71}$$

where ω_p' is the resonance frequency of the perturbed cavity. The closer the cavities are

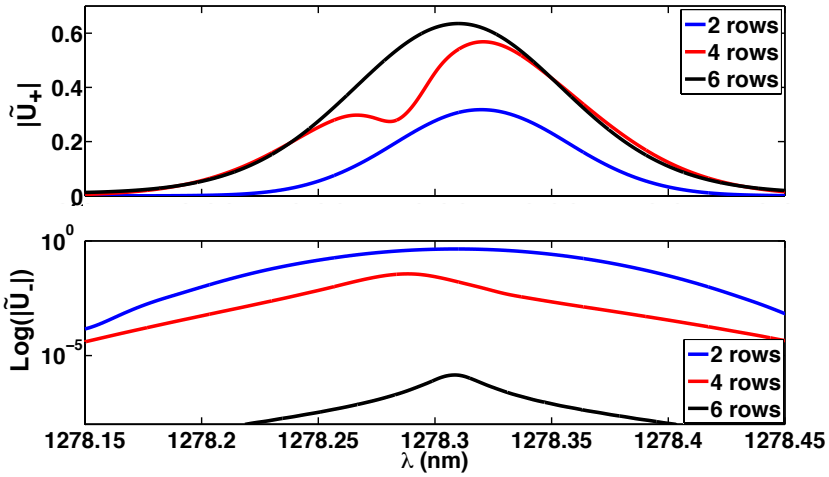

Figure 6.12: Spectra of the transmitted (top panel) and reflected (bottom panel) pulses, determined for different values of the separation distance between the waveguide and cavities and for $\lambda_0 = \lambda_1 = \lambda_2 = 1278.31\,\mathrm{nm}$.

to the waveguide, the larger the frequency detuning is. As we just discussed, another consequence of decreasing d_{cw} is that the cavity Q-factor decreases, too.

Based on these ideas, the features of the spectra presented in Fig. 6.12 can be understood as follows. When the waveguide and cavities are separated by just two rows (blue curves), the cavity Q-factor is so small that the cavity bandwidth completely overlaps with the spectrum of the input pulse and consequently no filtering effect are observed. Moreover, when the separation distance between the waveguide and cavities is increased to four rows (red curves), a cavity filtering effect becomes apparent. Importantly, in this case the spectrum of the transmitted pulse has two peaks, one at the wavelength of the input pulse, $\lambda_0 = 1278.31\,\mathrm{nm}$, and one at a blue-shifted value of the resonance wavelength of the cavity, $\lambda' = 1278.28\,\mathrm{nm}$. Finally, when the separation distance between the waveguide and cavities is further increased to six rows (black curves), there is very weak coupling between the waveguide and cavities, so that the spectrum of the transmitted pulse is very similar to that of the input pulse, whereas a very weak pulse is observed in the input port. This indicates that a vanishingly small amount of energy is transferred to the cavities.

The last issue we investigate in this section is the dependence of the optical properties

of the waveguide-cavities system on the center-to-center inter-cavity distance, d_{cc}. In particular, we seek to find optimize the separation distance so that the power of the reflected optical signal at the input port is minimized. This optimization process can be performed by simply imposing the condition that the successive reflected pulses arrive at the input port with a phase difference equal to an odd number of π, that is:

$$2\beta L_1 = 2\beta L_1 + 2\beta d_{cc} \pm n\pi, \tag{6.72}$$

where β is the propagation constant of the forward- and backward-propagating modes, L_1 is the distance to the first cavity, L_2 is the distance to the second cavity, $d_{cc} = L_2 - L_1$, and $n = 1, 3, 5, \ldots$. If we now choose the inter-cavity separation distance to be a multiple of the lattice constant, $d_{cc} = ma$ with m an integer, Eq. (6.72) becomes:

$$2\beta ma \pm n\pi = 0. \tag{6.73}$$

Using in this equation the system parameter values $a = 333\,\text{nm}$, $\lambda_0 = 1278.34\,\text{nm}$, and $\beta = 8.1993 \times 10^6\,\text{m}^{-1}$, we find that the value of m closest to an integer number is $m = 18.9852$ and corresponds to $n = 33$. Based on this analysis, we performed several simulations in which the waveguide-cavities separation distance was fixed to four rows and varied the inter-cavity separation distance from $d_{cc} = 15a$ to $d_{cc} = 26a$. We did not decreased any further the separation distance because we wanted to make sure that the cavity-cavity optical coupling remains negligible.

In Fig. 6.13 we show the dependence on d_{cc} of the transmission and reflection coefficients. Regarding the reflection coefficient, its minimum is achieved for $d_{cc} = 18a$, closely the value predicted by Eq. (6.73). The transmission coefficient, on the other hand, only slightly changes with d_{cc}. Finally, the insets presented in Fig. 6.13 show the temporal and spectral dispersion maps of the reflected pulse, determined for the values of d_{cc} indicated by the arrows. These maps clearly demonstrate the difference between the two scenarios, namely the destructive and constructive interference between consecutive pulses arriving

at the input port.

6.8 Conclusion

In summary, we have developed and discussed a novel, comprehensive, and rigorous mathematical model that describes the optical pulsed dynamics in a silicon photonic system consisting of a photonic crystal waveguide coupled to a set of optical photonic crystal cavities. Our model captures all relevant linear and nonlinear optical effects occurring in the physical system, including group-velocity dispersion, cross-mode disperion, intrinsic and free-carrier absorption, free-carrier dispersion, self- and cross-phase modulation, two-photon absorption, and cross-absorption modulation. Our model has been developed from first principles within the framework of the coupled-mode theory and accurately de-

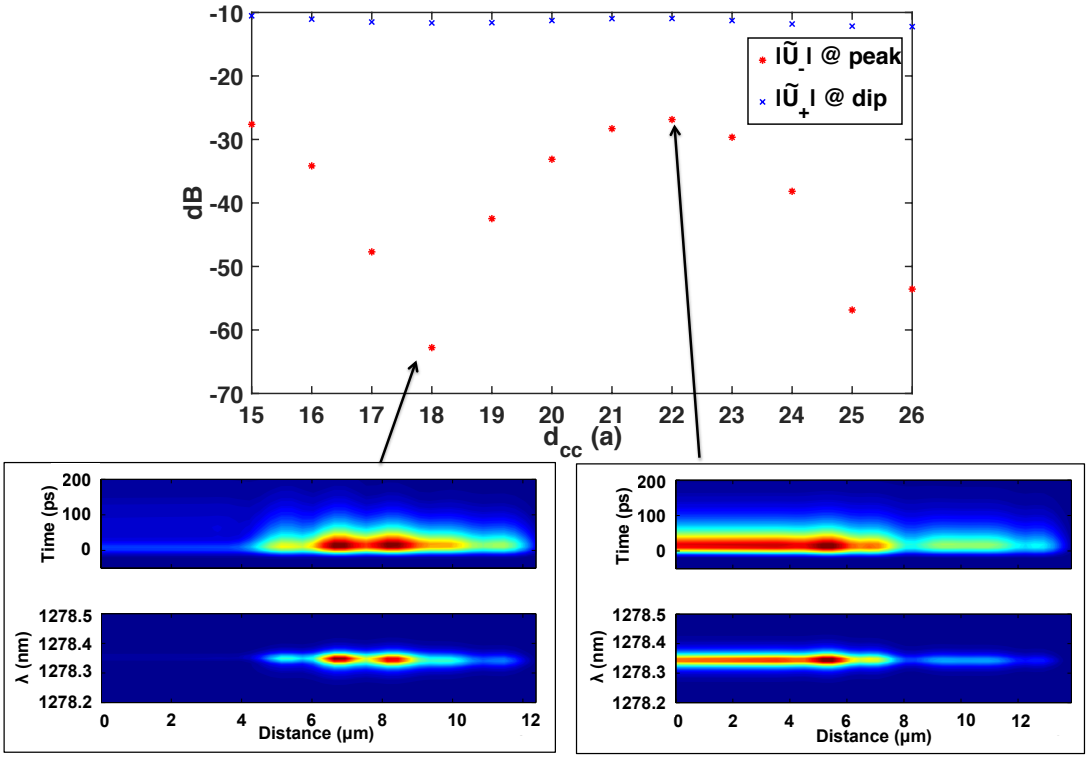

Figure 6.13: Transmission (×) and reflection (*) coefficients *vs.* cavity-cavity separation distance d_{cc} determined for $d_{cw} = 2.5\sqrt{3}a$, $T_0 = 10\,\text{ps}$, and $\lambda_0 = 1278.34\,\text{nm}$. The insets show the temporal and spectral dispersion maps of the reflected pulse, determined for the values of d_{cc} indicated by the arrows.

scribes the coupled dynamics of the optical fields and free-carriers photogenerated in the optical waveguide and optical cavities. The mathematical model has been implemented in a computer code that allowed us to investigate the dynamics of the optical field and free-carries in our optical system.

To illustrate the versatility of our theoretical model and its numerical implementation, we have used it for a particular optical system consisting of an optical waveguide coupled to two optical cavities. Several configurations of this optical system have been considered, namely a case in which the two optical frequencies have the same resonance frequency, a configuration in which the two optical cavities are spectrally detuned, a set of configurations for which the separation distance between the waveguide and the two cavities varies, a case in which the inter-cavity separation distance was tuned so as to cancel the reflected optical pulse, and a set of calculations in which the dependence of the optical response of the system on the temporal width of the input pulse have been established. Out of all the results presented from these investigations, the most relevant one, which also exhibits the in-depth insights that our theoretical model can provide, is the one depicted in Fig. 6.11. In there, we have shown how the practical use of the photonic structure may be limited by the input pulse width, which is of interest for applications in communications. Precisely, as the width of the input pulse decreases, the energy in the cavities does not decrease monotonously and exponentially, but additional pulses are observed after the initial energy build up. As a consequence the pulse shape at the output port becomes increasingly more asymmetric. Overall, the physical behaviour of the photonic structure is dictated mainly by three parameters: the characteristic decay time of the cavity energy, which can be critical when the input pulse width is similar, appearing most sensitive; the separation between cavity and waveguide, which should not be too large in order to efficiently couple energy from the waveguide but not too short in order to maintain the lifetime of the cavity resonance; and, the separation between cavities in order to produce the desired pulse response while controlling the strength of back reflections. Indeed, this analysis has allowed us to show that the waveguide-cavities

system can be effectively used as a drop-filter, thus illustrating the practical importance of our study. Before we conclude, we would like to stress that the analysis presented in this work is not restricted to silicon devices, but can be easily modified to describe optical system made of other semiconductor materials.

Chapter 7

Conclusions and future work

During the last decades, silicon photonics have proven to be the most attractive technology for the development of integrated optical chips with applications in telecommunications, data centres and bio-sensing. A huge research has focused on the design of photonic building blocks taking advantage of the linear and nonlinear characteristics of silicon. Furthermore, based on the fact that current communication systems employ optical pulses as the way of transferring bits from one element to another in the network, the linear and nonlinear dynamic effects on the pulses propagating through a waveguide must be predicted when designing a photonic device or system. Dispersion engineering techniques enable the designers to adjust the functionality of these devices and tailor them to satisfy the application requirements by controlling the strength and frequency dependence of the linear and nonlinear effects. One relevant technique consists of producing a photonic crystal lattice and, then, modify it to create waveguides or cavities. With this approach, apart from allowing a good degree of versatility in the design, operation in the slow-light regime is enabled, where very interesting phenomena occur. Alternatively to photonic crystals, photonic waveguides can be designed with sub-wavelength features in order to shape the linear dispersion and to enhance the nonlinear effects. Within this context, in this work we have focused on the development of rigorous mathematical models to analyse the linear and nonlinear pulsed dynamics in photonic nanostructures, and

especially applied to photonic crystals made of silicon and sub-wavelength waveguides made of diamond.

With regards to the former, this study has explored the pulse dynamics when the structure has been designed for Raman amplification and when several cavities, acting as resonators, are placed alongside the waveguide. In contrast with the majority of the already published work in the field of photonics, both scenarios contain the intrinsic difficulty of having more than one optical pulses travelling along the waveguide, even in counter-propagating directions. Therefore, the numerical methods developed in this work to find the solution to these complex problems require the right computational algorithm depending on the scenario. Whereas an already known computational method has been employed for the study of Raman amplification, the cavity-waveguide interaction work has inspired a new tailored algorithm not applied before for these type of problems. It is worth mentioning that this work has determined the key requirements for achieving efficient Raman amplification in silicon photonic crystal waveguides.

With respect to the latter, this work has demonstrated how synthetic diamond-fin waveguides can enable efficient soliton formation and propagation and, potentially, supercontinuum generation. In addition, we have demonstrated how these waveguides can be employed to generate frequency combs operating in the visible spectral domain. Importantly, our simulations show that it is possible to generate almost one octave span stable combs in the visible range with input continuous-wave powers as low as 0.5 W.

In the following sections, we present the contributions of this thesis to the research in silicon and diamond photonics as well as the future prospects and potential new projects.

7.1 Contributions to the field

As mentioned above, the work carried out in this thesis has been centred in unfolding the understanding of nonlinear pulsed dynamics in microstructured photonic materials, with attention to those that enable dispersion engineering and, also, present high nonlinear

interactions. Indeed, with the controlled co-existence of the linear and nonlinear effects, different photonic functions can be implemented by the same or similar structure. To this end, photonic crystals and waveguides characterised by subwavelength features, which can help satisfy the dispersion engineering requirement, are combined with highly nonlinear materials like silicon and diamond. Following this motivation, we have presented the mathematical formalism needed to analyse the pulsed dynamics in these structures, which may help researchers and photonic designers working in the field.

Regarding the study of pulsed dynamics in subwavelength diamond-fin waveguides, the initial objective was to help the investigation of nonlinear processes on real devices that were being fabricated by University of Pennsylvania, with whom we were collaborating at the beginning of this work. Rapidly, relevant results were obtained related to the nonlinear effects on pulses travelling through these type of waveguides. This made us set up the new goal of demonstrating their applicability for frequency comb generation, which may be the key practical contribution from this chapter.

With respect to the work around Si-PhCWGs as a Raman-enabled medium, the most important contribution may be that clear amplification in the order of few tens of dB can be achieved thanks to the tight mode confinement and slow group velocity that PhCWGs allow. However, it has been demonstrated the importance of the walk-off length between pulses. Indeed, the walk-off length must be clearly bigger than the waveguide length if it is required to amplify the signal and conserve its pulse shape simultaneously. Additionally, it has been provided a deep study based on different combinations of group velocity regimes for the pump and the signal for Raman amplification. The results can set some reference scenarios for the development of active Si-PhCWGs, taking the proposed theoretical model as a reference to understand and compare measurements made on real devices.

Finally, in the context of the Si-PhC cavity-waveguide study, the generic mathematical formalism that has been presented can help solve more complex problems where forwards and backwards pulses interact with photonic cavities. An original numerical method

to solve the resulting set of nonlinear differential equations has been presented, which is able to find the solution in time and space of all the unknowns simultaneously. By applying this model to a Si-PhC nanostructure with cavities alongside a waveguide, we have shown how it could be employed to analyse the use of these structures to design photonic components such as filters or delay lines, for instance.

7.2 Future perspective

The theoretical models developed in this work so far have revealed the added value to the design process they can provide, so more compact simulation platforms that could easily be embedded in commercial software in the field of photonics would definitely be very convenient for researchers and designers. Especially for the cavity-waveguide simulation tool, which requires important computer resources given the large matrix system needed to be solved, it would be beneficial to improve the current developed source code, which employs LAPACK libraries, into the parallel version of these.

With respect to the diamond-fin waveguide work, and continuing the investigation of frequency comb generation, it may be relevant to study different waveguide-ring coupling regimes, i.e. under-, critical and over-coupling, and find the most interesting results, in terms of comb span and power efficiency, out of all these. Another line of investigation could be centred in changing the material of the fin by another with higher index of refraction, for instance replacing diamond by silicon or silicon-nitride and determine whether these subwavelength structures could improve some aspects of the currently existing designs.

Future work may also integrate the Si-PhCWG model with several cavities in the structure, where all the linear and nonlinear effects, including Raman, are combined with tunneling through localized states. Clearly, adding Raman effect into the cavity-waveguide study, e.g. merging Chapters 5 and 6, would be a natural research work in continuation of this thesis. Indeed, it would be interesting to study how Raman

amplification could be enhanced by the use of cavities alongside the waveguide. For instance, using the filtering nature of cavities to correct undesired frequency components that appear throughout the propagation of the pulses in the waveguide due to SPM or XPM effects.

With regards to the cavity-waveguide tool on its own, it could readily be used to evaluate inter-pulse interaction, for instance by running the simulation with a few number of pulses as input, separated by a certain amount of time. Generally, it would be of interest to employ the developed cavity-waveguide tool to design practical devices by varying the modal characteristics of the waveguide and cavities, the number of the latter, and also the relative position between all elements. For instance, one idea would be to employ the tool in order to find the right configuration for the device to be used as an integrated optical buffer.

As a final point, it would be relevant to analyse, by employing similar CMT formalisms as we have done in this work, the pulsed dynamics in arrays of dispersion-engineered photonic waveguides. These structures are of interest since they are being proposed to increase the capacity of optical interconnects (mode-division-multiplexing [97]) as well as to spatially separate modes [139].

Bibliography

[1] D. Miller, "Rationale and challenges for optical interconnects to electronic chips", Proc. IEEE **88**, 728 (2000).

[2] A. Shacham, K. Bergman, and L. P. Carloni, "Photonic networks-on-chip for future generations of chip multiprocessors", IEEE Trans. Comput. **57**, 1246 (2008).

[3] F. Benner, M. Ignatowski, J. A. Kash, D. M. Kuchta, and M. B. Ritter, "Exploitation of optical interconnects in future server architectures", IBM J. Res. Dev. **49**, 755 (2005).

[4] J. A. Kash, A. F. Benner, F. E. Doany, D. M. Kuchta, B. G. Lee, P. K. Pepeljugoski, L. Schares, C. L. Schow, and M. Taubenblatt, "Optical Interconnects in Exascale Supercomputers", in 23rd Annual Meeting of the IEEE Photonics Society, 483 (2010).

[5] T. Ibrahim, W. Cao, Y. Kim, J. Li, J. Goldhar, P.-T. Ho, and C. Lee, "All-optical switching in a laterally coupled microring resonator by carrier injection", IEEE Photon. Technol. Lett. **15**, 36 (2003).

[6] V. Van, T. Ibrahim, K. Ritter, P. Absil, F. Johnson, R. Grover, J. Goldhar, and P.-T. Ho, "All-optical nonlinear switching in gaas-algaas microring resonators", IEEE Photon. Technol. Lett. **14**, 74 (2002).

[7] V. R. Almeida, C. A. Barrios, R. R. Panepucci, and M. Lipson, "All-optical control of light on a silicon chip", Nature **431**, 1081 (2004).

[8] J. S. Levy, A. Gondarenko, M. A. Foster, A. C. Turner-Foster, A. L. Gaeta, and M. Lipson, "Cmos-compatible multiple-wavelength oscillator for on-chip optical interconnects", Nat. Photonics **4**, 37 (2010).

[9] R. A. Soref, "The past, present, and future of silicon photonics", IEEE J. Sel. Top. Quantum Electron. **12**, 1678 (2006).

[10] H. Subbaraman, X. Xu, A. Hosseini, X. Zhang, Y. Zhang, D. Kwong, and R. T. Chen, "Recent advances in silicon-based passive and active optical interconnects", Opt. Express **23** 2487 (2015).

[11] R. Claps, D. Dimitropoulos, V. Raghunathan, Y. Han, and B. Jalali, "Observation of stimulated raman amplification in silicon waveguides", Opt. Express **11**, 1731 (2003).

[12] R. L. Espinola, J. I. Dadap, R. M. Osgood, S. J. McNab, and Y. A. Vlasov, "Raman amplification in ultrasmall silicon-on-insulator wire waveguides", Opt. Express **12**, 3713 (2004).

[13] I.-W. Hsieh, X. Chen, J. I. Dadap, N. C. Panoiu, R. M. Osgood, S. J. McNab, and Y. A. Vlasov, "Ultrafast-pulse self-phase modulation and third-order dispersion in si photonic wire-waveguides", Opt. Express **14**, 12380 (2006).

[14] L. Yin, Q. Lin, and G. P. Agrawal, "Soliton fission and supercontinuum generation in silicon waveguides", Opt. Lett. **32**, 391 (2007).

[15] H. Fukuda, K. Yamada, T. Shoji, M. Takahashi, T. Tsuchizawa, T. Watanabe, J. i. Takahashi, and S. i. Itabashi, "Four-wave mixing in silicon wire waveguides", Opt. Express **13**, 4629 (2005).

[16] N. C. Panoiu, X. Chen, and R. M. Osgood, "Modulation instability in silicon photonic nanowires", Opt. Lett. **31**, 3609 (2006).

[17] X. Chen, N. C. Panoiu, I. Hsieh, J. I. Dadap, and R. M. Osgood, "Third-order dispersion and ultrafast-pulse propagation in silicon wire waveguides", IEEE Photon. Technol. Lett. **18**, 2617 (2006).

[18] L. Zhang, Q. Lin, Y. Yue, Y. Yan, R. G. Beausoleil, A. Agarwal, L. C. Kimerling, J. Michel, and A. E. Willner, "On-chip octave-spanning supercontinuum in nanostructured silicon waveguides using ultralow pulse energy", IEEE J. Sel. Top. Quantum Electron. **18**, 1799 (2012).

[19] T. Tekin, N. Pleros, R. Pitwon, and A. Hakansson, *Optical interconnects for data centers*, 1st ed., Woodhead Publishing, Elsevier, 2017.

[20] B. Song, C. Stagarescu, S. Ristic, A. Behfar, and J. Klamkin, "3D integrated hybrid silicon laser", Opt. Express **24**, 10435 (2016).

[21] S. Ek, P. Lunnemann, Y. Chen, E. Semenova, K. Yvind, and J. Mork, "Slow-light-enhanced gain in active photonic crystal waveguides", Nat. Com. **5**, 5039 (2014).

[22] N. C. Panoiu, M. Bahl, and R. M. Osgood, "All-optical tunability of a nonlinear photonic crystal channel drop filter", Opt. Express **12**, 1605 (2004).

[23] Y. Akahane, T. Asano, B. Song, and S. Noda, "High-q photonic nanocavity in a two-dimensional photonic crystal", Nature **425**, 944 (2003).

[24] J. Joannopoulos, S. Johnson, J. Winn, and R. Meade, *Photonic crystals: molding the flow of light*, 2nd ed., Princeton Univ. Press, 2008.

[25] A. Mekis, J. C. Chen, I. Kurland, S. Fan, P. R. Villeneuve, and J. D. Joannopoulos, "High transmission through sharp bends in photonic crystal waveguides", Phys. Rev. Lett. **77**, 3787 (1996).

[26] S. Noda, K. Tomoda, N. Yamamoto, and A. Chutinan, "Full three-dimensional photonic bandgap crystals at near-infrared wavelengths", Science **289**, 604 (2000).

[27] J. Li, T. P. White, L. O'Faolain, A. Gomez-Iglesias, and T. F. Krauss, "Systematic design of flat band slow light in photonic crystal waveguides", Opt. Express **16**(9), 6227 (2008).

[28] T. F. Krauss, "Slow light in photonic crystal waveguides", Journal of Physics D: Applied Physics **40**(9), 2666 (2007).

[29] M. Notomi, E. Kuramochi, and T. Tanabe, "Large-scale arrays of ultrahigh-q coupled nanocavities", Nat. Photonics **2**, 741 (2008).

[30] M. Soljačić, S. G. Johnson, S. Fan, M. Ibanescu, E. Ippen, and J. D. Joannopoulos, "Photonic-crystal slow-light enhancement of nonlinear phase sensitivity", J. Opt. Soc. Am. B. **19**, 2052 (2002).

[31] T. Baba, "Slow light in photonic crystals", Nat. Photonics **2**, 465 (2008).

[32] Y. A. Vlasov, M. O'Boyle, H. F. Hamann, and S. J. McNab, "Active control of slow light on a chip with photonic crystal waveguides", Nature **438**, 65 (2005).

[33] B. Corcoran, C. Monat, C. Grillet, D. J. Moss, B. J. Eggleton, T. P. White, L. O'Faolain, and T. F. Krauss, "Green light emission in silicon through slow-light enhanced third-harmonic generation in photonic-crystal waveguides", Nat. Photonics **3**, 206 (2009).

[34] W. Bogaerts, R. Baets, P. Dumon, V. Wiaux, S. Beckx, D. Taillaert, B. Luyssaert, J. V. Campenhout, P. Bienstman, and D. V. Thourhout, "Nanophotonic waveguides in silicon-on-insulator fabricated with cmos technology", IEEE J. Lightwave Technol. **23**, 401 (2005).

[35] S. Assefa, W. M. J. Green, A. Rylyakov, C. Schow, F. Horst, and Y. A. Vlasov, "Cmos integrated nanophotonics - enabling technology for exascale computing systems", Optical Fiber Communication Conference and Exposition and the National Fiber Optic Engineers Conference, Los Angeles, CA, USA (2011).

[36] Y. A. Vlasov, "Silicon cmos-integrated nano-photonics for computer and data communications beyond 100g", IEEE Communications Magazine **50**, 67 (2012).

[37] D. Thomson, A. Zilkie, J. E. Bowers, T. Komljenovic, G. T. Reed, L. Vivien, D. Marris-Morini, E. Cassan, L. Virot, J.-M. Fedeli, J.-M. Hartmann, J. H. Schmid, D.-X. Xu, F. Boeuf, P. OBrien, G. Z. Mashanovich, and M. Nedeljkovic, "Roadmap on silicon photonics", Journal of Optics **18**(7), 073003 (2016).

[38] R. Halir, P.J. Bock, P. Cheben, A. Ortega-Monux, C. Alonso-Ramos, J.H. Schmid, J. Lapointe, D.X. Xu, J.G. Wanguemert-Perez, I. Molina-Fernandez and S. Janz, "Waveguide subwavelength structures: a review of principles and applications", Laser Photonics Rev. **9**, 25 (2014).

[39] R. M. Osgood, N. C. Panoiu, J. I. Dadap, X. Liu, X. Chen, I.-W. Hsieh, E. Dulkeith, W. M. Green, and Y. A. Vlasov, "Engineering nonlinearities in nanoscale optical systems: physics and applications in dispersion-engineered silicon nanophotonic wires", Adv. Opt. Photon. **1**, 162 (2009).

[40] D. J. Blumenthal, R. Heideman, D. Geuzebroek, A. Leinse, and C. Roeloffzen, "Silicon Nitride in Silicon Photonics", Proc. IEEE **106**(12), 2209 (2018).

[41] L. Chang, G. D. Cole, G. Moody, and J. E. Bowers, "CSOI: Beyond Silicon-on-Insulator Photonics", Opt. Photonics News **33**, 26 (2022).

[42] I. Aharonovich, A. D. Greentree, and S. Prawer, "Diamond photonics", Nat. Photonics **5**, 397 (2011).

[43] F. Xia, M. Rooks, L. Sekaric, and Y. Vlasov, "Ultra-compact high order ring resonator filters using submicron silicon photonic wires for on-chip optical interconnects", Opt. Express **15**, 11934 (2007).

[44] C.-Y. Chao, W. Fung, and L. J. Guo, "Polymer microring resonators for biochemical sensing applications", IEEE J. Sel. Top. Quantum Electron. **12**, 134 (2006).

[45] H. Jung, C. Xiong, K. Y. Fong, X. Zhang, and H. X. Tang, "Optical frequency comb generation from aluminium nitride microring resonator", Opt. Lett. **38**, 2810 (2013).

[46] G. P. Agrawal, *Nonlinear fiber optics*, 3rd ed., St. Louis, Missouri, USA: Academic Press, 2001.

[47] L. Pavesi and D. J. Lockwood, *Silicon photonics*, 1st ed., Springer Berlin, Heidelberg, 2004.

[48] G. T. Reed and A. P. Knights, *Silicon photonics: an introduction*, 1st ed., Wiley, 2004.

[49] T. K. Liang and H. K. Tsang, "Nonlinear absorption and raman scattering in silicon-on-insulator optical waveguides", IEEE J. Quantum Electron. **10**, 1149 (2004).

[50] P. Latawiec, V. Venkataraman, M. J. Burek, B. J. M. Hausmann, I. Bulu and M. Loncar, "On-chip diamond Raman laser", Optica **2**, 924 (2015).

[51] T. Schröder, S. L. Mouradian, J. Zheng, M. E. Trusheim, M. Walsh, E. H. Chen, L. Li, I. Bayn, and D. Englund, "Quantum nanophotonics in diamond [Invited]", J. Opt. Soc. Am. B **33**(4), B65 (2016).

[52] R. W. Boyd, *Nonlinear optics*, 3rd ed., Academic Press, 2008.

[53] S. G. Johnson and J. D. Joannopoulos, "Block-iterative frequency-domain methods for maxwells equations in a planewave basis", Opt. Express **8**, 173 (2001).

[54] X. Yang and C. W. Wong, "Design of photonic band gap nanocavities for stimulated raman amplification and lasing in monolithic silicon", Opt. Express **13**, 4723 (2005).

[55] R. D. Group, "Bandsolve photonics software", www.rsoftdesign.com.

[56] A. Oskooi, D. Roundy, M. Ibanescu, P. Bermel, J. Joannopoulos, and S. Johnson, "Meep: A flexible free-software package for electromagnetic simulations by the fdtd method", Computer Physics Communications **181**, 687 (2010).

[57] X.Chen, N.C.Panoiu, and R.M.Osgood, "Theory of raman-mediated pulsed amplification in silicon-wire waveguides", IEEE J. Quantum Electron. **42**, 160 (2006).

[58] E.Dulkeith, F.Xia, L.Schares, W.M.J.Green, and Y.A.Vlasov, "Group index and group velocity dispersion in silicon-on-insulator photonic wires", Opt. Express **14**, 3853 (2006).

[59] A.C.Turner, C.Manolatou, B.S.Schmidt, M.Lipson, M.A.Foster, J. Sharping, and A. L. Gaeta, "Tailored anomalous group-velocity dispersion in silicon channel waveguides", Opt. Express **14**, 4357 (2006).

[60] L.Yin, Q.Lin, and G.P.Agrawal, "Dispersion tailoring and soliton propagation in silicon waveguides", Opt. Lett. **31**, 1295 (2006).

[61] S. Lavdas and N. C. Panoiu, "Theory of pulsed four-wave mixing in one-dimensional silicon photonic crystal slab waveguides", Phys. Rev. B **93**, 115435 (2016).

[62] J. Zhang, Q. Lin, G. Piredda, R. W. Boyd, G. P. Agrawal, and P. M. Fauchet, "Anisotropic nonlinear response of silicon in the near-infrared region", Appl. Phys. Lett. **91**(7), 071113 2007.

[63] X. Chen, N. C. Panoiu, and R. M. Osgood, "Theory of Raman-Mediated Pulsed Amplification in Silicon-Wire Waveguides", IEEE J. Quantum Electron. **42**, 160 (2006).

[64] R. Soref and B. Bennett, "Electrooptical effects in silicon", IEEE J. Quantum Electron. **23**, 123 (1987).

[65] P. A. Temple and C. E. Hathaway, "Multiphonon raman spectrum of silicon", Phys. Rev. B **7**, 3685 (1973).

[66] R. Loudon, "The raman effect in crystals", Adv. Phys. **13**, 423 (1964).

[67] B. Jalali, R. Claps, D. Dimitropoulos, and V.Raghunathan, "Light generation, amplification, and wavelength conversion via stimulated raman scattering in silicon microstructures", Topics Appl. Phys. **94**, 199 (2004).

[68] Y. Shen, N. C. Harris, S. Skirlo, M. Prabhu, T. Baehr-Jones, M. Hochberg, X. Sun, S. Zhao, H. Larochelle, D. Englund, and M. Soljačić, "Deep learning with coherent nanophotonic circuits", Nat. Photonics **11**, 441 (2017).

[69] N. C. Harris, G. R. Steinbrecher, M. Prabhu, Y. Lahini, J. Mower, D. Bunandar, C. Chen, F. N. C. Wong, T. Baehr-Jones, M. Hochberg, S. Lloyd, and D. Englund, "Quantum transport simulations in a programmable nanophotonic processor", Nat. Photonics **11**, 447 (2017).

[70] D. A. B. Miller, "Meshing optics with applications", Nat. Photonics **11**, 403 (2017).

[71] J. Leuthold, C. Koos, and W. Freude, "Nonlinear silicon photonics", Nat. Photonics **4**, 535 (2010).

[72] I. Hartl, X. D. Li, C. Chudoba, R. K. Ghanta, T. H. Ko, J. G. Fujimoto, J. K. Ranka, and R. S. Windeler, "Ultrahigh-resolution optical coherence tomography using continuum generation in an air–silica microstructure optical fiber", Opt. Lett. **26**, 608 (2001).

[73] I.-W. Hsieh, X. Chen, X. Liu, J. I. Dadap, N. C. Panoiu, C.-Y. Chou, F. Xia, W. M. Green, Y. A. Vlasov, and R. M. Osgood, "Supercontinuum generation in silicon photonic wires", Opt. Express **15**, 15242 (2007).

[74] L. D. Negro, "Light emission from silicon nanostructures: Past, present and future perspectives", in Conference on Lasers and Electro-Optics/International Quantum Electronics Conference, OSA Technical Digest (CD), CTuN1 (2009).

[75] V. Sih, S. Xu, Y.-H. Kuo, H. Rong, M. Paniccia, O. Cohen, and O. Raday, "Raman amplification of 40 gb/s data in low-loss silicon waveguides", Opt. Express **15**, 357 (2007).

[76] V. Raghunathan, D. Borlaug, R. R. Rice, and B. Jalali, "Demonstration of a mid-infrared silicon raman amplifier", Opt. Express **15**, 14355 (2007).

[77] K. Yamada, H. Fukuda, T. Tsuchizawa, T. Watanabe, T. Shoji, and S. Itabashi, "All-optical efficient wavelength conversion using silicon photonic wire waveguide", IEEE Photon. Technol. Lett. **18**, 1046 (2006).

[78] W. Astar, J. B. Driscoll, X. Liu, J. I. Dadap, W. M. J. Green, Y. A. Vlasov, G. M. Carter, and R. M. Osgood, "Conversion of 10 gb/s nrz-ook to rz-ook utilizing xpm in a si nanowire", Opt. Express **17**, 12987 (2009).

[79] K. Zinoviev, L. G. Carrascosa, J. S. del Rio, B. Sepulveda, C. Dominguez, and L. M. Lechuga, "Silicon photonic biosensors for lab-on-a-chip applications", Advances in Optical Technologies **2008**, 383927 (2008).

[80] J. T. Robinson, L. Chen, and M. Lipson, "On-chip gas detection in silicon optical microcavities", Opt. Express **16**, 4296 (2008).

[81] K. Yamada, M. Notomi, A. Shinya, I. Yokohama, T. Shoji, T. Tsuchizawa, T. Watanabe, J.-I. Takahashi, E. Tamechika, and H. Morita, "Soi-based photonic crystal line-defect waveguides", Proc. SPIE Active and Passive Optical Components for WDM Communications II **4870**, 324 (2002).

[82] D. Mori, S. Kubo, H. Sasaki, and T. Baba, "Experimental demonstration of wide-band dispersion-compensated slow light by a chirped photonic crystal directional coupler", Opt. Express **15**, 5264 (2007).

[83] D. Mori and T. Baba, "Wideband and low dispersion slow light by chirped photonic crystal coupled waveguide", Opt. Express **13**, 9398 (2005).

[84] E. Kuramochi, T. Tanabe, H. Taniyama, M. Kato, and M. Notomi, "Observation of heavy photon state in ultrahigh-;q photonic crystal coupled resonator chain", in Conference on Lasers and Electro-Optics/Quantum Electronics and Laser Science Conference and Photonic Applications Systems Technologies, OSA Technical Digest (CD), QMG2 (2007).

[85] S. Lavdas, J. B. Driscoll, R. R. Grote, R. M. Osgood, and N. C. Panoiu, "Pulse compression in adiabatically tapered silicon photonic wires", Opt. Express **22**, 6296 (2014).

[86] A. Blanco-Redondo, C. Husko, D. Eades, Y. Zhang, J. Li, T. F. Krauss, and B. J. Eggleton, "Observation of soliton compression in silicon photonic crystals", Nat. Com. **5**, 3160 (2014).

[87] R. Mildren and J. Rabeau, *Optical engineering of diamond*, 1st ed., Weinheim, Germany: Wiley - VCH, 2013.

[88] B. J. M. Hausmann, I. Bulu, V. Venkataraman, P. Deotare and M. Loncar, "Diamond nonlinear photonics", Nat. Photonics **8**, 369 (2014).

[89] J. Liu, E. Lucas, A. S. Raja, J. He, J. Riemensberger, R. N. Wang, M. Karpov, H. Guo, R. Bouchand and T. J. Kippenberg ,"Photonic microwave generation in the X- and K-band using integrated soliton microcombs", Nat. Photonics **14**, 486 (2020).

[90] J. W. Cooley and J. W. Tukey, "An algorithm for the machine calculation of complex fourier series", Math. Comp. **19**, 297 (1965).

[91] W. H. Press, S. A. Teukolsky, W. T. Vetterling, and B. P. Flannery, *Numerical recipes in C: The art of scientific computing*, 2nd ed., Cambridge Univ. Press, 1992.

[92] S. Coen, H. G. Randle, T. Sylvestre, and M. Erkintalo, "Modeling of octave-spanning Kerr frequency combs using a generalized mean-field Lugiato-Lefever model", Opt. Lett. **38**, 37 (2013).

[93] J. A. Tatum, D. Gazula, L. A. Graham, J. K. Guenter, R. H. Johnson, J. King, C. Kocot, G. D. Landry, I. Lyubomirsky, A. N. MacInnes, E. M. Shaw, K. Balemarthy, R. Shubochkin, D. Vaidya, M. Yan, and F. Tang, "VCSEL-Based Interconnects for Current and Future Data Centers", J. Lightwave Technol. **33**(4), 727 (2015).

[94] M. Burek, Y. Chu, M. S. Z. Liddy, P. Patel, J. Rochman, S. Meesala, W. Hong, Q. Quan, M. D. Lukin, and M. Loncar, "High quality-factor optical nanocavities in bulk single-crystal diamond", Nat. Com. **5**, 5718 (2014).

[95] A.L. Gaeta, M. Lipson, and T.J. Kippenberg, "Photonic-chip-based frequency combs", Nat. Photonics **13**, 158 (2019).

[96] W. Bogaerts, P. De Heyn, T. Van Vaerenbergh, K. De Vos, S. Kumar Selvaraja, T. Claes, P. Dumon, P. Bienstman, D. Van Thourhout, and R. Baets, "Silicon microring resonators", Laser Photonics Rev. **6**, 47 (2011).

[97] L.-W. Luo, N. Ophir, C. P. Chen, L. H. Gabrielli, C. B. Poitras, K. Bergmen, and M. Lipson, "Wdm-compatible mode-division multiplexing on a silicon chip", Nat. Com. **5**, 3069 (2014).

[98] R. R. Grote and L. C. Bassett, "Single-mode optical waveguides on native high-refractive-index substrates", APL Photonics **1**(7), 071302 (2016).

[99] A. Shams-Ansari, P. Latawiec, Y. Okawachi, V. Venkataraman, M. Yu, B. Desiatov, H. Atikian, G. L. Harris, N. Picque, A. L. Gaeta, and M. Loncar, "Supercontinuum generation in angle-etched diamond waveguides", Opt. Lett. **44**(16), 4056 (2019).

[100] N. C. Panoiu, J. F. McMillan, and C.W.Wong, "Theoretical analysis of pulse dynamics in silicon photonic crystal wire waveguides", IEEE J. Sel. Top. Quantum Electron. **16**, 257 (2010).

[101] K. Ikeda, R. E. Saperstein, N. Alic, and Y. Fainman, "Thermal and Kerr nonlinear properties of plasma-deposited silicon nitride/silicon dioxide waveguides", Opt. Express **16**(17), 12987 (2008).

[102] N. C. Panoiu, X. Liu, and R. M. Osgood, "Self-steepening of ultrashort pulses in silicon photonic nanowires", Opt. Lett. **34**(7), 947 (2009).

[103] J. M. P. Almeida, C. Oncebay, J. P. Siqueira, S. R. Muniz, L. De Boni and C. R. Mendonca, "Nonlinear optical spectrum of diamond at femtosecond regime", Sci. Rep. **7**(1), 14320 (2017).

[104] T. M. Kardas, B. Ratajska-Gadomska, W. Gadomski, A. Lapini, and R. Righini, "The role of stimulated Raman scattering in supercontinuum generation in bulk diamond", Opt. Express **21**(20), 24201 (2013)

[105] A. J. Scroggie, W. J. Firth, G. S. McDonald, M. Tlidi, R. Lefever and L. A. Lugiato, "Pattern formation in a passive Kerr cavity", Chaos, Solitons & Fractals **4**(8-9), 1323 (1994).

[106] M. Tlidi and L. Gelens, "High-order dispersion stabilizes dark dissipative solitons in all-fiber cavities", Opt. Lett. **35**(3), 306 (2010).

[107] M. Tlidi, L. Bahloul, L. Cherbi, A. Hariz and S. Coulibaly, "Drift of dark cavity solitons in a photonic-crystal fiber resonator", Phys. Rev. A **88**(3), 035802 (2013).

[108] A. G. Vladimirov, S. V. Gurevich and M. Tlidi, "Effect of Cherenkov radiation on localized-state interaction", Phys. Rev. A **97**(1), 013816 (2018).

[109] A. G. Vladimirov, M. Tlidi and M. Taki, "Dissipative soliton interaction in Kerr resonators with high-order dispersion", Phys. Rev. A **103**(6), 063505 (2021).

[110] L. A. Lugiato and R. Lefever, "Spatial Dissipative Structures in Passive Optical Systems", Phys. Rev. Lett. **58**(21), 2209 (1987).

[111] M. Haelterman, S. Trillo, and S. Wabnitz, "Dissipative modulation instability in a nonlinear dispersive ring cavity", Opt. Commun. **91**(6), 401 (1992).

[112] P. Kockaert, P. Tassin, G. Van der Sande, I. Veretennicoff and M. Tlidi, "Negative diffraction pattern dynamics in nonlinear cavities with left-handed materials", Phys. Rev. A **74**(3), 033822 (2006).

[113] M. Tlidi, A. Mussot, E. Louvergneaux, G. Kozyreff, A. G. Vladimirov, and M. Taki, "Control and removal of modulational instabilities in low-dispersion photonic crystal fiber cavities", Opt. Lett. **32**(6), 662 (2007).

[114] J. E. Heebner, V. Wong, A. Schweinsberg, R. W. Boyd, and D. J. Jackson, "Optical Transmission Characteristics of Fiber Ring Resonators", IEEE J. Quantum Electron. **40**, 726 (2004).

[115] T. Christopoulos, O. Tsilipakos, N. Grivas and E. E. Kriezis, "Coupled-mode-theory framework for nonlinear resonators comprising graphene", Phys. Rev. E **94**(6), 062219 (2016).

[116] F. Benabid, J. C. Knight, G. Antonopoulos, and P. S. J. Russell, "Stimulated raman scattering in hydrogen-filled hollow-core photonic crystal fiber", Science **298**, 399 (2002).

[117] S. Coen, A. Chau, R. Leonhardt, J. Harvey, J. Knight, W. Wadsworth, and P. Russell, "Supercontinuum generation by stimulated raman scattering and parametric four-wave mixing in photonic crystal fibers", J. Opt. Soc. Am. B. **19**, 753 (2002).

[118] J. F. McMillan, X. Yang, N. C. Panoiu, R. M. Osgood, and C. W. Wong, "Enhanced stimulated raman scattering in slow-light photonic crystal waveguides", Opt. Lett. **31**, 1235 (2006).

[119] J. F. McMillan, M. Yu, D.-L. Kwong, and C. W. Wong, "Observation of spontaneous raman scattering in silicon slow-light photonic crystal waveguides", Appl. Phys. Lett. **93**, 251105 (2008).

[120] R. Loudon, "The raman effect in crystals", Adv. Phys. **50**, 813 (2001).

[121] A. W. Snyder and J. D. Love, *Optical Waveguide Theory*, Chapman and Hall, 1983.

[122] D. Michaelis, U. Peschel, C. Wächter, and A. Bräuer, "Reciprocity theorem and perturbation theory for photonic crystal waveguides", Phys. Rev. E **68**, 065601 (2003).

[123] T. Kamalakis and T. Sphicopoulos, "A new formulation of coupled propagation equations in periodic nanophotonic waveguides for the treatment of kerr-induced nonlinearities", IEEE J. Quantum Electron. **43**, 923 (2007).

[124] P. N. Butcher and D. Cotter, *The Elements of Nonlinear Optics*, Cambridge University Press, 1991.

[125] T. Kamalakis and T. Sphicopoulos, "A new formulation of coupled propagation equations in periodic nanophotonic waveguides for the treatment of kerr-induced nonlinearities", IEEE J. Quantum Electron. **43**, 923 (2007).

[126] T. Liang, L. Nunes, T. Sakamoto, K. Sasagawa, T. Kawanishi, M. Tsuchiya, G. Priem, D. V. Thourhout, P. Dumon, R. Baets, and H. Tsang, "Ultrafast all-optical switching by cross-absorption modulation in silicon wire waveguides", Opt. Express **13**, 7298 (2005).

[127] R. Ho, K. W. Mai, and M. A. Horowitz, "The future of wires", Proc. IEEE **89**, 490 (2001).

[128] T. Ibrahim, W. Cao, Y. Kim, J. Li, J. Goldhar, P. T. Ho, and C. Lee, "All-optical switching in a laterally coupled microring resonator by carrier injection", IEEE Photon. Technol. Lett. **15**, 36 (2003).

[129] Q. Lin, O. J. Painter, and G. Agrawal, "Nonlinear optical phenomena in silicon waveguides: Modeling and applications", Opt. Express **15**, 16604 (2007).

[130] J. I. Dadap, N. C. Panoiu, X. G. Chen, I. W. Hsieh, X. P. Liu, C. Y. Chou, E., Dulkeith, S. J., McNab, F. N. Xia, W. M. J. Green, L. Sekaric, Y. A. Vlasov, and R. M. Osgood, "Nonlinear-optical phase modification in dispersion-engineered Si photonic wires", Opt. Express **16**, 1280 (2008).

[131] J. B. Driscoll, R. M. Osgood, R. R. Grote, J. I. Dadap, and N. C. Panoiu, "Squeezing Light in Wires: Fundamental Optical Properties of Si Nanowire Waveguides", IEEE J. Lightwave Technol. **33**, 3116 (2015).

[132] S. Fan, P. R. Villeneuve, J. D. Joannopoulos, and H. Hauss, "Channel drop tunneling through localized states", Phys. Rev. Lett. **80**, 960 (1998).

[133] A. Faraon, E. Waks, D. Englund, I. Fushman, and J. Vuckovic, "Efficient photonic crystal cavity-waveguide couplers", Appl. Phys. Lett. **90**(7), 073102 (2007).

[134] A. R. M. Zain, N. P. Johnson, M. Sorel, and R. M. D. L. Rue, "Ultra high quality factor one dimensional photonic crystal/photonic wire micro-cavities in silicon-on-insulator (soi)", Opt. Express **16**, 12084 (2008).

[135] E. Waks, J. Vuckovic, "Coupled mode theory for photonic crystal cavity-waveguide interactio", Opt. Express **13**, 5064 (2005)

[136] S. Lavdas, *Optical pulse dynamics in sub-wavelength nano-patterned silicon photonic wires*, Ph. D. Thesis, University College London, 2015.

[137] Q. Ren, J. W. You, and N. C. Panoiu, "Giant enhancement of stimulated raman amplification in metasurfaces made of silicon photonic crystal nanocavities", Opt. Express **26**, 30383 (2018).

[138] E. Anderson, Z. Bai, J. Dongarra, A. Greenbaum, A. McKenney, J. Du Croz, S. Hammarling, J. Demmel, C. Bischof, and D. Sorensen, "Lapack: A portable lin-

ear algebra library for high-performance computers", in Supercomputing '90, IEEE Computer Society Press, Los Alamitos, CA, USA, 2 (1990).

[139] M. Heinrich, M.-A. Miri, S. Sttzer, R. El-Ganainy, S. Nolte, A. Szameit, and D. N. Christodoulides, "Supersymmetric mode converters", Nat. Com. **5**, 3698 (2014).

[140] H. Nishihara, M. Haruna, and T. Suhara, *Optical integrated circuits*, McGraw-Hill Book Company, 1989.

[141] A. Yariv and P. Yeh, *Photonics: optical electronics in modern communications*, 6th ed., Oxford University Press, 2007.